Petrogenesis of Proterozoic carbonatites and alkaline magmas from Ihouhaouene : In Ouzzal terrane, Western Hoggar, Algeria

Asma Djeddi

THESE POUR OBTENIR LE GRADE DE DOCTEUR DE L'UNIVERSITE DE MONTPELLIER

En Sciences de la Terre

École doctorale GAIA

Unité de recherche Géosciences Montpellier

En partenariat international avec l'Université des Sciences et de Technologie HOUARI BOUMEDIENE, Algérie

Pétrogenèse des carbonatites et magmas alcalins protérozoïques d'Ihouhaouene (terrane de l'In Ouzzal, Hoggar occidental, Algérie)

Présentée par Asma DJEDDI

Le 02 Juillet 2019

Sous la direction de Fleurice PARAT et Khadidja Ouzegane

Devant le jury composé de

Anne-Sylvie ANDRE-MAYER, Professeur, Géoressources - Université de Lorraine	Président du jury
Sébastien PILET, Professeur, Institut des Sciences de la Terre - Université de Lausanne	Rapporteur
Emilie BRUAND, Chargée de recherche, Laboratoire Magma et Volcans, Clermont-Ferrand	Examinatrice
Johann TUDURI, Ingénieur géologue, BRGM Orléans	Examinateur
Fleurice PARAT, Maître de conférence, Géosciences Montpellier - Université de Montpellier	Directrice de thèse
Khadidja OUZEGANE, Professeur, Université USTHB, Alger	Directrice de thèse
Jean-Louis BODINIER, Directeur de recherche, Géosciences Montpellier	Invité

GEOSCIENCES MONTPELLIER

ECOLE DOCTORALE GAÏA

THESE

présentée par

Asma DJEDDI

le 02 juillet 2019

en vue de l'obtention du

Doctorat de l'Université de Montpellier

spécialité : SCIENCES DE LA TERRE

Pétrogenèse des carbonatites et magmas alcalins protérozoïques d'Ihouhaouene (terrane de l'In Ouzzal, Hoggar occidental, Algérie)

Devant le jury composé de

Anne-Sylvie ANDRE-MAYER, Professeur, Géoressources - Université de Lorraine	**Président du jury**
Sébastien PILET, Professeur, Institut des Sciences de la Terre - Université de Lausanne	**Rapporteur**
Emilie BRUAND, Chargée de recherche, Laboratoire Magma et Volcans, Clermont-Ferrand	**Examinatrice**
Johann TUDURI, Ingénieur géologue, BRGM Orléans	**Examinateur**
Fleurice PARAT, Maître de conférence, Géosciences Montpellier - Université de Montpellier	**Directrice de thèse**
Khadidja OUZEGANE, Professeur, Université USTHB, Alger	**Directrice de thèse**
Jean-Louis BODINIER, Directeur de recherche, Géosciences Montpellier	**Invité**

Remerciements

Ce travail de thèse a pu voir le jour grâce à la participation des autorités, des guides de terrain et des chauffeurs durant ma mission de terrain dans le Hoggar. Je tiens à exprimer ma gratitude à Massinissa, Bouaalam et Basset pour l'aide qu'ils m'ont offerte lors de ces 15 jours de travail dans des conditions extrêmes dans le désert du Hoggar.

Je tiens en particulier à exprimer ma gratitude à mes directeurs de thèse :

Khadidja Ouzegane, merci de m'avoir proposé ce sujet passionnant et de m'avoir donner la chance de réaliser cette cotutelle de thèse. Merci pour tes encouragements et pour toutes les discussions lucratives à l'USTHB, à Montpellier ou par téléphone et de m'avoir fait confiance durant toutes ces années.

Fleurice Parat, je tiens particulièrement à te remercier pour toutes ces années de Carbonatites ! Merci de m'avoir initiée aux Processus magmatiques et d'avoir partagé avec moi la chasse aux trésors dans les britholites et les monazites. Oui, il ne me reste plus que! La phrase qui nous a fait tant rire. Merci d'avoir cru en moi et de m'avoir accompagnée jusqu'au bout de cette thèse.

Merci à *Jean Louis-Bodinier* de m'avoir donnée la chance de bénéficier et participer au Projet MEDYNA qui a financé une bonne partie de ma thèse et toutes les analyses réalisées dans le cadre de ma cotutelle. Merci pour toutes les discussions instructives et merci de m'avoir intégrée dans le monde de la modélisation géochimique.

Un grand merci à Jean-Marie Dautria (Dodo) pour tous les débats scientifiques et pourquoi pas parfois politiques ! Merci de m'avoir aidée dans tous les moments de stupeur des britholites et d'apatites et en général des carbonatites.

Je remercie très sincèrement les membres de mon jury, Anne-Sylvie ANDRE-MEYER, Sébastien PILET, Emilie BRUAND et Johan TUDURI d'avoir accepté d'évaluer mon travail et de m'avoir donnée des indications utiles pour la publication de mon travail.

Je souhaite remercier le laboratoire Géosciences Montpellier et l'équipe Manteau et Interface qui m'ont accueillis. Merci aux membres de l'équipe, et plus particulièrement Alain Vauchez pour son évaluation et son aide. Le travail que j'ai accompli pendant ma thèse n'aurait pas été possible sans les compétences de nombreuses personnes : Christophe Nevado, Doriane Delmas, Céline Martin, Léa Causse, Fabrice Barou, Bernard Boyer, Romain Lafay, Loïc Blanchard et Olivier Brugier.

Réaliser ce travail dans le contexte de la cotutelle n'aurait pas été possible sans ma famille, aussi loin mais toujours présente, qui m'a toujours encouragée et soutenue dans toutes mes idées et mes projets. Je souhaite remercier mon père Mohamed et ma mère Zakia, mes sœurs et mes frères, Massimo et Soussou pour leur soutien, leur patience et pour toutes les heures à discuter et me remonter le moral et l'intérêt qu'ils ont toujours porté à ce que je réalise. Merci d'avoir toujours été là et de m'avoir tant aidé.

Je souhaite aussi remercier tous mes très chers amis pour leur soutien et leur disponibilité à n'importe quelle heure du jour et de la nuit :

Merci particulièrement à Camille Tichadou, pour la super collocation de joie et de convivialité et toutes les heures de rire passées ensembles. Je ne te remercierai jamais assez pour toute l'aide que tu m'as apportée durant et à la fin de ma thèse, merci d'avoir été présente dans ces pires moments de stress et de m'avoir rendu les taches plus faciles. Merci pour tes conseils et explications et sans oublier la petite boule de douceur et de bonheur que tu nous as amené « Saul ». Merci pour les week-ends de détente avec Enora et Gaétan et les bons repas que tu m'as préparé.

Merci au Girl Power team, sans vous les copines ça n'allait pas être facile : Tiphaine, Lauranne, Enora, Camille et Justine. Merci pour tous les moments inoubliables passés ensembles, nos rires, nos folies et toutes les soirées de potins. Merci à Cam, Yves et Clément.

Je tiens à remercier Romain Lafay, pour son soutien et ses conseils qui sont arrivés un peu à la fin de ma thèse mais qui m'ont beaucoup aidé dans le développement de mes idées et en espérant que cela continue. Merci d'être là pour moi, à m'encourager et m'écrire même du Botswana !

Merci à Justine pour ton aide considérable pour les figures sur Illustrator ; à Rabia Benchaban pour toutes les discussions GeoEnglish et ton aide pour mon texte en anglais ; à Julie pour tes conseils et les discussions qu'on a eu.

Je souhaite par ailleurs remercier : Gaétan- avec tes blagues qui me font toujours autant rire, Enora- merci pour ta douceur et ton aide, Alex- t'inquiète pas je reprends le sport cette semaine, Christine- ta bonne humeur me fait toujours oublier mes bosbos, Cyprien- merci pour ta présence et ton aide jusqu'au bout, Thierry- tu m'as appris beaucoup de zir-conneries. Merci à Clément, Nestor, Agathe, Maël, Adeline, Timothée, Rémi, Romain pour la bonne ambiance et la bonne humeur dans la team des doctorants et pour toutes les discussions et les moments qu'on a partagé.

En dernier, je remercie très sincèrement tous mes amis et collègues en Algérie, Ahmed, Imene, Mydou et Zaki et toute l'équipe de la FSTGAT.

Pétrogenèse des carbonatites et magmas alcalins protérozoïques d'Ihouhaouene (terrane de l'In Ouzzal, Hoggar occidental, Algérie)

Asma DJEDDI*

Le craton archéen de l'In Ouzzal représente une succession d'événements intrusifs et métamorphiques depuis l'Eburnéen qui en font un marqueur important des processus géodynamiques à travers les temps géologiques. La région d'Ihouhaouene située au N-W du terrane de l'In Ouzzal en Algérie est unique de par la présence d'intrusions protérozoïques de carbonatites associées à des roches alcalines saturées. Ces carbonatites intracontinentales comptent parmi les plus anciennes et inhabituelles de par leurs diversités et la présence de minéraux à terres rares. Les carbonatites sont pegmatitiques ou bréchiques avec des fragments de syénite. Elles sont des calciocarbonatites composées de calcite (>50 vol.%), apatite, clinopyroxène et wollastonite et sont associées à des syénites rouges ou blanches présentes sous forme massive. Les syénites sont composées d'alternance de niveaux clairs de feldspaths alcalins rouges ou de wollastonites associées aux feldspaths blancs et de niveaux sombres d'apatites et de clinopyroxènes.

Les carbonatites et syénites forment une suite cogénétique caractérisée par une augmentation en SiO_2 et une diminution en CaO et CO_2. Les carbonatites ont des compositions en silice comprises entre 5 et 35 pds.%, 28 et 53 pds.% CaO et 11 à 36 pds.% CO_2. Les syénites montrent une forte teneur en K_2O (12 pds.%) et des teneurs très faibles en Na_2O (1 pds.%). Les carbonatites et syénites sont riches en éléments incompatibles avec des teneurs en REE supérieures à 7000 fois les chondrites et 1000 fois les chondrites dans les syénites, respectivement, et de fortes teneurs en U, Sr et Th. Les éléments en trace dans les minéraux magmatiques (apatite et pyroxène) mettent en évidence des processus complexes à l'origine de ces roches impliquant plusieurs étapes de cristallisation fractionnée et d'immiscibilité à partir d'un magma mélilititique riche en CO_2. Les minéraux des carbonatites riches en silice et des syénites blanches ont des signatures géochimiques similaires et se caractérisent par des rapports élevés en Nb/Ta typiques de magmas riches en carbonate par immiscibilité. Les syénites rouges ont des caractéristiques de liquides silicatés évolués par différentiation. Les minéraux des carbonatites pauvres en silice ont des rapports Nb/Ta très variables, sub-chondritiques (<10), indiquant une cristallisation à partir de liquides très évolués et la présence de magmas carbonatitiques tardifs.

Les apatites, en particuliers, enregistrent divers épisodes magmatiques et également supergènes. Elles présentent dans certaines roches une redistribution et un enrichissement en terres rares variables qui se caractérisent par des exsolutions de britholite dans les carbonatites riches en silice et monazite dans les carbonatites pauvres en silice. Ces exsolutions traduisent des rééquilibrations locales sub-solidus avec des fluides tardi-magmatiques de composition riche en Cl-Th-REE pour l'exsolution de la britholite et S-Ca-P-CO_2 pour les inclusions de monazite.

L'apatite et le zircon présents dans ces roches alcalines et carbonatites, ont permis de déterminer l'âge de mise en place du complexe magmatique de Ihouahouene à 2100 Ma syn-métamorphique et de confirmer l'âge panafricain de son exhumation. L'étude pétrologique, géochimique et géochronologique des carbonatites et syénites d'Ihouhaouene a permis de mettre en évidence l'origine magmatique de ces roches et de définir les interactions fluides-roches supergènes à l'origine des enrichissements en REE. Les carbonatites et syénites d'Ihouahouene proviennent d'un faible taux de fusion partielle d'un manteau Précambrien riche en CO_2. Plusieurs étapes de cristallisation fractionnée et d'immiscibilité ont permis la genèse de ces roches hybrides, piégées le long de grandes zones de cisaillement durant la période de transition Archéen /Eburnéen dans un régime extensif à l'In Ouzzal caractérisé par un environnement granulitique d'ultra-haute-température.

Mots-clés : Carbonatite ; Syénites ; Terres rares ; Immiscibilité ; Hybridation ; Ihouhaouene ; Archéen

* Géosciences Montpellier, Université Montpellier, Place E. Bataillon, 34095 Montpellier.

Petrogenesis of Proterozoic carbonatites and alkaline magmas from Ihouhaouene (In Ouzzal terrane, Western Hoggar, Algeria)

Asma DJEDDI *

The In Ouzzal Archaean craton represents a succession of intrusive and metamorphic events since Eburnean, and an important marker of geodynamic processes through geological time. The Ihouhaouene area located in the N-W of In Ouzzal terrane in Algeria is unique by the presence of Proterozoic carbonatite intrusions associated with silica-saturated alkaline rocks. These intracontinental carbonatites are among the oldest and exceptional because of their diversity and the presence of unusual rare earth minerals. Carbonatites are pegmatitic or brecciated with fragments of syenite. They are calciocarbonatites with calcite (> 50 vol.%), apatite, clinopyroxene and wollastonite and are associated with red or white syenites in massive outcrops. Syenites are composed of alternating light levels of red alkaline feldspar or wollastonite associated with white feldspar and dark levels of apatite and clinopyroxene.

Carbonatites and syenites form a cogenetic suite characterized by an increase in silica and decrease in calcium and CO_2 content. The carbonatites have silica content ranging from 5 to 35 wt.%, 28 to 53 wt.% CaO, and 11 to 36 wt.% CO_2. Syenites have high K_2O (12 wt.%) and low Na_2O content (1 wt.%). Carbonatites and syenites have high incompatible element concentrations with high REE content (7000*chondrites and 1000*chondrites, respectively) and high U, Pb, Sr and Th content. Trace elements (eg. Rare Earths, Nb-Ta, Zr-Hf) in magmatic minerals (apatite-pyroxene) of carbonatites and syenites reveal complex magmatic processes at the origin of these rocks involving several stages of fractional crystallization and immiscibility from a CO_2-rich melilititic magma. Silica-rich carbonatites and white syenites are characterized by high Nb/Ta, Y/Zr and Rb/Sr ratios, typical of carbonate-rich magmas by immiscibility. The red syenites have characteristics of immiscible differentiated silicate melt. Silica-poor carbonatite minerals have variable subchondritic Nb/Ta (<10) indicating crystallization from highly evolved liquids and the presence of late carbonatitic magmas.

Apatites, in particular, record various magmatic and supergene processes. They present, in some rocks, redistribution and enrichment in rare earth elements, which are characterized by exsolutions of britholite in silica-rich carbonatites and monazite-quartz-calcite inclusions in silica-poor carbonatites. These minerals reflect local sub-solidus re-equilibration with late-magmatic fluids rich in Cl-Th-REE for the exsolution of britholite and S-Ca-P-CO_2 for monazite inclusions.

The apatite and zircon present in these alkaline and carbonatite rocks, allow determination of the syn-metamorphic crystallization age of the Ihouahouene magmatic complex at 2100 Ma and confirm the pan-African age of its exhumation. The petrological, geochemical and geochronological study of Ihouhaouene carbonatites and syenites highlights the magmatic origin of these rocks and constrains the fluid-rock interactions at sub-solidus conditions leading to REE-enrichment. The carbonatites and syenites result from a low partial melting rate of a CO_2-rich Precambrian mantle. Several fractional crystallization and immiscibility stages allowed the genesis of these hybrid magmas, trapped along large shear-zones during the Archean/Eburnean transition period in the In Ouzzal terrane, characterized by extensive deformation in ultra-high-temperature granulitic environment.

Keywords: Carbonatite; Syenites; Rare earth element; Immiscibility; Hybridization; Ihouhaouene; Archaean

* Géosciences Montpellier, Université Montpellier, Place E. Bataillon, 34095 Montpellier.

Table des Matières

Introduction

Les carbonatites sont longtemps apparues comme des roches énigmatiques de par leur assemblage minéralogique proche des calcaires et leur association quasi-systématique à des roches magmatiques alcalines. Constituées de plus de 50 vol.% de carbonates (>30 pds.% CO_2) et moins de 20 pds.% SiO_2 (Le Maitre, 2002), les carbonatites sont donc principalement formées de cristaux de calcite ou de dolomite associées à de l'apatite et des pyroxènes et contiennent de nombreux minéraux accessoires telle la monazite et les minéraux à terres rares comme la bastnäsite, l'allanite et la britholite, leur conférant un intérêt économique indiscutable (Demaiffe, 2008).

Les complexes intrusifs alcalins sont généralement de forme cylindrique, avec des contacts nets à graduels le long des zones magmatiques et métasomatiques. Les carbonatites se présentent en forme de noyaux et/ou de veines affectant les autres roches du complexe (Heinrich, 1966). Elles peuvent être aussi de forme linéaire qui se distinguent des carbonatites annulaires par leur disposition structurale et leur mise en place en profondeur. Ces complexes se trouvent le long des zones de failles et sont syn- à post-orogéniques contrairement aux carbonatites annulaires qui sont généralement post-orogéniques d'âge essentiellement crétacé à actuel (Lapin et Plashko, 1988).

Les magmas carbonatitiques se mettent en place dans les zones de rift ou en domaine intraplaque affectant des blocs continentaux cratonisés (Demaiffe, 2008 ; Chakhmouradian et Wall, 2012) (Figure 1). Les carbonatites sont souvent associées à des complexes alcalins ignés intrusifs (Walter, 1991) en bordure de grands cratons et zones anorogéniques intraplaques (Bonin et Lameyre, 1978) ou le long des prolongements de failles dans les continents (Black *et al*. 1985). Deux hypothèses sont discutées sur le contexte de mise en place des carbonatites : la position des carbonatites en relation avec un stade de pré-rifting est l'hypothèse la plus appuyée pour expliquer leur mise en place (Henrich, 1966 ; Bowden, 1985) ; la seconde hypothèse propose l'existence d'un point chaud qui se traduit par une évolution des âges le long d'alignement des complexes carbonatitiques (Herz, 1977).

Les carbonatites existent depuis l'Archéen (e.g. les carbonatites et les syénites de la mine Lac Shortt au Québec, Nathalie Prud'Homme, 1990). Elles sont présentes aussi bien en contexte divergent (e.g. rifting) que convergent (e.g. subduction) et en domaine intraplaque (Figure 1). Sur le continent Africain, la plupart des massifs alcalins et carbonatitiques se distribuent autour des deux branches du rift Est-africain (Woolley, 1989) mais on les retrouve également sur le craton Ouest africain (Dahla, Bea *et al*. 2013, Montero *et al*. 2016) et en Afrique du Sud au Phalaborwa et en Namibie (Verwoerd, 1993). Cette activité peut être liée aux évènements orogéniques marqués par trois épisodes magmatiques : fin Protérozoïque, mi-Mésozoïque et Cénozoïque (Van Straaten, 1989 ; Woolley, 1989). La majorité des massifs alcalins et carbonatitiques déformés en Afrique et en Inde sont localisés dans les zones de suture d'âge protérozoïque correspondant à des zones de fermeture de domaines océaniques (Burke *et al*. 2003; Burke et Khan 2006 ; Demaiffe, 2008). La présence de

carbonatites dans un environnement océanique est rare. On peut citer celles du Cap Vert et des îles Canaries caractérisées par une minéralogie indiquant une source riche en H_2O (Cornu, 2017).

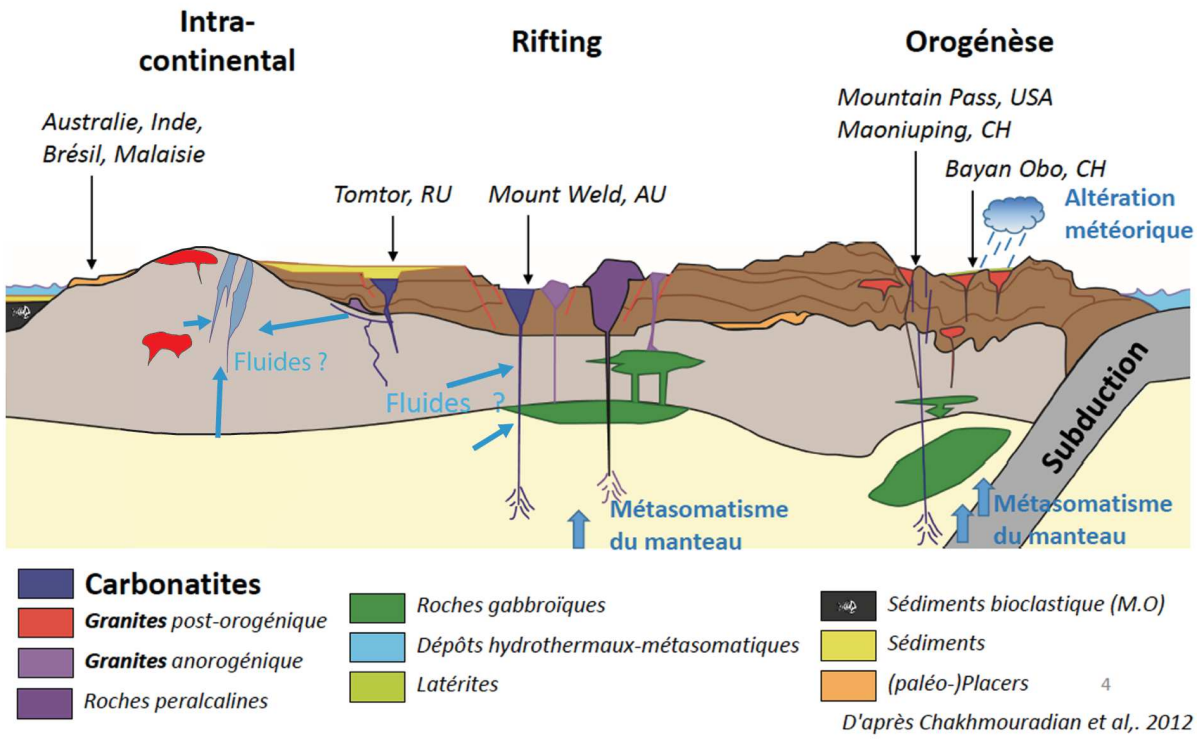

Figure 1. Représentation schématique des différents sites géodynamiques des magmas carbonatitiques en relation avec les gisements majeurs de dépôts de REE (modifiée après Chakhmouradian et Wall 2012).

Jusqu'à la fin des années cinquante, les carbonatites ont été cartographiées comme des calcaires (revue dans Louardi, 1994). En 1910, Daly, proposa le premier modèle d'assimilation de calcaire par les magmas granitiques. Puis en 1962, Pecora explique la genèse de ces roches alcalines par le transfert d'éléments volatils ou par précipitation à partir de solutions hydrothermales. Borodin et Pavlenko (1974) ont attribué quand à eux une origine métasomatique aux complexes ultrabasiques alcalins. L'origine magmatique des roches carbonatées a été longtemps rejetée pour des raisons physiques dû au point de fusion élevé de la calcite (1310ºC) incompatible avec les températures de mise en place des carbonatites obtenues à partir des équilibres minéralogiques (Bowen, 1928).

L'origine magmatique est définitivement acceptée pour les carbonatites après plusieurs travaux expérimentaux menés durant les 3 dernières décennies et suite aux études du seul volcan carbonatitique actif d'Oldoinyo Lengai en Tanzanie célèbre pour ses extrusions de natrocarbonatites (Bell et Keller, 1995). Cependant, les températures de mise en place des carbonatites font toujours l'objet de plusieurs études et controverses. Gittins (1979) propose une température de 885ºC à partir des carbonates pour les carbonatites de Goldary (Ontario). Romanchev et Sokolov (1980) proposent

des intervalles de températures de 550 à 850ºC et de 760 à 1180ºC à partir de l'étude des inclusions fluides dans diverses carbonatites (e.g. Kodvor, Péninsule de Kola, Russie).

Les derniers travaux expérimentaux proposent trois hypothèses selon lesquelles les magmas carbonatés sont: (1) des magmas mantelliques primaires provenant de la fusion partielle d'une péridotite carbonatée (Dalton et Wood, 1993 ; Gudfinnsson et Presnall, 2005 ; Dasgupta et Hirschmann, 2006) (Figure 2); (2) Un liquide résiduel d'une melilitite riche en CO_2 par cristallisation fractionnée (Gittins et Jago, 1998); (3) Un liquide immiscible d'un liquide silicaté saturé en CO_2 (Freestone et Hamilton, 1980 ; Baker et Wyllie, 1990 ; Brooker et Kajarsgaard, 2011).

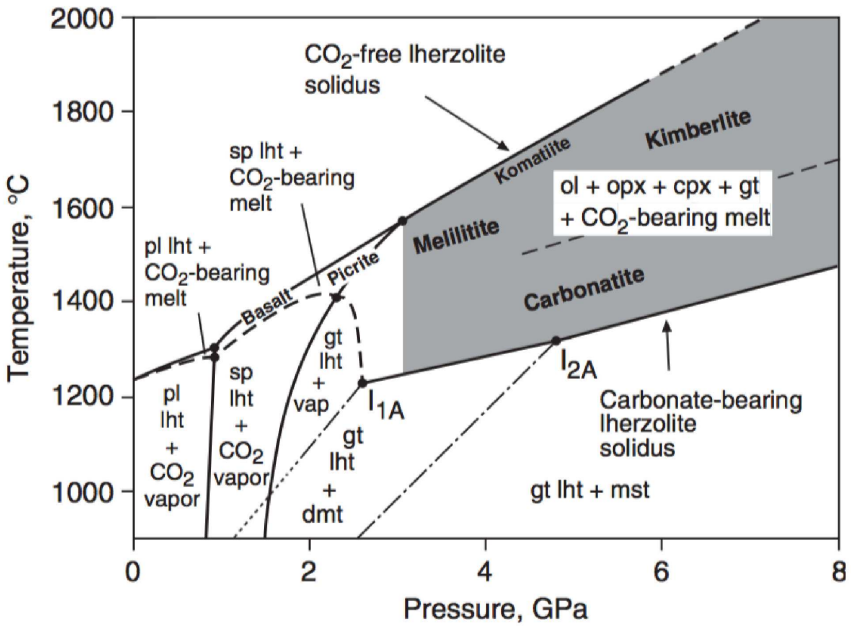

Figure 2. Conditions de formation des carbonatites dans le manteau à partir de la fusion partielle d'une lherzolite riche en CO_2 (Gudfinnsson et Presnall 2005).

(1) Les magmas carbonatitiques ont été reproduit expérimentalement à partir de faible taux de fusion d'un manteau péridotitique à olivine + opx + cpx + grenat riche en CO_2 à forte pression (P > 3GPa, Figure 2). Ces magmas sont principalement des magnesiocarbonatites (Dalton et Wood, 1993 ; Dasgupta et Hirschmann, 2006 ; Hamouda et Keshav, 2015 ; Figure 3). Les calciocarbonatites qui représentent la plupart des carbonatites naturelles peuvent être quand à elles le résultat de la fusion partielle d'une éclogite riche en CO_2 (Hammouda, 2003 ; Novella et Keshav, 2010 ; Hammouda et Keshav, 2015) (Figure 3). Cependant malgré les fortes teneur en calcium, les magmas expérimentaux diffèrent significativement des calciocarbonatites naturelles, souvent plus riches en fer et plus pauvres en magnésium (Figure 3) (Hammouda et Keshav, 2015).

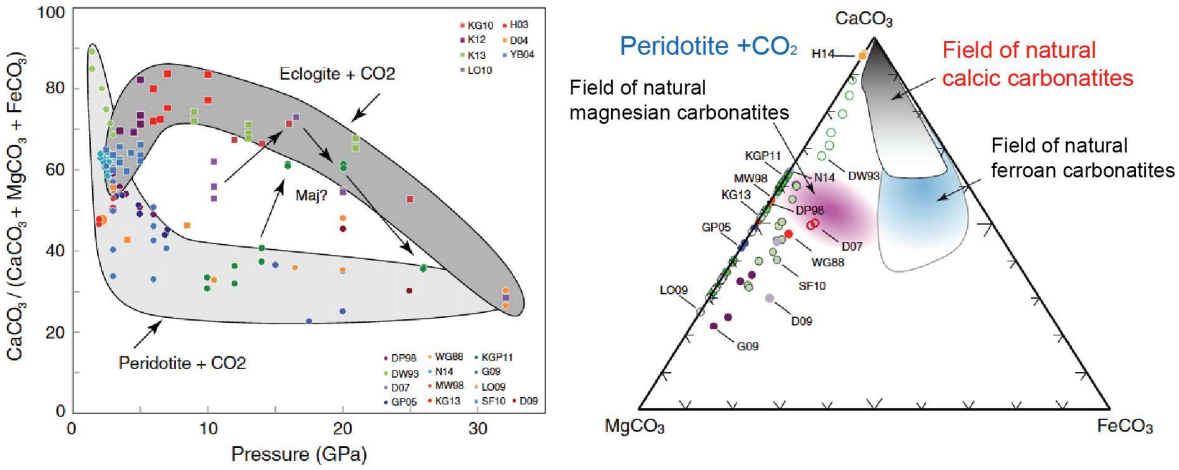

Figure 3. Compositions et conditions de formation des carbonatites issue de la fusion partielle d'une péridotite ou d'une éclogite riche en CO_2 et diagramme ternaire représentant la composition des carbonatites expérimentales et des carbonatites naturelles d'après Hammouda et Keshav, 2015.

(2) Les études pétrologiques et géochimiques démontrent que les carbonatites peuvent être également issues de la cristallisation fractionnée d'une melilitite riche en CO_2 (Dawson, 1998 ; Gittins et Jago, 1998 ; Baudouin *et al*. 2016 ; Weidendorfer *et al*. 2016). Les roches alcalines silicatés associées aux carbonatites représentent des suites plutoniques melteigite – ijolite - urite et néphéline-syenite et volcaniques nephelinite-phonolite dont les magmas parents sont des magmas sous-saturés mélilititiques (Figure 2). Ces séries alcalines sont composées essentiellement de mélilite, olivine, phlogopite, clinopyroxene, perovskite et néphéline. Si les derniers liquides lors de la différentiation de ces suites sont riches en carbonate, ils peuvent se différencier en carbonatite résiduelle et finalement un résidu carbothermal (Mitchell, 2005) (Figure 4).

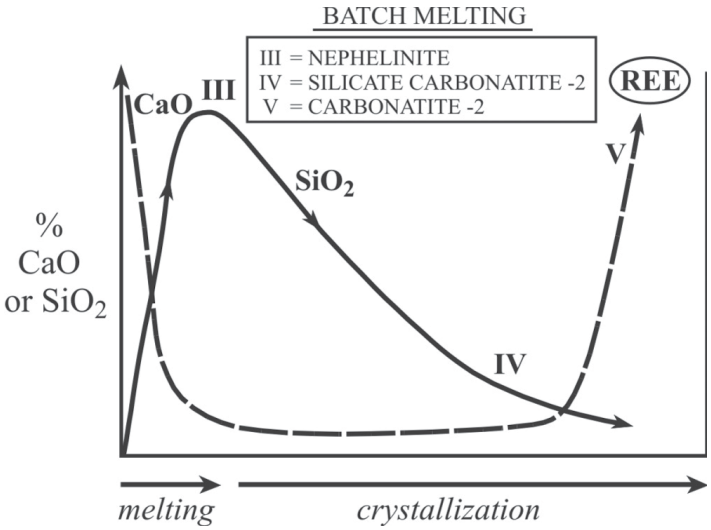

Figure 4. Modèle de formation des carbonatites par cristallisation fractionnée d'une melilitite (Mitchell, 2005).

(3) Les données expérimentales de Koster van Groos et Wyllie (1966, 1968), Freestone et Hamilton (1980), Kjarsgaard et Peterson (1991), Kjarsgaard *et al*. (1995), Dasgupta (2006), Mitchell (2009), Novella et Keshav (2010), Brooker et Kjarsgaard (2011) proposent l'hypothèse selon laquelle des compositions de carbonatite à faible taux d'aluminosilicates et riches en alcalins peuvent être produites par immiscibilité à partir d'un liquide silicaté per-alcalin (Figure 5). Ces travaux ont été réalisés dans des systèmes chimiques simples (SiO_2-Na_2O-Al_2O_3-CaO +CO_2 ; CaO-MgO-Al_2O_3-SiO_2 +CO_2) et des conditions différentes (0,1 à 3 GPa) afin de définir les profondeurs dans lesquelles les deux liquides coexistent (revue dans Brooker et Kjarsgaard 2011).

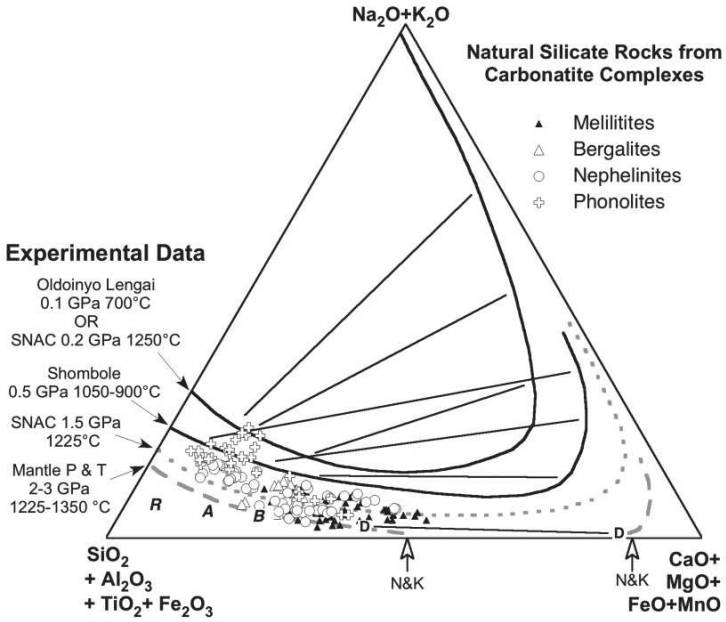

Figure 5. Diagramme ternaire d'immiscibilité des liquides silicatés et carbonatés et composition des roches silicatés phonolitiques, néphélinitiques et mélilititiques du Lengai d'après Brooker et Kjarsgaard, 2011.

Une des particularités des magmas carbonatitiques et alcalins, en plus de leur forte teneur en CO_2, est leur forte teneur en éléments incompatibles. Issus d'un très faible taux de fusion partielle, les magmas sous-saturés (e.g. melilitite) contiennent jusqu'à 100000 fois le manteau primitif et 10000 fois la croûte continentale (Chakhmouradian et Zaitsev, 2012 ; Figure 6). Les fortes teneurs en Terres Rares des carbonatites et magmas alcalins ont suscitées de nombreuses études expérimentales afin de déterminer la distribution et le fractionnement de ces éléments lors des processus de fusion partielle, de cristallisation et d'immiscibilité (Veksler *et al*. 1998, 2012 ; Martin *et al*. 2013). Présents en faible quantité dans les minéraux, les coefficients de partage déterminés expérimentalement ($Kd^{minéraux/magmas}$) permettent de contraindre l'origine des magmas et les processus de différentiation (Green *et al*. 1992 ; Sweeney *et al*. 1992 ; Blundy et Dalton, 2000 ; Klemme et Dalpé, 2003 ; Hammouda *et al*. 2010). De même les variations de concentrations en éléments en trace des liquides silicatés et des carbonatites en font un outil puissant pour déterminer les processus d'immiscibilité et de fusion partielle (Martin *et al*. 2013).

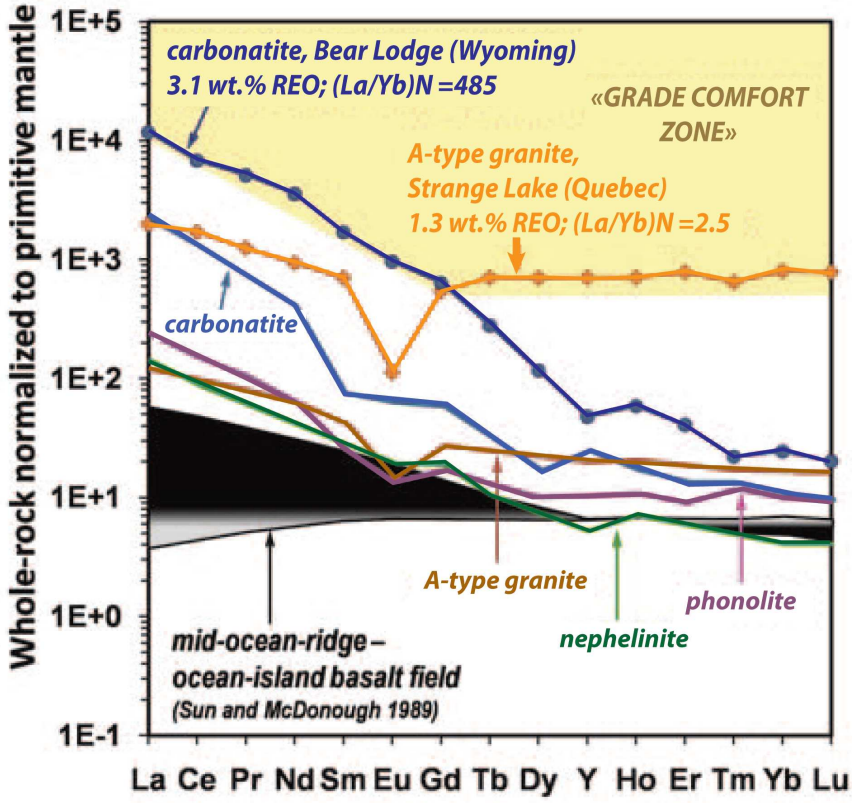

Figure 6. Composition moyenne des magmas alcalins anorogéniques comparée aux données de basaltes océaniques (normalisées par rapport au manteau primitif de McDonough et Sun 1995) (*Chakhmouradian et Zaitsev, 2012*).

Les liquides carbonatés sont enrichit en éléments lithophiles (LILE) (Rb, Ba, Sr) et en REE par rapport aux magmas alcalins silicatés (Martin *et al*. 2013). Les éléments LILE et REE sont préférentiellement distribués dans les magmas carbonatitiques lors des processus d'immiscibilité (Kd^{REE}>1 entre les liquides carbonatés et les liquides silicatés) et les coefficients de partage diminuent avec une augmentation de la température (Wendlandt et Wendy, 1979). Cependant, la pression peut-également être un facteur important, même si les solvus sont principalement contrôlés par la température et la composition (Wendlandt et Harrison, 1979 ; Veksler *et al*. 1998, 2012 ; Martin *et al*. 2013). Martin *et al*. (2013) démontrent que dans les systèmes hydratés, les différences de composition ont une faible influence sur le gap d'immiscibilité et que les coefficients de partage sont plus élevés d'un ordre de magnitude par rapport aux systèmes anhydres (Figure 7). Les systèmes alcalins riches en H_2O-SiO_2-Al_2O_3 favorisent une augmentation des coefficients de partage des éléments incompatibles dans les liquides carbonatés par rapport aux systèmes anhydres et sous-saturés en silice. Les éléments incompatibles HFSE (high field strength elements) comme le Zr, Hf, Nb, et Ta demeurent préférentiellement dans les liquides silicatés. On observe cependant des rapports Nb/Ta et Zr/Hf plus élevés dans les liquides carbonatés que dans les liquides silicatés durant l'immiscibilité et le fractionnement de ces éléments augmente avec la largeur du gap d'immiscibilité (Veksler *et al*. 1998, 2002, Martin *et al*. 2013).

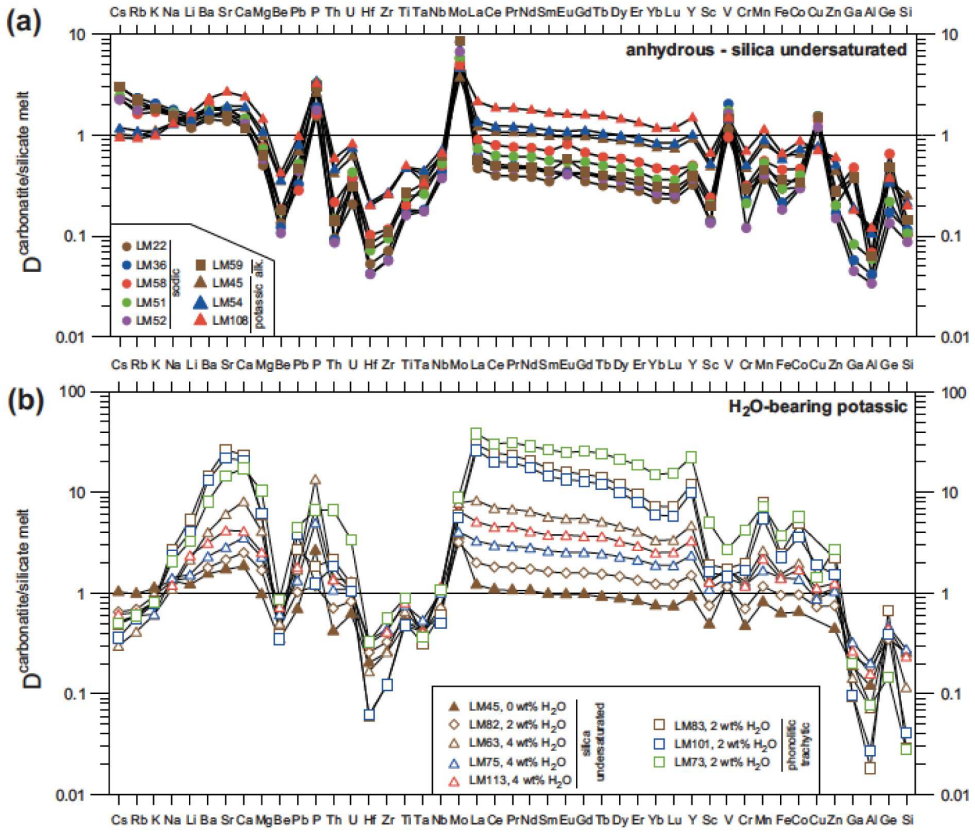

Figure 7. Les coefficients de partage des éléments entre les liquides carbonatés et silicatés. a. Magmas anhydres et sous-saturés en silice ; b. Magmas potassiques et riches en eau (Martin *et al*. 2013).

La plupart des carbonatites sont des roches plutoniques et leur mise en place implique souvent des processus tardi-magmatiques subsolidus (Chen *et al*. 2017). Les processus supergènes, à basses températures et en présences de fluides peuvent engendrer une remobilisation et un fractionnement des éléments incompatibles au sein des minéraux, qu'il est important de prendre en compte pour retracer l'évolution des magmas.

Les terres rares en particuliers sont remobilisés et peuvent former des minéraux sub-solidus riches en terres rares (e.g. monazite, bastnaésite) à partir des minéraux magmatiques (Harlov, 2015 ; Chen *et al*. 2017). Ces minéraux sont essentiels car concentrent les terres rares et autres métaux (Nb, Ta) qui sont des éléments chimiques essentiels pour de nombreuses industries modernes et le développement de produits de haute technologie en particulier dans le domaine de la transition énergétique et de la lutte contre les pollutions et le réchauffement climatique (Hatch, 2012). Bien qu'il ne soit pas aussi rares que leur nom l'indique, les gisements économiques de terres rares ne sont pas courants et la production mondiale d'éléments de terres rares ne provient que deux types de gisements (Chen *et al*. 2017) : (1) Les gisements liés aux carbonatites (Bayan Obo en Chine et le Mountain Pass aux USA) qui fournissent les terres rares légères (LREE) et (2) les argiles à adsorption ionique dans le sud de la Chine qui fournissent les terres rares lourdes (HREE). Les trois plus importants minéraux riches en

terres rares dans les carbonatites sont la bastnäsite, la monazite et le xénotime qui présentent des minéraux primaires et hydrothermaux par plusieurs processus d'enrichissement supergènes (Mariano et Mariano Jr, 2012 ; Harlov, 2015 ; Chen *et al*. 2017).

- **Problématique**

Les carbonatites sont des roches magmatiques relativement rares dont les processus à l'origine sont encore mal contraints. Différentes études s'intéressent à comprendre les diverses occurrences de roches alcalines et carbonatitiques dans le monde ainsi que l'évolution du manteau sub-continental source à travers les temps géologiques. L'étude de ces roches est cruciale car elle permettent de caractériser le manteau lithosphérique et/ou asthénosphérique riche en carbone dont elles sont issues et apporter de nouvelles contraintes sur le cycle du carbone et l'échange de carbone entre les grands réservoirs terrestres à grandes échelles depuis l'Archéen jusqu'à l'actuel. Au delà de leur intérêt scientifique, les carbonatites ont une importance économique non-négligeable de par leur richesse en terres rares.

L'étude des carbonatites et des magmas alcalins d'Ihouhaouene présentée dans ma thèse adresse plusieurs questions :

- Quelle est la composition du manteau source des liquides carbonatés et magmas alcalins riches en CO_2?
- Les calciocarbonatites dérivent-elles directement du manteau ? Ou dérivent-elles de processus d'immiscibilité et cristallisation fractionnée à partir d'un magma carbonaté-silicaté ?
- Quelles sont les relations co-génétiques entre les carbonatites et les roches alcalines silicatés associées ? Les carbonatites sont-elles seulement associées à des roches alcalines sous-saturées ?
- Comment ces liquides carbonatés migrent et affectent la croûte continentale encaissante ? et quelle est la composition des fluides présents lors de l'evolution des magmas et lors des processus-subsolidus?
- Quelle est la distribution et le fractionnement des terres rares entre les liquides carbonatés et les liquides silicatés et les minéraux magmatiques? Et quels sont les processus/environnements supergènes permettant l'enrichissement en terres rares des carbonatites ?
- Quelle est la relation des magmas carbonatitiques avec leur contexte de mise en place ?

Le complexe carbonatitique et les syénites associées d'Ihouhaouene dans le Hoggar occidental forment un exemple original de par leur âge éburnéen et leur positionnement dans une zone de suture cratonique archéenne stable. Elles permettent d'apporter de nouvelles contraintes sur la genèse des magmas carbonatées et la géodynamique au Protérozoïque.

Ces carbonatites ont été décrites pour la première fois par K. Ouzegane en 1987. Intimement liées aux syénites, les carbonatites partagent les mêmes assemblages minéralogiques à clinopyroxene,

apatite et wollastonite. La présence exceptionnelle de minéraux riches en terres rares tel la britholite [$(REE_3Ca_2(SiO_4)_3(F,Cl,OH)$] et la monazite [$(Ce,La,Nd,Th)PO_4$] confère aux carbonatites et aux syénites un intérêt particulier en faisant des traceurs importants des processus profonds et supergènes et des gisements potentiels pour les Terres Rares. La distribution et l'enrichissement de ces éléments durant les processus magmatiques et sub-solidus est essentielle pour déterminer les conditions de cristallisation et les compositions des fluides tardi-magmatiques (éléments volatils, REE) en lien avec la formation de ces minéraux de Terres Rares.

Les études précédentes ont démontrés une origine mantellique de ces carbonatites (Ouzegane, 1987 ; Bernard-Griffiths *et al*. 1988) alors que les syenites d'Ihouhaouene ont été considérées comme le résultat de fénitisation par métasomatisme de magmas alcalins (Fourcade *et al*. 1996). Le complexe alcalin d'Ihouhaouene s'est mis en place durant une période de transition entre la terre primitive archéenne et le grand évènement métamorphique régional d'ultra haute température (UHT) à l'Eburnéen. Une seule étude par Bernard-Griffiths *et al*. (1988) a défini un âge protérozoïque pour les carbonatites d'Ihouhaouene (datation U/Pb sur un zircon). De par le contexte géodynamique complexe et les relations entre carbonatites, syenites et granulite (encaissant), une étude géochronologique plus détaillée est cependant indispensable afin de comprendre la chronologie des évènements magmatiques et métamorphiques.

- **Objectifs et approche**

L'objectif de cette thèse est d'étudier la genèse des carbonatites et magmas alcalins d'Ihouhaouène présent dans le Nord-Ouest du Hoggar au Sud de l'Algérie. Ce travail se focalise sur une étude de terrain et sur la caractérisation des signatures pétrologiques et géochimiques des carbonatites et des syénites associées dans les trois secteurs d'Ihouhaouene. Ce travail permettra de plus, de définir leurs conditions de genèse et les conditions d'enrichissement sub-solidus (éléments volatils, REE) dans le but de :

- Comprendre la relation à grande et petite échelle entre les syenites et carbonatites.
- Caractériser les compositions des magmas en équilibre avec les minéraux magmatiques (apatite, pyroxène) dans les carbonatites et les syénites afin de contraindre les processus magmatiques liés à la genèse des magmas alcalins et des carbonatites dans une zone cratonique au Paléoprotérozoïque.
- Déterminer les concentrations en terres rares dans les magmas mantelliques et dans les fluides sub-magmatiques du complexe d'Ihouhaouene.
- Définir l'âge des épisodes magmatiques du complexe alcalin et les situer dans le contexte régional du craton de l'In Ouzzal.

Une étude géochimique des roches et minéraux et une modélisation basées sur les données expérimentales des coefficients de partage entre les liquides carbonatés et silicatés et des calculs simples de fusion et de cristallisation fractionnée a été développée afin de caractériser les magmas en équilibre avec les minéraux magmatiques (apatite, pyroxène) dans les carbonatites et syénites et contraindre les processus magmatiques. Un modèle a été développé afin d'expliquer les compositions complexes des liquides primaires des carbonatites et des syénites d'Ihouhaouene. Dans un deuxième temps, l'étude in-situ des apatites et minéraux de terres rares dans les carbonatites et syénites et l'imagerie EBSD et EMP, ont permis de caractériser les environnements subsolidus et la composition des fluides liée à l'enrichissement en terres rares à un stade sub-magmatique précoce. Par ailleurs, des datations U-Pb in situ sur apatites et zircons dans les syénites et carbonatites ont été effectuée afin de déterminer l'âge magmatique du complexe alcalin d'Ihouhaouene et le lien avec l'évènement tectono-métamorphique granulitique de l'In Ouzzal à l'Eburnéen.

- **Organisation du manuscrit**

Cette thèse comporte quatre chapitres dont trois articles scientifiques (II, III et IV) rédigés en anglais et intégrés dans le corps du texte en respectant le format du manuscrit dont le déroulé est le suivant.

Le ***chapitre I*** présente le contexte géodynamique de la zone d'étude Ihouhaouene lié à la formation des granulites de l'unité de l'In Ouzzal au Hoggar occidental. Il présente aussi une étude pétrographique détaillée des carbonatites et des syénites de la région d'Ihouhaouene et les différentes méthodes utilisées pour les analyses en roches totales (éléments majeurs, volatils et en trace), in situ des minéraux et des datations.

Le ***chapitre II*** correspond à l'étude pétrographique et minéralogique des phases liquidus et l'étude géochimique multi-échelle et multi-élément (majeur, volatils et en trace) des roches carbonatitiques et des roches alcalines dans le craton de l'In Ouzzal afin de caractériser la composition des liquides profonds et les processus complexes d'immiscibilité, de cristallisation fractionnée et d'hybridation à l'origine des roches. Ce chapitre correspond à un article scientifique soumis et accepté dans la revue internationale *Contributions to Mineralogy and Petrology*.

Le ***chapitre III*** se focalise sur l'étude des apatites et des inclusions minérales riches en terres rares (britholite-monazite) afin de caractériser la composition magmatique en terres rares des minéraux et déterminer la composition des fluides tardi-magmatiques lors des processus de diffusion sub-solidus. Ce chapitre correspond à un article en préparation qui sera soumis prochainement dans la revue scientifique *Minerals*.

Le ***chapitre IV*** inclut une étude géochronologique préliminaire des complexes alcalins d'Ihouhaouene à partir des dations U-Pb in situ sur apatite et zircon dans les carbonatites et les syénites afin de déterminer l'âge de cristallisation de ces roches et de comprendre leur lien avec l'évènement tectono-métamorphique régional éburnéen de l'In Ouzzal. Ce chapitre correspond à un article en préparation.

Une discussion générale, conclusions et perspectives résument ce travail de thèse. La relation temporelle entre l'activité magmatique et tectono-métamorphique durant la transition archéenne et protérozoïque est un enjeu majeur pour comprendre la mise en place des carbonatites dans les cratons anciens.

Les carbonatites d'Ihouhaouene dans le terrane de l'In Ouzzal au Hoggar occidental

Ce chapitre introduit le contexte géologique de la zone d'étude Ihouhaouene dans l'In Ouzzal avec : l'histoire géodynamique du bouclier Touareg et l'amalgamation des terranes au Panafricain ; L'evolution tectono-métamorphique du terrane de l'In Ouzzal dans le Hoggar occidental de l'Archéen au Panafricain; Les relations de terrain entre les carbonatites et les syénites d'Ihouhaouene dans les trois secteurs de l'Oued Ihouahouene, Wadi Tirahart Sud et Wadi Tirahart Nord. Il présente aussi une étude pétrographique détaillée des carbonatites et des syénites associées et les différentes méthodes utilisées pour les analyses des éléments majeurs, volatils et en traces, en roches totales des minéraux et des datations in situ.

I.1 Cadre géologique de la zone d'étude

I.1.a Le Bouclier Touareg

Le bouclier Touareg constitue un site géologique important par la présence de diverses roches qui comptent parmi les plus anciennes au monde et qui permettent de retracer leur évolution tectonique et géochimique à l'échelle des continents au cours des temps. Le bouclier Touareg comprend trois massifs (Figure. I.1 et Figure. I.2): (1) le Hoggar qui forme la majeure partie du bouclier et se situe au sud de l'Algérie (2) l'Adrar des Iforas au Mali et (3) le massif de l'Aïr au Niger. Il présente un bloc cénozoïque de 550 000 km^2 composé de roches précambriennes entourées de sédiments paléozoïques déposés après la fin de l'orogenèse panafricaine (Liégeois et *al*. 2019). Il expose le résultat d'une exhumation généralisée du bouclier à l'Eocène (Rougier et *al*. 2013, English et *al*. 2017, Liégeois et *al*. 2019), suivie par différents épisodes volcaniques intraplaques allant de 35 Ma au quaternaire (Liégeois et *al*. 2005).

Le bouclier Touareg fait partie de la ceinture transsaharienne où la tectonique des plaques était encore active au précambrien (Black et *al*. 1994). Caby et *al*. (1981) ont montré que le bouclier a été comprimé entre deux grands continents convergents (Figure. I.1), le craton Ouest Africain à l'Ouest et le métacraton saharien à l'Est, durant l'orogenèse panafricaine due à la fermeture d'un large océan.

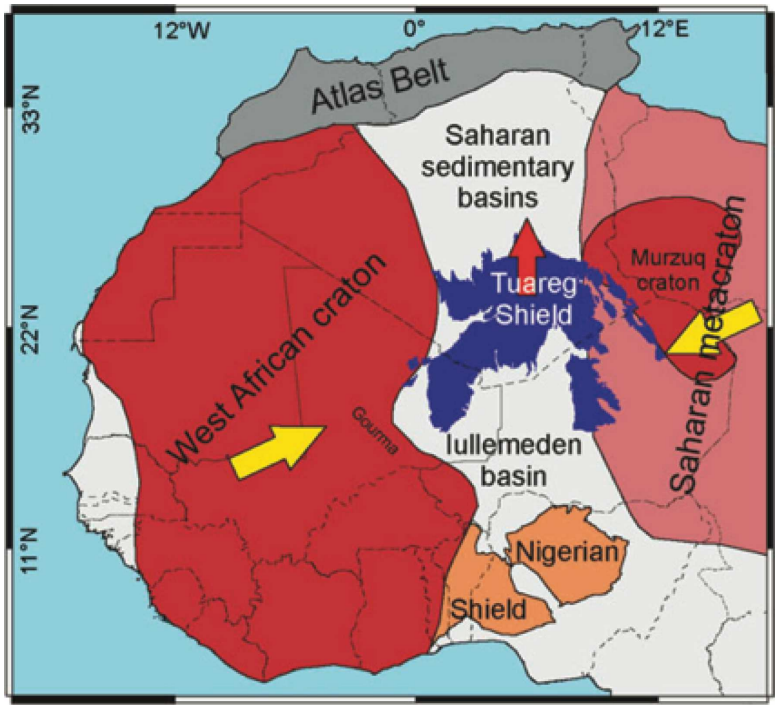

Figure. I.1. Carte de l'Afrique de l'Ouest avec les principales entités géodynamiques (Liégeois et *al*. 2019). La bande au centre correspond à la ceinture transsaharienne, avec le bouclier nigérien et le bouclier touareg et le socle situé au-dessous des bassins sédimentaires d'Iullemeden et du Sahara.

Black et *al*. (1994) et Liégeois et *al*. (1994) ont subdivisé le bouclier Touareg en 23 terranes (Figure. I.2) séparés par de grandes shear-zones qui se sont joints au panafricain. Liégeois et *al*. (2019) ont ajouté 2 nouveaux terranes au bouclier, le terrane de Aouilène et le terrane d'Afara. Chacun des terranes se caractérise par une lithologie et une histoire tectono-métamorphique et magmatique différente.

Ces terranes sont des domaines juvéniles panafricains (Caby et *al*. 1982, 1989, Bendaoud et *al*. 2008) associés à d'autres domaines archéens à éburnéens remobilisés durant le panafricain avec des évidences d'anciennes lithologies préservées sur de grandes étendues comme dans le terrane de l'In Ouzzal (Ouzegane et *al*. 1987, 2003, Benbatta et *al*. 2017).

Bertrand et Caby (1978) ont subdivisé le bouclier en trois grands compartiments: le Hoggar occidental, central et oriental suivant les deux grands accidents N-S 4°50' et 8°30'.

Le Hoggar occidental (Figure. I.2) est caractérisé par la présence de deux zones, le rameau occidental et le rameau oriental, séparées par l'unité granulitique de l'In Ouzzal composée de roches archéennes remobilisées au Paléoprotérozoïque (2000 Ma, Ouzegane, 1987 ; Haddoum et *al*. 1994 ; Peucat et *al*., 1996 ; Ouzegane et *al*. 2003).

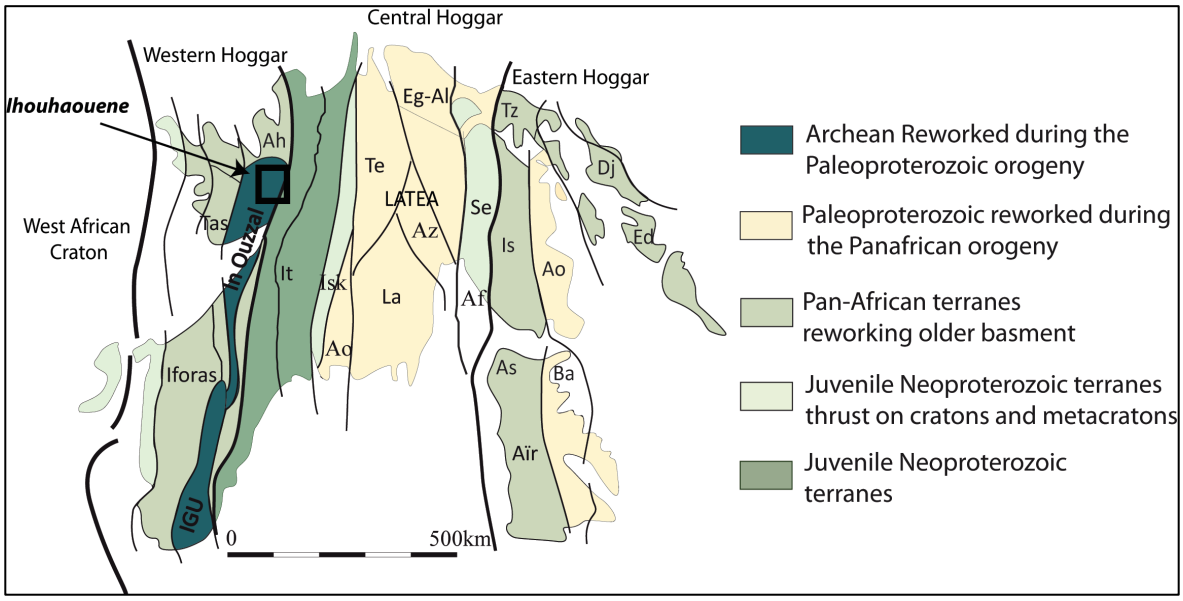

Figure. I.2. Carte géologique simplifiée du bouclier touareg avec les 23 terranes de Black et *al*. (1994) et Liégeois et *al*. (2003) avec attribution géodynamique modifiée de Liégeois et *al*. (2019).

I.1.b. Le terrane de l'In Ouzzal

Le terrane de l'In Ouzzal (Figure. I.2) est un bloc rigide de 450 km de long et 80 km de large dans sa partie septentrionale, orienté N-S, situé au centre du Hoggar occidental entre deux grands bassins volcano-sédimentaires d'âge protérozoïque moyen à protérozoïque terminal constituant la chaine pharusienne (Ouzegane et *al*. 2003 ; Bendaoud et *al*. 2008 ; Haddoum et *al*. 2013 ; Liégeois et *al*. 2019).

Il est bordé par deux grandes zones de cisaillement sub-verticales s'enracinant profondément sous la base de croûte traversant une lithosphère très épaisse sous l'In Ouzzal (Liégeois *et al*. 2005 ; Bouzid et *al*. 2008). Caby (1996) et Djemai (1996) ont montré que les mouvements opposés des deux décrochements déplacent le terrane vers le Nord au cours de la compression panafricaine.

L'histoire de l'In Ouzzal s'étale entre 3200 et 2000 Ma et se caractérise par divers activités orogéniques entre l'Archéen, le Protérozoïque et le Panafricain. Deux unités composent le terrane de l'In Ouzzal ; (i) l'unité inférieure en dômes essentiellement à TTG (tonalite, trondjhémites, granodiorites) formant une série de gneiss charnokitiques et d'enderbites, granulitiques orthodérivés et (ii) l'Unité supracrustale granulitique occupant des bassins, composée de granulites alumino-magnésiennes, granulites alumino-ferrifères, marbres, quartzites et des leptynites (Ouzegane, 1987 ; Ouzegane et Kienast, 1996 ; Haddoum et *al*. 1994 ; Ouzegane et *al*. 2003). Toutes ces roches ont donné des âges archéens et ont été remobilisés au Paléoprotérozoïque à 2000 Ma (Ferrara et Gravelle, 1996 ; Haddoum et *al*. 1994 ; Peucat et *al*. 1991 ; Peucat et *al*. 1996).

L'histoire archéenne de l'In Ouzzal remonte à plus de 3200 Ma (Allègre et Caby, 1972 ; Lancelot et *al*. 1976 ; Ben Othman et *al*. 1984 ; Ferrara et Gravelle, 1996 ; Haddoum et *al*. 1994 ; Peucat et *al*. 1991 ; Peucat et *al*. 1996 ; Ouzegane et *al*. 2003) et se caractérise par trois stades majeurs (Ouzegane et *al*. 2003 ; Drareni et *al*. 2007, Figure. I.3). Un premier stade se définit par la mise en place de croûte continentale composée de roches d'affinité andésitique et de TTG entre 3200 et 3300 Ma, formée par accrétion d'arcs (Ouzegane et *al*. 2003 ; Drareni et *al*. 2007). Le deuxième stade se caractérise par une autre série de TTG (ceinture de roches vertes) qui s'est mise en place vers 2700 Ma suivie par l'intrusion de granites de type A vers 2600 Ma et le dépôt des protolithes des granulites Al-Mg des formations ferrifères et carbonatées associées à des tholéiites magnésiennes et des komatiites dans des bassins d'arrières arcs (Figure. I.3). La période archéenne à 2500 Ma se termine par un raccourcissement homogène et le développement de structures en dôme et bassin caractérisées par la mise en place de plutons granitiques calco-alcalins issus de la fusion partielle de la croûte inférieure (Ouzegane et *al*. 2003 ; Drareni et *al*. 2007).

Stade 1: 3300 à 3200 Ma

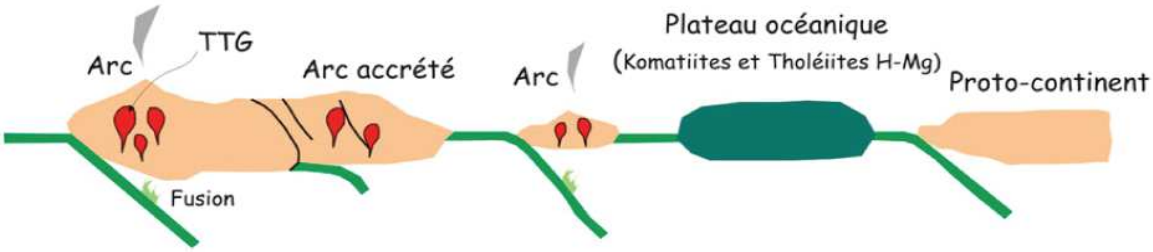

Stade 2: à 2700 Ma

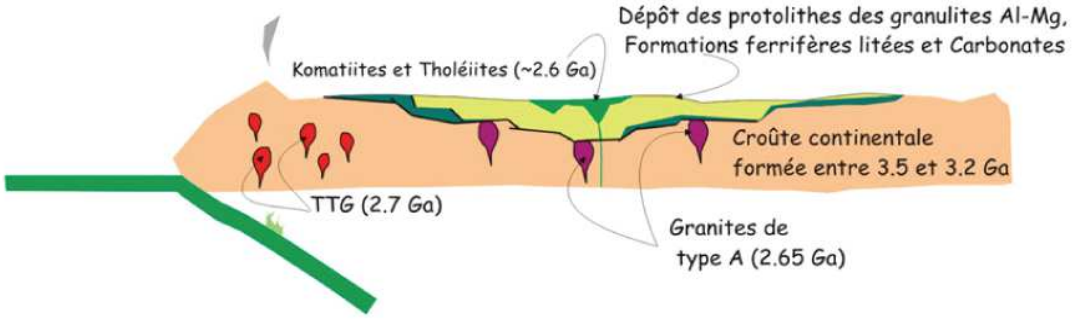

Stade 3: 2600 Ma à 2500 Ma

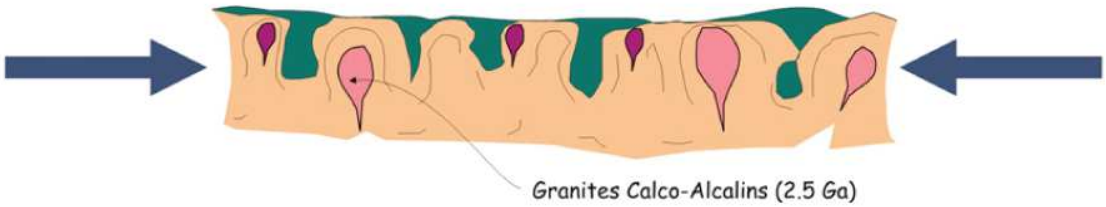

Figure. I.3. Modèle géodynamique montrant trois stades de formation de la croûte continentale et des séries supracrustales du terrane de l'In Ouzzal à l'Archéen entre 3200 et 2500 Ma (Drareni et *al.* 2007).

L'histoire paléoprotérozoïque de l'In Ouzzal se caractérise par la succession de plusieurs évènements métamorphiques granulitiques de très haute température durant l'orogenèse éburnéenne (Ouzegane, 1987 ; Ouzegane et *al*. 2003 ; Bendaoud, 2008 ; Adjerid et *al*. 2008 ; Adjerid et *al*. 2013 ; Benbatta et *al*. 2017) dont la phase majeure a lieu à 2000 Ma (BenOthman et *al*. 1984).

L'évolution P-T du métamorphisme granulitique de l'In Ouzzal est enregistrée à travers différentes paragenèses : dans les granulites Al-Mg (Ouzegane, 1987 ; Kienast & Ouzegane, 1987 ; Bertrand et *al*. 1992 ; Ait Djafer, 1996 ; Boumaza, 1996 ; Mouri et *al*. 1996 ; Ouzegane & Boumaza, 1996 ; Adjerid, 2002 ; Bendaoud, 2008 ; Benbatta et *al*. 2017) avec les températures les plus élevées, les granulites Al-Fe (Ait Djafer, 1996 ; Djemai, 1996 ; Ouzegane et *al*. 1996), les quartzites à corindon-magnétite (Guiraud et *al*. 1996), les granulites à silicates-calciques (Benyahia, 1996) et les pyroxénites à grenat (Ouzegane, 1987 ; Kienast & Ouzegane, 1987 ; Djemai, 1996, Bendaoud 2008).

Deux stades métamorphiques majeurs sont connus dans l'In Ouzzal (Figure. I.4): (i) un stade prograde caractérisé par de hautes pressions et températures, de 10 à 11 Kbar et de 800 à 1050ºC, respectivement ; (ii) un stade rétrograde marqué par une décompression de 9 à 5 Kbar avec un maintien des températures autour de 900-1000ºC (Ouzegane, 1987 ; Bertrand et *al*. 1992 ; Ouzegane et *al*. 2003). Cet évènement tectono-métamorphique se manifeste par un cisaillement ductile plat, une foliation contemporaine du métamorphisme granulitique prograde et d'une fusion partielle limitée (Peucat et *al*. 1996, Haddoum et *al*. 2013). L'histoire éburnéenne (stade rétrograde) se termine par un relâchement des contraintes et la mise en place du complexe alcalin des carbonatites et syénites associées (Ouzegane et *al*. 2003).

Stade précoce **:** poursuite de la tectonique en dômes et bassins archéens avec un raccourcissement et un épaississement crustal.

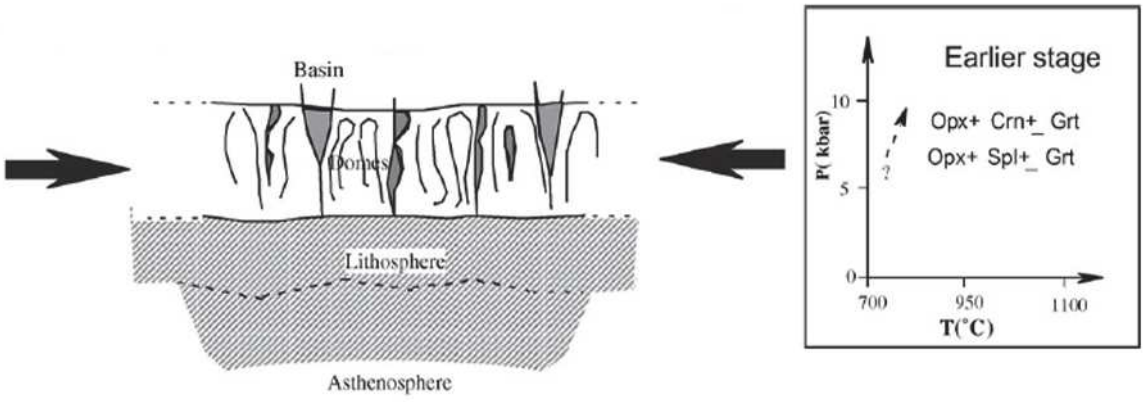

***Stade 1* :** Délamination du manteau lithosphérique et remonté de l'asthénosphère.

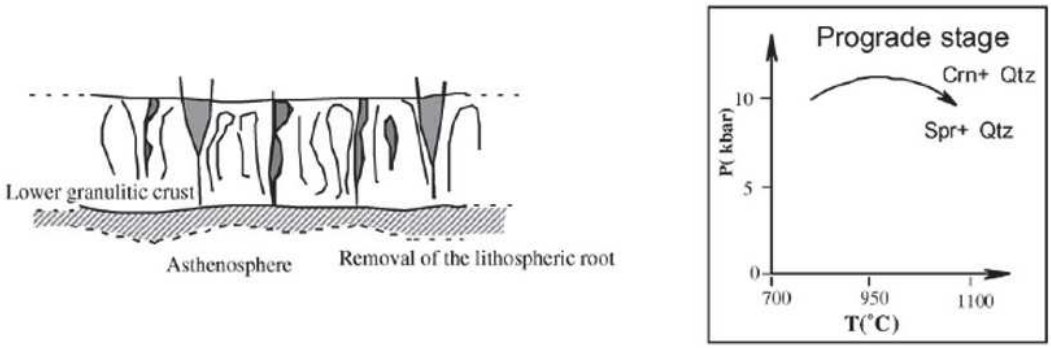

***Stade 2* :** Décompression et rééquilibrage isostatique avec reprise du manteau lithosphérique dans les conditions postérieures post-collisionnelles et d'équilibre thermique.

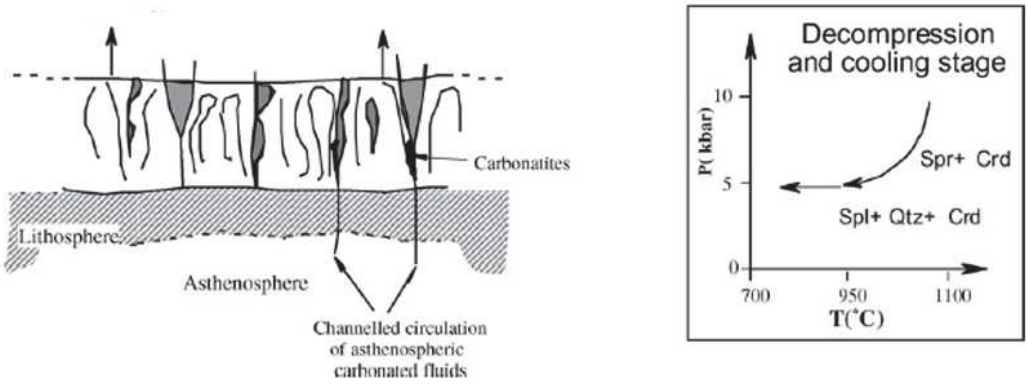

Figure. I.4. Modèle géodynamique (Ouzegane et *al.* 2003) montrant l'évolution tectono-métamorphique (cheminements P – T) du terrane granulitique de l'In Ouzzal et la mise en place des carbonatites à la suite d'une délamination lithosphérique et la remonté asthénosphérique lors de l'événement Eburnéen.

L'histoire panafricaine de l'In Ouzzal se manifeste par d'importante schistosité et rétromorphose des granulites dans le facies amphibolite localisée dans les grandes shear-zones délimitant le terrane (Djemai et *al*. 2009). Un magmatisme acide localisé au Nord avec les plutons granitiques alcalins, des champs filoniens de dolérites et gabbro-dolérites au Sud, orientés NNW-SSE témoignant d'une distension pré-panafricaine, aussi observée dans le Craton Ouest africain (Haddoum et *al*. 2013).

Le terrane de l'In Ouzzal est limité par deux grands- décrochements, l'Ouest-ouzzalien est senestre (Caby, 1970) et l'Est-ouzzalien est dextre (Caby, 1970, 1996 ; Attoum, 1983, 1993 ; Haddoum, 1992 ; Haddoum et *al*. 1994 ; Ferkous, 1995 ; Semiani, 1995 ; Djemai, 1996 ; Djemai et *al*. 2009) faisant expulsé l'In Ouzzal vers le Nord (Haddoum et *al*. 2013).

Caby et Monié (2003) considèrent ces décrochements comme des zones de subduction convergentes actives entre 900 et 850 Ma, transformées en sutures entre 620 et 580 Ma en considérant

que l'In Ouzzal n'a pas été affecté par le métamorphisme et la déformation panafricains en préservant les paragenèses éburnéennes granulitiques (2000 Ma).

Haddoum et *al*. (2013), considèrent quand à eux que l'In Ouzzal a été remobilisé durant le panafricain, particulièrement dans sa partie Sud où des formations volcano-sédimentaires pharusiennes (Protérozoïque supérieur- Protérozoïque terminal) affleurent en discordance sur les granulites paléoprotérozoïques.

I.1.c. La zone d'étude Ihouhaouene

La zone d'étude Ihouhaouene se situe au Nord du terrane de l'In Ouzzal (23°36'14"N, 3°10'32"E) au Hoggar occidental (Sud de l'Algérie) (Figure. I.5). Elle est recoupée par de grandes zones de cisaillement méridiennes auxquelles sont associés des granites panafricains et des minéralisations aurifères.

La région d'Ihouhaouene contient de nombreux corps de carbonatites associées à des syénites (Figure. I.5) d'âge éburnéen (~ 2000 Ma ; Bernard-Griffiths et *al*. 1988) qui comptent parmi les plus anciennes connues au monde. Les complexes de carbonatites d'Ihouhaouène sont syn-orogéniques et se distinguent, par la forme de leur gisement linéaire en relation avec leur mode de mise en place le long de grandes zones de cisaillement (Ouzegane et *al*., 1988, Lapin et Plashko 1988).

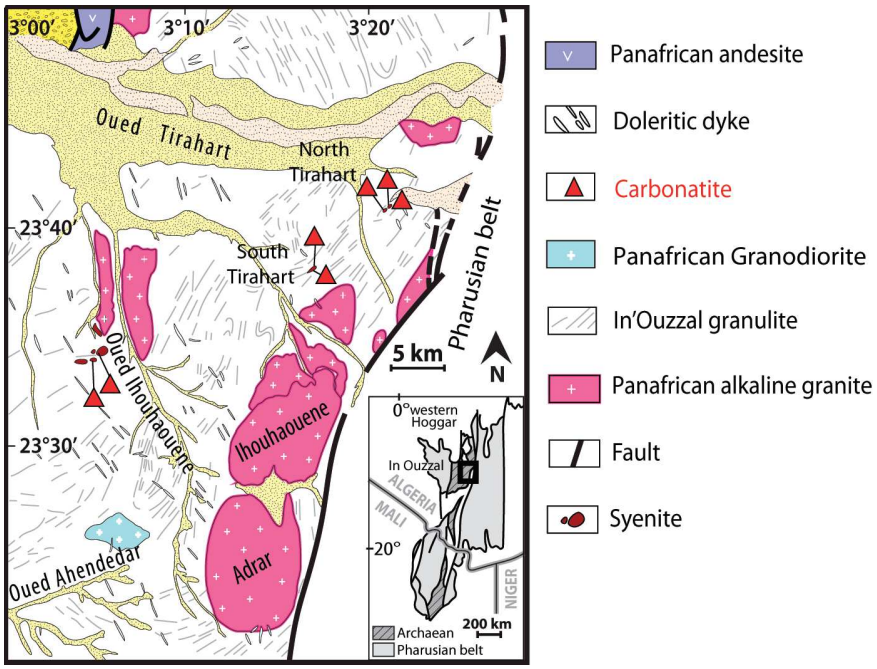

Figure. I.5. Carte géologique simplifiée de la région d'Ihouhaouene dans la partie Nord-Ouest du terrane de l'In Ouzzal et emplacement des carbonatites et syénites associées d'après Ouzegane et *al*. (1988).

Les carbonatites et syénites affleurent dans trois secteurs dans la région d'Ihouhaouene, à l'Oued Ihouhaouene, à Wadi Tirahart Sud et à Wadi Tirahart Nord, décrits comme trois centres par Ouzegane (1987) (Figure. I.6).

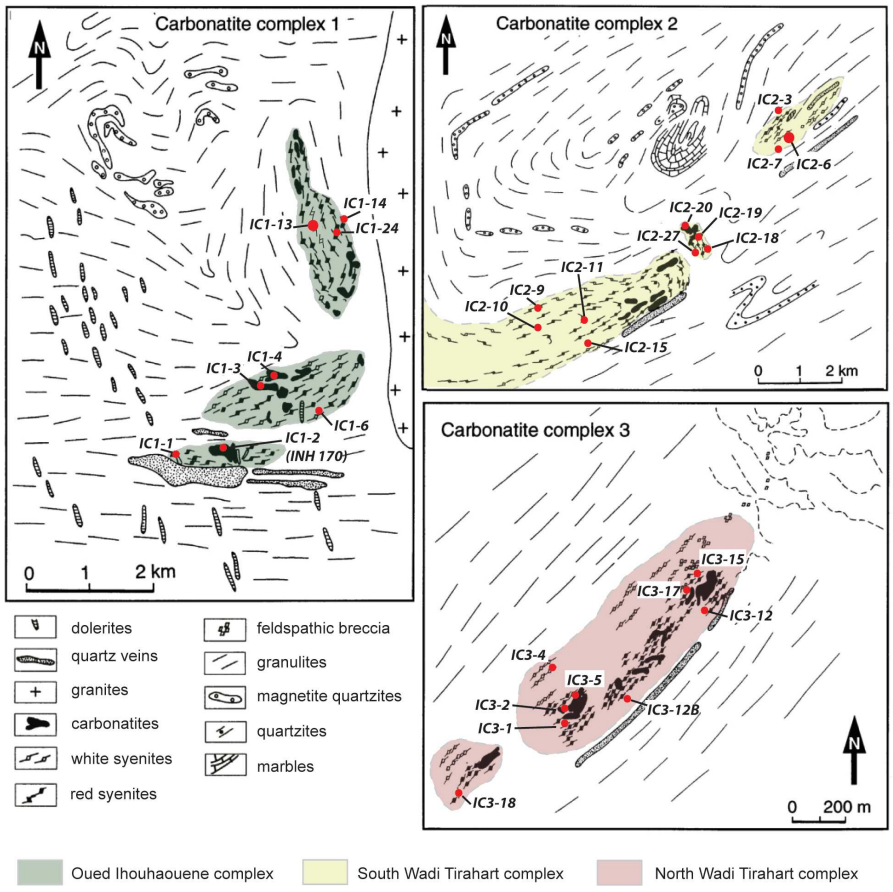

Figure. I.6. Carte géologique des trois centres carbonatitiques linéaires (Ouzegane, 1987) dans la région d'Ihouhaouene montrant la distribution des carbonatites, des syénites rouges et blanches et leur concordance avec l'encaissant granulitique d'après Fourcade et *al*. (1996). Coordonnées GPS en annexe D.

Dans le complexe de l'Oued Ihouhaouene (centre 1), les syénites affleurent sous forme de plusieurs chainons orientés EW à NW-SE (Figure. I.7a) recoupés par des veines ou filons plus où moins massifs de carbonatites bréchiques et pegmatitiques (Figure. I.7b, c, d). Dans cette zone les carbonatites sont essentiellement associées à des syénites rouges rubanées avec une alternance de niveaux clairs et sombres, cm à dcm composés de feldspath rouges et de pyroxène (Figure. I.7e).

Les carbonatites et syénites du Sud Wadi Tirahart (centre 2) affleurent sur environ 4 km de long et 1 km de large (Figure. I.8a). Les syénites dans ce complexe sont majoritairement blanches (Figure. I.8c, d, e) avec des niveaux de wollastonite intercalés (Figure. I.8d) entre les pyroxènes et les feldspaths blancs. Les carbonatites sont blanches en forme de veines bréchiques métriques (Figure. I.8c, d) ou en poches pegmatitiques décimétriques (Figure. I.8e).

Le complexe alcalin du Nord Wadi Tirahart (centre 3) forme un ensemble qui s'étale sur 2,5 km de long et 250 m de large (Figure. I.9a). Les syénites sont rouges ou blanches (Figure. I.9b, c, d, e) recoupées par les carbonatites en veines (Figure. I.9b, d) ou massives (Figure. I.9c) de couleur rose bréchiques et pegmatitiques. Des brèches feldspathiques sont présentes dans sa partie Nord avec de gros fragments de syénites blanches et de gros cristaux de pyroxènes cimentés par des feldspaths alcalins (Figure. 1 ; en annexe A). Des dykes de dolérites recoupent ces complexes notamment à Oued Ihouhaouene (Figure. 2 ; en annexe A).

Dans les trois complexes d'Ihouhaouene les carbonatites recoupent nettement les syénites parfois à bords mylonitisés. Les carbonatites bréchiques comprenant des fragments de syénites et des xénocristaux de pyroxènes de taille allant d'1 cm à 70 cm avec des formes arrondies ou anguleuses, se composent d'une matrice de calcite et d'apatite. Les carbonatites pegmatitiques sont en veines de calcite avec des phénocristaux d'apatites jusqu'à des tailles métriques associées à quelques cristaux de pyroxènes.

Le contact entre les roches alcalines et les carbonatites d'Ihouhaouene et l'encaissant granulitique n'est pas visible sur le terrain. La région désertique d'Ihouahouene est couverte par de grandes masses de sables dissimulant tout contact entre granulite et carbonatite. Les syénites d'Ihouhaouene ont été désignées de fénites par Fourcade et *al*. 1996, résultant du métasomatisme des granulites par des fluides carbonatitiques et alcalins.

Kresten *et* al. 1987 définissent la fénitisation induite par des fluides métasomatiques riches en alcalins autours des intrusions carbonatitiques par une auréole à degré de métasomatisme progressif. L'encaissant granulitique, réfractaire, affleurant à 20 m des carbonatites et des syénites dans l'Oued Ihouhaouene et le complexe de Wadi Tirahart Nord ne montre aucune évidence de texture à degré métasomatique progressif évoluant des intrusions des carbonatites.

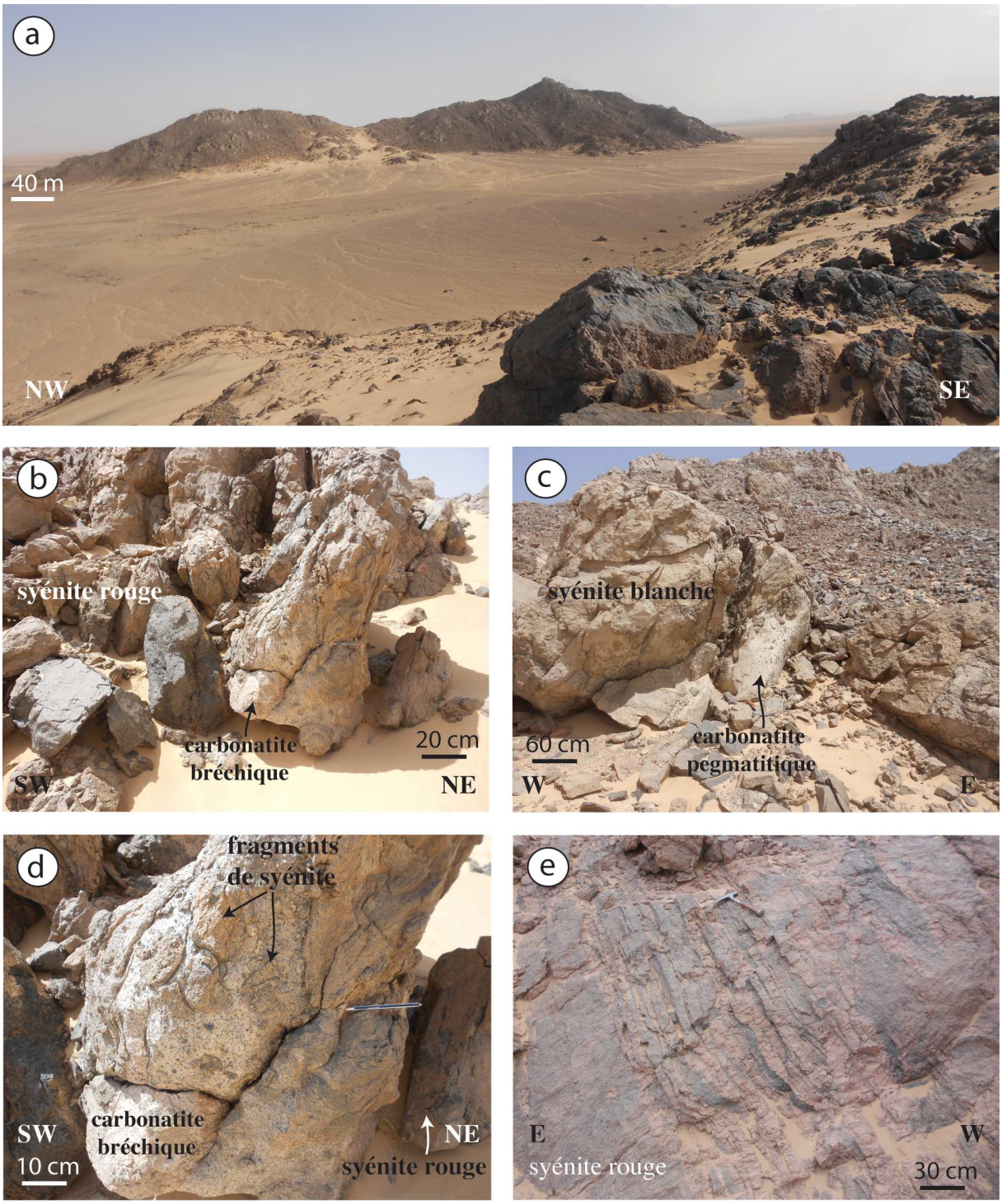

Figure. I.7 Photographies d'affleurements des carbonatites et des syénites associées à l'Oued Ihouhaouene (centre1). **a.** le complexe de syénites et carbonatites en chaînons linéaires de l'Oued Ihouhaouene (N23°33'55'', E03°04'51'') orientés E-W. **b.** filon de carbonatite bréchique en contact avec des syénites rouges. **c.** filon de carbonatite pegmatitique en contact avec des syénites blanches. **d.** fragments de syénite dans une carbonatite béchique. **e**. syénite rouge rubanée avec une alternance de niveaux clairs et sombres de clinopyroxène et feldspath alcalin.

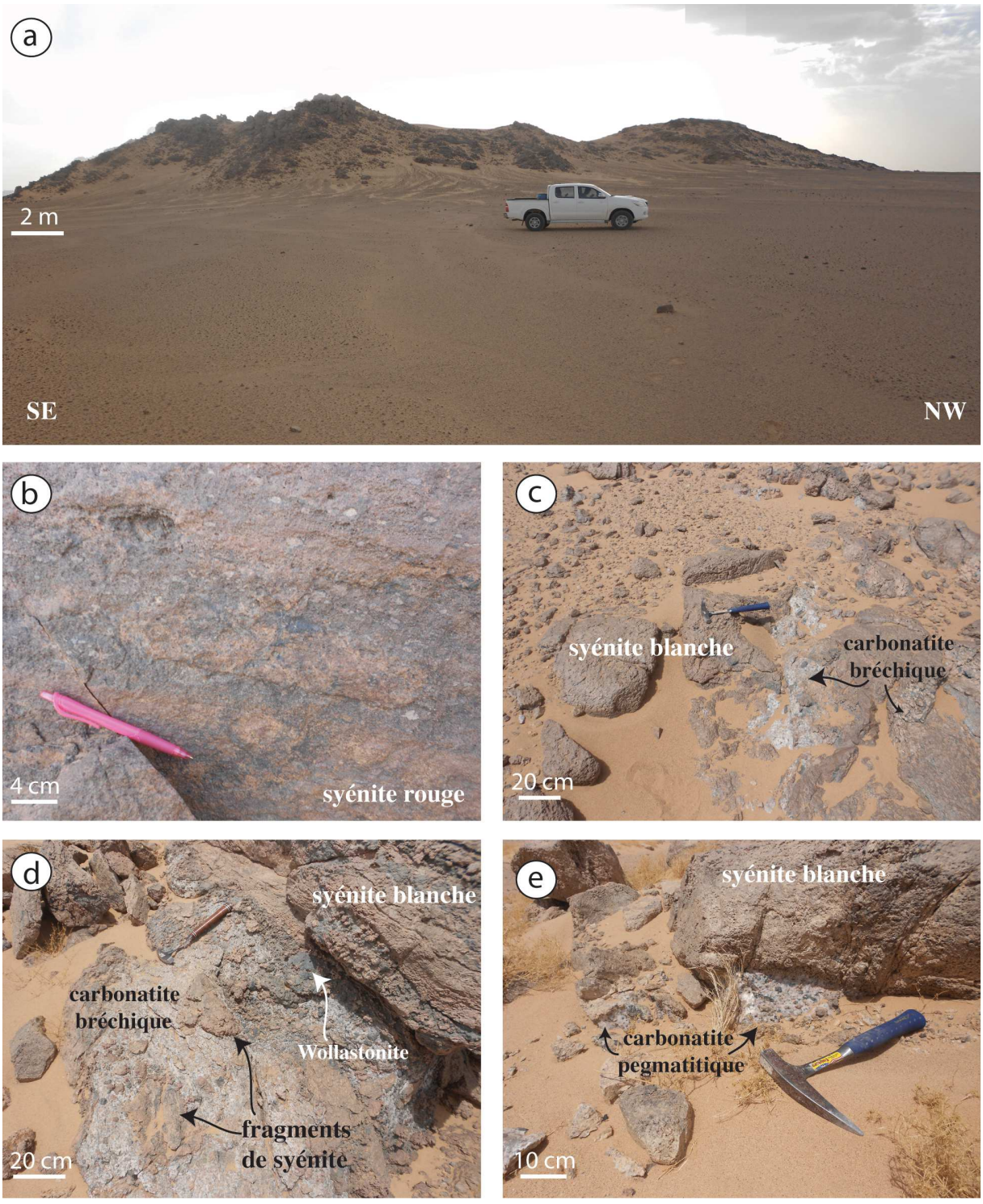

Figure. I.8. Photographies d'affleurements des carbonatites et des syénites associées au Sud Wadi Tirahart (centre 2). **a.** le complexe de syénites et carbonatites en chaînons linéaires (N23°39'29'', E03°18'02'') orientés NNE-SSW. **b.** syénite rouge rubanée avec une alternance de niveaux clairs de feldspath alcalin et sombres de clinopyroxène. **c.** filon de carbonatite bréchique en contact avec des syénites blanches. **d.** fragments de syénite dans une carbonatite bréchique. Niveau de wollastonite intercalé entre les pyroxènes et les feldspaths alcalins de la syénite blanche. **e.** veine de carbonatite pegmatitique dans les syénites rouges

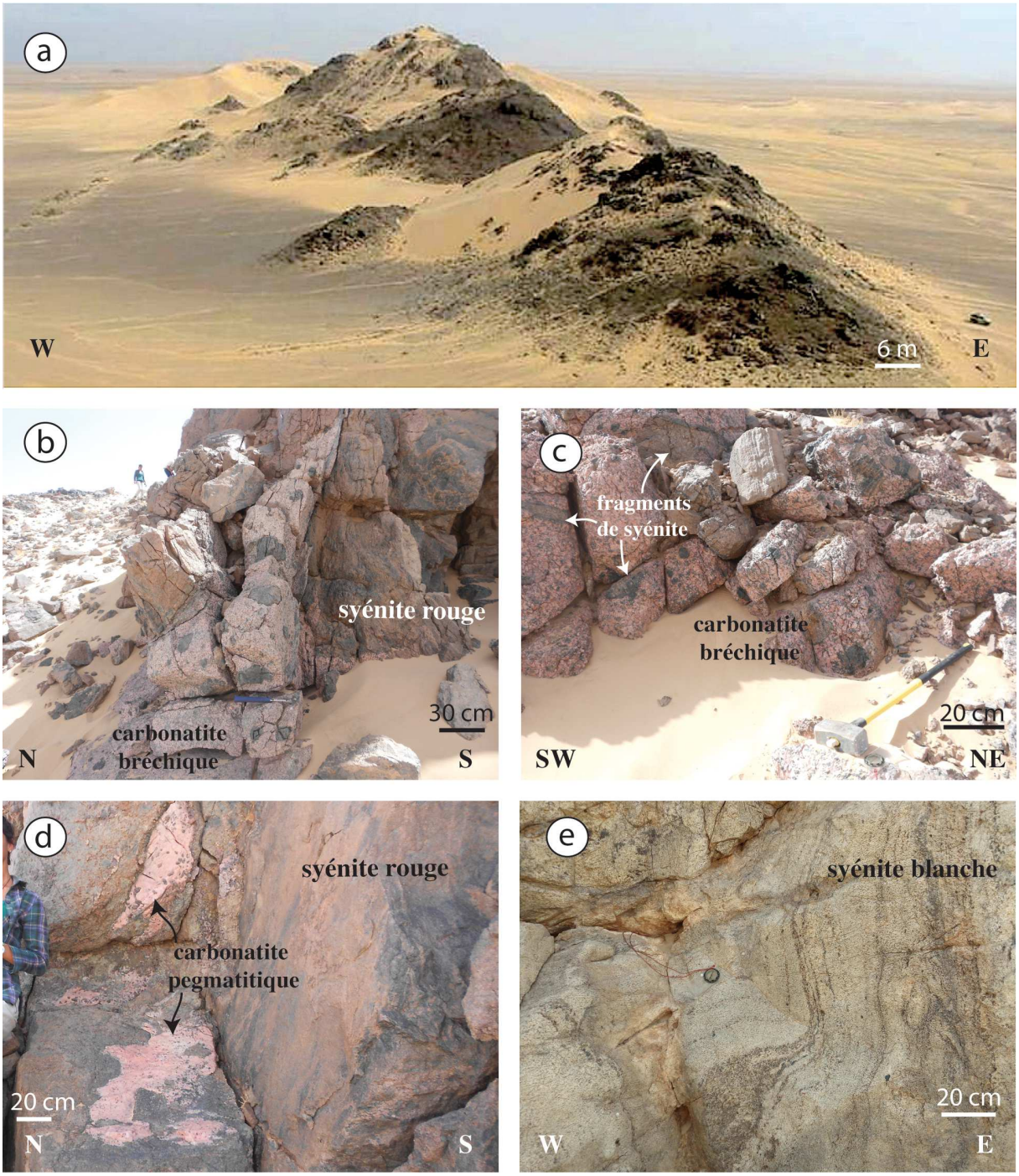

Figure. I.9. Photographies d'affleurements des carbonatites et des syénites associées au Nord Wadi Tirahart (centre 3). **a.** le complexe de syénites et carbonatites en chaînons linéaires (N23°40'22'', E03°20'43'') orientés N-S. **b.** filon de carbonatite bréchique recoupant les syénites rouges. **c.** fragments de syénite dcm dans une carbonatite béchique. **d.** poches de carbonatite pegmatitique dans une syénite rouge. **e.** syénite blanche rubanée avec une alternance de niveaux clairs et sombres de clinopyroxène et feldspath alcalin.

I.2 Etude Pétrographique:

77 lames d'échantillons de carbonatites et de syénites d'Ihouhaouene ont été étudiées pour la caractérisation pétrographique du complexe. L'assemblage minéralogique de chaque échantillon est détaillé dans la Table 1 en annexe A.

I.2.a. Les carbonatites

Toutes les carbonatites d'Ihouhaouene sont des calciocarbonatites (Streckeisen, 1974) et contiennent des *carbonates de calcium* primaires qui sont dominants par rapport aux autre minéraux (supérieurs à 50 vol.%). Les deux autres minéraux omniprésents dans le complexe carbonatitique d'Ihouhaouene sont les apatites et les clinopyroxènes avec des tailles et des proportions différentes selon la texture bréchique ou pegmatitique de la roche.

Les carbonatites bréchiques sont à grain moyen à grossier (Fig.I.10) avec une texture grenue porphyroïde à phénocristaux d'apatites automorphes vertes, vert-jaunâtre ou rose (3-5 mm, 1 à 22 vol.%), de clinopyroxènes verdâtres (3 mm, 1-20 vol.%), dans une matrice de calcite rose, grise ou blanche (3-8 mm, 50 à 70 vol.%). Les carbonatites bréchiques contiennent des fragments de syénites avec des contacts concentrés en clinopyroxène (Figure I.10.a) ou s'infiltrent dans les syénites où les feldspaths et clinopyroxènes syénitiques sont entourés d'allanites (Figure I.10.b).

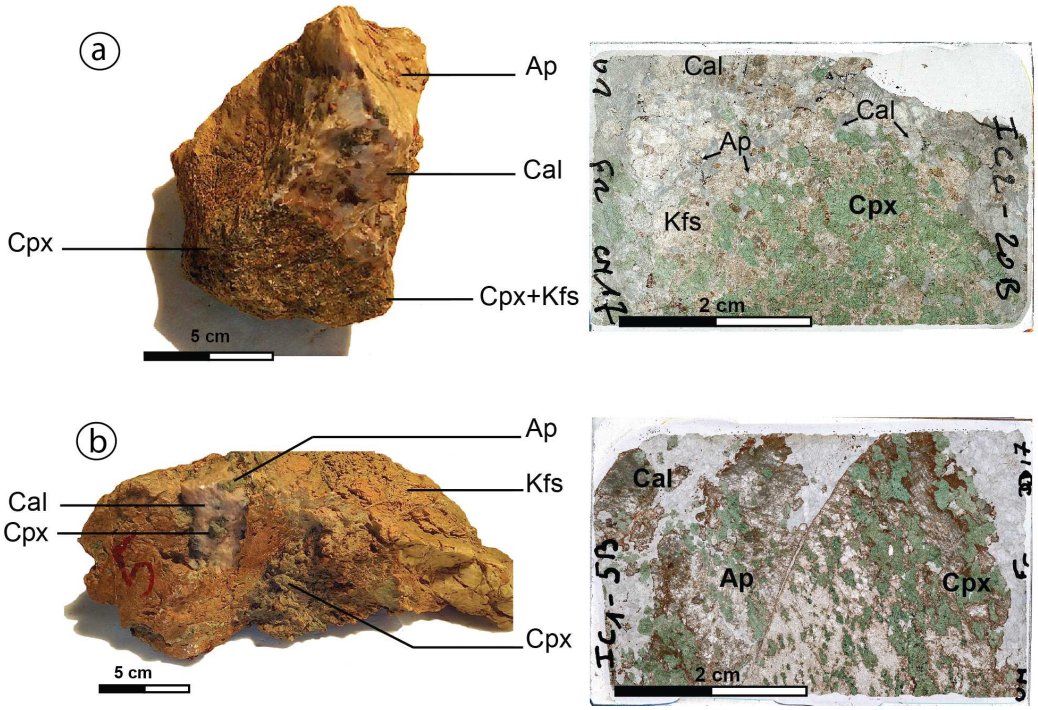

Figure I.10. Photos d'échantillons et d'assemblages minéralogiques de carbonatites bréchiques montrant **a.** le contact riche en clinopyroxènes entre carbonatite bréchique et syénite. **b.** l'infiltration de la carbonatite dans la syénite.

Dans une texture pegmatitique (Fig.I.11) s'assemblent des phénocristaux hexagonaux automorphes d'apatite (jusqu'à 10 cm, 1 à 10%) de couleur verte (Figure I.11.a), vert-jaunâtre (Figure I.11.b), ou rose (Figure I.11.c), similaires aux apatites dans les carbonatites bréchiques avec la présence des mêmes inclusions, dans une matrice de calcite rose, grise ou blanche (1-3 cm, jusqu'à 70 vol.%). Des cristaux sub-automorphes de wollastonite (8 mm, <10 vol.%) et de clinopyroxènes (1 à 5 vol.%) sont présents.

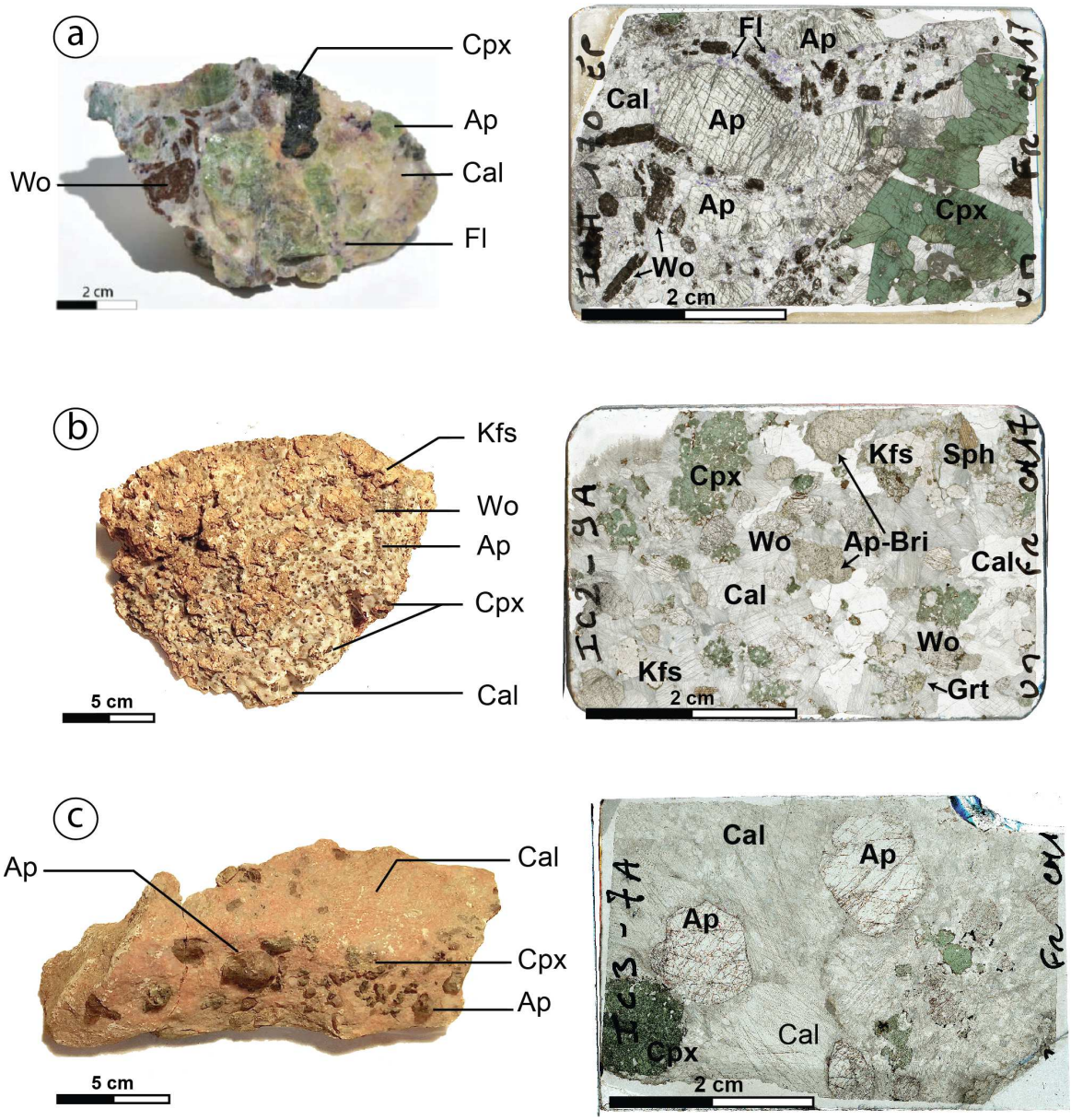

Figure I.11. Photos d'échantillons et d'assemblages minéralogiques des carbonatites pegmatitiques. **a.** la carbonatite à apatite verte sans inclusions. **b.** la carbonatite à apatite vert-jaunâtre riche en britholite. **c.** la carbonatite à apatite rose sans inclusions.

Les apatites sont très fracturées perpendiculairement à l'axe d'allongement (001) (Figure I.11 et Figure I.12.a). Elles sont présentes sans inclusions ou avec de nombreuses inclusions de quartz, calcite, fluorite, allanite, monazite et britholite.

Les apatites sans inclusions ont des cœurs limpides avec parfois de l'allanite dans les fractures (Figure I.12.a).

Les apatites à britholite sont fracturées et troubles avec de nombreuses exsolutions de britholite (Figure I.12.b) sous forme de petits grains de couleur jaune d'or. La britholite est présente sous forme lamellaire avec des tailles inferieures à 10μm ou sous forme de grains plus ou moins arrondis de taille supérieure à 200μm. L'allanite est aussi présente dans les fissures de l'apatite à britholite (Figure I.12.c).

Les apatites à monazite sont automorphe avec de nombreuses inclusions de monazite sous forme de petits grains <20μm (Figure I.12.d) associés à des inclusions de quartz et de calcite. Les monazites sont présentes aussi sous forme de couronne autour des apatites avec des tailles jusqu'à 100 μm.

Les clinopyroxènes sont sub-automorphes et fracturés (Figure I.12.e), souvent en forme de cumulas. Ils présentent des inclusions d'allanite ≤ 20 μm.

Les wollastonites sont sub-automorphe avec des fractures selon leurs plans de clivages (Figure I.12.f). Elles sont parfois altérées et entourées de couronne composée de grains micrométriques de quartz et de calcite. La wollastonite est le minéral dominant dans les carbonatites bréchiques et pegmatitiques à apatite jaune riche en britholite.

Les minéraux accessoires dans les carbonatites bréchiques et pegmatitiques sont les feldspaths potassiques parfois à texture perthitiques (4-8 mm, <1 vol.%), la magnétite (<1vol.%) sous forme d'inclusions dans les clinopyroxènes, l'allanite (0,5-1vol.%) autour du clinopyroxène ou en inclusion, le sphène (<2 vol.%), le quartz (<1 vol.%) autour des wollastonites associé à la calcite ou en inclusion dans les apatites et grenat coronitique (<3 vol.%) dans des zones réactionnelles autours des clinopyroxènes, des wollastonites ou autours des feldspaths alcalins.

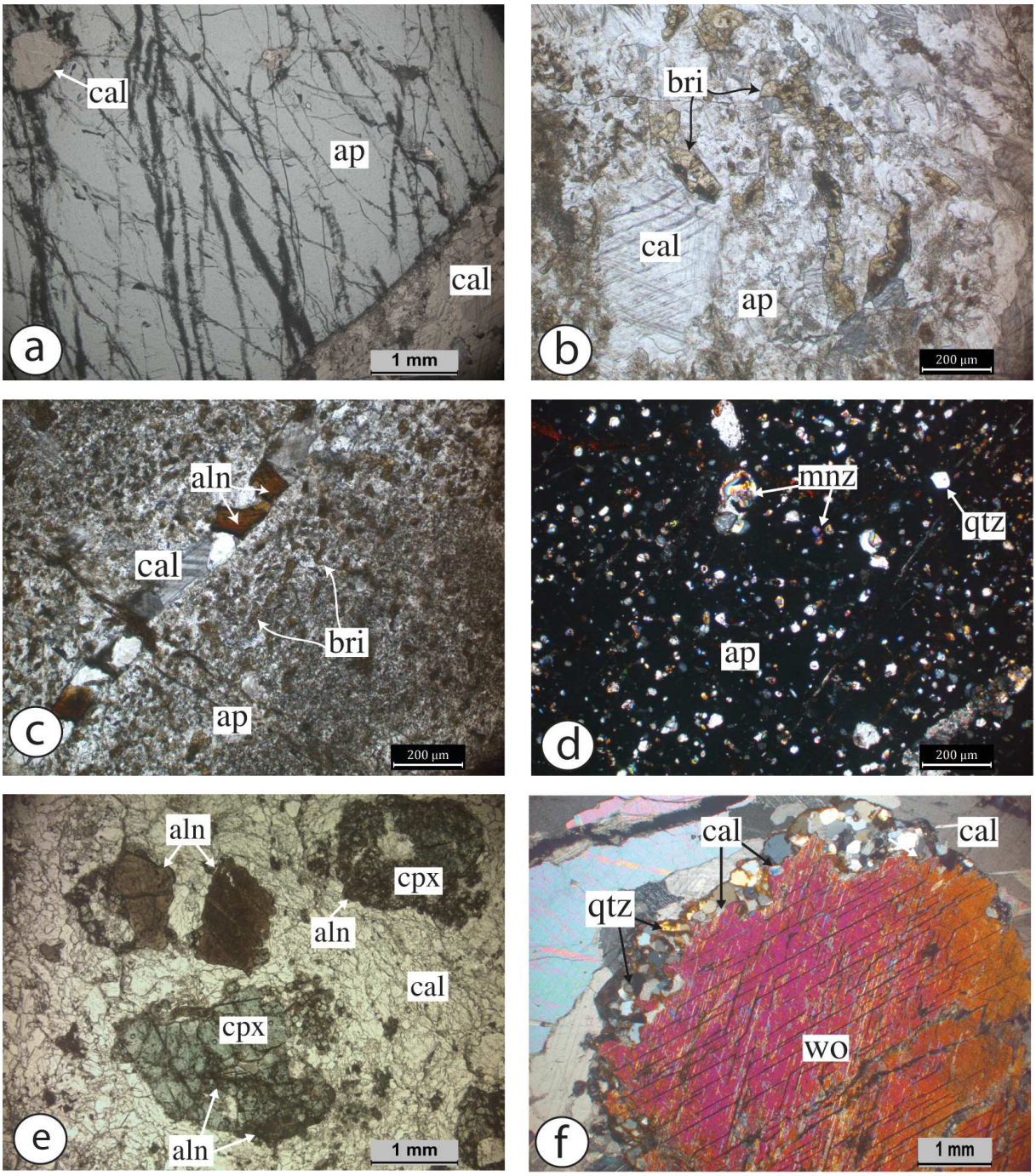

Figure I.12. Microphotographies des carbonatites pegmatitiques et bréchiques d'Ihouhaouene. **a.** apatite verte sans inclusions et calcite. **b.** apatite vert-jaunâtre riche en exsolutions de britholite. **c.** l'allanite dans les fissures d'apatites à britholite. **d.** Apatite riche en inclusions de monazite et quartz. **e.** clinopyroxène sub-automorphe entouré d'allanite. **f.** wollastonite automorphe déstabilisé en quartz calcite.

I.2.b. Les syénites

Les syénites d'Ihouhaouene présentent généralement une texture grenue rubanée, à grains moyens ou grossiers, avec une alternance de niveaux clairs et sombres montrant une continuité entre les niveaux centimétriques et tous les intermédiaires jusqu'aux niveaux épais métriques (observé sur le terrain). Ces roches se caractérisent par de fortes proportions de feldspath potassique (supérieurs à 50 vol.%) et de clinopyroxène (20 à 40 vol.%). Les syénites sont de deux couleurs rouges ou blanches selon la couleur du feldspath présent (rouge ou blanc, respectivement). Les syénites blanches se caractérisent aussi par la présence de niveaux de wollastonite associée à des apatites jaunes à britholite.

Les syénites rouges présentent une texture stratifiée à grain moyen à grossier parfois porphyroclastique (5-10 mm, Figure I.13.a). Dans la matrice à grains fins à moyens les textures sont équigranulaires en mosaïque.

Les syénites blanches ont une texture stratifiée à grain moyen à grossier (Figure I.13b) avec des niveaux clairs de feldspath potassique et de niveaux sombres de clinopyroxène (3-8 mm,%) présentant les mêmes caractéristiques que les syénites rouges.

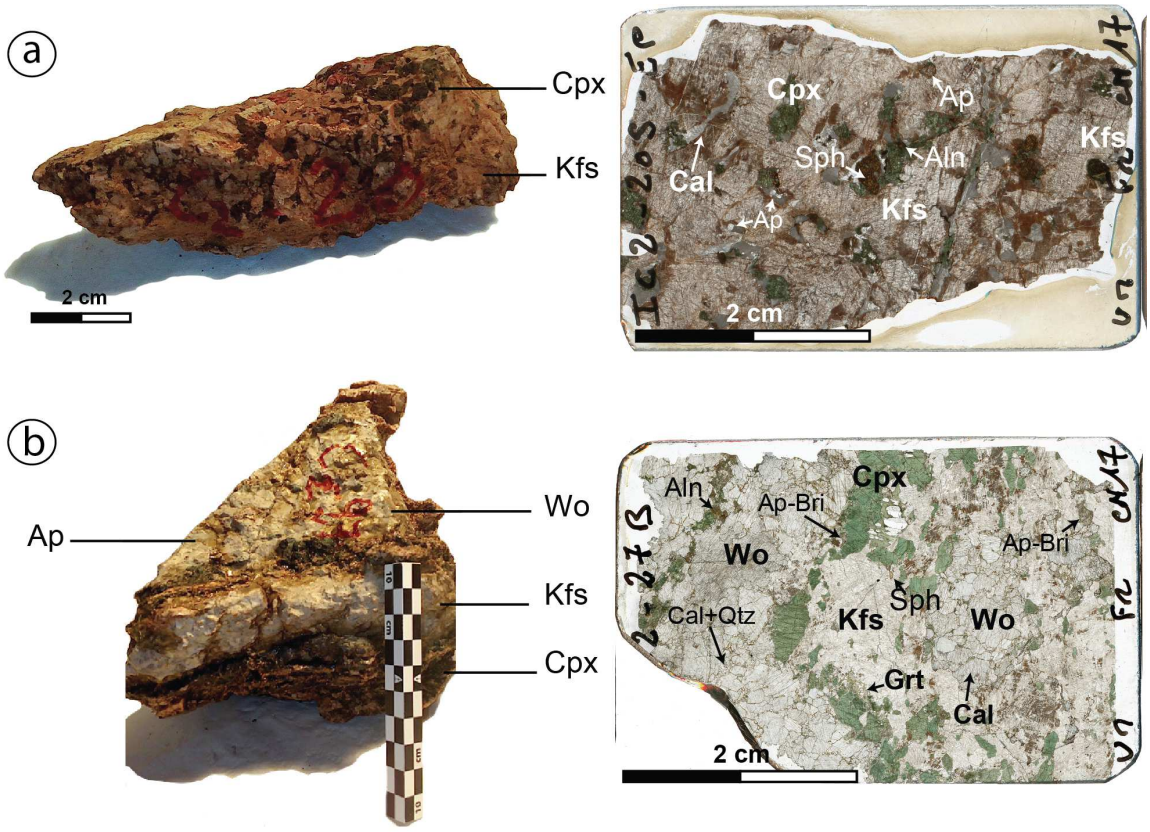

Figure I.13. Photos d'échantillons et d'assemblages minéralogiques des syénites. **a.** la syénite rouge riche en allanite et à gros cristaux automorphes de feldspath potassique. **b.** la syénite blanche à apatite vert-jaunâtre riche en britholite montrant de gros cristaux de wollastonite associées aux clinopyroxènes.

Les feldspaths potassiques (3-9 mm, 40 à 80% en volume) sont souvent présents avec des textures perthitiques. Les perthites montrent un réseau de filaments fins d'albite (Figure I.14.a).

Les clinopyroxènes apparaissent, généralement fracturés, sous différentes formes. Ils sont présents en megacristaux (1 cm) sub-automorphes ou en cristaux allongés non-déformés associés aux apatites (Figure I.14.a et Figure I.14.b).

La wollastonite (5-10 mm, 5 à 20%) et l'apatite jaune à exsolution de britholite sont présents dans ces syénites blanches souvent intercalés dans les niveaux riches en clinopyroxène. Elles sont parfois entourées de grenat comme pour les clinopyroxènes (Figure I.14.a).

Le quartz (1 à 3 vol.%) présent en petites grains xénomorphes à extinction ondulante souvent sous forme interstitielle. Il est associé à la calcite dans les syénites blanches en petits grains en couronne autour de la wollastonite (Figure I.14.b).

L'apatite (1-4 mm 1 à 3%) verte et rose est présente dans les syénites rouges avec les mêmes caractéristiques que les apatites des carbonatites mais avec des tailles beaucoup plus petites.

L'apatite à britholite vert-jaunâtre est plutôt présente dans les syénites blanches associées aux wollastonites intercalée dans les niveaux à pyroxène (Figure I.14.a).

Les minéraux accessoires dans les syénites sont le sphène et l'allanite (Figure I.14.b). L'allanite est développée en couronne continue autour des clinopyroxènes et des apatites ou associée à la magnétite comme inclusion dans les clinopyroxènes. Elle est aussi présente dans les fissures de ces minéraux.

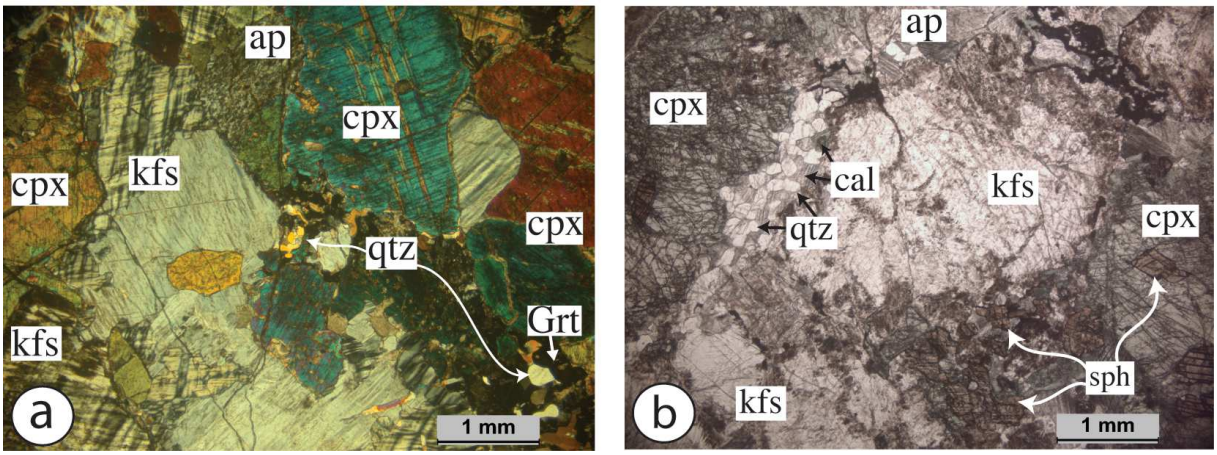

Figure I.14. Microphotographies des syénites d'Ihouhaouene. **a.** assemblage minéralogique d'une syénite blanche avec le grenat et le quartz autours des clinopyroxènes. **b.** assemblage minéralogique d'une syénite rouge avec une alternance des cristaux automorphes de clinopyroxène et de feldspath potassique.

I.2.c. Les échantillons des études antérieures

Plusieurs échantillons récoltés par K. Ouzegane durant les missions de terrain antérieures (1987) ont été triés et classés selon les trois secteurs de carbonatites dans la région d'Ihouhaouene (Table 2 ; en annexe A).

Les échantillons présentent les mêmes caractéristiques pétrographiques que les carbonatites et syénites échantillonnées durant ma mission de terrain et ont été utilisés dans l'étude géochimique de ma thèse. Quelques échantillons à minéraux d'altération locale tardive, telle la biotite et l'amphibole décrits dans la thèse de Ouzegane, (1987) ont été écartés dans cette étude petrogénique du complexe alcalin d'Ihouhaouene.

Les carbonatites de types I dans les travaux de Ouzegane (1987), Bernard-Griffiths *et al*. (1988) et Fourcade *et al*. (1996) représentent les carbonatites bréchiques dans cette étude et les carbonatites II et III sont les carbonatites pegmatitiques.

I.3. Méthodes analytiques

I.3.a. Analyse des roches totales

Une soixantaine de roches intrusives de syénite et de carbonatite représentant la diversité et l'hétérogénéité des roches de la région d'Ihouhaouene ont été sélectionnées pour les études pétrologiques et géochimiques détaillées. Les échantillons ont été choisis en fonction des localités et des deux types de syénites rouges et blanches et des différents types de carbonatites : en veines bréchiques, pegmatitiques ou en veines de calcite. Les carbonatites bréchiques ont été concassées progressivement et nettoyées afin d'enlever des fragments de syénite avant le broyage fin. Une quantité significative de carbonatites pegmatitiques par rapport à la grande taille des minéraux (~ 3 kg) a été broyée et cartée pour avoir une composition représentative pour chaque échantillon (Table 3 ; en annexe A).

Analyse des éléments en trace (ICP-MS)

Les éléments en trace ont été analysés par spectrométrie de masse couplée à un plasma inductif à Géosciences Montpellier (plate-forme AETE OSU-OREME). Une attaque à l'acide sur 100 mg de poudre d'échantillon, pesé à l'aide d'une balance de précision (± 1mg), dans des Savilex en téflon est réalisée avec 1 ml de $HClO_4$ et 2,5 ml de HF sur une plaque chauffante à 100 ° C pendant 24 heures. L'acide fluorhydrique brise les liaisons chimiques des silicates dans la roche et met les ions libérés en solution, tandis que l'acide perchlorique agit comme un oxydant comme le nitrique et l'objectif de cet acide est d'assurer une évacuation aussi complète que possible de l'excès de HF. Ensuite, les échantillons sont évaporés à sec à 150ºC et 50W. Une seconde attaque à l'acide est appliquée avec 0,5 ml de $HClO_4$ et 1 ml de HF pendant 24 heures suivie par une évaporation, puis les

échantillons sont repris en trois fois, séparés par des évaporations, en 0,5 ml, 0,25 ml, puis 0,25 ml de $HClO_4$. L'échantillon est évaporé en un résidu solide. Une première dilution est réalisée avec ce résidu en ajoutant de l'acide nitrique et de l'eau MilliQ jusqu'à obtenir une solution de 20,6 g. Avant l'analyse par spectromètre de masse, la solution d'échantillon est diluée avec 9,45 ml d'H_2O, 0,25 ml d'HNO_3 et 0,1 d'InBi selon un facteur de 10 000 choisi pour les carbonatites et les syénites associées pour éviter la saturation en éléments en trace lors de l'analyse. Pour chaque série d'analyses (20 échantillons), 4 blancs (seuls des acides ont été introduits dans le savilex) et quatre standards: BHVO-1, BEN, UBN et COQ-1 ont été analysés pour détecter les traces de contamination au cours de la série d'attaques et/ou d'analyses et la dérive interne de la machine. Le spectromètre de masse utilisé pour quantifier les concentrations des éléments en traces dans la roche totale est l'Agilent 7700x, dont la sensibilité est de l'ordre de 200 x 106 cps / ppm sur 115In (Indium). Les étalons internes A2 et A4 sont étalonnés pour les concentrations de Zr-Nb et de Hf-Ta et des courbes d'étalonnage sur Rb, Sr, Y, Zr et Ce sont effectuées pour vérifier l'étalonnage interne.

Analyse des éléments majeurs

Les éléments majeurs sur roche totale ont été analysés par ICP-OES (iCap 6500 ThermoFisher) au service SARM du CRPG (Nancy, France). La procédure suivie est conforme au protocole de Carignan (Carignan *et al*. 2001). La poudre de roche entière est fondue avec du $LiBO_2$, puis le verre de fusion est dissous dans un mélange de HNO_3, H_2O et Glycérol. L'écart-type relatif pour les principaux éléments est inférieur à 5%.

Analyse des éléments volatils

Les éléments volatils ont été analysés au SARM à l'aide d'un analyseur d'éléments pour le contenu en soufre et en carbone de la roche totale. Les teneurs en F et Cl ont été déterminées par spectrophotométrie de ferrithiocyanate de précipitation humide avec le spectrophotomètre Varian Cary 50 (Vernet *et al*. 1987).

I.3.b Analyse in-situ des minéraux

Analyse à la microsonde électronique (EPMA)

Les concentrations en éléments majeurs, mineurs et volatils dans les minéraux ont été analysées sur lames minces polies par microsonde électronique CAMECA SX100 de Géosciences Montpellier (service Microsonde Sud). La tension d'accélération et le courant du faisceau ont été réglés sur 20 keV et 10 nA, respectivement. Le faisceau est focalisé (1 μm) à l'exception des carbonates analysés avec un faisceau défocalisé. Le temps d'analyse a été fixé à 20 s pour chaque élément majeur, 40 s pour les éléments mineurs tels les Terres Rares, Ni, Cr, Mn, Th, Sr, et Ba et 40 s pour le F, Cl et S. Les analyses ont été calibrées sur des standards internes choisis pour chaque élément: Al_2O_3 pour Al, TiO_2 pour Ti, wollastonite pour Ca et Si, albite pour Na, orthose pour K,

forstérite pour Mg, hématite pour Fe, apatite pour P, métal natif pour Ni, Mn, Cu, célestine pour Sr, ThO_2 pour Th, verres enrichis pour les REE : REE2 pour Nd, Sm, Yb, Lu; REE3 pour La, Ce, Pr, Y; REE4 pour Dy, baryte pour S et Ba, fluorite pour F et chloroapatite pour Cl. L'erreur sur les mesures est inférieure à 0,5 pds.% (Table I.1).

La distribution de cinq éléments majeurs (Ca, P, Si, Ce, La) au sein des cristaux d'apatite et des inclusions de monazite a été caractérisée par la collecte de cartes d'éléments aux rayons X par dispersion de longueur d'onde (WDS) avec une taille de pas de 16 μ sur un cristal de 1cm couplées à des analyses quantitatives ponctuelles (20 points).

Table I.1: Ecart type et limites de détection (pds %) des éléments majeurs dans l'apatite et la britholite.

	Std déviation		limite de détection
	Ap (n=55)	Bri	Bri (n=40)
SiO_2	0,01	0,03	0,01
FeO	0,01	0,02	0,01
MgO	0,001	0,004	0,01
MnO	0,01	0,003	0,002
CaO	0,03	0,05	0,01
Na_2O	0,01	0,01	0,02
K_2O	0,003	0,000	0,01
P_2O_5	0,05	0,03	0,01
La_2O_3	0,01	0,03	0,04
Ce_2O_3	0,02	0,07	0,04
Pr_2O_3	0,002	0,005	0,05
Nd_2O_3	0,01	0,02	0,04
Sm_2O_3	0,002	0,01	0,03
Gd_2O_3	0,01	0,005	0,07
Dy_2O_3	0,02	0,01	0,07
Y_2O_3	0,001	0,01	0,02
Lu_2O_3	0,02	0,02	0,03
ThO_2	0,01	0,01	0,03
SO_2	0,01	0,003	0,01
Cl	0,001	0,003	0,01
F	0,03	0,04	0,17

Analyses des éléments en trace par ablation laser (LA-ICPMS)

Les analyses des éléments en trace dans les minéraux ont été déterminées par LA-ICP-MS de Géosciences Montpellier (plate-forme AETE, OSU-OREME), à l'aide de GeoLas Q + Excimer CompEx102 couplé avec un spectromètre de masse à source plasma (ThermoFinnigan Element XR). Un diamètre de faisceau laser de 26 μm a été utilisé pour l'apatite et la britholite, 51 μm pour les minéraux silicatés et de 77 μm pour la calcite et la wollastonite avec une fréquence de 7 Hz, une puissance laser de 5 J/cm^2 et un mélange d'hélium et d'argon en tant que gaz vecteur. Chaque analyse consiste en une impulsion de pré-ablation de 10 secondes, 2 minutes de mesure de fond avant ablation et de 60 secondes de temps d'intégration après le déclenchement du laser. Les analyses sont calibrées à partir de deux standards le NIST 612 comme standard interne et le BIR comme standard externe. Les concentrations de SiO_2 - CaO pds% déterminées précédemment à la microsonde électronique pour chaque minéral sont utilisées pour calculer les concentrations des éléments en trace. Puis le traitement des données est réalisé sous le logiciel GLITTER (Van Achterbergh *et al*. 2001 ; Griffin *et al*. 2008).

Géochronologie U-Pb

La géochronologie U-Pb sur apatite a été réalisée par ablation laser (LA-ICP-MS) sur lames épaisses à Géosciences Rennes à l'aide d'un laser à Excimer ESI NWR193UC couplé à un spectromètre de masse à source plasma quadripôle Agilent 7700x ICP-MS équipé d'un double système de pompage pour améliorer la sensibilité (Paquette *et al*. 2014). Des images par cathodoluminescence (CL), utilisant un système Reliotron CL équipé d'une caméra couleur numérique disponible à Géosciences Rennes, ont été réalisées sur les apatites analysées afin de vérifier l'homogénéité des cristaux et éviter toute contamination par la présence d'inclusions.

La calibration du spectromètre et des masses analysées a été effectuée avant chaque session d'analyse sur le verre de référence NIST SRM 612, en vérifiant le signal ^{238}U et en minimisant le rapport ThO^+/Th^+ (<0,5%). Au cours d'une analyse, les signaux des masses ^{43}Ca, ^{204} (Pb + Hg), ^{206}Pb, ^{207}Pb, ^{208}Pb et ^{238}U sont acquis. Le signal ^{235}U est calculé à partir de ^{238}U sur la base du rapport $^{238}U/^{235}U$=137,88. Les analyses consistaient en une mesure de fond de 20 s suivie de 60 s temps d'intégration, puis de 10 s entre deux analyses pour éliminer d'éventuelles contaminations par l'échantillon précédent. Un diamètre de faisceau d'ablation de 40 μm avec des taux de répétition de 7 Hz ont été utilisés.

Les standards d'apatite utilisés comme matériau de référence interne pour les analyses d'apatite sont l'apatite de Madagascar (âge ID-TIMS de 473,5 ± 0,7 Ma; Cochrane *et al*. 2014), l'apatite de Durango (31,44 ± 0,18 Ma; McDowell *et al*. 2005) et l'apatite de McClure (523,51 ± 2,09 Ma; Schoene et Bowring 2006).

Les données ont été corrigées pour le fractionnement U–Pb et pour l'influence de masse par les mesures répétées du standard d'apatite de Madagascar. Les mesures des standards d'apatite, de Durango et de McClure ont été traitées comme des standards externes et utilisées pour contrôler la reproductibilité et la précision des corrections. Au cours des analyses, ils ont fourni des âges corrigés au ^{207}Pb de 32,27 ± 0,70 Ma (MSWD = 0,44; probabilité = 0,98) et 527,2 ± 5,6 Ma (MSWD = 0,21; probabilité = 0,99), respectivement. Le traitement des données a été réalisé à l'aide du logiciel Igor Pro fonctionnant avec Iolite + VizualAge_UcomPbine (Chew *et al*. 2014). Cette correction de données consiste à une correction du Pb commun à l'aide de la méthode ^{207}Pb pour la composition initiale en isotope du Pb spécifiée dans les valeurs de référence du standard Madagascar. Ainsi la courbe de fractionnement ^{207}Pb/^{235}U est ajustée avec une correction du Pb commun basée sur ^{207}Pb en utilisant une valeur initiale de ^{207}Pb/^{206}Pb de 0,8681 (Cochrane *et al*. 2014).

Les analyses U-Pb des zircons des échantillons de carbonatite (IC2-9A) et de syénite (IC2-6A) ont été réalisées par la méthode LA-ICP-MS au laboratoire « Instituto Andaluz de Ciencias de la Tierra » (IACT) (Grenade, Espagne). L'analyse est effectuée à l'aide d'un laser de type Excimer d'une longueur d'onde 193 nm couplé à un spectromètre de masse à multicollecteurs Agilent 8800 Triple Quadripole ICP-MS.

L'ablation du cristal est réalisée à l'aide du faisceau laser de 15 µm avec une fréquence de 10 Hz et une puissance laser de 8 J/cm^2. Le matériel ablaté est transporté dans un mélange gazeux à 100% d'hélium vers la source de plasma pour être ionisé. Chaque analyse consiste en une impulsion d'ablation de 30 secondes de temps d'intégration. Les différentes masses isotopiques (^{204}Pb, ^{206}Pb, ^{207}Pb, ^{208}Pb, ^{232}Th, ^{235}U et ^{238}U) sont mesurées simultanément en mode statique avec un temps de balayage entre les masse de 150 ms pour ^{204}Pb, ^{206}Pb, ^{207}Pb, ^{208}Pb et ^{238}U, 100 ms pour ^{235}U et ^{232}Th et 60 ms pour ^{202}Hg en utilisant des détecteurs de type Faraday.

Les corrections pour les fractionnements isotopiques et élémentaires ainsi que pour la dérive de l'Isoprobe sont effectuées à partir de deux standards : Le zircon 91500 (1065,4 ± 0.3 Ma, Wiedenbeck *et al*. 1995) utilisé comme standard interne et le Plesovice (337 ± 0.7 Ma, Slama *et al*, 2008) utilisé comme standard externe. Les données sont traitées sur le logiciel Igor Pro Iolite 2.5 + VisualAge Data Reduction (School of Earth Sciences, University of Melbourne). Les âges sont ensuite établis à partir des calculs de régression linéaire selon la méthode de York (1969) et effectués en utilisant le logiciel ISOPLOT version 3 (Ludwig, 2003).

Analyse des microstructures cristallines à l'EBSD

L'orientation cristallographique préférentielle (CPO) des apatites, des britholites et des monazites a été caractérisée par l'indexation des diagrammes de diffraction des électrons rétrodiffusées (EBSD) à Géosciences Montpellier (CNRS-Université de Montpellier, France) à l'aide d'un MEB haute résolution CamScan Crystal Probe X500FE de type (FEG). Ce MEB est équipé d'un

détecteur HKL NordlysNano EBSD pour l'analyse cristallographique et un détecteur EDS X-Max^N 20mm^2 à spectrométrie à rayon X pour l'analyse chimique qualitative. Une tension d'accélération de 15 à 20 kV, un courant de faisceau d'environ 5 nA, une taille de pas de 2,7 et 10 μm et une distance de travail de 25 mm sont les conditions d'analyses utilisées. La déviation angulaire pour les mesures est de 20º entre le faisceau d'électrons et la surface de l'échantillon pour atteindre une intensité maximale de diffraction. Les données sont réduites en bruit à l'aide d'une correction pour remplir les pixels non indexés «Wild spikes» en fonction des pixels voisins à l'aide du logiciel CHANNEL5 (Oxford Instruments HKL).

Des cartes de phases et des cartes de 11 éléments (Th, Ce, La, Nd, P, Si, Al, Ca, S, Cl, et C) ont été réalisées afin de mettre en évidence les propriétés chimiques des apatites et des exsolutions en britholite et la distribution des éléments dans les minéraux. Les cartographies microstructurales et les figures de pôles ont été réalisées afin de mettre en évidence l'orientation cristallographique des minéraux. Les cartographies d'orientation représentent l'orientation cristallographique de chaque pixel par une couleur fonction de la figure de pôles inverses, selon un des trois axes principaux (X, Y, Z). A partir de l'orientation cristallographique de chacun des pixels, il est dès lors possible de déterminer l'orientation cristallographique préférentielle (Crystallographic Preferred Orientation CPO), qui est définie par la fabrique des minéraux et indique l'orientation dominante.

Modélisation géochimique des processus de cristallisation fractionnée, d'immiscibilité et d'hybridation durant l'évolution magmatique des carbonatites et syénites d'Ihouhaouene

Ce chapitre correspond à l'étude des intrusions magmatiques des carbonatites et des syénites d'Ihouhaouene. Une étude, sous forme d'article soumis et accepté dans Contributions to Mineralogy and Petrology, se focalise dans une première partie sur les caractéristiques minéralogiques, pétrologiques et géochimiques afin de contraindre les processus magmatiques à l'origine de la formation de ces roches. Une deuxième partie se focalise sur la modélisation géochimique des processus d'immiscibilité et d'hybridation durant la différentiation des magma carbonatés et silicatés dans la région d'Ihouhaouene.

Immiscibility and hybridization during carbonatite and alkaline magma evolution (Ihouhaouene, In Ouzzal terrane, Western Hoggar)

A. Djeddi[1,2*], F. Parat[1], J.-L. Bodinier[1,3], K. Ouzegane[2], J.-M. Dautria[1]

[1] Géosciences Montpellier, UMR 5243, CC60, Université de Montpellier, Place Eugène Bataillon, 34095 Montpellier cedex 5, France

[2] FSTGAT-USTHB, BP32, El Alia 16111 Bab Ezzouar, Algeria

[3] Geology & Sustainable Mining Program, UM6P, Hay Moulay Rachid, Ben Guerir, Morocco

Submitted article in Journal of Contributions to Mineralogy and Petrology

*E-mail : asma.djeddi@gm.univ-montp2.fr

Abstract

The Ihouhaouene alkaline complex, in Southern Algeria, contains among the oldest known carbonatites on the Earth, emplaced in the In Ouzzal terrane (Hoggar) at 2 Ga. The complex shows a range of carbonatite facies closely associated with syenites – also showing mineralogical variations. In such, the Ihouhaouene alkaline complex represents a unique opportunity to study the relationships between these two types of rocks and thus to bring major constraints on the origin of carbonatites. The Ihouhaouene carbonatites and syenites display similar pegmatitic/brecciated textures and mineral assemblages of diopside/hedenbergite, apatite, wollastonite +/- calcite and alkali-feldspar, suggesting that they were emplaced during a single igneous event. The Carbonatites are calciocarbonatites showing a continuous range of whole-rock major and trace element compositions from Si-poor carbonatite (<20 wt.% SiO_2; 24-36 wt.% CO_2) to Si-rich carbonatite (20-35 wt.% SiO_2; 11-24 wt.% CO_2), white syenite (52-58 wt.% SiO_2; 0.1-6.5 wt.% CO_2) and red syenite (57-65 wt.% SiO_2; 0.1-0.4 wt.% CO_2). The Si-rich carbonatites and the white syenites are both distinguished by higher REE content and LREE/HREE fractionation (Ce/Lu= 1690-6182) as well as higher Nb/Ta ratio (>50), in calculated apatite equilibrium melts than in their clinopyroxene counterpart (Ce/Lu= 49-234; Nb/Ta<10). This indicates that apatite in carbonatites was equilibrated with REE-enriched carbonate melts, whereas clinopyroxene precipitated from evolved silicate melts. Then the two mineral phases were assembled to form hybrid mineral aggregates and did not re-equilibrate afterwards. The Si-poor carbonatites resemble the Si-rich carbonatites, with both rock types characterized by more elevated REE contents in equilibrium melts calculated from apatite compared with clinopyroxene. Nb/Ta ratios display a wide range with a majority of subchondritic values (<10) reflecting the segregation of the carbonate fraction from an evolved parental melt. Finally, the red syenites are characterized by similar REE contents in apatite and clinopyroxene equilibrium melts suggesting that they were formed from similar, midly differentiated melt fractions (Nb/Ta>10). To reproduce both the overall and the micro-scale trace element systematics of the suite, we propose a stepwise differentiation process involving alternating stages of fractional crystallization and melt exsolution, partly counterbalanced by intermingling of partially crystallized melt fractions of contrasted compositions. The variation of Kd's between silicate and carbonate liquids is function of the composition of melts during magmas evolution. In this scheme, a high degree of differentiation of the parental melt may account for the segregation of the low Nb/Ta in Si-poor carbonatites. Progressive cooling of a melilititic silico-carbonated mantle melt resulted in the segregation of both cumulus minerals (clinopyroxene, wollastonite, apatite…) and immiscible carbonate melt fractions, as well as in the concomitant chemical evolution of the silicate parental melt.

Keywords: Carbonatite; alkaline silicate magma; liquid immiscibility; hybridization; Hoggar

II.1. INTRODUCTION

The close spatial association of carbonatite and alkaline silicate rocks formed the key question of several experimental studies to explain their complex relationships, the processes at their co-genetic origin or not and the kind of parental melt they derived from. Almost all carbonatites are associated with alkali silicate rocks that are usually of nephelinitic or melilititic affinity or their plutonic equivalents (Bell & Kjarsgaard 1998). The study of natural carbonatite-alkaline rocks and experimental studies suggest that carbonatites may result from two processes involving (1) direct partial melting of carbonate-rich mantle (Stoppa *et al*. 2005; Gudfinnsson & Presnall 2005; Dasgupta & Hirschmann 2006); (2) magmatic differentiation and immiscibility of carbonated silicate melts (Freestone & Hamilton 1980; Baker & Wyllie 1990; Dawson 1998; Gittins & Jago 1998; Dasgupta *et al*. 2006; Brooker & Kajarsgaard 2011). But this kind of carbonatites can only be magnesio-carbonatites, isolated in the mantle and risen rapidly to the surface (Dalton & Presnall 1998; Wyllie & Lee 1998). Based on experimentally equilibrated silicate and carbonate melt, calciocarbonatites may be generated through reaction of carbonate melts rich in volatiles with depleted lherzolite or harzburgite at low pressures (Dalton & Wood 1993).

The Ihouhaouene (~ 2 Ga; Bernard-Griffiths *et al*. 1988) carbonatite massifs (In Ouzzal terrane, south of Algeria) are plutonic rocks and are systematically associated with SiO_2-saturated syenitic rocks. The syenite complexes associated to carbonatites were emplaced concordantly with respect to the foliation of granulites, (Ouzegane 1987; Bernard-Griffiths *et al*. 1988; Fourcade *et al*. 1996, Ouzegane *et al*. 1988) and represent a unique opportunity to understand carbonatites and alkaline magmas genesis during the Paleoproterozoic.

In this paper, we study the major, trace and volatile elements of bulk-rock and *in situ* mineral of carbonatites and syenites to understand the genetic relationship between carbonatite and alkaline magmas in order to determine the origin of carbonate-rich silicate magmas and magmatic evolution in Archean crust during Proterozoic time. A numerical model is proposed in order to simulate the processes at the origin of composition evolution observed in Ihouhaouene and similar carbonatite complexes.

II.2. GEOLOGICAL SETTING AND FIELD RELATIONSHIPS

The Ihouhaouene area is located in the northern part of In Ouzzal terrane (Western Hoggar, South of Algeria) (23º36'14"N, 3º10'32"E) and contains carbonatite bodies associated with syenites that are among the oldest in the world (~ 2 Ga, Bernard-Griffiths *et al*. 1988). The In Ouzzal terrane is an Archaean crust remobilized during the Paleoproterozoic ultra-high-temperature metamorphism (2 Ga, T = 800-1050°C at 10-11 kbar, Ouzegane *et al*. 2003a). Two Archaean units occur: a lower crustal unit mainly composed of orthogneiss with igneous activity at 3.2 Ga (Peucat *et al*. 1996) and a supracrustal unit that depositional age falls within the range 2.7 -2.6 Ga (Peucat *et al*. 1996) with

quartzites, banded iron formations, marbles, Al-Mg and Al-Fe granulites associated with mafic and ultramafic rocks (Ouzegane *et al*. 2003a; Guiraud *et al*. 1996; Peucat *et al*. 1996; Adjerid *et al*. 2013).

The carbonatites and syenites occur as linear deposits along shear zones in three sectors (Ouzegane *et al*. 1988; Lapin & Plashko 1988; Figure II.1): (i) Oued Ihouhaouene characterized by several small hills oriented EW and NW-SE; (ii) the South Tirahart wadi complex with approximately 4 km long and 1 km wide outcrops, and (iii) Tirahart wadi north, a hill spreading over 2.5 km long and 250 m wide. Carbonatites outcrop as veins or massive formations in syenites. The contact is sharp and syenites have mylonitized edges (< 20 cm).

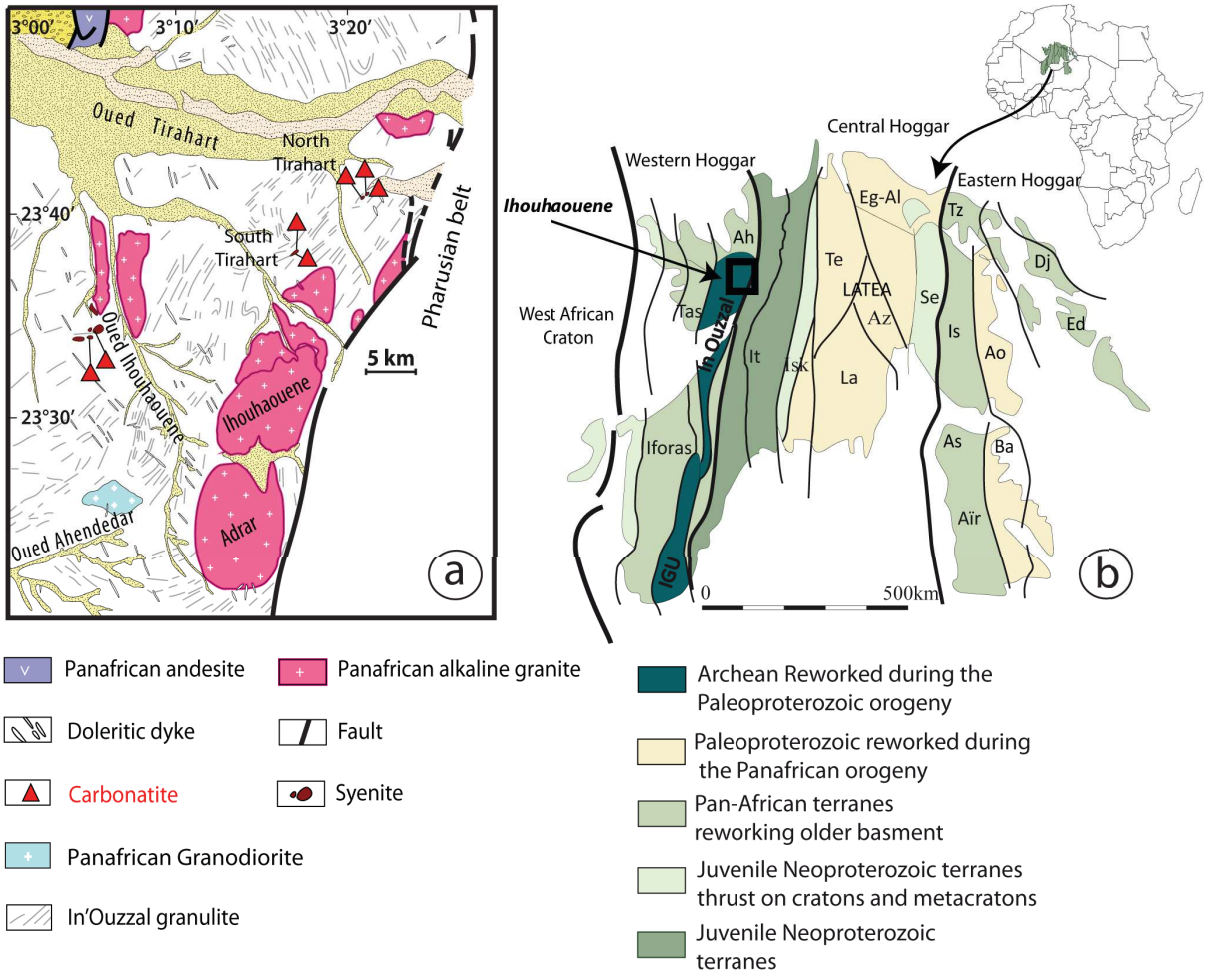

Figure II.1.a Geological map of the Ihouhaouene area in N.W part of the In Ouzzal terrane and localization of carbonatites and associated syenites (Ouzegane *et al*. 1988). **b** The Tuareg Shield map with the 23 terranes (Black *et al*. 1994) modified by Liégeois *et al*. (2003) and position of the Ihouhaouene area in Western Hoggar.

Two types of carbonatite according to their texture are present: (i) brecciated carbonatites up to 50 m thick massive structures and max. 500 m length including syenite fragments with sizes ranging from 1 cm to 70 cm and surrounded by a clinopyroxene reaction aureole (Figure II.2.a, c); (ii) pegmatitic carbonatites with apatite (3 to 50 mm) (Figure II.2.b, d) and calcite phenocrysts in form of pockets or small veins (< 2m width and < 10m length). Clinopyroxene and alkali feldspar megacrysts are often present in these pegmatitic carbonatites (Figure II.2.d).

The syenites form large outcrops in all three sectors. They are red (Figure II.2.e) and white (Figure II.2.f) according to the presence of red alkali feldspar and wollastonite + white alkali feldspar, respectively. Both syenites present structures with segregation of dark-level minerals of pyroxenes interposed in feldspar and quartz levels with the same orientation as the surrounding granulites.

Red syenites are more abundant in Oued Ihouhaouene and north wadi Tirahart complexes. In Tirahart wadi North complex outcrops a feldspathic breccia, which present fragments of white syenite with wollastonite, garnet and large crystals of pyroxene cemented by feldspars. The contact between red and white syenites is brecciated. Only in Oued Ihouhaouene, we observed sharp contacts, with large white syenite bodies crosscutting red syenites (previously mapped as granites by Fourcade *et al*. 1996).

The contact between syenites and granulitic basement is not obvious because of sand in this area, but the outcropping granulites (far from ~ 20 m) in Oued Ihouhaouene and north wadi Tirahart present no evidence of fenitization. The granulitic crust has undergone high temperature metamorphism during paleoproterozoic and preserved refractory chemical compositions (Ouzegane *et al*. 2003), hardly consistent with metasomatism and fenitization induced by a second local fluid (e.g. in situ alkali-metasomatism of country rock around intrusions of carbonatites and/or alkaline rocks, Kresten *et al*. 1987; Drüppel *et al*. 2005). In Ihouhaouene area, syenites have the same mineralogy from the contact with carbonatite veins to the granulite host-rock. No fenitization aureole has been observed.

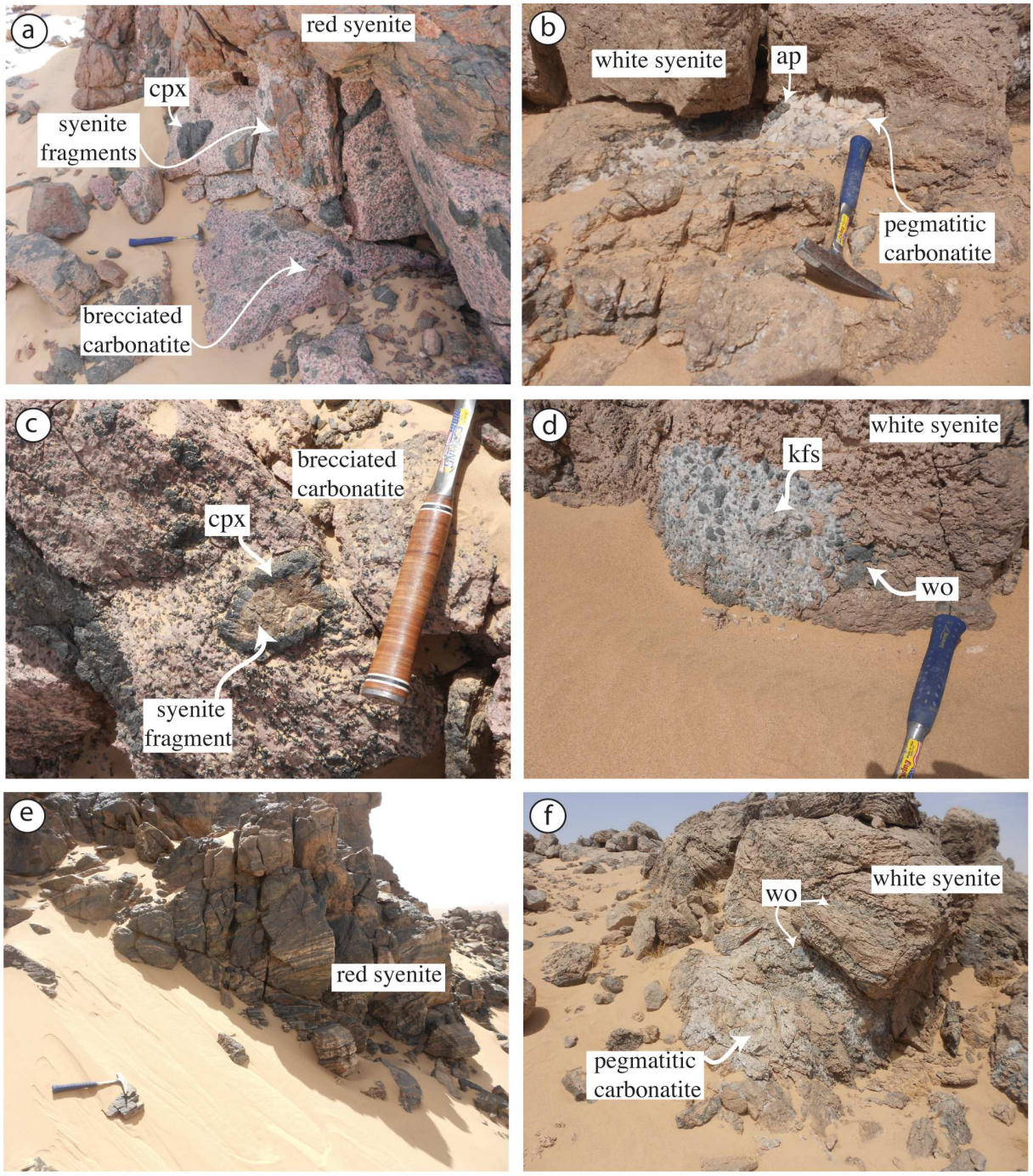

Figure II.2. Field photographs of the alkaline syenites and carbonatites in the three sectors of Ihouhaouene area. **a** North wadi Tirahart brecciated carbonatite vein with clinopyroxene (cpx) and syenite fragments intruding a red syenite. **b** South wadi Tirahart pegmatitic carbonatite with apatite (ap) crystals in white syenite. **c** Oued Ihouhaouene syenite fragment surrounded by clinopyroxene aureole in brecciated carbonatite. **d** South wadi Tirahart carbonatite pocket rich in wollastonite (wo) and k-feldspar (kfs) in white syenite. **e** North wadi Tirahart layered red syenite with light k-feldspar levels and dark clinopyroxene levels. **f** South wadi Tirahart pegmatitic carbonatite vein intruding a white syenite rich in wollastonite levels.

II.3. PETROGRAPHY

II.3.a. Carbonatites

All carbonatites from Ihouhaouene contain apatite and clinopyroxene set in a matrix with up to 50 vol.% of primary calcite and can be defined as calciocarbonatite (Streckeisen 1974).

Brecciated carbonatites are medium to coarse grained (3-8 mm, Figure II.3.a) with clinopyroxene (3 mm 1-20 vol.%), wollastonite (8 mm, < 10 vol.%), green or pink apatite (3-5 mm 1 to 22 vol.%) set in groundmass of pink, gray or white calcite (3-8 mm, 50 to 70 vol.%). Green apatites have quartz, calcite and fluorite as inclusions, whereas monazite, calcite, quartz and allanite occur as inclusions or around pink apatites. Accessory minerals are K-feldspars (4-8 mm, < 1 vol.%), magnetite (< 1 vol.%) as inclusions in clinopyroxenes, allanite (0.5-1 vol.%) around clinopyroxene, sphene (< 2 vol.%), quartz (< 1 vol.%) and coronitic garnet (< 3 vol.%).

The pegmatitic carbonatites (Figure II.3.b) have large calcite grains (1-3 cm, up to 70 vol.%), clinopyroxene (1 to 5 vol.%) and green, pink or yellow apatite (up to 10 cm, 1 to 10 vol.%). Green and pink apatites are similar to apatites in brecciated carbonatite with the same inclusions. Yellow apatites differ from apatite in brecciated carbonatite with britholite exsolutions (up to 40 vol.%). Allanite, fluorite, quartz, wollastonite and alkali feldspar are present as accessory minerals (< 1 vol.%).

II.3.b. Syenites

Red syenites have medium to coarse-grained layered texture (5-10 mm, Figure II.3.c) with K-feldspar (3-9 mm, 40 to 80 vol.%) with perthitic exsolution, clinopyroxene (3-8 mm, 20 to 40 vol.%), pink apatite (1-4 mm, 1 to 3 vol.%) and interstitial xenomorphe quartz grains (1 to 3 vol.%). Sphene is present as accessory mineral. Allanite and magnetite are present around and as inclusion in clinopyroxene, respectively.

White syenites (Figure II.3.d) are layered with light bands of K-feldspar, wollastonite (5-10 mm, 5 to 20%) and yellow apatite with britholite and dark bands with clinopyroxene (3-8 mm, 40 vol.%) surrounded by garnet and magnetite. They show a coronitic texture composed of calcite associated with quartz and garnet around the wollastonite.

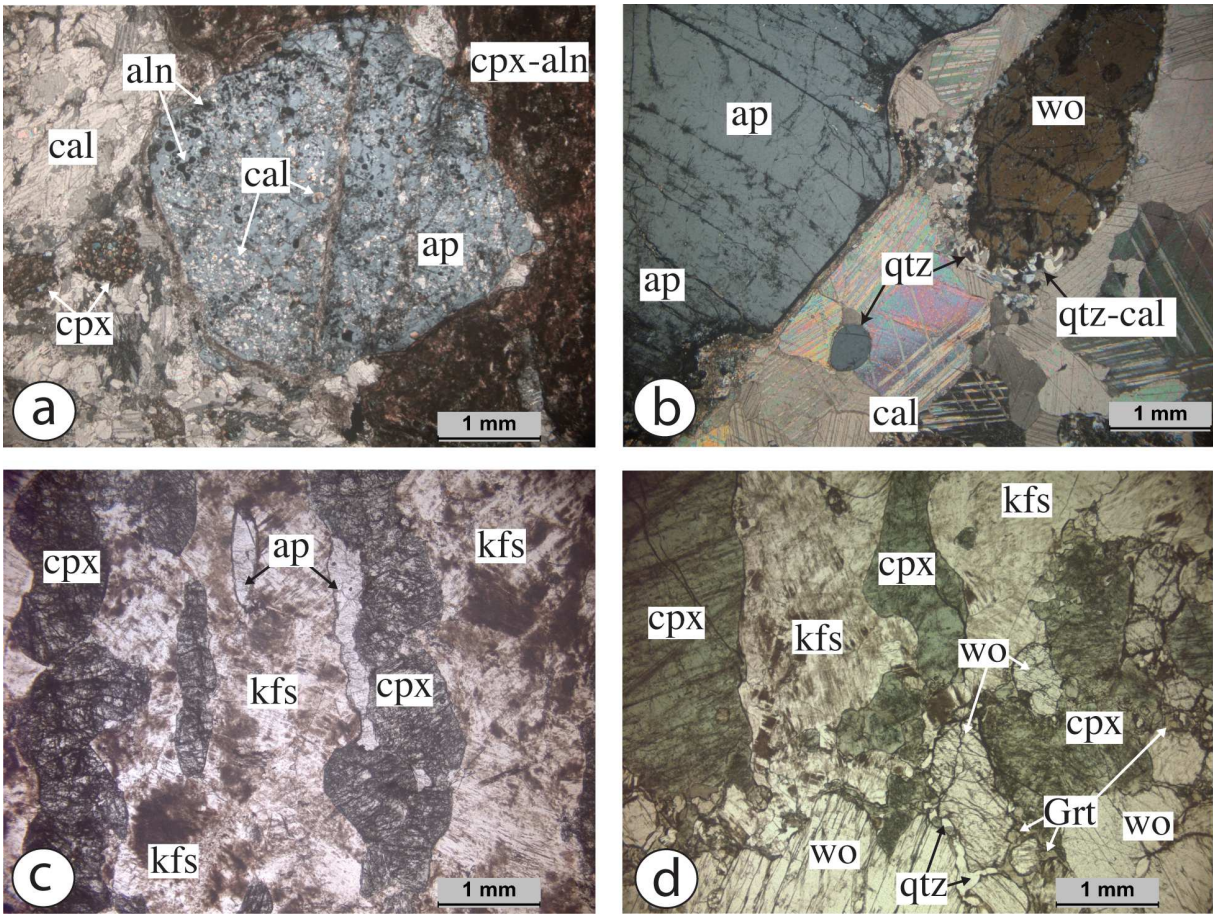

Figure II.3. Microphotographs of (**a**-**b**) carbonatites and (**c**-**d**) syenites. **a** Si-poor brecciated carbonatite with apatite (ap), clinopyroxene (cpx) and calcite (cal). Clinopyroxene with allanite (aln) inclusions and apatite with calcite and allanite inclusions. **b** Pegmatitic Si-rich carbonatite with apatite and wollastonite (wo) surrounded by quartz (qtz) and calcite. **c** Red syenite with altered k-feldspar (kfs) with apatite and clinopyroxene. **d** White syenite with K-feldspar, clinopyroxene and wollastonite surrounded by garnet (Grt).

II.4. METHODOLOGY

Fifty-four intrusive silicate and carbonatite rocks representing the diversity of rock types in the Ihouhaouene area were selected for petrological and geochemical study. All granulitic basement rocks from the three sectors of carbonatites and syenites are presented in table 1 of supplementary data B. Samples were chosen according to the localities and the different types of carbonatites (brecciated, pegmatitic or calcite veins) and the two types of red and white syenites. Brecciated carbonatites were well separated and cleaned of syenite fragments before milling. A significant amount (~ 3 kg) of pegmatitic carbonatites was milled to have a representative bulk-rock composition.

II.4.a. Whole-rock major, trace and volatile element analysis

All samples were cut, crushed and milled in agate into fine powders (≥5 µm) without using

water. Major elements were analysed by ICP-OES (iCap ThermoFisher) at the SARM service of the CRPG (Nancy, France). The procedure followed is according to the Carignan protocol (Carignan *et al*. 2001). The whole rock powder is fused with $LiBO_2$ then the fusion glass is dissolved in a HNO_3, H_2O and Glycerol mixture. The relative standard deviation for the major elements is less than 5%. Volatile elements were determined at the SARM by element analyser for sulphur and carbon whole rock contents. F and Cl contents were determined by wet precipitation ferrithiocyanate spectrophotometry using Varian Cary 50 spectrophotometer.

Trace elements were analysed by ICP-Mass Spectrometry at Geosciences Montpellier (AETE platform OSU-OREME). An acid attack on 0.1 g of sample powder weighed in Teflon Savilex is carried out with 1 ml of $HClO_4$ and 2.5 ml of HF on a hot plate at 100ºC for 24 hours. Hydrofluoric acid breaks the silicate link of rocks and puts the released ions in solution, while nitric acid acts as a powerful oxidant. Then the samples were evaporated to dryness at 150ºC and 50W. A second attack is applied with 0.5 ml of $HClO_4$ and 1 ml of HF for 24 hours followed by evaporation, and the samples are then taken up in three steps, separated by evaporation, in 0.5 ml, 0.25 ml and then 0.25 ml of $HClO_4$. The sample is evaporated to a solid residue. A first dilution is accomplished with this residue by adding nitric acid and MilliQ water until having a solution of 20.6 g. Before mass spectrometer analysis, the sample solution is diluted with 9.45 ml of H_2O, 0.25 ml of HNO_3, and 0.1 of InBi according to a factor of 10000, which has been chosen for the associated carbonatites and syenites. For each series of analysis (20 samples), 4 blanks (only acids were introduced into savilex) and four standards: BHVO-1, BEN, UBN and COQ-1 have been analysed to monitor internal drift. The mass spectrometer used to quantify trace element concentrations in whole-rock is the Agilent 7700x, whose sensitivity is of the order of 200 x 106 cps/ppm on ^{115}In (Indium). Internal standards A2 and A4 are calibrated for Zr-Nb and Hf-Ta concentrations and calibration curves on Rb, Sr, Y, Zr and Ce are performed to verify the internal calibration.

II.4.b. *In situ* mineral analysis for major, trace and volatile elements

Major and volatile element concentrations in minerals were analysed using electron microprobe (Cameca SX100 at Geosciences Montpellier, France). Acceleration voltage and beam current were set to 20 kV and 10 nA and a beam focalized (1 μm) except for carbonates that were analysed with a defocused beam. The background counting time was fixed at 20 s for major element and 40 s for F, Cl and S. The analyses were calibrated on internal standards chosen for each element: Al_2O_3 for Al, TiO_2 for Ti, wollastonite for Ca and Si, albite for Na, orthose for K, forsterite for Mg, hematite for Fe, apatite for P, native metal for Ni, Mn, Cu, celestine for Sr, ThO_2 for Th, enriched glasses for REE, baryte for S and Ba, fluorite for F and chloroapatite for Cl.

Trace element analyses of mineral were determined by LA-ICP-MS at Geosciences Montpellier (AETE platform, OSU-OREME), using GeoLas Q + Excimer CompEx102. A diameter of 26 μm laser

beam was used for apatite and britholite, 51 μm for silicate minerals and 77 μm for calcite and wollastonite with a repetition rate of 7 Hz, a laser power of 5 J/cm^2 and a mixture of helium and argon as carrier gas. Each analysis consisted of a pre-ablation pulse of 10 s, 2 min measurement of the background and 60 s integration while the laser fires. The concentrations were calibrated with NIST 612 and the SiO_2 - CaO concentrations determined previously with electron microprobe for each mineral. BIR-1 standard is used as external standard. Data were processed with Glitter software (Griffin *et al*. 2008).

II.5. WHOLE ROCK COMPOSITION

II.5.a. Carbonatites

All carbonatites are calciocarbonatites with CaO / (CaO + MgO + FeOt + MnO)> 0.8 (Gittins & Harmer 1997). The silica and calcium contents in carbonatite range from 3 to 35 wt.% and 32.42 to 53.02 wt.%, respectively (Table II.1). According to the classification from Woolley & Kempe (1989), we distinguish two groups of carbonatites as a function of silica content: Si-poor carbonatites with SiO_2 < 20 wt.% and Si-rich carbonatites or silicocarbonatites with SiO_2 > 20 wt.%.

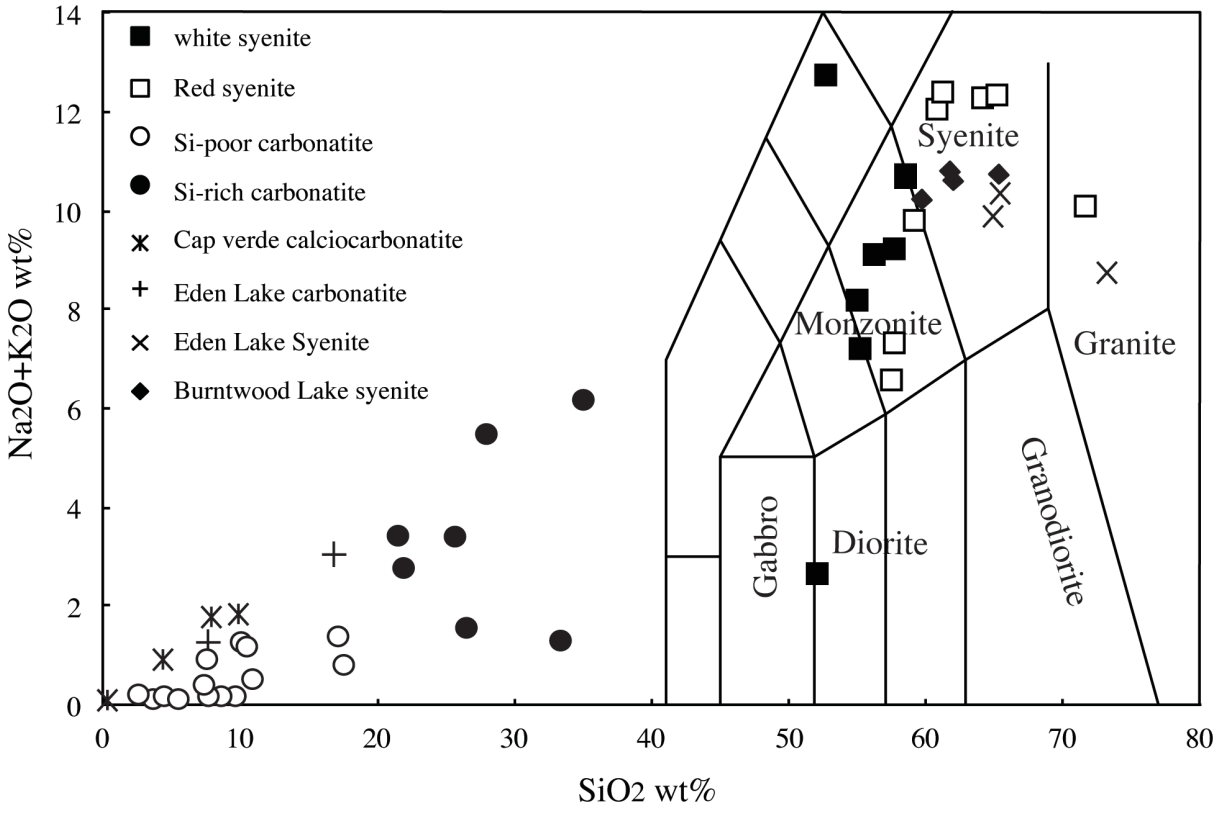

Figure II.4. Ihouhaouene carbonatites and associated syenites in total alkali-silica (TAS) diagram (after Le Maitre *et al*. 1989). Cap verde carbonatites (Weinderdorfer *et al*. 2016), Eden Lake carbonatites and syenites (Chakhmouradian *et al*. 2008), Burntwood Lake syenites (Martins *et al*. 2011).

Table 1 Representative major and trace element whole-rock compositions of carbonatites and syenites

Rock type	**Carbonatites**																
Localization	**OI**						**SWT**					**NWT**					
Sample	IC1-4C	IC1-2	IC1-4	IC1-12	IC1-12B	IHN170	INH604	IC2-9	IC2-20	IC2-11	IC2-21	IC3-1	IC3-2	IC3-7	IC3-5	IC3-15	IC3-21
SiO2 (wt%)	3,94	35,1	10,82	26,52	10,47	33,38	8,81	21,91	21,58	27,88	5,42	9,63	10,11	4,56	17,68	17,18	2,7
Al2O3	0,47	8,14	2,1	2,2	1,67	2,01	0,16	3,33	4,46	6,53	0,11	2,03	1,78	0,81	2,52	2,82	0,58
Fe2O3	0,89	1,09	2,41	4,09	1,18	2	0,37	1,84	2,08	2,04	0,85	4,1	0,89	1,08	3,67	2,3	0,5
MnO	0,19	0,1	0,16	0,49	0,17	0,31	0,1	0,17	0,22	0,12	0,14	0,17	0,16	0,17	0,2	0,17	0,08
MgO	0,87	0,69	1,74	3,31	1,19	1,22	0,11	0,58	1,54	0,77	1,01	2,11	1,19	1,05	3,21	3,12	0,26
CaO	51,87	28,7	47	37,46	46,63	42,88	51	41,18	37,16	32,42	50,63	45,33	47,42	50,97	42,18	42,31	53,02
Na2O	0,03	0,88	0,27	0,24	0,15	0,25	-	0,16	0,38	0,46	0,03	0,08	0,13	0,08	0,26	0,33	0,05
K2O	0,07	5,32	0,26	1,3	1	1,04	-	2,63	3,03	5,04	-	0,07	1,12	0,12	0,57	1,06	0,2
TiO2	-	0,06	0,07	0,06	0,06	0,06	0,04	0,63	0,09	0,19	-	0,07	0,04	0,03	0,15	0,12	0,02
P2O5	2,39	1,61	3,2	0,71	1,24	4,02	5,62	2,12	0,98	1,64	0,79	3,48	0,81	5,47	2,15	2,01	1,07
LOI	37,96	17,15	30,6	24,38	34,87	10,91	29,61	24,44	26,39	22,72	38,75	31,51	35,26	33,86	26,58	27,23	40,59
Total	98,66	98,82	98,62	100,74	98,62	98,07	95,8	98,97	97,89	99,8	97,71	98,57	98,91	98,19	99,17	98,65	99,08
CO2	34,38	15,91	26,08	21,83	31,73	11,34	28,05	22,65	24,56	20,41	36,02	29,75	32,42	30,10	24,83	26,08	36,15
F	0,2	0,37	0,24	0,07	0,11	0,62	0,37	0,19	0,07	0,15	0,06	0,26	0,06	0,39	0,18	0,16	0,08
S	<0,01	0,06	<0,01	<0,01	<0,01	0,13	0,08	0,03	0,13	0,03	0,11	0,04	<0,01	0,03	0,01	<0,01	0,01
Cl (ppm)	130	195	76	125	53	135	210	140	52	100	120	110	95	88	71	88	105
Mg#	0,79	0,71	0,74	0,76	0,8	0,71	0,54	0,55	0,75	0,6	0,82	0,67	0,84	0,79	0,78	0,84	0,68
(N+K)ox/Alox	0,2	0,76	0,25	0,7	0,69	0,64	-	0,84	0,76	0,84	-	0,07	0,7	0,25	0,33	0,49	0,44
Cs (ppm)	0,02	1,46	0,02	0,31	0,3	0,24	0,01	0,49	0,9	1	0,01	0,02	0,24	0,04	0,08	0,26	0,02
Rb	1,73	183	5,86	39,7	28,43	29,79	0,55	57,72	84,4	148	0,15	0,53	30,78	6,16	16,24	33,66	5,94
Ba	71	2505	229	898	931	559	1221	1364	3104	2620	672	290	745	120	606	995	270
Th	36,26	85,89	22,91	93,77	75,67	154	493	201	29	112	17,92	7,77	68,83	187,16	62,28	69,52	32,85
U	4,81	11,52	2,1	13,25	9,08	20,74	74,62	34,28	14,67	41,53	11,11	0,1	6,14	10,59	4,57	3,59	2,91
Nb	0,79	11,15	0,39	6,05	5,94	3,96	6,57	60,09	32,27	18,75	0,73	0,04	4	0,53	2,18	1,87	3,4
Ta	0,05	1	0,06	0,83	1,13	0,38	1,3	11,95	9,51	4,58	0,46	0,08	0,76	0,07	0,22	0,25	0,39
La	655	857	878	780	1216	1379	3956	1372	624	1790	627	297	1845	1377	1050	1357	1130
Ce	1348	1578	1650	1480	2213	2719	8185	3111	1196	3861	1196	585	3275	2715	1939	2603	1988
Pb	59	325	88	421	259	104	129	54	1436	68	1933	18	54	70	84	47	66
Pr	166	173	189	167	243	309	845	332	134	399	134	70	353	322	216	296	216
Sr	6259	5310	3124	5105	6786	3541	3664	3397	8546	3308	11446	1969	4091	5451	3729	5342	3705
Nd	657	618	710	606	867	1111	3037	1228	480	1461	487	270	1227	1218	788	1091	779
Zr	9,52	78,74	14	22	26,15	23,05	59,7	205	34,22	81,28	13,79	19,29	25,17	9,12	46,13	66,45	8,43
Hf	0,32	2,83	0,38	0,98	1,27	0,63	0,51	4,34	0,96	1,37	0,29	0,35	0,9	0,2	1,68	2,08	0,21
Sm	115	93	113	92	127	170	444	190	72	217	74	44	172	196	121	165	112
Eu	25,07	18,22	23,8	18,7	25,09	31,71	86,54	39,58	14,49	44,92	14,9	9,49	34,54	38,82	24,08	33,28	22,06
Gd	81,22	59,3	75	56,62	82	115	281	115	44,42	130	47,62	29,21	111	126	77,11	101	71,63
Tb	8,63	6,53	7,92	5,97	8,12	12,11	26,56	12,1	4,71	13,65	5,17	3,04	10,58	13,09	8,33	10,22	7,42
Dy	37	29	33,47	24,8	32,72	51,81	104	49,34	19,7	55,62	22,44	12,61	41,32	55	35,7	41,3	31,16
Y	144	117	127	91	121	217	369	184	73	207	95	46	163	208	137	149	125
Ho	5,39	4,39	4,88	3,57	4,64	7,83	14,06	6,89	2,86	7,88	3,39	1,8	5,74	7,96	5,32	5,75	4,62
Er	10,75	9,39	9,78	7,25	9,49	17,09	27,32	13,55	5,75	15,78	7,3	3,54	11,5	16,04	11,07	11,22	9,44
Tm	1,2	1,13	1,09	0,83	1,07	2,02	2,83	1,49	0,65	1,73	0,88	0,38	1,27	1,78	1,26	1,2	1,08
Yb	6,23	6,15	5,72	4,44	5,48	11,19	13,45	7,57	3,48	8,8	4,98	1,94	6,51	9,06	6,81	6,18	5,61
Lu	0,8	0,79	0,73	0,6	0,7	1,46	1,57	0,92	0,46	1,05	0,64	0,24	0,82	1,09	0,88	0,75	0,7
Eu/Eu*	0,79	0,75	0,79	0,79	0,75	0,69	0,75	0,82	0,79	0,82	0,77	0,81	0,76	0,76	0,76	0,79	0,75
Nb/Ta	17,35	11,14	6,79	7,27	5,27	10,44	5,04	5,03	3,39	4,09	1,6	0,56	5,25	7,88	9,76	7,45	8,63
Zr/Hf	29,73	27,81	36,93	22,29	20,52	36,62	116,3	47,2	35,56	59,2	48,24	55,77	28,03	45,64	27,5	31,92	40,68

Mg# = Mg/(Mg+Fe$_{tot}$)

Table 1 continued

Rock type	Carbonatites				Red syenites						White syenites					
	NWT				OI				SWT	NWT	SWT			NWT		
Sample	IC3-19	IC3-20	IC3-17	INH642	IC1-24A	IC1-24B	IC1-12A	IC1-13	IC2-6A	IC3-4	IC2-11S	IC2-10	IC2-27	IC3-10	IC3-12B	IC3-18
SiO2 (wt%)	25,62	8,63	7,88	5,52	64,13	65,21	60,91	57,49	71,67	61,36	52,75	58,47	52,08	55,26	57,83	52,66
Al2O3	4,64	1,23	1,26	0,67	16,09	15,14	15,28	8,61	13,6	14,59	14,97	12,89	3,35	18,87	13,02	13,88
Fe2O3	2,36	2,51	3,84	1,32	2,4	2,02	3,32	4,22	1,76	1,82	0,69	1,25	4,41	4,53	2,16	7,01
MnO	0,2	0,16	0,19	0,14	0,06	0,09	0,17	0,43	0,09	0,14	0,03	0,2	0,57	0,08	0,25	0,16
MgO	1,8	1,52	1,36	1,06	0,77	0,68	1,57	7,68	0,53	3,34	0,18	0,22	1,31	2,99	0,81	1,65
CaO	35,78	49,03	48,57	50,62	2,56	2,74	5,11	12,78	1,8	5,33	10,14	13,7	33,87	6,89	13,19	14,26
Na2O	0,6	0,1	0,12	0,05	2,87	1,64	2,07	1,33	2,89	1,21	0,93	1,01	0,24	5,42	1,59	1,95
K2O	2,8	0,1	0,04	0,07	9,41	10,68	9,97	5,23	7,19	11,2	11,84	9,69	2,41	1,77	7,62	2,29
TiO2	0,12	0,06	0,07	0,04	0,55	0,38	0,32	0,17	0,22	0,03	0,09	0,03	0,16	0,05	0,21	2,05
P2O5	1,35	3,44	4,02	5,86	0,25	0,12	0,48	0,43	0,21	0,55	0,45	0,76	0,29	2,03	0,72	0,43
LOI	23,54	32,21	31,31	33,31	0,87	1,07	1,04	1,02	0,92	0,62	7,41	1,60	1,13	2,16	2,53	3,28
Total	98,8	98,98	98,64	98,65	99,94	99,76	100,24	99,37	100,87	100,19	99,47	99,83	99,82	100,04	99,91	99,6
CO2	20,64	29,97	27,15	30	0,14	0,4	0,42	0,22	0,11	0,19	6,49	1,19	0,91	0,18	1,42	2,02
F	0,12	0,24	0,3	0,44	0,05	0,03	0,05	0,1	0,03	0,07	0,04	0,06	0,03	0,19	0,07	0,1
S	<0,01	<0,01	0,01	0,03	<0,01	0,02	<0,01	0,03	<0,01	<0,01	0,01	0,02	0,01	<0,01	0,04	0,09
Cl (ppm)	87	64	120	105	78	72	135	83	50	115	37	45	36	210	115	570
Mg#	0,75	0,71	0,59	0,76	0,56	0,57	0,65	0,88	0,54	0,88	0,51	0,41	0,54	0,72	0,6	0,48
(N+K)ox/Alox	0,73	0,16	0,12	0,17	0,76	0,81	0,76	0,79	0,74	0,85	0,85	0,83	0,79	0,38	0,71	0,3
Cs (ppm)	0,69	0,01	0,01	0,01	0,55	0,75	1,82	0,48	0,22	2,82	2,71	1,48	0,55	0,09	2,05	0,9
Rb	88,18	2,86	0,9	2,88	219	275	251	138	171	388	321	229	63,5	23,5	217	82,3
Ba	1868	215	279	264	2194	2940	4198	698	2073	1297	6015	4760	1316	900	13198	1228
Th	114	40	36	174	9	63	48	32	80	16	20	62	32	5	109	23
U	32,7	3,63	1,22	9,7	0,8	6,02	5,07	2,04	8,81	1,55	5,21	15,61	5,69	0,32	45,99	1,88
Nb	25,75	0,42	0,65	0,9	64,61	48,04	16	10,54	26,7	0,73	7,82	1,59	3,96	0,12	61,26	86
Ta	3,83	0,12	0,13	0,33	6,02	4,82	1,38	1,78	3,37	0,03	1,1	0,2	0,77	0,03	8,21	8
La	891	1014	941	2089	136	242	206	261	219	226	385	323	175	207	441	231
Ce	1881	1958	1825	4006	362	523	498	540	468	494	843	821	419	408	1070	574
Pb	302	16	39	73	44	47	204	28	56	31	28	33	22	16	88	49
Pr	200	227	212	454	53	63	65	66	56	63	89	94	50	48	108	77
Sr	3481	4751	4329	5204	982	553	2313	781	793	744	1571	871	433	1410	1595	1531
Nd	734	859	805	1679	219	230	256	245	208	246	333	355	198	177	399	306
Zr	66,4	29,32	15,89	11,37	22,76	22	45,86	56,24	197	6,8	22,36	13,03	24,68	1,21	58,93	160
Hf	1,84	0,74	0,37	0,33	1,7	1,1	2,18	3,11	6,61	0,43	0,41	0,19	0,59	0,07	1,87	7,65
Sm	115	136	131	256	41,74	35,9	42	39,7	34,62	42,18	51,14	57	36,67	27,18	65,85	51,77
Eu	22,72	28,43	27,51	49,62	5,53	7	8	8,11	6,1	8,33	11,51	12,38	8,35	3,28	12,9	9,57
Gd	72	91,13	87,22	168	30,82	22,24	26,7	26	23,37	28	30,25	34,77	28,23	19,27	46,03	35,37
Tb	7,67	9,44	9,04	16,75	4,09	2,43	2,9	2,67	2,68	3	3,22	3,85	3,53	2,14	5	3,91
Dy	32,02	39,67	37,7	68,36	21,2	10,44	12,42	11,06	12,2	12,43	13,37	16,71	17,7	9,87	21,8	17,76
Y	117	150	146	248	83,02	38	43,13	40,55	50,33	44	49,39	72,37	84,15	38,17	84,42	74,6
Ho	4,6	5,75	5,4	9,66	3,54	1,52	1,81	1,54	1,86	1,73	1,9	2,5	3,02	1,56	3,22	2,82
Er	9,17	11,47	10,81	19,34	8,3	3,21	3,78	3,22	4,07	3,56	3,8	5,37	7,36	3,35	6,93	6,48
Tm	1,03	1,26	1,19	2,08	1,02	0,36	0,44	0,4	0,5	0,4	0,42	0,67	1,02	0,37	0,83	0,81
Yb	5,45	6,48	6,11	10,31	5,53	1,92	2,4	2,3	2,73	2,15	2,1	3,77	6,41	1,85	4,62	4,74
Lu	0,7	0,82	0,78	1,25	0,67	0,25	0,33	0,34	0,35	0,3	0,25	0,5	0,95	0,24	0,6	0,63
Eu/Eu*	0,76	0,78	0,79	0,73	0,47	0,76	0,73	0,77	0,66	0,74	0,89	0,85	0,79	0,44	0,72	0,68
Nb/Ta	6,73	3,38	4,97	2,71	10,73	9,96	11,55	5,92	7,91	21,52	7,13	7,81	5,14	4,22	7,46	10,85
Zr/Hf	36,14	39,7	42,72	34,33	13,48	19,95	21,02	18,1	29,88	15,98	54,83	70	41,7	16,18	31,5	21

Mg# = Mg/(Mg+Fe$_{tot}$)

OI: Oued Ihouhauene; SWT: South Wadi Tirahart; NWT: North Wadi Tirahart

Si-poor carbonatites have high CaO and CO_2 content (42.18 to 53.02 wt.% and 24.83 to 36.15 wt.%, respectively) decreasing with increasing SiO_2 content, variable FeO (0.37 to 4.10 wt.%), MgO (0.11 to 3.21 wt.%, Mg#= 0.54- 0.84), Al_2O_3 (0.11 to 2.82 wt.%) and P_2O_5 (0.79 to 5.86 wt.%) and very low Na_2O and K_2O contents (Na_2O+K_2O = 0.15 to 1.39 wt.%) (Figures II. 4 and 5). Volatile contents range from 53 to 130 ppm Cl, 0.05 to 0.44 wt.% F and 0.01 to 0.11 wt.% S.

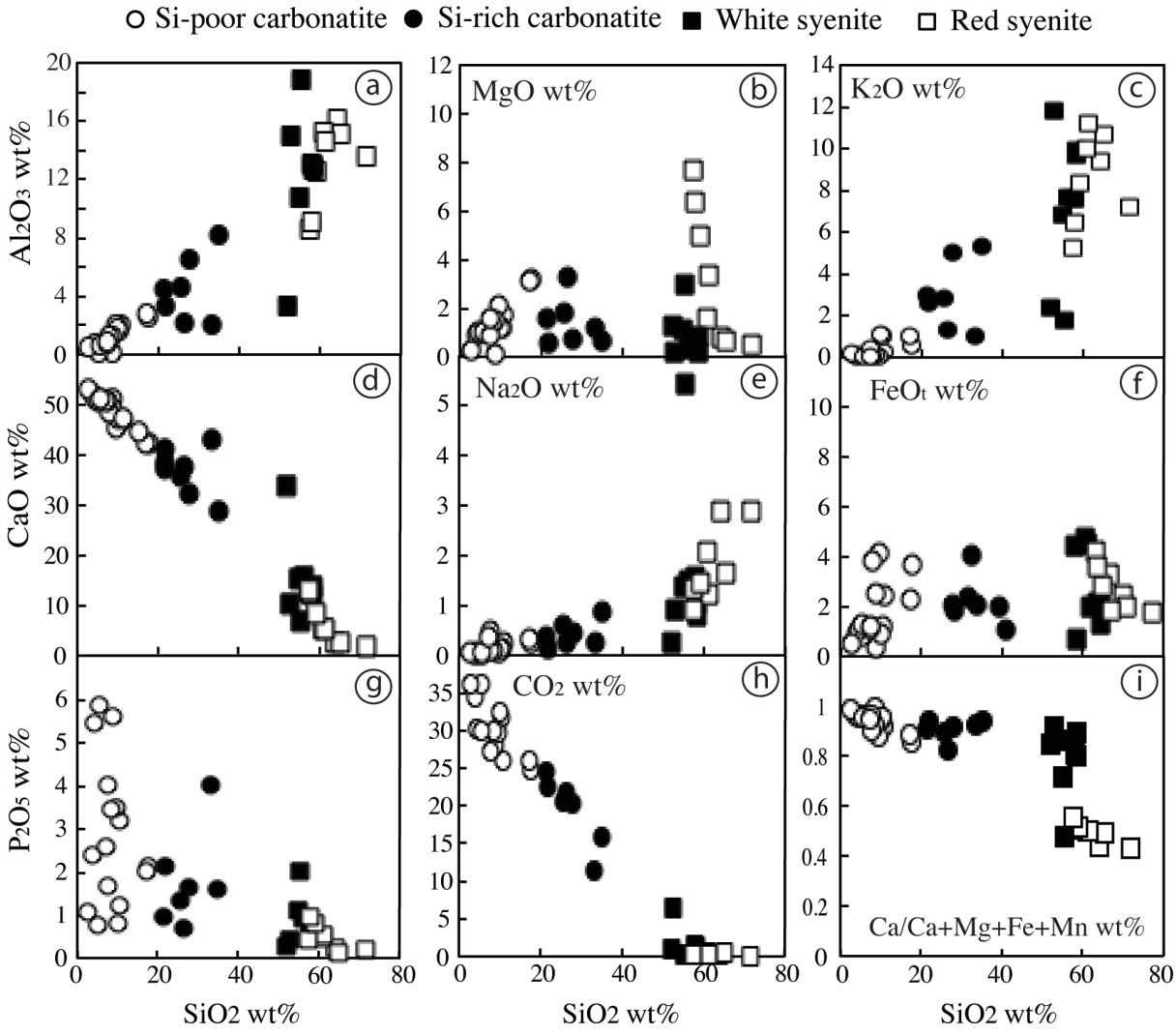

Figure II.5. Bulk rock major oxide compositions of the Ihouhaouene carbonatites and syenites.

Si-rich carbonatites have lower CaO (28.69 to 42.88 wt.%) and CO_2 (11.34-24.56 wt.%) and higher Al_2O_3 (2.01 to 8.14 wt.%) contents than Si-poor carbonatites that decrease linearly with increasing SiO_2 content. The concentrations are variable for P_2O_5 (0.71 to 4.02 wt.%), MgO (0.58 to 3.31 wt.%, Mg#= 0.55- 0.76) and FeO (1.09 to 4.09 wt.%). The alkali contents increase from 1.28 to 6.20 wt.% Na_2O+K_2O (Figures II. 4 and 5) and volatile contents range from 52 to 195 ppm Cl, 0.07 to 0.62 wt.% F and 0.03 to 0.13 wt.% S (Table 1).

Carbonatites have high trace element concentrations (Table II.1, Figures II. 6 and 7). Si-poor carbonatites have straight REE patterns with negative anomaly in Eu (Eu/Eu* = 0.69 to 0.81) and high fractionation in light rare earth elements (LREE) compared to heavy rare earth elements (HREE) (e.g 1845 ppm La, La_N/Yb_N = 75-211). Relative to the primitive mantle (PM), Si-poor carbonatites have low LILE concentrations (e.g 0.018 ppm Cs 1.73 ppm Rb, 71.48 ppm Ba) with a positive anomaly in Th. They have fractionation in Nb compare to Ta (Nb/Ta = 1.59-17.34) with high fractionation and negative anomaly in Zr-Hf (Zr/Hf = 20.51-55.76).

Si-rich carbonatite REE patterns are similar to those of Si-poor carbonatites. They are enriched up to 7000*Chondrite with a slight negative anomaly in Eu and La_N/Yb_N ratio from 88 to 145. LILE and HFSE concentrations in Si-rich carbonatites are higher than in Si-poor carbonatites (e.g 1 ppm Cs, 29 ppm Rb, 2504 ppm Ba) with positive anomalies in U and Th and Nb-Ta and Zr-Hf fractionation (Zr/Hf = 22.28-59.20, Nb/Ta = 3.39-11.14).

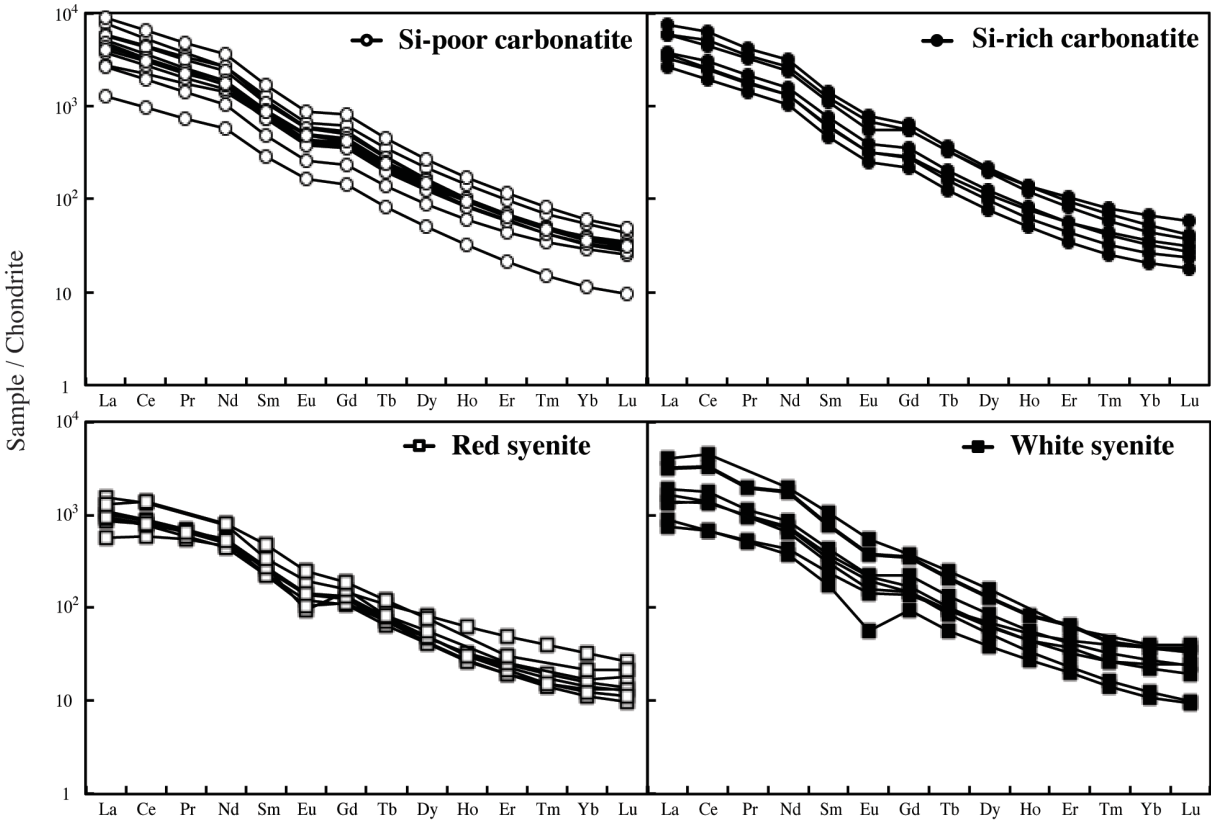

Figure II.6. Normalized REE content of Ihouhaouene carbonatites and associated syenites. Chondrite values from Sun and McDonough (1989).

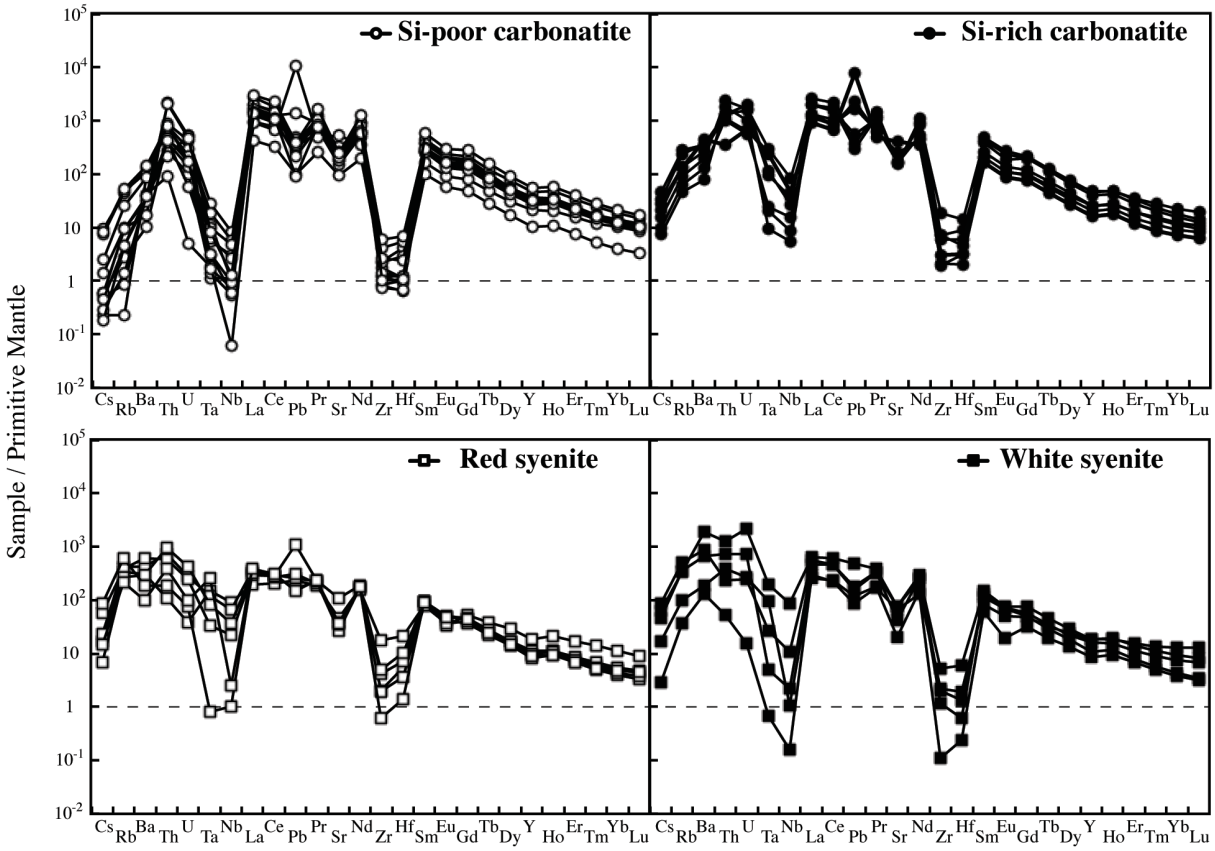

Figure II.7. Normalized trace element composition of Ihouhaouene carbonatites and syenites. Primitive mantle values from Sun and McDonough (1989).

II.5.b. Syenites

Red syenites have high silica and high alkali contents ranging from 57.49 to 71.67 wt.% and 5.60 to 12.40 wt.% Na_2O+K_2O, respectively (Figure II.4), and 2.50 to 12.83 wt.% CaO. MgO content ranges from 0.53 to 7.68 wt.% (Mg#= 0.54- 0.87), and FeO content ranges from 1.76 to 4.22 wt.% (Figure II.5).

White syenites have lower alkali contents (Na_2O+K_2O = 7.19 to 12.7 wt.%) (Figure II.4) than red syenites with 52.75 to 58.47 wt.% SiO_2 10.14 to 15.5 wt.% CaO, 0.18 to 2.99 wt.% MgO (Mg#= 0.4- 0.72), and 0.69 to 4.76 wt.% FeO (Figure II.5). We can note that one wollastonite-rich white syenite has very low alkali content (2.65 wt.% Na_2O+K_2O) and very high CaO (33.87 wt.%) (Table II.1, IC2-27, Figure II.2.f).

Red syenites are enriched up to 1000*Chondrite with a negative Eu anomaly (Eu/Eu* = 0.47 to 0.84) (Figure II.6). They have higher LILE concentrations than Si-poor carbonatites, with negative anomalies in Nb-Ta and Zr-Hf (Zr/Hf = 13.47-29.88, Nb/Ta = 0.16-11.54) (Figure II.7).

REE white syenite patterns are similar to red syenite patterns with high fractionation of LREE compare to HREE (La= 441 ppm, La_N/Yb_N= 131.25) (Figure II.6). They have low concentrations in Cs

(0.09 ppm Cs) and Rb (63 ppm Rb), high Ba contents (13197 ppm Ba) and negative anomalies in Sr, Zr-Hf and Nb-Ta (Zr/Hf = 16.18-54.83, Nb/Ta = 0.19-7.81) (Figure II.7).

II.6. MINERAL CHEMISTRY

II.6.a. Clinopyroxene

All clinopyroxenes in carbonatites have small compositional variations. They present diopsidic ($En_{28–33}Fs_{17–23}Wo_{48–50}$) and hedenbergitic compositions ($En_{18–22}Fs_{30–32}Wo_{46–48}$) (Figure II.8).

In Si-poor carbonatites, clinopyroxenes are diopsides with relatively high Mg# (Mg# = $Mg/[Mg + Fe^{2+}]$ = 0.67-0.74), low Cr_2O_3, Na_2O, TiO_2 and Al_2O_3 contents (TiO_2 = 0.01-0.31 wt.%, Al_2O_3 = 0.65-3.6 wt.%) (Table II.2). Diopside has very low LREE concentrations (La_N<1.2*Chondrite, La_N/Yb_N= 0.12-0.72) with regular flat patterns in MREE (Sm_N/Yb_N= 1- 3.6) (Figure II.9) and positive anomalies in Ba, U, Pb and Sr (Figure II.10, Table II.3).

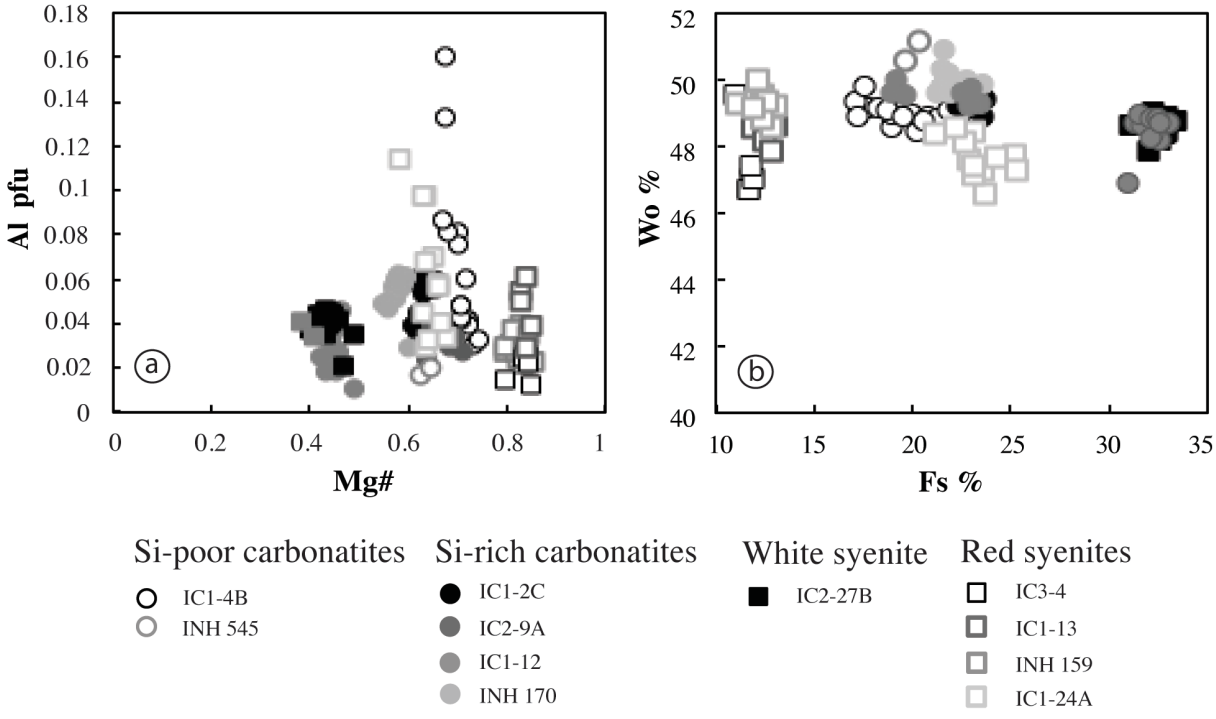

Figure II.8. Clinopyroxene mineral chemistry of the Ihouhaouene carbonatites and syenites in molar units. **a** Al versus Mg# (p.f.u.); Mg# = Mg/Mg+Fetot. **b** Wo versus Fs diagram.

Table II.2 Representative major element composition of clinopyroxene

Rock type	Si-poor carbonatite			Si-rich carbonatite			Red syenite			White syenite		
Sample	IC1-4B.18	IC1-4B.23	IC1-4B.30	IC2-9A.4	INH170a.6	IC1-2C.35	INH159.7	IC3-4.11	IC1-24A.2	IC2-27B.9	3-24.2	IC3-18.7
Mineral	Di	Di	Di	Hd	Di	Di	Di	Di	Di	Hd	Hd	Hd
Type	Core	Rim	Core	Core	Core	Core	Core	Core	Middle	Core		Core
SiO2	50.46	51.1	48.91	50.19	52.24	50.94	53.41	53.31	49.8	50.274	49.49	48.13
TiO2	0.1	0.02	0.3	0.05	0.1	0.1	0.04	0.06	0.26	0.06	0.04	0.15
Al2O3	1.92	0.66	3.67	0.62	1.41	1.33	0.6	0.6	2.2	0.9	0.74	2.15
Fe2O3	12.8	10.75	13.32	18.55	12.7	13.28	7.03	6.81	14.65	19.02	18.58	20.89
MnO	0.4	0.35	0.52	1.02	0.75	0.74	0.78	0.63	0.71	1.0304	1	0.54
MgO	10.44	11.58	9.81	6.84	9.59	10.01	13.64	14.49	9.29	6.34	5.86	5.14
CaO	23.71	24.61	23.54	23.51	23.74	24.1	24.08	23.03	22.75	23.32	22.54	21.83
Na2O	0.38	0.33	0.44	0.4	0.41	0.46	0.54	0.64	0.80	0.52	0.78	0.79
K2O	-	-	-	0.01	-	-	0.01	0.01	-	-	0.01	0.01
Cr2O3	-	0.02	-	-	0.02	-	-	0.03	-	-	-	-
NiO	-	-	-	-	0.02	0.05	-	-	0.04	-	-	0.04
Total	100.23	99.42	100.52	101.19	100.98	101.05	100.14	99.67	100.5	101.51	117.62	99.68
Mg#	0.67	0.75	0.67	0.45	0.58	0.66	0.82	0.84	0.63	0.42	0.41	0.36
Numbers of ions on the basis of 6O												
Si	1.91	1.94	1.85	1.94	1.98	1.92	1.98	1.98	1.89	1.94	1.96	1.9
Ti	-	-	0.01	0.002	0.003	0.003	0.001	0.002	0.007	0.002	0.001	0.005
Al	0.09	0.03	0.16	0.03	0.06	0.06	0.03	0.03	0.1	0.04	0.03	0.1
Fe3+	0.11	0.12	0.15	0.12	0.01	0.13	0.05	0.06	0.16	0.11	0.1	0.15
Fe2+	0.29	0.22	0.27	0.48	0.39	0.29	0.17	0.15	0.31	0.5	0.5	0.54
Mn	0.01	0.01	0.02	0.03	0.02	0.02	0.02	0.02	0.02	0.03	0.03	0.02
Ni	-	-	-	-	0.001	0.002	-	-	0.001	-	-	0.001
Mg	0.59	0.65	0.55	0.39	0.54	0.56	0.75	0.8	0.53	0.36	0.35	0.3
Ca	0.96	1	0.95	0.97	0.96	0.98	0.96	0.92	0.93	0.96	0.96	0.92
Na	0.03	0.02	0.03	0.03	0.03	0.03	0.04	0.05	0.06	0.04	0.06	0.06
K	-	-	-	-	-	-	-	-	-	-	-	-
Cr	-	0.001	-	-	0.001	-	-	0.001	-	-	-	-
Total	4	4	4	4	4	4	4	4	4	4	4	4

Di: Diopside Hd: Hedenbergite Mg# = Mg/(Mg+Fetot)

Table II.3 Trace element composition of clinopyroxene

Rock type	Si-poor carbonatite			Si-rich carbonatite			Red syenite				White syenite	
Sample	IC1-4B.19	IC1-4B.23	IC1-4B.20	IC2-9A.4	INH 170a.6	IC1-2C.47	INH 159.6	IC3-4.11	IC1-24A.2	IC1-13.3	IC2-27B.9	IC3-18.7
Mineral	Di	Di	Di	Hd	Di	Di	Di	Di	Di	Di	Hd	Hd
Type	Core	Rim	Core	Core	Core	Core	Core	Core	Middle	Core	Core	Core
Rb	0.01	6.18	0.01	0.08	0.21	0.01	0.01	0.03	1.71	2.49	0.004	0.1
Ba	0.41	158	1.56	0.30	0.16	0.04	0.04	0.06	4.71	1.11	0.21	0.78
Th	0.001	<0.001	0.01	0.003	0.001	0.004	0.06	0.07	0.03	0.17	0.03	0.03
U	0.02	0.22	0.04	0.03	0.06	0.03	0.03	0.03	0.15	0.04	0.03	0.003
Nb	0.06	0.38	0.35	0.04	0.005	0.09	0.01	0.23	0.11	0.04	0.001	0.01
Ta	0.003	0.002	0.03	0.02	0.004	0.001	0.003	0.02	0.002	0.02	0.001	0.004
La	0.47	0.36	0.22	1.86	2.74	1.49	3.14	75.12	3	15.46	1.63	9.29
Ce	2.32	1.52	1.27	6.23	7.81	4.87	16.15	292	5.78	64.8	6.34	29.5
Pb	14.41	66.1	11.85	5.07	28.78	26.88	2.38	7	5.23	1.67	3.48	3.93
Pr	0.58	0.39	0.37	0.84	1.4	0.8	3.3	51.31	1.95	12.46	0.95	4.24
Sr	347	571	723	509	368	382	83	523	99.62	57.66	290	187
Nd	3.49	2.98	2.66	3.36	6.83	3.49	18.6	244	10.49	66.74	4.24	16.83
Zr	23.12	7.92	6.88	18.54	50.61	50.78	21.01	35.02	13.5	38.37	84.12	64.46
Hf	1.32	0.4	0.58	0.68	1.93	2.16	2.1	1.63	1.83	3.15	1.85	2.63
Sm	1.5	1.85	1.43	0.59	1.66	0.72	5.37	56.46	3.51	17.78	0.81	2.99
Eu	0.47	0.73	0.44	0.15	0.34	0.16	1.29	11.59	0.49	3.6	0.17	0.57
Gd	1.47	3.81	1.79	0.34	0.91	0.47	3.82	39.53	3.59	13.23	0.47	1.94
Tb	0.22	0.66	0.32	0.04	0.12	0.06	0.48	4.71	0.63	1.64	0.05	0.23
Dy	1.13	4.3	1.82	0.18	0.68	0.31	2.27	20.77	3.84	7.87	0.25	1.13
Y	4.82	22.02	9.11	1.15	3.34	1.46	9.37	78.62	20.19	33.1	1.75	5.59
Ho	0.19	0.8	0.33	0.03	0.1	0.05	0.33	3.01	0.76	1.18	0.05	0.18
Er	0.43	1.73	0.73	0.11	0.39	0.16	0.76	6.44	2.15	2.55	0.27	0.59
Tm	0.07	0.24	0.12	0.05	0.09	0.05	0.14	0.78	0.36	0.35	0.11	0.13
Yb	0.44	1.98	0.87	0.69	1.07	0.76	1.12	5.39	3.47	2.49	2	1.58
Lu	0.09	0.25	0.13	0.20	0.29	0.24	0.26	0.77	0.95	0.42	0.51	0.45
Sc	20.81	26.03	17.76	10.29	21.58	22.78	31.41	29.22	118	24.56	8.08	21.56
V	33.94	50.43	20.54	25.6	41.87	50.13	10.4	16.9	45.63	18.47	38.05	124
Zn	211	498	191	391	277	349	385	227	532	405	415	224
Cu	0.57	2.18	0.73	0.18	0.43	0.22	0.56	0.68	0.68	0.74	0.14	0.26
Ni	7.96	19.38	8.05	8.1	15.08	18.92	0.29	2.64	17.09	0.45	3.44	11.72
Cr	9.91	16.85	10.58	6.4	28.92	28.57	7.21	5.83	12.19	4.89	5.7	7.33

Di: Diopside Hd: Hedenbergite

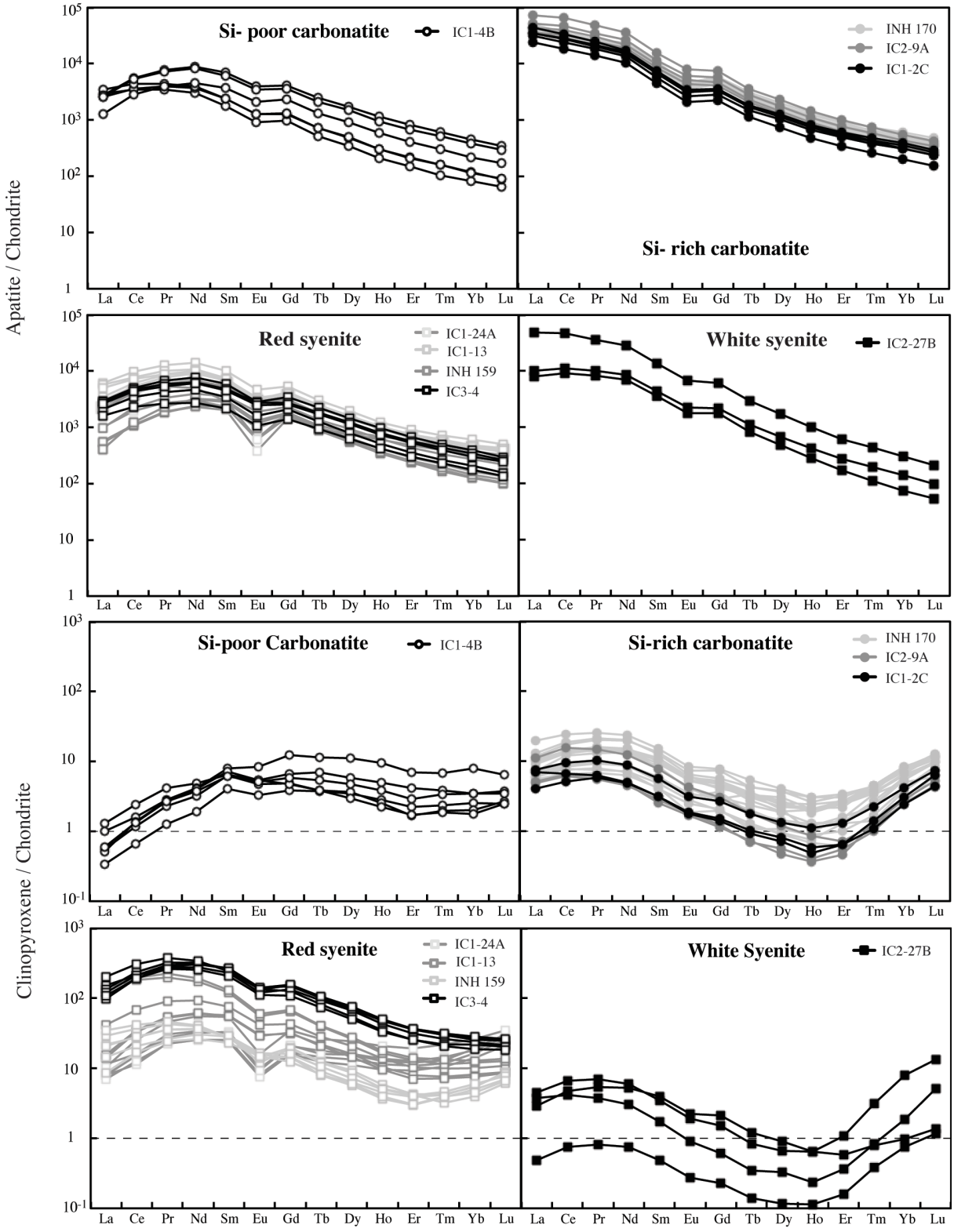

Figure II.9. Normalized REE content of apatite and clinopyroxene from Ihouhaouene carbonatites and associated silicate rocks. Chondrite values from Sun and McDonough (1989).

Si-rich carbonatites have both diopside and hedenbergite pyroxenes. Mg# ranges from 0.54 to 0.70 and 0.42 to 0.49 for diopside and hedenbergite, respectively. Diopside and hedenbergite have low TiO_2 contents (TiO_2 = 0.02-0.33 wt.%) and Al_2O_3 contents range from 0.53 to 1.41 wt.% and 0.22 to 1.03 wt.%, respectively. REE patterns have a sinusoidal to asymmetric U-shaped with slight high concentrations in LREE than HREE (La_N/Yb_N= 1.17- 4.6) (Figure II.9, Table II.3). Large variations in LILE concentrations are observed in Si-rich carbonatite pyroxenes with strong positive anomalies for Pb and Sr in addition to Zr-Hf and Nb-Ta fractionation (Zr/Hf= 20.71-33.93, Nb/Ta= 0.63-74.43) (Figure II.10).

In red syenites, pyroxenes are diopsides ($En_{27–41}Fs_{11–25}Wo_{46–49}$). They have high Mg# ranging from 0.63 to 0.85 with Na_2O = 0.4-0.79 wt.%, TiO_2 = 0.01-0.21 wt.%, Al_2O_3 = 0.27-2.21 wt.% and Cr_2O_3<0.05 wt.% (Figure II.8, Table II.2). Chondrite-normalized patterns of diopside in red syenites display a convex LREE section (La_N/Sm_N= 0.12- 1.2) and a negative Eu anomaly (Figure II.9, Table II.3). Relative to the primitive mantle, they have high fractionation in Nb-Ta (Nb/Ta= 1.51-95.75) with negative anomalies in Ba, Pb, Sr, Zr and enrichment in Th (Figure II.10).

White syenites are characterized by Fe-rich pyroxenes with hedenbergitic composition ($En_{15–19}Fs_{32–38}Wo_{47–49}$) (Figure II.8, Table II.2) and 0.39-0.98 wt.% Na_2O, 0.76-2.58 wt.% Al_2O_3, < 0.16 wt.% TiO_2, and < 0.03 wt.% Cr_2O_3. The REE patterns of hedenbergite in white syenites have the same sinusoidal to asymmetric U-shaped pattern than Si-rich carbonatites with high LREE and HREE concentrations compared to MREE (La_N/Yb_N = 0.55-2.94, La_N/Sm_N = 0.7-2.2) (Figure II.9). They have more pronounced Nb-Ta fractionation (Nb/Ta= 0.4-4.34) and less positive Pb and Sr anomalies than pyroxenes in red syenites (Figure II.10).

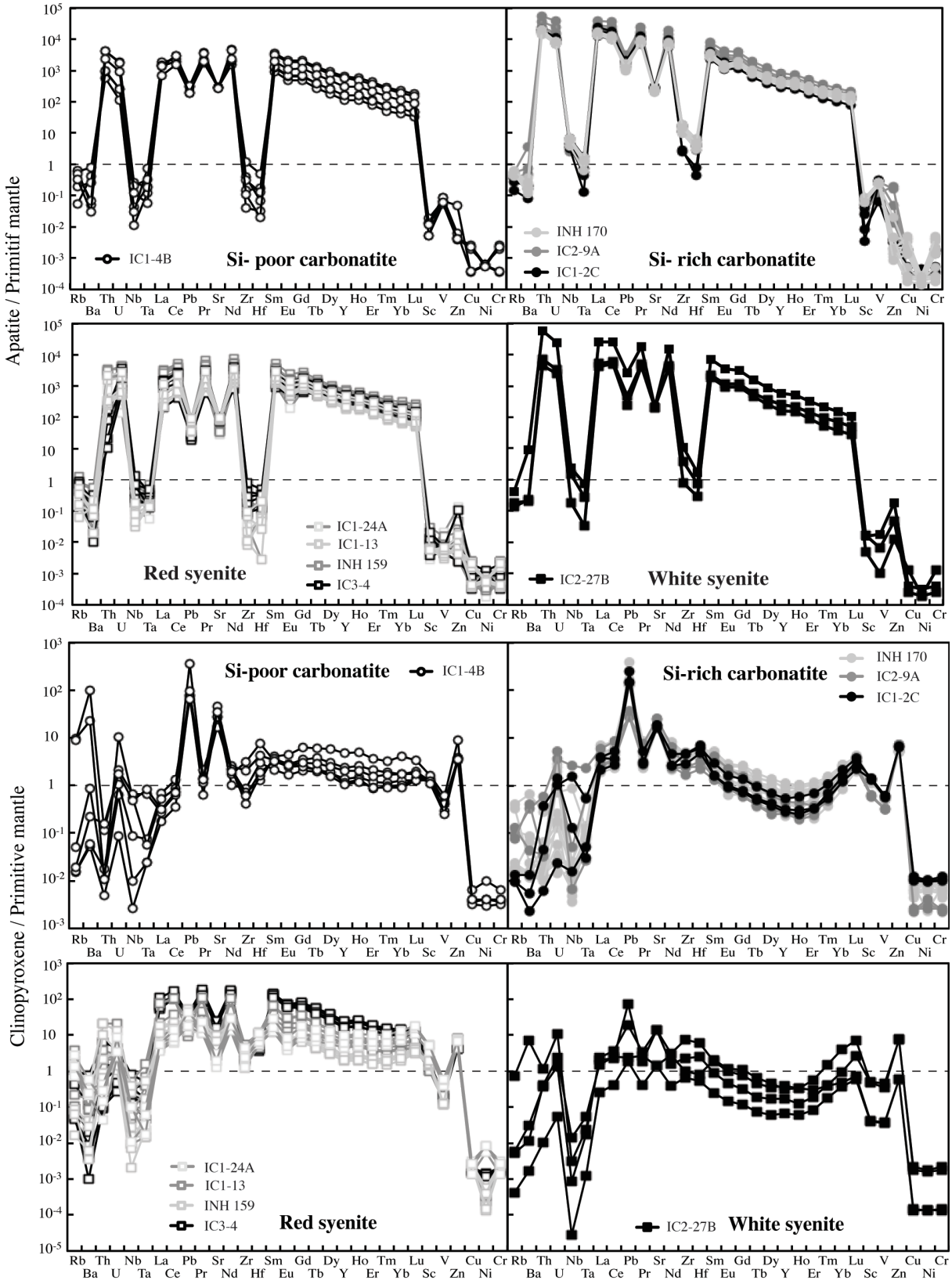

Figure II.10. Normalized trace element content of apatite and clinopyroxene from Ihouhaouene carbonatites and associated silicate rocks. Primitive mantle values from Sun and McDonough (1989).

II.6.b. Wollastonite

Wollastonite is present in Si-rich carbonatites and white syenites and has a homogeneous composition ($En_{0-0.05}Fs_{1-2}Wo_{97-99}$, Supplementary data B1). It has U-shaped REE patterns with high LREE content in carbonatites (La_N/Yb_N= 8.65-9.82) and flat regular patterns in syenites (10-50*Chondrite, La_N/Yb_N= 0.37-0.53) and small negative Eu anomaly (Figure II.11.a). Wollastonite in white syenites has a higher negative anomaly in Nb-Ta than in carbonatites (Nb/Ta= 1.53 and 18.94 respectively, Supplementary data B1).

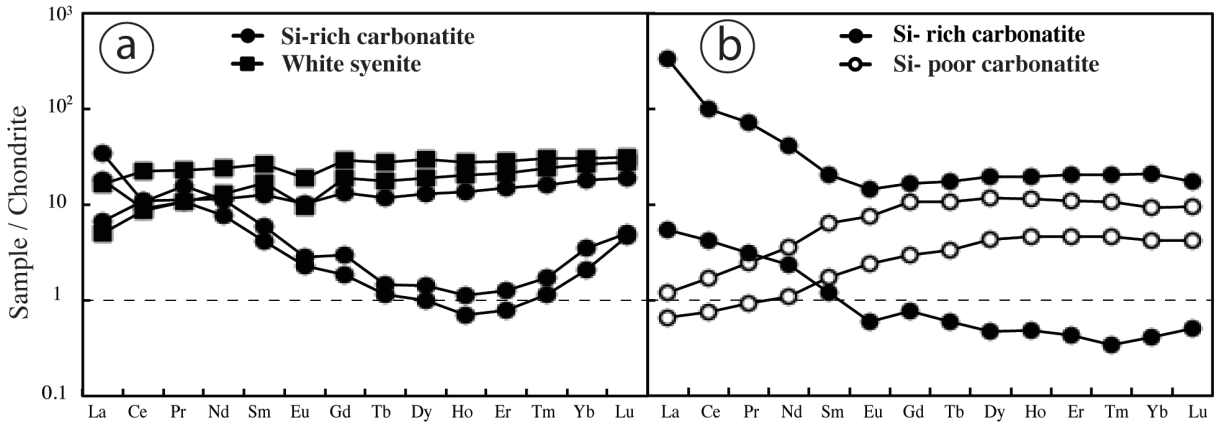

Figure II.11. Normalized REE content of wollastonite and calcite from Ihouhaouene carbonatites and associated silicate rocks. Chondrite values from Sun and McDonough (1989).

II.6.c. Apatite

Apatites in carbonatites and syenites are fluor-apatites (2.7-6.31 wt.% F). Despite their relative large size (up to 5 mm), apatites do not have significant zonation from core to rim although they have different compositions in silica and phosphorus as well as in calcium and rare earth elements depending of the host rock (Figure II.12).

In Si-poor carbonatites, apatite has low silica contents SiO_2 (0.48-1.45 wt.%) with P_2O_5 contents from 37.57 to 40.25 wt.% and low REE (ΣREE = 0.8-2.5 wt.%) (Table II.4). Apatite has low LREE concentrations compared to HREE with convex shaped patterns (La_N/Sm_N= 0.34- 1.65, La_N/Yb_N= 5.94 -35.46) (Figure II.9). They have negative Nb-Ta and Zr-Hf anomalies in (Nb/Ta = 0.71-35.41, Zr/Hf = 43.9-204.7) and positive anomalies are observed for Th and U (Th = 49-348 ppm, U = 2.3-39.3 ppm) (Figure II.10, Table II.5).

In Si-rich carbonatites, apatite is silica- and REE-rich (SiO_2 = 4.6-6.05 wt.%, ΣREE = 4.32-11.21 wt.%, respectively). P_2O_5 content ranges from 28.67 to 37.42 wt.% and CaO from 47.77 to 52.39 wt.% (Table II.4). Apatite REE patterns in Si-rich carbonatites are straight with a slight Eu anomaly. They have high fractionation in LREE compare to HREE (La_N/Yb_N = 82.18-134.38) (Figure II.9) and negative Nb-Ta, Zr-Hf anomalies (Nb/Ta = 33.66-101.9, Zr/Hf = 102.35-241.32) and a

pronounced enrichment of Th and U (Th = 1200-4731 ppm, U = 147-818 ppm) (Figure II.10, Table II.5).

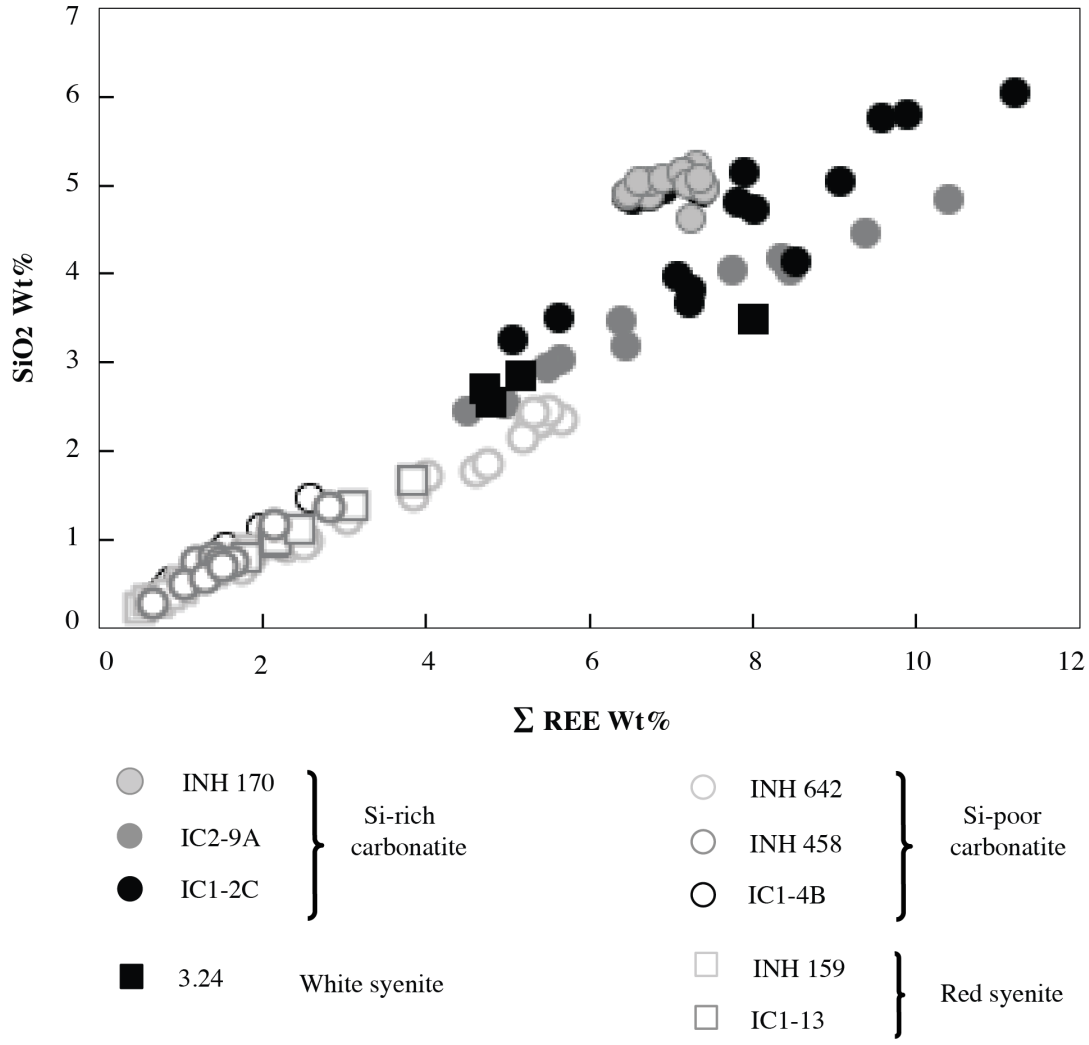

Figure II.12. SiO_2 versus REE_{ox} wt.% of apatite from the Ihouhaouene carbonatites and syenites.

Apatites in red syenites have low silica contents (SiO_2 = 0.36-1.59 wt.%) with 37.84 - 40 wt.% P_2O_5 and 54.08 wt.% CaO with total REE from 2.74 to 4.78 wt.%. They have fractionation in LREE compared MREE (La_N/Sm_N = 0.13-0.76, La_N/Yb_N = 1.49-10.15) with a convex shaped patterns and an important negative anomaly in Eu (Figure II.9). Negative anomaly is observed for Ba and Nb-Ta and Zr-Hf fractionation (Nb/Ta = 3.44-90.96, Zr/Hf = 4.33-127.77) (Figure II.10).

White syenites have silica-rich apatites with 2.55-3.48 wt.% SiO_2, 33.39- 37.87 wt.% P_2O_5, and 51.8-54.78 wt.% CaO. REE patterns of apatite in white syenites display the same regular shape than Si-rich apatite patterns with high fractionation in LREE compared to HREE (La_N/Yb_N = 71.96-158.48) (Figure II.9). They have high contents in Th (Th= 372-4984 ppm) and negative Zr-Hf and Nb-Ta anomalies (Nb/Ta = 54.09-98.46, Zr/Hf = 97.66-232.34) (Figure II.10).

Table II.4 Representative major element composition of apatite

Rock type	Si-poor carbonatite			Si-rich carbonatite			Red syenite			White syenite	
Sample	IC1-4B.33	INH 642.7	INH 458.35	IC2-9A.51	INH 170a.5	IC1-2C.9	INH 159.1	IC1-13.2	IC1-24A.2	IC2-27B.9	3-24.1
Mineral	Ap	Ap	Ap	Ap	Ap	Ap	Ap	Ap	Ap	Ap	Ap
Type	Core	Rim	Core	Core	Core	Core	Core	Core	Middle	Core	Core
SiO2	0.43	1.85	0.74	4.03	5.04	5.8	0.31	0.8	0.43	2.89	2.85
Fe2O3	0.01	-	-	-	0.06	-	0.03	0.01	0.02	-	-
MnO	-	-	-	-	-	-	0.02	0.06	0.03	-	-
CaO	54.28	53.23	55.21	50.42	50.29	48.67	56.72	54.60	56.11	50.78	54.1
Na2O	0.001	-	0.02	-	-	-	0.01	0.01	0.003	-	-
K2O	-	-	-	-	-	-	-	-	-	-	-
P2O5	39.9	37.38	40.18	33.05	31.1	28.96	45.11	41.64	43.32	38.53	36.54
La2O3	0.04	0.95	0.19	1.45	1.42	2.33	0.04	0.14	0.04	0.85	0.81
Ce2O3	0.23	2.31	0.69	3.53	3.26	4.39	0.16	0.53	0.24	2.24	2.35
Pr2O3	0.06	0.21	0.1	0.36	0.33	0.44	0.05	0.11	0.07	0.23	0.26
Nd2O3	0.29	1.03	0.46	1.73	1.34	1.96	0.25	0.65	0.3	1.21	1.23
Sm2O3	0.09	0.15	0.09	0.48	0.21	0.52	0.1	0.2	0.08	0.34	0.35
Gd2O3	0.06	0.1	0.1	0.14	0.14	0.15	0.07	0.1	0.05	0.12	0.14
Dy2O3	0.001	0.01	0.01	0.06	0.04	0.09	0.04	0.06	-	0.05	0.01
Lu2O3	0.02	-	-	0.02	-	-	-	0.01	-	-	-
Y2O3	0.04	0.13	0.04	0.21	0.22	0.28	0.08	0.19	0.16	0.1	0.16
SrO	-	-	0.31	-	-	-	-	-	-	-	-
ThO2	0.01	0.06	0.01	0.24	0.24	0.21	0.01	0.02	0.002	0.08	0.14
SO2	0.13	0.11	0.16	1.07	1.78	1.98	0.07	0.11	0.04	0.58	0.77
F	4.73	5.16	5.59	4.11	4.48	3.85	4.49	3.73	4.36	4.08	4.03
Cl	0.02	0.002	0.08	0.04	0.04	0.07	0.03	0.09	0.04	0.07	0.01
Total	100.35	102.66	103.98	100.93	100	99.7122	107.59	103.07	105.28	102.16	103.76
∑ REEox	0.83	4.88	1.68	7.96	6.96	10.17	0.80	2	0.93	5.15	5.32
Numbers of ions on the basis of 26O											
Si	0.07	0.41	0.12	0.72	0.9	1.06	0.04	0.13	0.07	0.49	0.49
Fe2+	0.002	-	-	-	0.009	-	0.003	0.002	0.002	-	-
Mn	-	-	-	-	-	-	0.006	0.008	0.004	-	-
Ca	9.96	9.97	9.85	9.62	9.60	9.52	9.61	9.77	9.75	9.26	9.88
Na	-	-	0.006	-	-	-	0.001	0.004	0.001	-	-
P	5.79	5.25	5.66	4.98	4.69	4.47	6.08	5.89	5.95	5.55	5.27
La	0.003	0.07	0.01	0.09	0.09	0.16	-	0.01	0.002	0.05	0.05
Ce	0.01	0.17	0.04	0.23	0.21	0.29	0.007	0.03	0.01	0.14	0.15
Pr	0.004	0.01	0.006	0.02	0.02	0.03	0.003	0.007	0.004	0.01	0.02
Nd	0.02	0.07	0.03	0.11	0.09	0.13	0.01	0.04	0.02	0.07	0.08
Sm	0.005	0.009	0.005	0.03	0.01	0.03	0.004	0.01	0.005	0.02	0.02
Gd	0.003	0.007	0.005	0.008	0.008	0.009	0.001	0.006	0.003	0.007	0.008
Dy	-	0.001	0.001	0.003	0.002	0.005	0.002	0.003	-	0.003	0.001
Lu	0.001	-	-	0.001	-	-	-	-	-	-	-
Sr	-	-	0.03	-	-	-	-	-	-	-	-
Y	0.003	0.01	0.004	0.02	0.02	0.03	0.003	0.02	0.01	0.009	0.01
Th	-	0.004	-	0.01	0.01	0.009	-	0.001	-	0.003	0.006
S	0.02	0.08	0.03	0.18	0.3	0.34	0.01	0.02	0.01	0.09	0.12
F	2.56	2.57	2.94	2.31	2.53	2.22	2.06	1.97	2.24	2.2	2.17
Cl	0.006	0.001	0.02	0.01	0.01	0.02	0.01	0.03	0.01	0.02	0.002
Total	18.46	18.65	18.76	18.35	18.5	18.32	17.84	17.94	18.09	17.94	18.27

Table II.5 Trace element composition of apatite

Rock type	Si-poor carbonatite		Si-rich carbonatite			Red syenite			White syenite	
Sample	IC1-4B.37	INH 458.35	IC2-9A.46	INH 170a.5	IC1-2C.1	INH 159.2	IC3-4.1	IC1-24A.2	IC2-27B.1	IC3-18.1
Mineral	Ap	Ap	Ap	Ap	Ap	Ap	Ap	Ap	Ap	Ap
Type	Core	Core	Core	Core	Core	Core	Core	Core	Core	Core
Rb	0.41	0.38	0.24	0.3	0.23	0.04	0.31	0.35	0.09	0.21
Ba	0.36	6.98	3.51	2.56	1.45	1.03	0.07	0.16	1.58	1.2
Th	351	350	2083	1201	1601	29.53	1.8	12.03	589	158
U	39.31	39.32	344	150	198	19.13	21.27	3.06	69.79	9.47
Nb	0.18	0.19	2.52	3.92	2.54	0.12	0.3	0.24	1.09	0.12
Ta	0.008	0.05	0.04	0.05	0.02	0.007	0.01	0.007	0.01	0.01
La	995	3103	16022	9841	12753	203	764	370	3731	1327
Ce	5239	10081	38385	19008	26079	1048	3321	1901	10794	3419
Pb	56.82	65.18	366	201	328	6.86	3.98	4.32	88.89	13.86
Pr	1050	1474	4205	2158	2837	256	581	377	1386	443
Sr	6199	7063	5736	4805	5846	1668	2027	627	4349	1007
Nd	6356	6796	15684	8295	10930	1720	3341	2126	6079	1993
Zr	4.3	6.86	205	162	33	0.09	2.07	0.35	43.31	4.29
Hf	0.02	0.13	1.33	1.46	0.14	0.02	0.09	0.0092	0.23	0.04
Sm	1602	1455	2260	1207	1572	559	789	534	1004	369
Eu	343	299	451	206	275	85.71	138	52.81	195	48.12
Gd	1268	1089	1435	925	1013	493	635	479	674	299
Tb	144	112	134	86.44	100	52.05	74.12	55.49	64.03	31.04
Dy	662	491	559	367	445	218	308	282	259	152
Y	2985	2047	2476	1599	2019	861	1376	1798	1178	748
Ho	96.89	68.21	77.74	53.63	63.68	30.48	43.98	51.42	35.56	26.1
Er	203	136	155	115	135	60.35	89.39	119	67.72	62.8
Tm	21.67	14.32	17.08	13.06	14.81	6.25	9.42	14.17	6.98	8.24
Yb	112	69.31	91.33	70.68	78.41	32.18	50.84	80.2	35.03	52.09
Lu	13.16	8.66	10.38	8.36	9.13	3.99	5.97	10.43	3.74	6.69
Sc	0.22	0.65	1.15	1.11	0.13	0.1	0.19	0.1	0.27	0.12
V	7.27	4.62	22.16	19.05	5.42	0.29	0.42	1.6	0.54	15.43
Zn	0.24	2.43	9.05	1.13	0.17	0.31	0.31	0.19	2.57	2.9
Cu	0.34	0.27	0.53	0.132	0.23	0.29	0.33	0.14	0.49	0.46
Ni	1.23	16.99	0.61	0.27	0.68	1.17	2.23	0.77	0.38	1.03
Cr	5.1	9.91	3.88	3.56	5.13	6.33	0.87	0.79	0.65	3.78

Ap: Apatite

II.6.d. Carbonates

Carbonate in the carbonatites of Ihouhaouene is calcite (CaO = 56-59 wt.%, MgO<0.16 wt.%, FeO<0.15, supplementary data B1). REE patterns of calcite in Si-poor carbonatites have low LREE concentrations (La_N/Yb_N=0.12-0.15), whereas calcites in Si-rich carbonatites have high LREE contents compared to HREE (La_N/Yb_N=13.3-16.16) (Figure II.11.b).

II.6.e. Alkali feldspar

In red and white syenites, the alkali feldspars are potassic with Or_{57-96} contents and have perthitic exsolutions with Ab_{66-94}. In Si-rich carbonatites, alkali feldspars have high orthoclase content of Or_{95-98} (Supplementary data B1).

II.6.f. Accessory minerals

Britholite

Britholite is a REE-rich mineral with general formula $(Na,Ca, REE)_{10}(Si,P)_6O_{24}(OH,F)_2$ and Si > P (Oberti *et al*. 2001). In Ihouhaouene carbonatites, britholite occurs as fine lamellar exsolutions (<10 um) or as irregular-shaped grains (10-200 um) in apatite. The apatite-britholite exsolutions correspond to a substitution of Ca^{2+} and P^{5+} for REE^{3+} and Si^{4+}. All britholites contain 8-16 wt.% La_2O_3 21-43 wt.% Ce_2O_3 and 7-12 wt.% Nd_2O_3. They contain up to 60 % ΣREE, dominated by LREE (La_N/Yb_N= 147-198) (Supplementary data B1).

Monazite

Monazite is composed of more than 60% of REE, mainly rich in La and Ce (La= 16.53- 23.34 wt.%, Ce= 32.52-34.95 wt.%) (Supplementary data B1).

Allanite

Allanite is a rare-earth-bearing epidote mineral, characterized by SiO_2 (31.82-33.01 wt.%), CaO (12.73-14.93 wt.%), Al_2O_3 (11.39-15.98 wt.%), FeO (10.4-16.94 wt.%) and ΣREE (18.76-22.44 wt.%) (Supplementary data B1). Allanites are very rich in LREE than HREE (La_N/Yb_N = 2053-9323) with positive anomaly in Th (Th= 892.61 ppm) also fractionation in Nb-Ta and Zr-Hf.

Garnet

Garnet has intermediate composition between grossular (63 to 72 %) and andradite (25 to 33 %) (Supplementary data B1) with low TiO_2 content (0.01 to 0.78 wt.%) and high FeO content (15.37-26.14 wt.%). Titanian andradite-rich garnet with Fe^{3+} > Ti is referred to melanite (Deer *et al*. 1982).

Oxide and sphene

Oxide in carbonatites and syenites is magnetite (FeO= 91.56-93.98 wt.%) (Supplementary data B1). Sphene is present as an accessory mineral in carbonatites and syenites. It has 27.64 to 29.83 wt.% SiO_2, 31.06 to 35.03 wt.% TiO_2 25.13 to 17.36 wt.% CaO, and 1.37 to 3.25 wt.% FeO (Supplementary data B1).

II.7. DISCUSSION

Among carbonatite/alkaline rock complexes worldwide, carbonatites are mostly associated to silica-undersaturated rocks (e.g. Cap verde in Brava Island, Weidendorfer *et al*. 2016) and only few are associated to silica-saturated rocks (e.g. see review in Chakhmouradian *et al*. 2008). The calciocarbonatites associated solely with silica-saturated syenites (e.g. The Eden Lake in Canada, Chakhmouradian *et al*. 2008) resemble their Ihouhaouene counterparts in term of mineral assemblage (diopside-hedenbergite, Si-rich apatite) and trace-element compositions (e.g. low Nb/Ta, Chakhmouradian *et al*. 2008, Figure II.4). For all carbonatite/syenite complexes, a genetic relation between alkaline rocks and carbonatites has been presumed although in most cases, the occurrence of hydrothermal/metamorphic imprint does not allow to access to original magmatic processes (e.g. Wyllie and Jones, 1985; Ramasamy 1986; Smith et al. 2000; Chakhmouradian *et al*. 2008; Saha *et al*. 2011).

In Ihouhaouene complex, the coexistence of unaltered syenites and carbonatites with a wide range of silica content (3 – 35 wt.% SiO_2) makes it a key area to decipher the relationships between these two rock types and contributes to our knowledge on the origin of carbonatites. A petrogenetic model to link the carbonatites and syenites must integrate salient features of the Ihouhaouene complex, such as the structural relationships between rock facies and the major- and trace-element systematics of whole rocks and minerals. These notably include:

(1) *Close spatial relationships between carbonatites and syenites in the field*, as well as similar, pegmatitic/brecciated textures in the two rock types (Figure II.2), suggesting that they were emplaced during a single igneous event.

(2) *Almost continuous range of whole-rock major-element compositions*, from silica-poor carbonatites to silica-rich (red) syenites (Figures II. 4, 5) suggesting genetic relationships between all rock facies.

(3) *Striking similitudes of pyroxene and apatite compositions in carbonatites and syenites,* particularly in the silica-rich carbonatites and white syenites (hedenbergite and wollastonite, Figures II. 8, 9). These two facies differ from each other chiefly by the presence of carbonate

and alkali feldspar in Si-rich carbonatite and white syenite, respectively, a feature that also strongly supports a cogenetic relationship.

(4) *Extreme enrichment of LREE and other incompatible trace elements in apatite from carbonatites (particularly the silica-rich ones) and white syenites*, compared with coexisting pyroxene (Figures II. 10, 11, and 12). The contrasted compositions of coexisting apatite and clinopyroxene are at odds with mineral equilibrium deduced from experimental partition coefficients. We chose carbonatitic apatite Kd from Hammouda *et al*. 2010, silicate melt apatite Kd from Prowatke & Klemme 2006 and trachyandesitic apatite Kd from Mahood & Stimac 1990. For clinopyroxenes we chose Kd from Green *et al*. 1992 and Klemme *et al*. 1995 experiments for carbonatite; trachytic clinopyroxene Kd from Blundy & Dalton 2000, Mahood & Stimac 1990 and Larsen 1979 for silicate melts (supplementary data illustration). However, recalculated apatite and clinopyroxene equilibrium liquids imply that apatite and clinopyroxene crystallized from markedly distinct melt compositions (Figure II.13 and see below section on equilibrium melt compositions) were assembled to form hybrid, mineral aggregates and did not re-equilibrate afterwards – perhaps due to the very coarse-grain, pegmatitic/brecciated textures.

(5) *An extremely wide range of Nb/Ta ratios in minerals*, from subchondritic to superchondritic (0.8-110; $Nb/Ta_{chondrite}$=18; Sun & McDonough 1989), which is reflected in a variation range of more than three orders of magnitude in equilibrium melts (Nb/Ta= 0.6-603; Kd from Larsen 1979; Mahood & Stimac 1990; Green *et al*. 1992; Klemme *et al*. 1995; Blundy & Dalton 2000; Prowatke & Klemme 2006; Hammouda *et al*. 2010 – Figure II.14). Partial melting of heterogeneously carbonated mantle and separation of immiscible carbonate melts from silicate melts have been advocated to explain substantial Nb-Ta fractionation in melts (Koster van Groos & Wyllie 1968; Wyllie & Huang 1975; Freestone & Hamilton 1980; Kjarsgaard & Peterson 1991; Dalton & Wood 1993; Kjarsgaard *et al*. 1995; Mitchell 2009; Novella & Keshav 2010; Brooker & Kjarsgaard 2011; Martin *et al*. 2013). These processes would notably account for the elevated, superchondritic Nb/Ta values frequently observed in carbonatites. In the Ihouhaouene complex, however, both carbonatites and syenites show subchondritic Nb/Ta values with - hardly significant - high range of values (0.5-17.3 and 0.06-21.5, respectively; Table1). This suggests that the fractionation of Nb-Ta was largely obscured in whole rocks compositions by the hybridization process. However, most samples, including the syenites, contain high Nb/Ta minerals (Figures II. 11 and 12) that were likely crystallized from - or formerly equilibrated with – carbonate-silicate melts.

(6) *The paradoxical, comparatively low LREE content in minerals of the Si-poor carbonatite ICI-48 compared with other rock types* (Figure II.9). Carbonate-rich melts produced by low melting degree of a carbonated mantle source or via segregation of immiscible carbonate melt from a silicate parental melt are expected to be strongly LREE enriched (Hamilton *et al*. 1989; Jones *et al*. 1995; Martin *et al*. 2013). Together with the low Nb/Ta values observed in several minerals from Si-poor carbonatites including sample IC1-4B (down to 1.9, Figures II. 11 and 12), the low LREE signature rules out its origin either as a pristine carbonate melt from the mantle, or as a carbonate fraction segregated from a primary silicate melt. Rather, the Si-poor carbonatites of the Ihouhaouene complex were segregated from geochemically evolved silicate melts. In this scheme, the low LREE/HREE and Nb/Ta ratios of sample IC1-4B is chiefly the reflection of its parental melt composition, inherited from former differentiation stages involving several steps of carbonated melt immiscibility.

Due to their complex compositions resulting from the assemblage of disequilibrium minerals of different origins, the analyzed whole-rocks do not provide full information on the extent and nature of the differentiation processes in the Ihouhaouene complex. Moreover, the whole-rock compositions do not represent melt compositions and therefore cannot be straightforwardly used for modelling the differentiation.

In order to evaluate the whole extent of geochemical differentiation in the complex and assess the ability of igneous differentiation mechanisms (segregation of cumulus minerals and immiscible melts) to account for the differentiation, we used two complementary approaches:

(1) *Calculation of equilibrium melts from clinopyroxene and apatite composition*, using experimental mineral/melt partition coefficients;
(2) *Modelling the differentiation of a silico-carbonated melt with a stepwise approach* combining distillation equations for the immiscibility and – alternately – fractional crystallization.

II.7.a. Equilibrium melts

The compositions of equilibrium melt calculated from clinopyroxene and apatite are illustrated on Figure 13 for chondrite-normalized REE and on Figure 14 for selected trace-element ratios (Ce/Lu, Nb/Ta, Rb/Sr, and Y/Zr). The calculated melts show considerable variation ranges, encompassing - roughly - 4 orders of magnitude for LREE (Figure II.13), 3 for Ce/Lu and Nb/Ta, 5 for Y/Zr, and 7 for Rb/Sr (Figure II.14). However, some systematics are observed according to the rock facies.

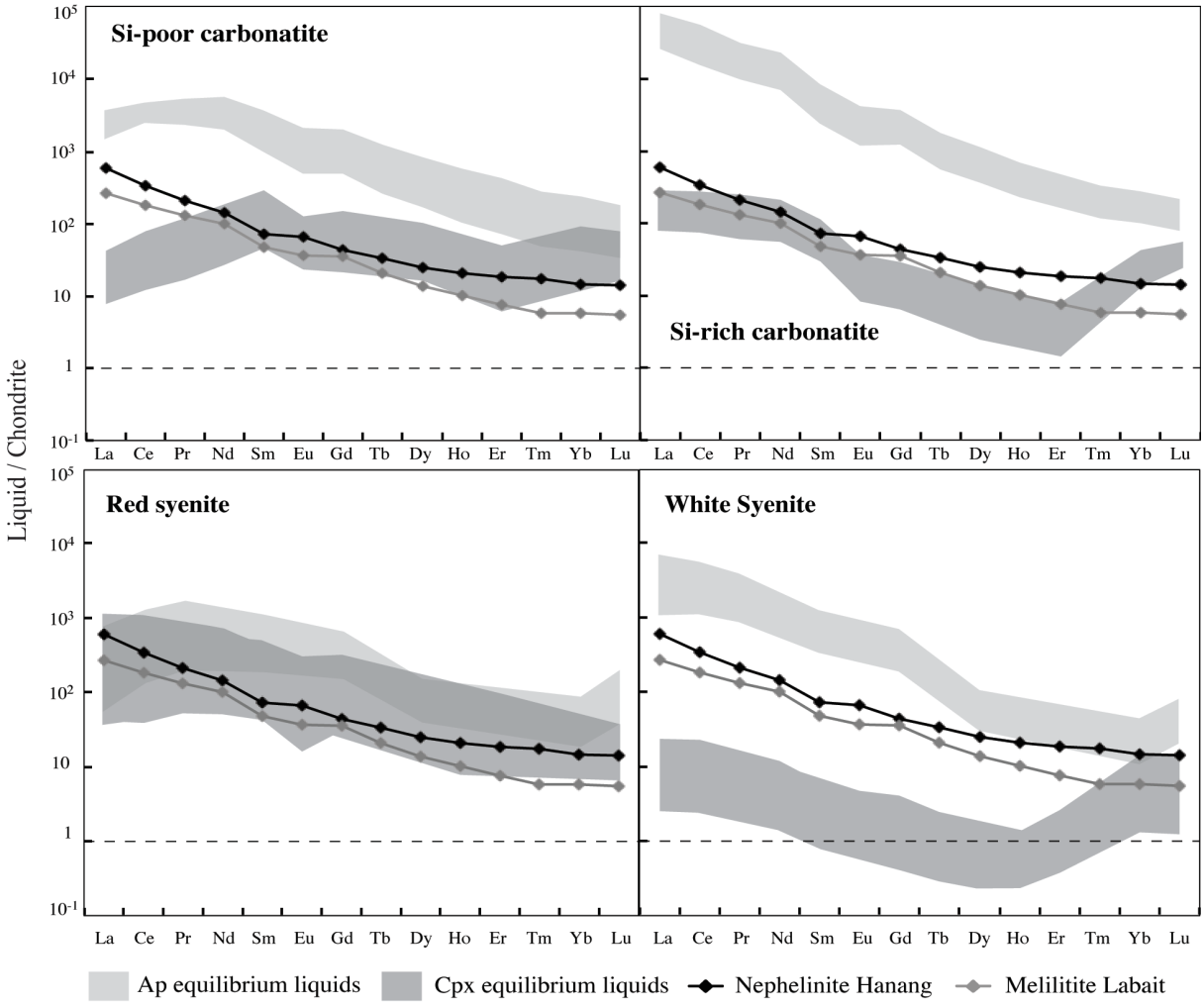

Figure II.13. Normalized REE content of recalculated apatite and clinopyroxene equilibrium liquids from Ihouhaouene carbonatites and associated syenites compared to nephelinite, melilitite REE compositions. Chondrite values from Sun and McDonough (1989). Hanang nephelinite and Labait melilitite from Baudouin *et al*. 2016.

The white syenites and the Si-rich carbonatites are distinguished by both:

- much higher REE content and Ce/Lu ratios in calculated apatite equilibrium melts than in their clinopyroxene counterparts (Figures II. 13, 14.a, and 14.b),
- high, superchondritic Nb/Ta ratios (> 50) in apatite equilibrium melts compared with low, subchondritic ratios (< 10) in most of the clinopyroxene equilibrium melts (Figure II.14.a, b).

Combined together, these features indicate that apatite was equilibrated with REE-enriched carbonate melts whereas the coexisting clinopyroxene was precipitated from evolved silicate melts. The non-primary (evolved) composition of the latter is indicated by its low REE content compared with primary mantle melts (nephelinite and melilitite – Baudouin *et al*. 2016). Based on the few analyses available for this facies, this is particularly true for the white syenites, whose clinopyroxene equilibrium melts are strongly depleted in REE (Figure II.13) and show very low Nb/Ta values (< 5 – Figure II.14.b). In the silica-rich carbonatites, the apatite equilibrium melts are further distinguished from their clinopyroxene counterparts by much lower Rb/Sr and higher Y/Zr values consistent with the inferred, carbonated and silicated, melt compositions (Figure II.14.c - Martin *et al*. 2013). Rb/Sr *vs*. Y/Zr covariation in the silica-rich carbonatites equilibrium melts also lends support to the hypothesis that the segregation of immiscible carbonate melts fractions played a significant role in the overall differentiation of the Ihouhaouene complex. Si-rich carbonatites are hybrid rocks with alkali feldspar, cpx, and Si-rich apatite that crystallized from Si-rich carbonated melt. The Rb/Sr *vs*. Y/Zr systematics is less clear for the white syenites, whose apatite equilibrium melts show similar Y/Zr ratios than their clinopyroxene counterparts, but higher Rb/Sr. Further interpretation is however hampered by the small number of analyses available for this facies.

The Si-poor carbonatites resemble the Si-rich carbonatites (and the white syenites) in showing elevated REE contents in apatite equilibrium melts compared with clinopyroxene equilibrium melts and primary mantle melts (Figure II.13). Contrasted compositions (carbonated and silicated, respectively) of equilibrium melts are also corroborated in this facies by the much lower Rb/Sr and higher Y/Zr ratios observed in the apatite equilibrium melts compared with clinopyroxene equilibrium melts (Figure II.14.c). At first sight, the Nb/Ta systematics is at variance with this interpretation since the apatite equilibrium melt in this rock type shows a wide range Nb/Ta ratios, overlapping much of the range of clinopyroxene equilibrium melts and showing a majority of subchondritic values (< 10, Figure II.14.a). In fact, this paradoxical Nb-Ta systematics may simply reflect the segregation of the carbonate fraction from an evolved parental melt, characterized by very low Nb/Ta values – an hypothesis that needs to be verified with modelling.

The red syenites are distinguished from the other rock types by similar REE contents in apatite and clinopyroxene equilibrium melts (Figure II.13). Moreover, these compositions are roughly comparable to those of nephelinitic and melilitic primary melts (Baudouin *et al*. 2016), suggesting that the red syenites have crystallized from less evolved melts, compared with the other facies. The

similarities of apatite and clinopyroxene equilibrium melts in term of REE content may also suggest that the red syenites were formed from homogeneous melt batches.

In detail however, the equilibrium melts calculated from apatite and clinopyroxene differ by from each other by:

- higher Ce/Lu ratios in the majority of the clinopyroxene equilibrium melts (higher in fact than in most clinopyroxene equilibrium melts and more comparable to the values observed in apatite equilibrium melts – Figure II.14.b),
- somewhat higher Nb/Ta values in the apatite equilibrium melts, compared with their clinopyroxene counterparts (Figure II.14.b),
- above all by a significant difference in term of Rb/Sr and Y/Zr, with the apatite equilibrium melts distinguished from the clinopyroxene equilibrium melts by higher Rb/Sr and lower Y/Zr values (Figure II.14.c).

These differences are not consistent with the duality of parental melts (carbonate and silicate liquids) suggested for the other facies. However, although their compositional differences were less pronounced, heterogeneous parental melts were nevertheless involved in the formation of the red syenites. This indicates that the formation of this rock type also involved immiscibility/fractional crystallization processes. The comparatively less contrasted parental melt compositions may reflect the formation of the red syenites in an earlier differentiation stage of the Ihouhaouene complex, compared with the other rock types.

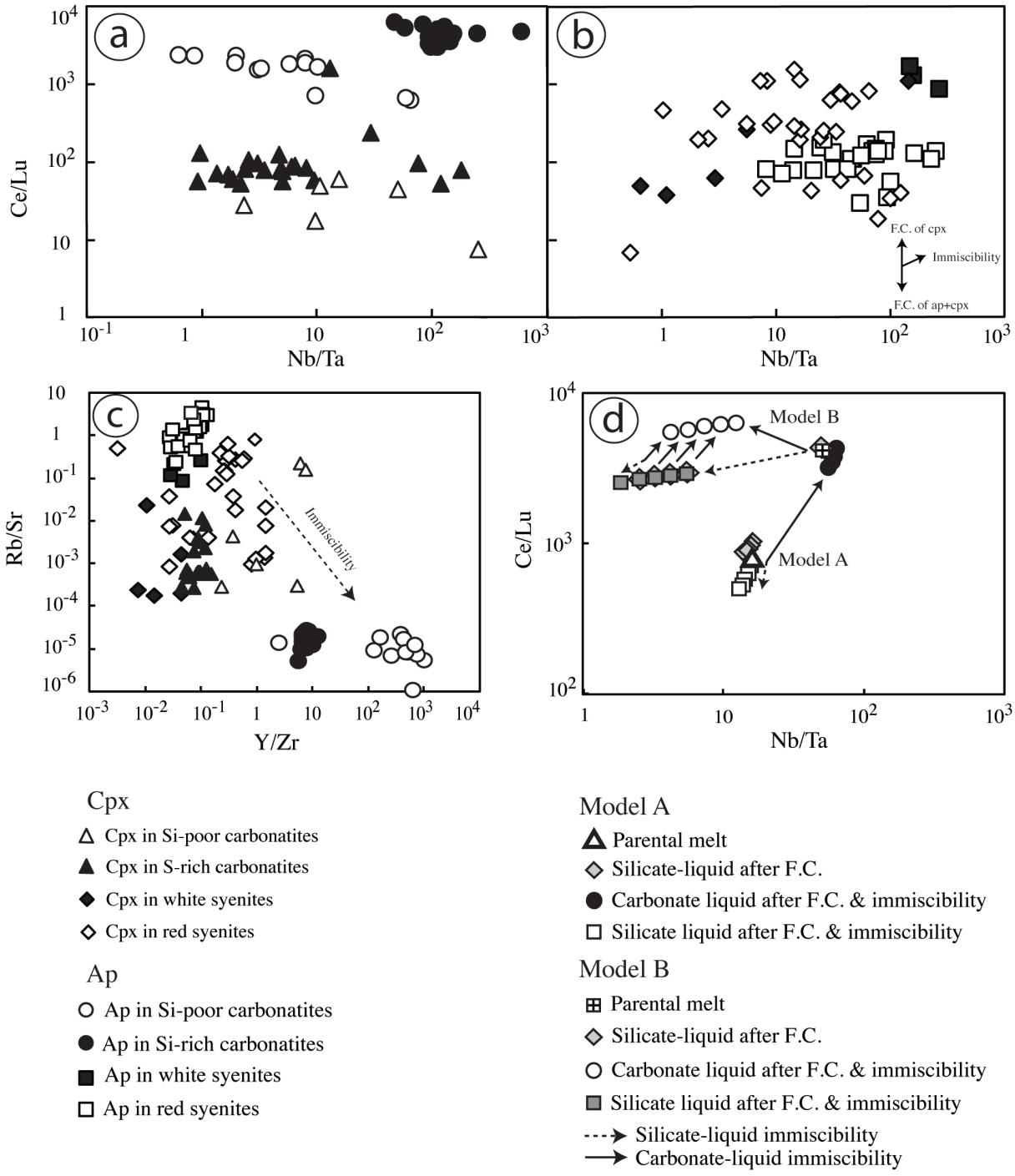

Figure II.14. Recalculated apatite (ap) and clinopyroxene (cpx) equilibrium liquids **a** Ce/Lu versus Nb/Ta of Ihouhaouene carbonatites **b** Ce/Lu versus Nb/Ta of associated syenites. **c** Rb/Sr versus Y/Zr of carbonatites and syenites. FC: Fractional crystallization. For Si-poor and Si-rich carbonatite, we chose partition coefficient between carbonatite and apatite from Hammouda *et al*. 2010 (experiments performed with green apatite from Ihouahouene) and carbonatite and clinopyroxene from Klemme *et al*. 1995 and Blundy & Dalton (2000). For syenites, we selected partition coefficients between silica-rich melt and apatite from Mahood & Stimac (1990) and Prowatke & Klemme (2006) and partition coefficients between silica-rich melt and clinopyroxene from Larsen

(1979) and Mahood & Stimac (1990). **d** Ce/Lu versus Nb/Ta of silicate and carbonate liquids from numerical modelling of immiscibility-fractional crystallization (FC) and mingling processes. The silicate/carbonate liquid partition coefficients used in the model are calculated from apatite and clinopyroxene equilibrium liquids from Ihouhaouene carbonatites and associated syenites (see text for further details and supplementary data B2). (A) Fractional immiscibility model of carbonate liquids from a melilitite (Baudouin *et al*. 2016). (B) Fractional immiscibility model of carbonate liquids from an evolved parental silicate liquid after mingling with carbonate liquid (supplementary data B2). Arrow represents compositional carbonate liquid evolution and dashed arrow represents compositional silicate liquid evolution after immiscibility (Table II.II. 6).

II.7.b. Modelling

To simulate the superimposed effects of crystal fractionation and segregation of immiscible melts on trace-element differentiation, we used a stepwise approach combining two Rayleigh distillation equations, alternately: the fractional crystallization equation for the mineral (clinopyroxene and apatite) segregation and an equation formally similar to the fractional melting equation (Shaw 1970) for the segregation of immiscible melt fractions (supplementary data B2, supplementary data illustration). In the latter, element partition coefficients between carbonate and silicate melts stand for the bulk solid/liquid partition coefficients of the modal fractional melting model. This approach is used to assess the ability of the inferred crystal fractionation–melt segregation model to account for Ce/Lu *vs*. Nb/Ta systematics in the calculated equilibrium melts, notably the paradoxically low Nb/Ta values inferred for carbonatitic melts in the Si-poor carbonatites (Figure II.14.a).

Critical parameters of the model include:

- *Initial melt compositions*. To reproduce the whole complexity of the Ce/Lu *vs*. Nb/Ta systematics, we used two distinct compositions for parental melts: a primary, melilitic composition (Baudouin *et al*. 2016) for the less differentiated rock types (the red syenites, notably) and an evolved, syenite-carbonatite melange for the most evolved facies (the Si-poor carbonatites).
- *Partition coefficients between carbonate and silicate melts*. The experimentally determined values available in the literature were determined for "pure" carbonate/silicate immiscibility (Hamilton *et al*. 1989; Jones *et al*. 1995; Veksler *et al*. 1998; Martin *et al*. 2013) and do not allow us to account for trace element concentrations and ratios of Ihouhaouene magma compositions (supplementary data B2). Therefore we used liquid/liquid partition coefficients deduced from the equilibrium melt compositions calculated in our study. Partition coefficients are considered constant within a given step of melt segregation but they are allowed to vary to account for changes in parental melt compositions (Martin *et al*. 2013).

- *The residual melt proportion ("f") and the immiscible melt fraction ("F")* represent melt fractions after each increment of 50% Cpx fractional crystallization (early mineral) and immiscible melt segregation, respectively. We used a trial-and-error approach to provide a best fit of our data. Given the uncertainties on several parameters and the relative inadequacy of the model to reproduce the whole complexity of the differentiation processes in the Ihouhaouene complex, constraining the actual *f* and *F* values was clearly beyond the scope of our approach. The aim of our numerical experiments was merely to assess the ability of the crystal fractionation–melt segregation model to account for the Ce/Lu and Nb/Ta variations within a reasonable range of *f* and *F* values (Table II.6).

Table II.6. Input segregated and residual melt fractions and output melt compositions for the fractional crystallization-immiscibility model

	residual melt fraction	*segregated melt fraction*	*Csil*	*Ccarb*	*Csil*	*Ccarb*
	f	*F*	Ce/Lu		Nb/Ta	
Parental melt A			793		16.31	
Model A	0.55	0.01	709	4269	15.72	63.96
	0.5	0.011	637	3836	15.09	61.42
	0.45	0.012	578	3483	14.44	58.76
	0.4	0.013	533	3212	13.77	56.02
	0.35	0.014	503	4154	13.08	53.03
Parental melt B			4176		51.09	
Model B	0.95	0.08	2931	6341	5.58	12.54
	0.96	0.01	2855	6176	4.27	9.61
	0.97	0.01	2767	5986	3.27	7.36
	0.98	0.01	2669	5774	2.5	5.63
	0.99	0.01	2562	5560	1.92	4.31

Csil: Silicate melt composition; Ccarb: Carbonate melt composition

Results of the numerical experiment are displayed on Figure 15d. Model A uses a primary melilitite composition as initial parental melt and liquid/liquid partition coefficients inferred from equilibrium between:

- a silico-carbonated melt component represented by the average of clinopyroxene equilibrium melts in the Ihouhaouene red syenites (Figure II.14.b), considered to represent a poorly evolved magma.
- a carbonate melt component represented by the average of apatite equilibrium melts in the Ihouhaouene Si-rich carbonatites (Figure II.14.a), considered to be segregated from a poorly to mildly evolved parental magma.

The carbonate melt fractions generated by Model A are distinguished by elevated values of both Ce/Lu and Nb/Ta ratios, comparable to the values yielded by the apatite equilibrium melts in the Si-rich carbonatites and the white syenites (Figure II.14.a, b). Both equilibrium melts were considered to represent carbonate melts. The residual liquid after segregation of carbonate melt shows only a subtle decrease of Ce/Lu at constant Nb/Ta, a feature which might explain the dispersion of Ce/Lu values in the clinopyroxene equilibrium melts of the red syenites (Figure II.14.b).

For Model B we used a parental melt with a hybrid composition with evolved carbonate and silicate melts (Model A, Nb/Ta= 51) (Figure II.14.d) and liquid/liquid partition coefficients inferred from equilibrium between:

- a silico-carbonated melt component represented by the average of clinopyroxene equilibrium melts in the Ihouhaouene white syenites (Figure II.14.b), considered to represent an evolved magma.
- a carbonate melt component represented by the average of apatite equilibrium melts in the Ihouhaouene white syenites (Figure II.14.b), considered to be segregated from an evolved magma.

The liquid/liquid partition coefficients calculated for Nb/Ta from evolved carbonate-silicate melts are higher than those calculated from poorly evolved melt (Model A) and segregated carbonated melts after immiscibility can only have lower Nb/Ta ratio compared to the parental melt. The carbonate melt fractions generated by Model B have high Ce/Lu and low Nb/Ta ratios similar to the apatite equilibrium melts in the Si-poor carbonatites (Figure II.14.a). The high Ce/Lu ratios modelled for silicate melts do not reproduce the low Ce/Lu ratio of clinopyroxene equilibrium liquids in Si-poor carbonatite. Further hybridizations are required to account for the low REE concentrations.

II.8. SUMMARY AND CONCLUDING REMARKS

At first sight, the extreme diversity of trace-element compositions recorded by the Ihouhaouene equilibrium melts might suggest that the complex was formed from a range of primary mantle melts generated by variable degrees of melting of a carbonated, heterogeneous mantle source. This would also account for the almost continuous range of major-element compositions, from Si-poor carbonatites to Si-rich syenites (Figures II. 4 and 5).

This simple scheme is however at odds with the occurrence of LREE-depleted minerals (e.g., clinopyroxene on Figure II.9 and wollastonite on Figure II.11) in the Si-poor carbonatites, whereas the melting model would predict the opposite – i.e. selective LREE enrichment in carbonate-rich melts produced by the lowest melting degrees. Moreover, variable-melting degrees would hardly account for the considerable range of Nb/Ta variations in equilibrium melt (Figure II.14), a feature, which cannot be explained by fractional crystallization alone, either. Conversely, the segregation of carbonated immiscible melt from a silico-carbonated parental magma may account for substantial Nb-Ta fractionation (e.g. Martin *et al*. 2013). However, carbonatites generated by liquid-liquid separation from a primary mantle melt are expected to show elevated Nb/Ta values. This is the case for the equilibrium melts calculated from apatite in the Si-rich carbonatites, but not for the apatite equilibrium melts in the Si-poor carbonatites (Figure II.14.a). The latter are mostly characterized by low, subchondritic Nb/Ta ratios. As illustrated by our modeling (Figure II.14.d), this signature may reflect the segregation of carbonated melts from an evolved parental melt residual after previous stages of immiscible melt separation.

Previous studies of volcanic alkaline/carbonatite systems clearly demonstrated the role of fractional crystallization to reach carbonate saturation and immiscibility. To our knowledge, although complex cyclic processes including several stages of fractional crystallization and immiscibility are mentioned as the fractional crystallization models proposed by Holm *et al*. *2006* and Weidendorfer *et al*. 2016, no models considered a multi-stage process involving alternating steps of fractional crystallization and melt exsolution.

Additional complexity in the petrogenesis of the Ihouhaouene complex arises from the fact that all rock facies show hybrid compositions resulting from the assemblage of minerals crystallized from distinct melt types. Equilibrium melts show only moderate differences of compositions in the red syenites, which also represent the less differentiated silicate melt. In contrast, the more differentiated silicate melt for the white syenites and the carbonatites show contrasted equilibrium melt compositions where the apatite is equilibrated with carbonate liquids while the clinopyroxene is equilibrated with silicate melts.

Altogether, these observations suggest an evolutionary scheme for the Ihouhaouene alkaline complex whereby all rock facies are intimately related. Progressive cooling of a silico-carbonated

mantle melt resulted in the segregation of both cumulus minerals (clinopyroxene, wollastonite, apatite…) and immiscible carbonate melt fractions, as well as in the concomitant chemical evolution of the silicate parental melt. However, this process was partly counterbalanced by intermingling of partially crystallized melt fractions of contrasted compositions. This resulted in the formation of hybrid crystal aggregates composed of disequilibrium "cumulus" phases on one hand, and mobile carbonate melt fractions on the other hand. In this scheme, the differentiation of Si-rich carbonatites from syenites (at least the white ones) is mostly due to the late segregation and spatial redistribution of the interstitial carbonate fraction. Local segregation of carbonate melts also generated the Si-poor carbonatites.

Acknowledgements

This study was financially supported by the FP7-PEOPLE-IRSES project MEDYNA (2014–2017) "Maghreb-EU research staff exchange on geodynamics, geohazards, and applied geology in North-west Africa", the French Embassy of Algiers through a PROFAS B+ research grant to A.D (2016-2017) and by the French National Institute of Earth Sciences (INSU-SYSTER 2016). We thank the authorities, field guided and drivers of Ahaggar National Park (Tamanghasset), and M. Amara for their valuable assistance during field campaigns. The help of C. Martin, L. Causse and B. Boyer for analytical work is gratefully acknowledged. We thank C. Nevado and D. Delmas for their appreciated technical assistance, Justine Villard and Rabia Benchabane for their support.

Les conditions sub-solidus d'enrichissement en REE : inclusions de britholite et monazite dans les apatites des carbonatites et syénites d'Ihouhaouene

Ce chapitre se focalise sur l'étude des apatites et des inclusions minérales riches en terres rares (britholite-monazite) afin de caractériser la composition magmatique en terres rares des minéraux et déterminer la composition des fluides tardi-magmatiques lors des processus de diffusion sub-solidus.

Apatite-britholite and apatite-monazite-quartz-calcite: REE enrichment in carbonatite at fluid-assisted sub-solidus conditions (In Ouzzal, NW Hoggar, Algeria)

A. Djeddi[1,2*], F. Parat[1], K. Ouzegane[2], J. -L. Bodinier[1,3], J. -M. Dautria[1]

[1] Géosciences Montpellier, UMR 5243, CC60, Université de Montpellier, Place Eugène Bataillon, 34095 Montpellier cedex 5, France

[2] FSTGAT-USTHB, BP32, El Alia, 16111 Bab Ezzouar, Algeria

[3] Geology & Sustainable Mining, UM6P, Hay Moulay Rachid, Ben Guerir, Morocco

*E-mail : asma.djeddi@gm.univ-montp2.fr

Abstract

Apatite is a solvus mineral in carbonatites and syenites located in the Archaean In Ouzzal craton (Ihouhaouene, NW Hoggar). Ihouhaouene carbonatitic and alkaline complex includes diverse REE mineral assemblages in apatite (britholite, monazite) formed during different stages and/or environments and reveals an outstanding case because of their potential as geochemical tracers and increasing interest in the mineralogy and geochemistry of rare-earth element ore deposits. Apatites in Ihouhaouene complex are Si-rich and Si-poor, present without inclusions and metasomatic features or they are inclusion-bearing apatites with REE-rich britholite exsolutions or monazite inclusions associated to quartz and calcite, respectively that reflect variable fluid compositions or sub-solidus environments. Inclusion-free and inclusion-bearing apatites in Ihouhaouene carbonatites present key minerals to understand the evolution of carbonatite-related REE mineralization from magmatic to late-magmatic stages and their secondary post-magmatic overprint.

Si-rich apatites (~5 wt.%SiO_2) contain high REE contents 6.5 to 7.4 wt.% ΣREE_{ox} in inclusion-free apatites and 3.95 to 19.18 wt.% ΣREE_{ox} in britholite-bearing apatites. Whereas, Si-poor apatites (<2.4 wt.% SiO_2) have <5.3 wt.% ΣREE_{ox} in inclusion-free apatites and monazite bearing apatites.

Britholite (REE: 38 to 67 wt.%) occurs always as exsolutions in apatite and monazite (REE: 66 to 69 wt.%) occurs as inclusions and rim grains in apatite, often associated to quartz and calcite. Geochemical analyses and microstructure orientation of both apatites suggest that britholite exsolutions are topotactic and precipitate as solvus phases and requires the contribution of Cl-Th-Si-REE-rich fluid by an oriented fluid reaction following the substitution mechanism of $Si^{4+} + S^{6+} + 2REE^{3+} = 2P^{5+} + 3Ca^{2+}$ and $F^- = Cl^-$. However, monazite, quartz and calcite inclusions in Si-poor apatites suggest an epitaxial relationship and they are formed during S-Si-REE mass transfer by Ca-P-CO_2-rich fluid-assisted and apatite re-equilibration at sub-magmatic conditions.

Silica and Sulphur content of precursor apatites and/or P-T sub-magmatic conditions mainly control REE distribution and remobilization in apatites and REE-rich mineral inclusions. Ihouhaouene apatites attest of little fluids-rock interaction and re-equilibration during metamorphic episode and underwent sub-magmatic to supergene history of REE-deposition and enrichment.

III.1. Introduction

Apatite is a liquidus phase in carbonatite magmas (Elby 1975; Le Bas & Handley 1979; Erikson et al. 1985) and is also known to crystallize throughout alkaline and carbonatite magma fractional crystallization (e.g. Hogarth et al. 1985; Gittins 1989; Djeddi et al. 2019). Its abundance and common occurrence in alkaline and carbonatite rocks favour fluorapatites as a petrogenetic and geochemical tracer among comagmatic suite of igneous rocks (e.g. alkaline and carbonatite complex of Kola Peninsula in Russia, Brassinnes et al. 2005). The importance of apatite as a tracer of magma evolution in carbonatite and alkaline complexes was first recognized by Le Bas & Handley (1979) and further explored by Hogarth (1989), Hornig & Kjarsgaard (1988) and Bühn et al. (2001) that examined the apatite composition in carbonatite and associated rocks from a number of localities and supplied first reliable trace-element data for this mineral (Chakhmouradian et al., 2017).

The crystal structure of apatite $Ca_5(PO_4)_3(F,Cl,OH)$ allows a wide range of structural distortions and chemical substitutions at magmatic conditions including water, halogens, S, C and significant amounts of trace elements comprising Sr, Th, U and rare earth elements (REE) (Pan & Fleet 2002; Webster & Piccoli 2015; Chakhmouradian et al. 2017). Apatite is among the most important minerals in controlling rare-earth element (REE) variations in igneous rocks (Watson & Green 1981; Harrison & Watson 1984; Hoskin et al. 2000). At subsolidus-conditions, magmatic REE-rich apatites re-equilibrate in the presence of fluid (McCubbin & Jones 2015; Harlov 2018) and are often found associated to monazite and bastnasite (Humphries, 2013). They represent the igneous source for REE and further evolution through sub-solidus remobilisation and formation of REE ore deposits (Wei Chen et al. 2017). Furthermore, apatite is highly susceptible to various fluid induced (metasomatic) chemical and textural changes over a wide range of pressure and temperature making it an ideal mineral for fingerprinting metasomatic processes (Harlov, 2018).

Most of petrological and geochemical studies have been performed on evolved carbonatite and alkaline complexes that have undergone complex hydrothermal and metamorphic events (Mountain Pass, Mariano & Mariano Jr, 2012; Bayan Obo, Möller 1989), whereas few study have considered early stage of REE remobilization (Andrade et al. 1999). In Ihouhaouene carbonatites, the occurrence of igneous apatite free of sub-solidus inclusions and apatite with britholite and monazite inclusions is exceptional because they record early stage of REE remobilization and enrichment leading to the crystallization of REE-phosphates that are often associated to REE oxides in more evolved magmatic complexes (Chakhmouradian et al. 2017). They are precursor for the crystallization of rare-earth oxides.

This paper is devoted to a petro-geochemical characterization of the apatite-inclusions in Ihouhaouene carbonatites to highlight apatite and REE-phosphate equilibrium and determine the sub-

solidus environment and fluid composition in carbonatite and alkaline rocks at early stage of REE remobilization.

III.2. Ihouhaouene carbonatite/syenite complex – Geological background

The Ihouhaouene alkaline complex consists of syenites and carbonatites intruded in the Archaean granulites of the In Ouzzal block in Algeria (Lelubre, 1952; Kienast *et al*., 1987; Ouzegane, 1987; Ouzegane *et al*., 1988; Djeddi *et al*. 2019) (Figure III.1). The close spatial relationships between carbonatite and syenite of Ihouhaouene complex (2 Ga; In Ouzzal terrane, Hoggar, South of Algeria) and the similar pegmatitic/brecciated textures and mineral assemblages of diopside/hedenbergite cpx, apatite, wollastonite +/- calcite and alkali-feldspar in the two rock types suggest that they were emplaced during a single igneous event (Djeddi et al. 2019). Progressive cooling of a silico-carbonated mantle melts result in the crystallisation and segregation of cumulus minerals and immiscible carbonate melt fractions that formed Si-rich carbonatite and syenite, whereas local segregation of carbonate melts from evolved silica-rich carbonated melt generated Si-poor carbonatite (Djeddi *et al*. 2019).

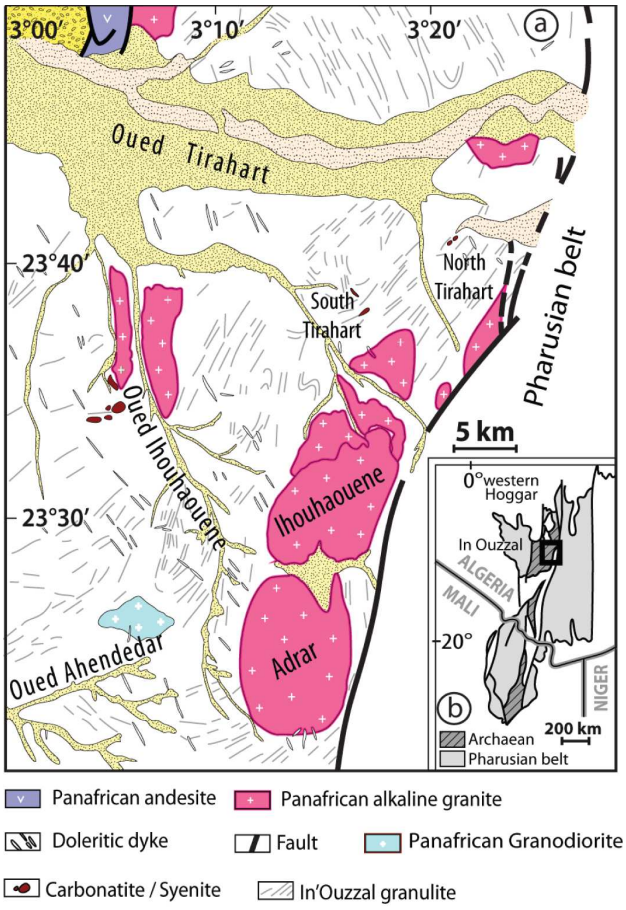

Figure III.1 a Geological map of the Ihouhaouene area in N.W part of the In Ouzzal terrane and localization of carbonatites and associated syenites (Ouzegane *et al*. 1988). **b** Location of the studied zone in Western Hoggar.

Large euhedral magmatic apatites (2 to 5 cm) are present in both carbonatites and syenites. They are liquidus phases with cpx and calcite or alkali feldspar and crystallized at high temperature from REE-enriched carbonate-rich silicate melts (Djeddi *et al*. 2019). Apatites have either no inclusions, numerous inclusions of monazite, quartz and calcite or britholite inclusions. No systematic distribution has been observed according to the outcrop localities (Oued Ihouhaouene, South Wadi Tirahart or North Wadi Tirahart), or mineral assemblage and proportions in the host carbonatite and syenite rocks. The occurrence of various apatite *textures* is more likely the result of different sub-solidus environments. They are key minerals to determine the sub-solidus conditions that controlled REE-enrichment in carbonatites and syenite by comparing the chemical composition (major, trace and volatile elements) and crystallographic relationship of apatite and secondary REE-rich minerals.

III.3. Apatite as tracer of magmatic and sub-solidus evolution

Magmatic apatite crystallized from silicate melts, concentrated hydrothermal brines, low-temperature aqueous solutions and possibly from the vapour phase (McConnell, 1973). Apatite is REE-rich mineral and it is one of the most important minerals affecting rare earth element trends in igneous rocks and volatile evolution in magmas (Nash, 1972; Picolli & Candella, 2002; Rakovan, 2002).

Trace elements partition in favour of silicate melts relative to apatite and in apatite relative to carbonate melts and in both systems, REE are preferentially incorporated in apatite (Prowatke & Klemme, 2006; Webster & Piccoli, 2015). In the apatite/carbonatite system, REE are compatible in apatite depending on apatite silica content (Hammouda et al., 2010).

The apatite-group minerals have a general formula of $[M_{10}(ZO_4)_6X_2]$ (Pan & Fleet, 2002), allowing wide chemical substitutions. The M cation site is principally occupied by Ca^{2+} and can also hold other common divalent cations Sr^{2+}, Ba^{2+}, Pb^{2+}, Cd^{2+}, Mg^{2+}, Mn^{2+}, Ni^{2+}, Cu^{2+}, Zn^{2+} and monovalent cations as Na^{1+} or trivalent cations, mostly REE^{3+} and Y^{3+}. The typically P^{5+} Z site can be replaced by Si^{4+}, C^{4+}, S^{6+}, As^{5+}, V^{5+} and B^{3+} (Pan & Fleet, 2002; Hughes & Rankovan, 2015; Riker *et al*. 2018). The halogen-monovalent anions- X site is occupied by F^-, Cl^- and OH^- and sometimes by O_2^-, O_3^-, BO_2^-, NCO^-, NO_3^-, NO_2^- and S^{2-} (Mc Connell, 1973; Pan & Fleet, 2002; Kim *et al*. 2017; Konecke *et al*. 2017a). All these element incorporations yield a large variety of apatite compositions.

Apatite crystallizes over a wide temperature range (>200ºC; Webster & Piccoli, 2015) and the REE substitution increases with decreasing temperature and increasing SiO_2 content of the melt (Watson & Green, 1981). REE^{3+} substituted Ca^{2+} in apatite structure by the main four substitution reactions with charge-compensating mechanisms (Pan & Fleet, 2002; Hughes & Rakovan, 2015; Harlov, 2018):

(1) $REE^{3+} + M^{+} = 2\ Ca^{2+}$ (M= Ca, Sr, Pb, Na, Th..)

(2) $REE^{3+} + X^{2-} = Ca^{2+} + F^{-}$ (X= F, OH, Cl…….)

(3) $2\ REE^{3+} + \text{——} = 2\ Ca^{2+}$ (——, Ca-vacancy site)

and

(4) $REE^{3+} + Si^{4+} = Ca^{2+} + P^{5+}$

Substitution of P^{5+} in apatite by high amounts of Si^{4+} yields other minerals belonging to different chemical classe namely silicates (e.g. britholite, Passero *et al*. 2010).

Britholite is considered as a subgroup of the apatite group (Pekov et al., 2007) and present a solid solution of apatite indicative of extensive substitutions of $PO4^{3-}$ by $SiO4^{4-}$ and Ca^{2+} by REE^{3+} (Ransbo, 1989; Pan & Fleet, 2002; Passero *et al*. 2010). It's a rare mineral, known in only ten regions all over the world. It was described in nepheline-sodalite syenite of Greenland (Winther et al., 1899; Boggild, 1905), in Oka magnetite veins, Quebec (Guirault, 1953; Hughson et al., 1964), in alkaline syenites and granites of Soviet Union and China (Valsov, 1966), in the highly differentiated sodic syenites of Montana, USA, where britholite is observed instead of apatite (Nash, 1972) as well as alkaline rocks of the Pilansberg Complex, South Africa (Von Backstrom, 1976). In the In Ouzzal terrane, britholite is found in carbonatites as inclusions in apatite. This is original considering that in all the other occurrences; it does not coexist with apatite (Nash, 1984).

Britholite is mainly described in nepheline syenites and contact metasomatic deposits. It generally forms during hydrothermal processes related to the replacement of apatite or monazite (Budzyń *et al*. 2011; Uher *et al*. 2015; Zirner *et al*. 2015; Giebel *et al*. 2017). Britholite is assumed to be a late stage to post-magmatic origin for most occurrences (subsolidus alteration of primary minerals) (Wall *et al*. 1993; Uher *et al*. 2015). The relationship between intergrown REE-rich fluorapatite and fluorbritholite indicate a continuous to sudden crystallization in this mineral sequence during fluid evolution (Zozulya *et al*. 2017).

The amounts of REE in apatite are also linked to wether apatite has undergone metasomatism. REE can be removed from apatite by fluid-transfer to form other REE-bearing minerals such as monazite (Harlov, 2015). Monazite has the nominal composition $(LREE)PO_4$ with LREEs (La+Ce+Nd) generally comprise approximately 75% of the total cation proportions (Spear & Pyle, 2002). Monazite is commonly found as inclusions in apatite and attests of a fluid-rock interaction.

The association of monazite and apatite is common in carbonatites (e.g., Mountain Pass, Moriano & Moriano Jr 2012; Bayan Obo Smith *et al*. 2000) where monazite occurs as small crystals on the edge of crystal replacing apatite or included within apatite crystals formed in a hydrothermal scenario

from REEs rich fluids reacted with apatite (Chen *et al*. 2017). These fluids can be the result of internal mineral reaction or from outside the rock system (Harlov, 2018).

The hypothesis that fluids can induce monazite inclusions to form in apatite in nature under a wide range of P-T conditions is supported experimentally (Harlov *et al*. 2002b, 2005; Harlov & Forster, 2003; Harlov, 2018). The crystallization of monazite inclusions or rim grains is the result of coupled dissolution-reprecipitation process during the metasomatic alteration of apatite (Putnis, 2009; Harlov, 2018). The crystallographic continuity in the monazite host apatite, reveal that the regions affected by coupled dissolution and precipitation are characterized by a three dimensional micro- and nano-porosity in reacted regions allowing fluids to infiltrate the apatite structure (Harlov et al. 2005; Putnis, 2009; Harlov, 2018).

According to the monazite and apatite unit-cell parameters, there is a poor correspondence between the lattices of monazite and apatite in the plane of interface (Pan *et al*. 1993). The only similarity in the crystal structures of monazite and apatite in the orientation of the intergrowth is in the layering of the phosphate groups normal to the b-axis of monazite and c-axis of apatite (Pan *et al*. 1993). This may explain that monazite inclusions have precipitated by oriented reaction and suggest an epitaxial relationship with host-apatite (Pan *et al*. 1993; Pan & Fleet 2002; Harlov, 2015).

III.4. Analytical methods

III.4.a. In situ mineral analysis for major, trace and volatile elements

The concentrations of major, trace and volatile element in minerals were measured by electron microprobe (Cameca SX100 at the Microsonde sud, University of Montpellier, France). Operating conditions are: acceleration voltage of 20 kV, beam current of 10 nA and a beam focalized (1 μm). Background counting time of 09min for all elements was applied: 30 s for each REE Th and K except Ce, Y and Th that were analysed for 60s as for major elements, F and S and 20s for Cl. The internal standards chosen for each element were: Al_2O_3 for Al, TiO_2 for Ti, wollastonite for Ca and Si, albite for Na, orthose for K, forsterite for Mg, hematite for Fe, apatite for P, native metal for Ni, Mn, Cu, celestine for Sr, ThO_2 for Th, enriched glasses for REE: REE2 for Nd, Sm, Yb, Lu; REE3 for La, Ce, Pr, Y; REE4 for Dy, baryte for S and Ba, fluorite for F and chloroapatite for Cl. Distribution of five major elements (Ca, P, Si, Ce, La) within apatite crystal and monazite inclusions was characterized by collecting WDS X-ray element maps with a step size of 16 μ.

In-situ trace element analyses were conducted by LA-ICP-MS at Geosciences Montpellier (AETE platform, OSU-OREME), using GeoLas Q + Excimer CompEx102 with a spot diameter of 26 μm laser beam for apatite and britholite, a repetition rate of 7 Hz, a laser power of 5 J/cm^2 and a mixture of helium and argon as carrier gas. The concentrations were calibrated with NIST 612 and the

SiO_2 – CaO concentrations determined previously with electron microprobe for each mineral. BIR-1 standard is used as external standard. Data were processed with Glitter software (Griffin *et al*. 2008).

III.4.b. Bulk mineral analysis for major, trace and volatile elements

Bulk-apatite trace element analyses were realised by ICP-Mass Spectrometry at Geosciences Montpellier (AETE platform OSU- OREME). Several acid attacks on powder samples are carried out with $HClO_4$ and HF on a hot plate at 100ºC (Detailed protocol in Djeddi *et al*. 2019). 4 blanks (only acids were introduced into savilex) and four standards: BHVO-1, BEN, UBN and COQ-1 have been analysed to monitor internal drift. Before mass spectrometer analysis, the sample solution is diluted with 9.45 ml of H_2O, 0.25 ml of HNO_3, and 0.1 of InBi according to a factor of 10000. The mass spectrometer used to quantify trace element concentrations in bulk-mineral is the Agilent 7700x, whose sensitivity is of the order of 200 x 106 cps/ppm on ^{115}In (Indium). Internal standards A2 and A4 are calibrated for Zr-Nb and Hf-Ta concentrations and calibration curves on Rb, Sr, Y, Zr and Ce are performed to verify the internal calibration.

III.4.c. Microstructure orientation

The crystallographic preferred orientations CPOs of apatite, britholite and monazite were characterized by the indexing of electron backscattered diffraction (EBSD) patterns using a SEM high resolution CamScan Crystal Probe X500FE type (FEG) equipped with a NordlysNano EBSD HKL detector for crystallographic analysis and an X-ray spectrophotometer EDS X-Max^N detector for qualitative chemical analysis at Geosciences Montpellier (CNRS-University of Montpellier, France). An accelerating voltage of 15–20 kV, a beam current of 5 nA, a step size of 2, 7 and 10 μm, a hit rate of 92% and a working distance of 20–25 mm were used for automatic measurements. The angular deviation for measurements of 20º between the electron beam and the sample surface is used to reach maximum diffraction intensity. The data have then been noise-reduced using a "wild spikes" correction to fill non-indexed pixels based on neighbouring pixels using the CHANNEL5s software (Oxford Instruments HKL). The microstructural maps and the pole figures were made to highlight the crystallographic orientation of the minerals. The orientation maps represent the crystallographic orientation of each pixel by a colour function of the inverse pole figure (IPF), along one of the three main axes (X, Y, Z).

III.5. Results

Apatite in carbonatite and syenite are large prismatic magmatic crystals enclosed by calcitic matrix or K-feldspar and clinopyroxene, respectively. According to the host-rock of apatite, apatites display a compositional range of composition from Si-rich apatite in Si-rich carbonatite and white syenite to Si-poor apatite in Si-poor carbonatite and Red syenite (0.48 to 6 wt.% SiO_2) (Figure II.12 in Djeddi *et al*. 2019; Chapter II). The diversity of apatite composition is then related to the

crystallization at different stage of fractional crystallization and immiscibility during alkaline magma differentiation (Djeddi *et al*. 2019).

III.5.a. Si-rich apatite and britholite exsolution

Si-rich apatites are present as phenocryst (3 mm- 10 cm) in Si-rich carbonatites. They may be free of inclusions (Figures III.2.a) or may contain up to 40 vol.% of britholite (Figures III.2.b). Both textures have never been found together in one single sample whereas, they occurs in samples with similar primary mineral assemblages. Britholites are present in the core and the rim of apatite crystals as yellow grain exsolutions (1 to 200 μm, Figures III.2.b). They occur as large irregular- or amoeboidal-shaped grains (10-200 μm) (Figures III.2.b) and fine elongated hexagonal lamellae (<2-10 μm) in apatite (Figures III.2.b).

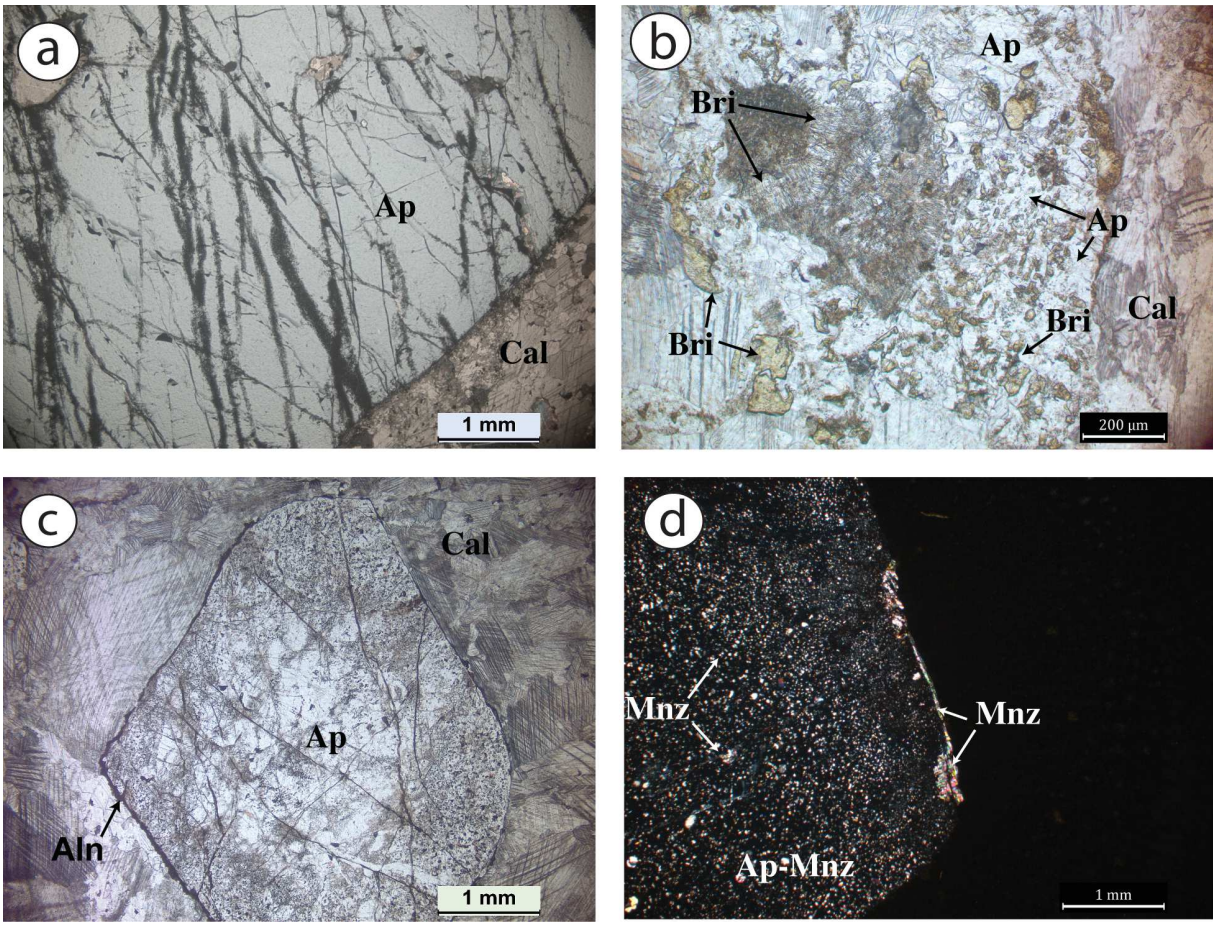

Figure III.2 Microphotographs of apatites and apatite-inclusions. **a** Si-rich apatite free-inclusion (Ap). **b** Britholite (Bri) exsolutions in apatite. **c** Si-poor apatite free-inclusion. **d** Monazite (Mnz) inclusions and rim grains in apatite.

Mineral chemistry

Inclusion-free apatites are Si-rich with SiO_2 ranging from 4.6 to 5.2 wt.% and P_2O_5 and CaO content of 30.5-32.1 wt.% and 49-50.8 wt.% respectively (Tables 1 in supplementary data C). They have high total REE content from 6.5 to 7.4 wt.%. Apatite is fluorapatite with 4.3 to 5.24 wt.% F contents and 0.03-0.06 wt.% Cl. In-situ REE patterns of Si-rich apatites display high enrichment in LREE relative to HREE (La_N/Yb_N= 86-101) (Figure III.4, (Tables 2 in supplementary data C) with slight Eu negative anomaly. They have Nb-Ta and Zr-Hf fractionation (Nb/Ta = 66-101, Zr/Hf = 67-150) (Figure III.4).

The bulk inclusion-free apatite has similar REE pattern as in-situ patterns with high fractionation of LREE compare to HREE (La_N/Yb_N= 103, Figure III.4) and displays Nb-Ta and Zr Hf fractionation (Nb/Ta = 120, Zr/Hf = 126) (Figure III.4).

Britholite-bearing apatites are Si-rich with the silica concentration increasing with decreasing P_2O_5 contents (2.08 to 5.99 wt.%. SiO_2, 39.23 to 29.8 wt.% P_2O_5, respectively) (Figure III.3.a, Table III.1 in supplementary data C). Apatites have 3.95 to 19.18 wt.% ΣREE_{ox} and 42.12 to 53.75 wt.% CaO (Figure III.3.b) with F contents ranging from 2.73 to 5.24 wt.% and Cl< 0.38 wt.% (Figure III.3.c).

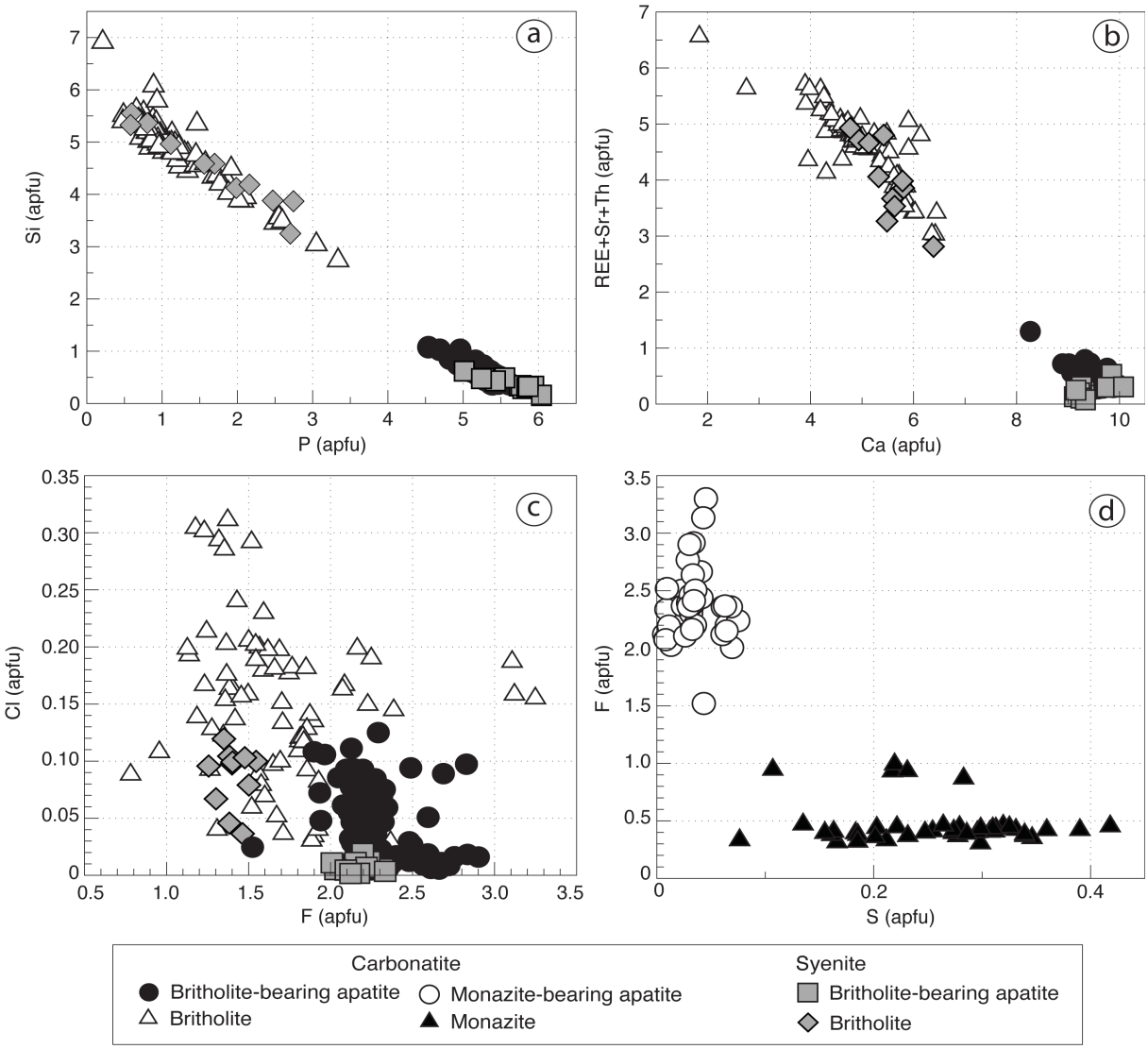

Figure III.3 Chemical substitutions in apatite-britholite exsolutions and apatite-monazite inclusions from the Ihouhaouene carbonatites and syenites. **a** Si versus P (a.p.f.u). **b** REE+Sr+Th (a.p.f.u) versus Ca. **c** Cl versus F (a.p.f.u). d F versus S.

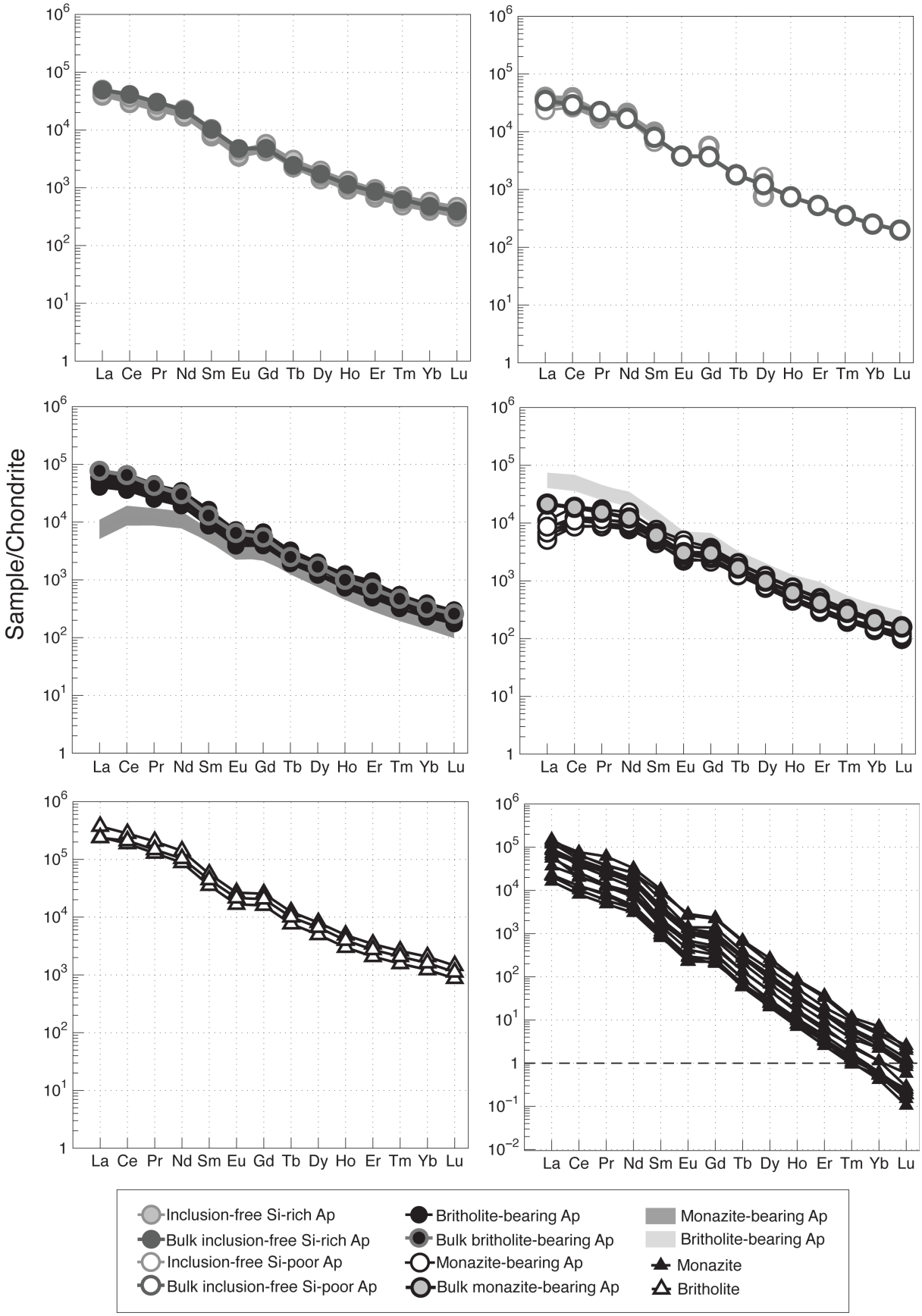

Figure III.4 Normalized REE content of free-inclusion apatites, apatite-britholite and apatite-monazite from Ihouhaouene carbonatites. Chondrite values from Sun and McDonough (1989).

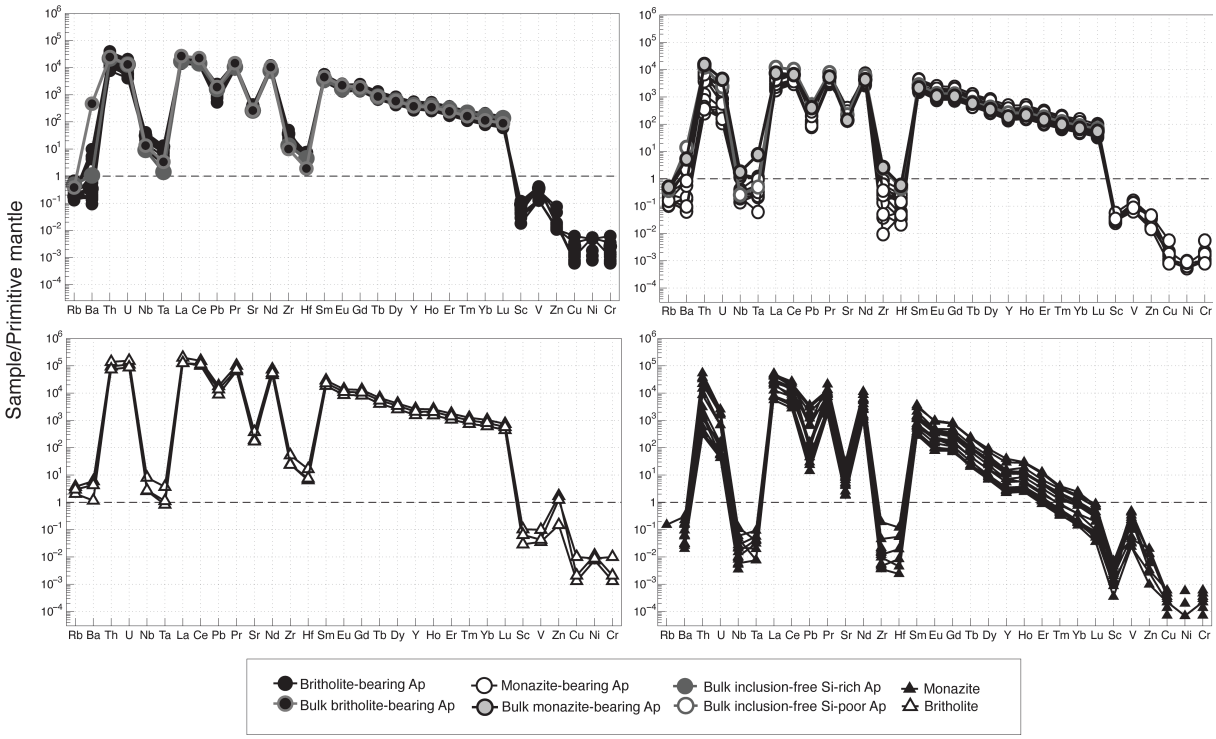

Figure III.5. Normalized trace element content of apatite free-inclusions, britholite-exsolutions and monazite from Ihouhaouene carbonatites. Primitive mantle values from Sun and McDonough (1989).

In-situ REE patterns for apatite have a high enrichment in LREE relative to HREE (La_N/Yb_N= 143-201) (Figure III.4) with slight Eu negative anomaly. Trace element patterns display Nb-Ta and Zr-Hf fractionation (Nb/Ta = 42-59, Zr/Hf = 179-292) (Figure III.5) and high Th and U concentrations (Th= 651- 2404 ppm; U= 85- 227 ppm).

The bulk britholite-bearing apatite has similar REE shape-pattern as in-situ analyse patterns with high fractionation of LREE compare to HREE (La_N/Yb_N= 234, Figure III.4). They have Nb-Ta and Zr-Hf fractionation (Nb/Ta = 69, Zr/Hf = 189) and high Th and U levels (Th= 2085 ppm; U= 275 ppm) (Figure III.5).

Britholites are silicia-rich with 9.76-25.95 wt.% SiO_2 and 0.18 to 24.23 wt.%. P_2O_5 (Figure III.3.a). They have high total REE contents (ΣREE_{ox} = 31.09 - 60.46 wt.%) with 15.83 to 43.57 wt.% Ce_2O_3, 2.48 to 12.4 wt.% La_2O_3 and 7.24 to 12.3 wt.% Nd_2O_3 for CaO contents ranging from 2.26 to 37.3 wt.% (Figure III.3.b, Table III.2 in supplementary data C). Moreover, britholite has more chlorine than apatite, ranging from 0.02 to 0.74 wt.% and similar fluorine concentrations (0.63 to 4.12 wt.% F, Figure III.3.c, Table III.2 in supplementary data C).

Britholites have high LREE content and REE patterns display high fractionation of LREE compare to HREE (La_N/Yb_N = 156-210) similar to those of host apatite (Figure III.4, Table III.5 in supplementary data C). Th and U content are high in britholite (Th= 6292-11781 ppm; U= 1841-3228

ppm) and negative anomalies in Nb-Ta and Zr-Hf are observed in trace element patterns (Nb/Ta = 37-54, Zr/Hf = 115-139) (Figure III.5).

Crystallographic orientation

EBSD analyses were performed to determine the crystal orientation relationships between apatite and britholite. We selected perpendicular section to the c-axis and performed apatite map orientation of entire apatite crystal (7 mm, Figure III.6.a) and closer map at apatite rim (Figure III.6.b).

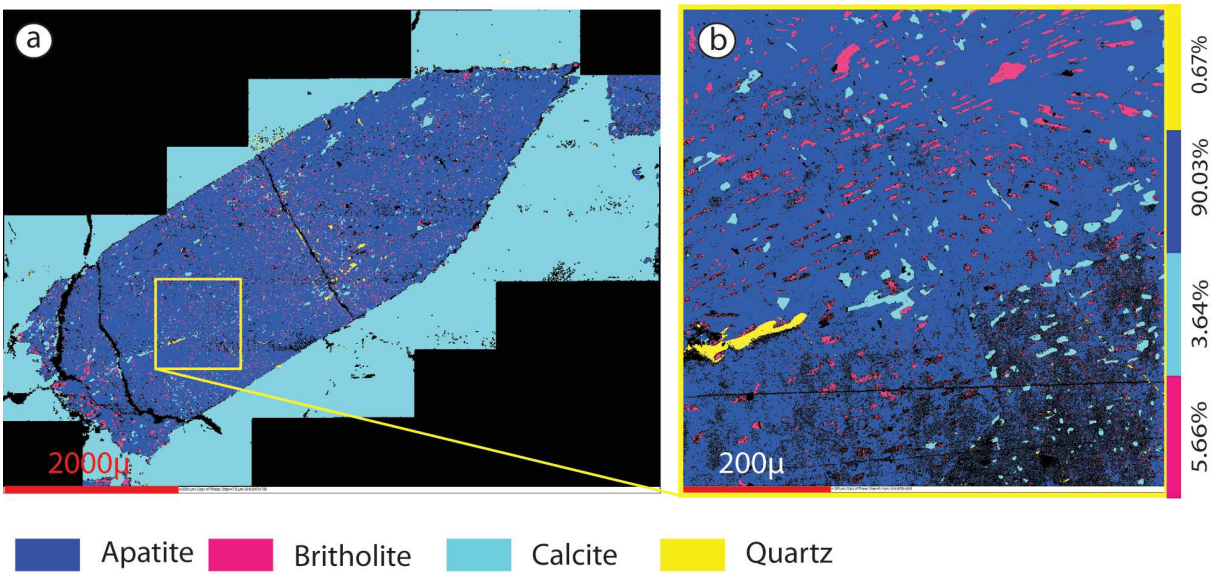

Figure III.6 EBSD- phases maps of apatite-britholite exsolutions from carbonatite INH604a. **a** All apatite crystal. **b** Apatite-britholite exsolutions zone from the apatite crystal.

From the core to the rim, EBSD orientation maps parallel to the c-axis (0001) show different grain orientation with 5° to 30° rotation of a- and m- axis around the c-axis (Figure III.7). It can be noted that britholite (5.66 vol.%) crystallized in the same orientation than apatite (90.03 vol.%). The a, m and c axes of britholite are parallel to the a, m, and c axes of apatite. The britholite orientation rotates as observed for apatite (Figures III.7 and 8). However, the rotation is progressive and crosscut the apatite sub-grains (i.e. we observe one britholite orientation in two apatite sub-grains with two different orientations: see red britholite orientation in red and yellow apatite orientations, Figure III.7).

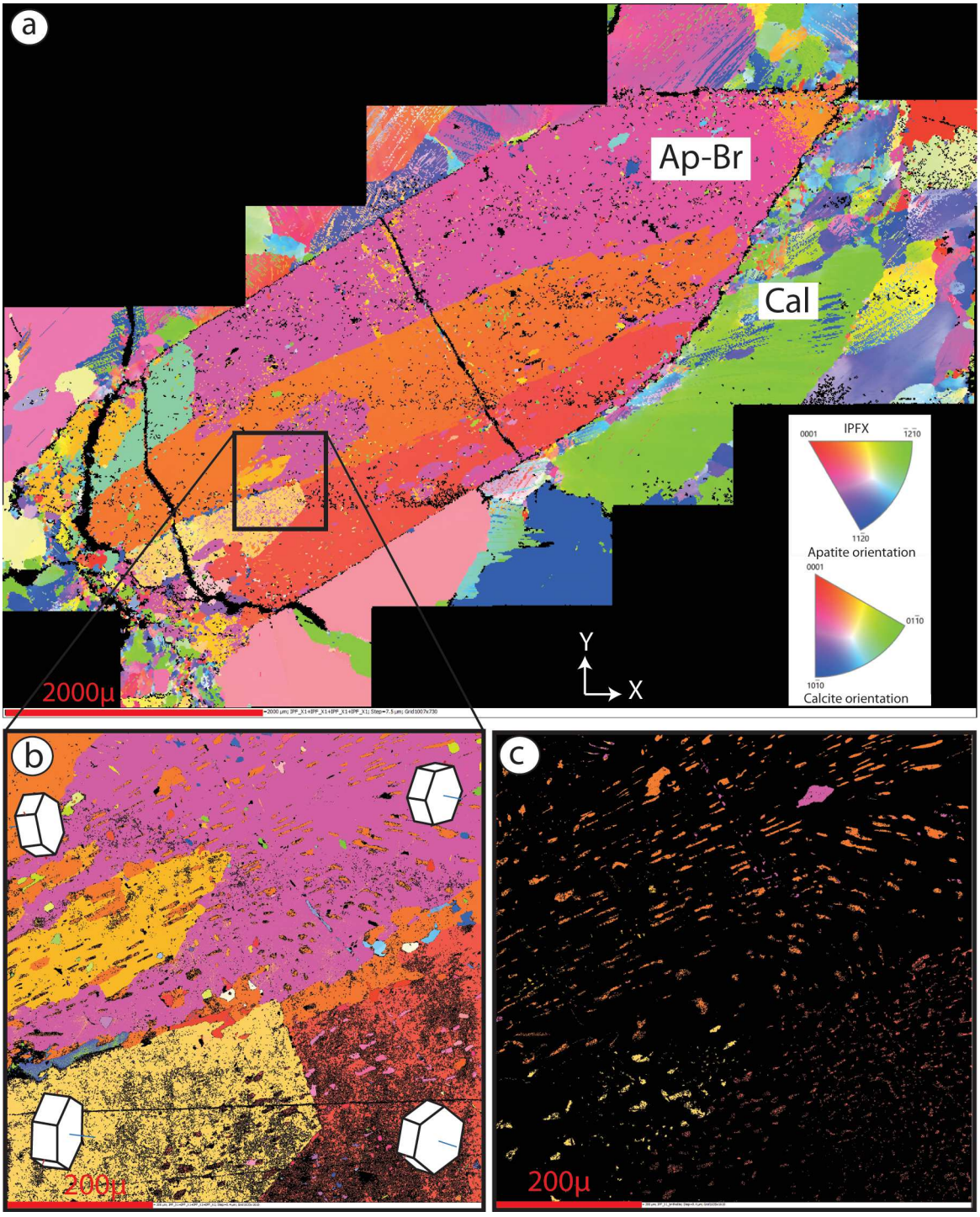

Figure III.7 EBSD- orientation maps of apatite-britholite exsolutions from carbonatite INH604a along the IPFX-axis of sample reference system **a** All apatite crystal orientation. **b** Apatite-britholite exsolutions orientation of a zone from the apatite crystal. **c** Britholite exsolutions orientation. (IPF: Inverse Pole Figure).

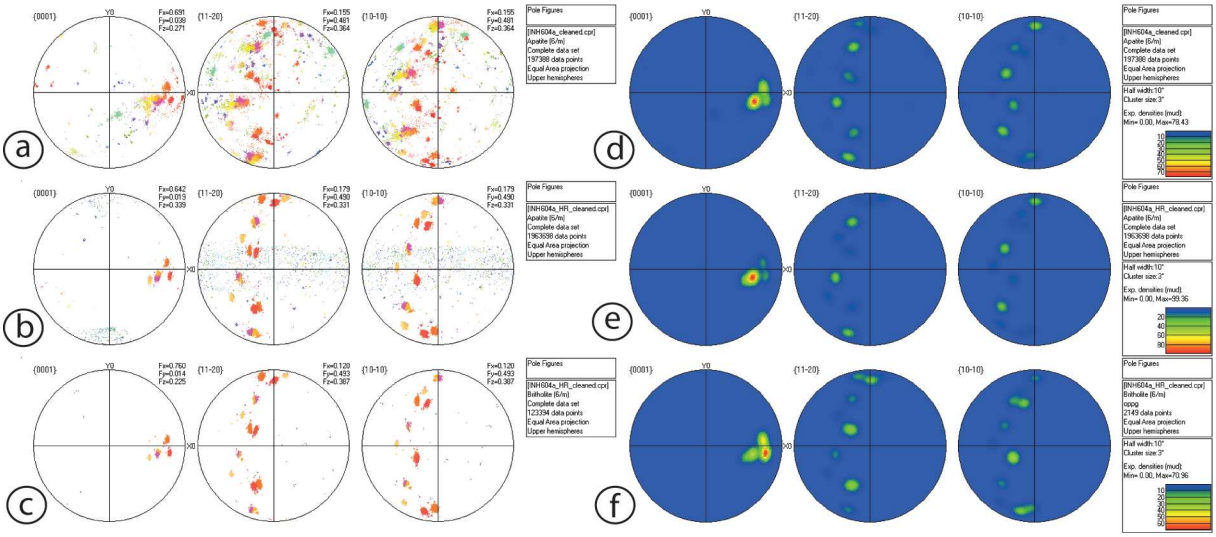

Figure III.8. Apatite-britholite crystallographic preferred orientation in pole figures. Pole figures are generated as equal-area of upper hemisphere stereographic projection of the orientation of three crystallographic axes of all crystals for each phase individually. Crystallographic orientations are plotted along IPF-X axis of sample reference system. **a** scatter plot of crystallographic axes of all apatite crystal from carbonatite INH604a. **b** scatter plot of crystallographic axes of apatite from the focused-zone. **c** scatter plot of crystallographic axes of britholite exsolutions from the focused-zone. Contoured plots (**d, e, f**) with contours levels in normalized multiples of uniform distribution where relative high concentrations of axis orientation are reported in dark red. **d** all apatite crystal. **e** apatite-britholite exsolutions. **f** britholite exsolutions.

III.5.b. Si-poor apatite and monazite-quartz-calcite mineral assemblage

Si-poor apatites are present in Si-poor carbonatite as large prismatic crystals with pyramidal endings surrounded by calcitic matrix. Two apatite textures are present in Si-poor carbonatites. Apatites are free of inclusions (Figures III.2.c) or contain up to 20 vol.% of numerous inclusions of monazite, quartz, and calcite (Figures III.2.d). Both apatites textures have never been found together and are present in rocks with similar mineral assemblages as observed for Si-rich apatites. Inclusions are homogeneously distributed in the entire crystal. Monazite crystals have prismatic to irregular shape (<10um to 20-100 μm), often associated with quartz and calcite and rarely as individual inclusions (Figures III.2.d).

Mineral Chemistry

Inclusion-free apatites are Si-poor with SiO_2 ranging from 0.6 to 2.4 wt.% and P_2O_5 and CaO content ranging from 35.1 to 42.0 wt.% and 51.0 to 58.0 wt.%, respectively (Table 1 in supplementary data C). They have low to high REE contents from 1.7 to 5.3 wt.% ΣREE_{ox}. Apatites are fluorapatites with 2.7 to 6.7 wt.% F contents and Cl is below detection limit.

The REE patterns of inclusion-free Si-poor apatite (bulk and in situ) display high enrichment in LREE relative to HREE (La_N/Yb_N = 137) (Figure III.4, Table 2 in supplementary data C) with slight Eu negative anomaly and have Nb-Ta and Zr-Hf fractionation in primitive mantle-normalized patterns (Nb/Ta = 9, Zr/Hf = 198) (Figure III.5).

Monazite-bearing apatites in Si-poor carbonatites are Si-poor (0.4 to 1.9 wt.% SiO_2) with P_2O_5 and CaO contents ranging from 35.5 to 40.9 wt.% and 51.8 to 56.4 wt.%, respectively (Table III.3 in supplementary data C). Apatites are fluorapatites with high S (0.03 to 0.4 wt.%), 2.8 to 5.9 wt.% F and low Cl concentrations (<0.05 wt.%). The apatites are REE-rich (1.5 to 4.8 wt.% ΣREE_{ox}) with slightly higher high Ce contents in the rim than the core (Table III.3 in supplementary data C, Figure III.9) and display high enrichment in LREE relative to HREE (La_N/Yb_N= 27-56) with low fractionation of LREE compare to MREE (La_N/Sm_N= 0.8-1.6) (Figure III.4). Related to primitive mantle, apatites have negative anomalies in Zr-Hf and Nb-Ta (Zr/Hf=7-190; Nb/Ta= 6-61) (Figure III.5) and low contents in Th and U (Th=21-673 ppm; U= 2-17 ppm). Bulk REE pattern of monazite-bearing Si-poor apatite displays high fractionation of LREE compare to HREE (La_N/Yb_N = 104) (Figure III.4) and present Nb-Ta and Zr-Hf fractionation (Nb/Ta = 4, Zr/Hf = 162) (Figure III.5).

Monazite crystals have 25-31 wt.% P_2O_5 and 0.2-1.2 wt.% CaO (Table III.4 in supplementary data C). The volatile contents range from 0.4 to 1.3 wt.% F, 0.1 to 1.7 wt.% SO_2 and Cl is under the detection limit (Figure III.3.d). Monazites are (Ce)-monazites with Ce_2O_3 content ranging from 32.83 to 36.11 wt.%, La_2O_3 = 15.43 to 23.34 wt.%, Nd_2O_3 = 7.06 to 11.4 wt.% (REE_2O_3 = 66 – 69 wt.%, Table III.4 in supplementary data C) (Nickel *et al*. 1987) and high Th content (ThO_2 = 0.1 – 4 wt.%).

Monazites REE patterns have very high LREE fractionation compare to HREE (La_N/Yb_N= 20030-84060) (Figure III.4; Table III.5 in supplementary data C). They have high content in U (U= 0.8-53.4 ppm) and negative anomalies in Nb-Ta and Zr-Hf (Nb/Ta = 5-108; Zr/Hf = 19-77) (Figure III.5).

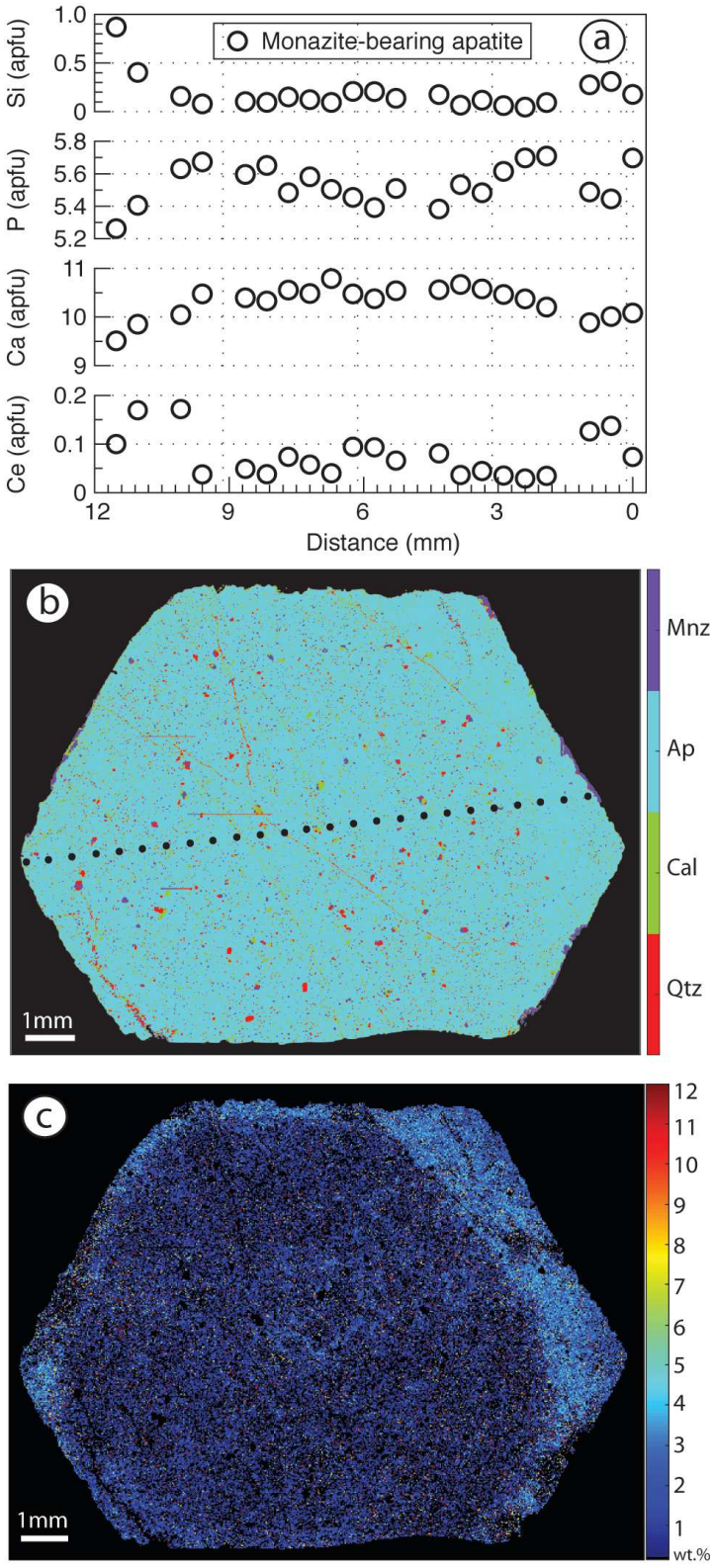

Figure III.9 a Ce, Ca, P and Si compositions in monazite bearing apatite. **b** EMP phase-map of apatite-monazite crystal from INH693 carbonatite **c** EMP cerium-map of apatite crystal from INH693 carbonatite.

Crystallographic orientation

The apatite-monazite crystal orientation map of c- axis perpendicular apatite section (1.2 cm) (INH 693, Figure III.10) clearly shows one single apatite crystal (94.6 vol.%) orientation around the c-axis (0001) (Figure III.11).

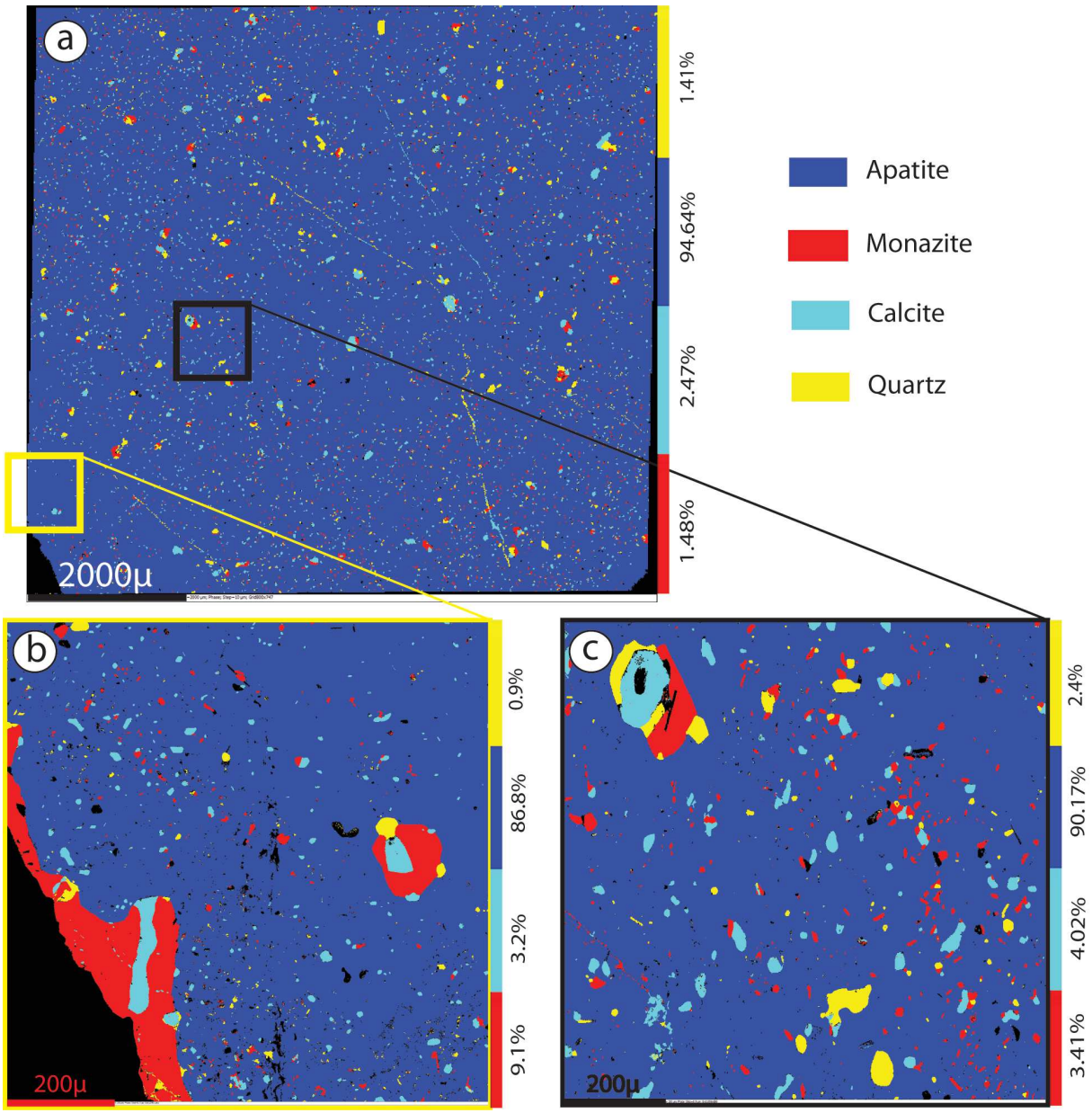

Figure III.10 EBSD- phases maps of apatite, monazite-quartz and calcite inclusions from carbonatite INH693. **a** all apatite crystal. **b** monazite rim grains zone in the apatite-rim crystal. **c** monazite inclusions in the apatite-core crystal.

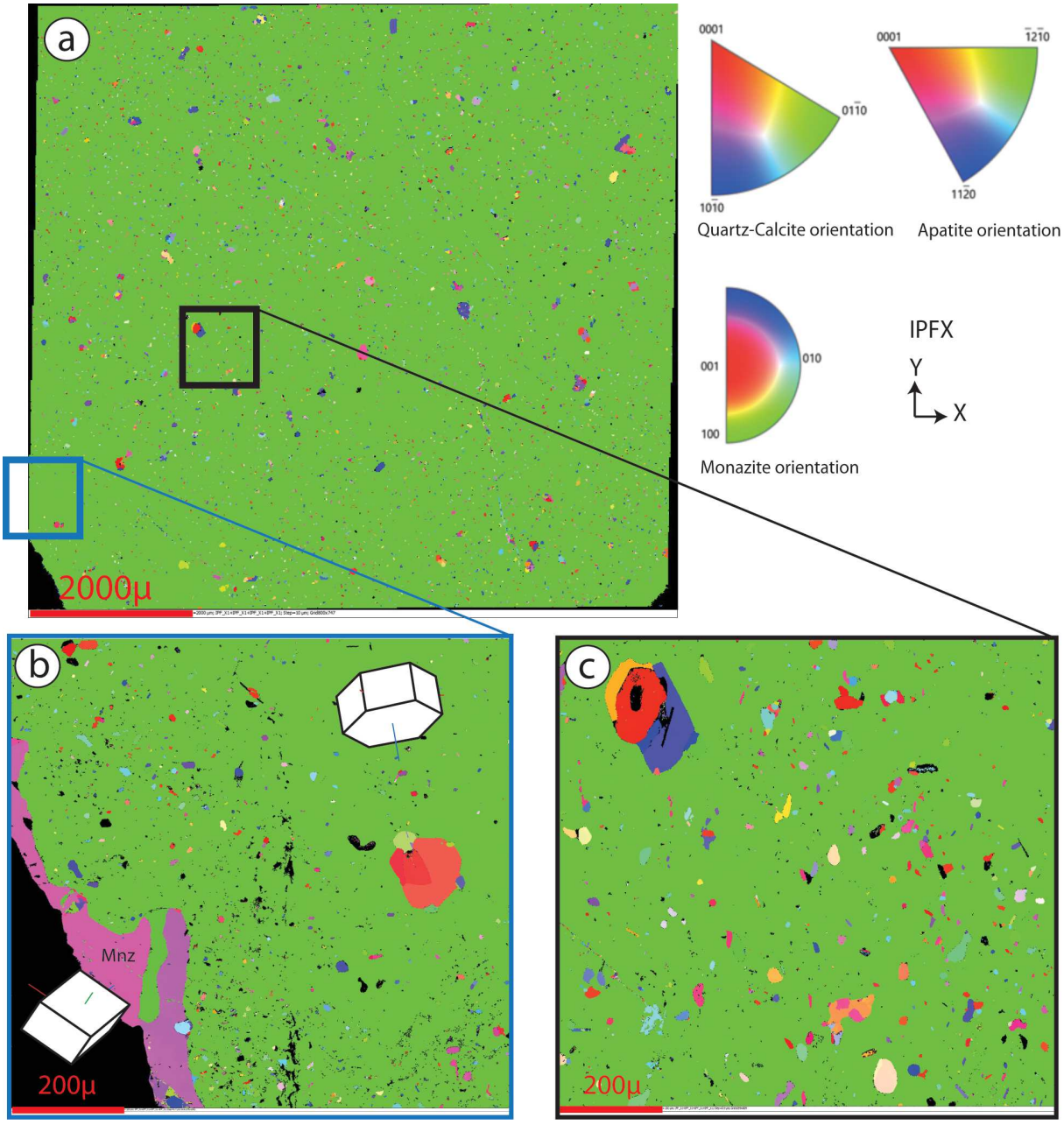

Figure III.11 EBSD- orientation maps of apatite, monazite and calcite inclusions from carbonatite INH693 along the IPFX-axis of sample reference system **a** all apatite crystal orientation. **b** monazite rim grains orientation in the apatite-rim crystal. **c** monazite inclusions orientation in the apatite-core crystal .(IPF: Inverse Pole Figure).

Monazite in apatite represents 1.48 vol.% (Figure III. 12f) and crystallized with the b axis parallel to the c axis (0001) of apatite, whereas the a- and c- axes follow the a- and m- axes of apatite (density figure, Figure III.13.f, h). Density figure for calcite (2.47 vol.%) show no preferential orientation relative to apatite or monazite crystals (Figure III.12.h) whereas quartz (1.41 vol.%) has the same axes orientation than apatite (i.e. a, c, and m axes, Figure III.12.g).

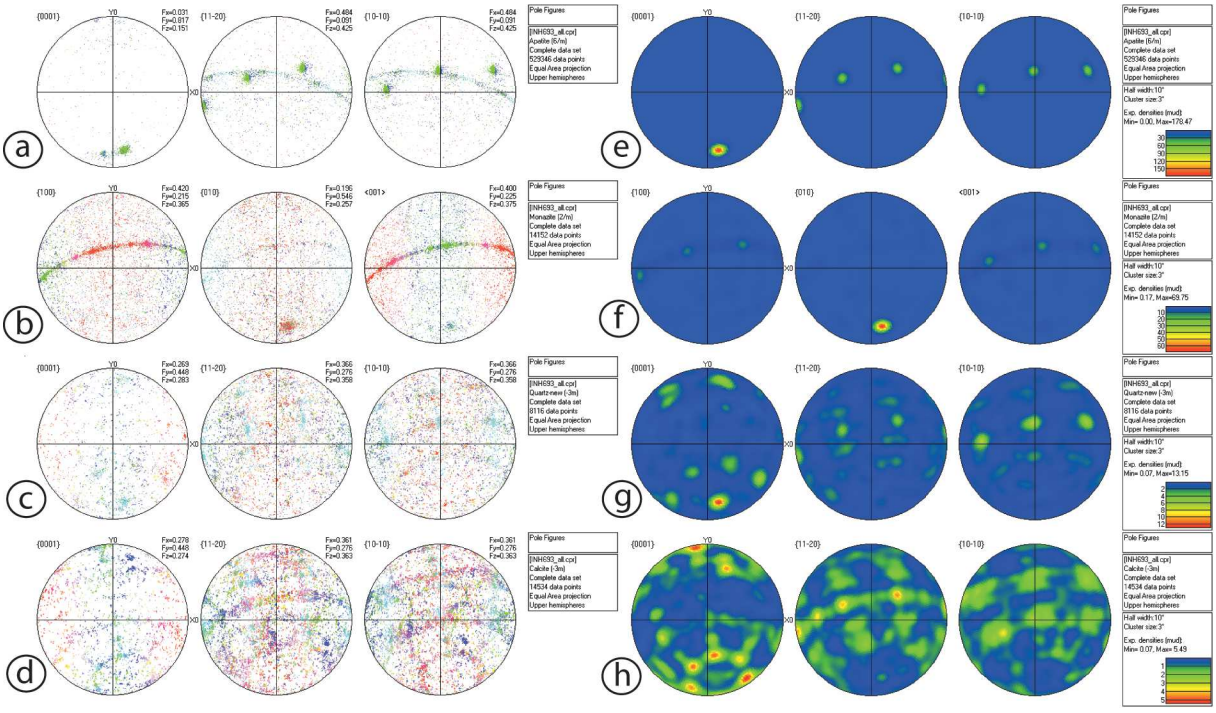

Figure III.12 Apatite-monazite-quartz and calcite crystallographic preferred orientation in pole figures. Pole figures are generated as equal-area of upper hemisphere stereographic projection of the orientation of three crystallographic axes of all crystals for each phase individually. Crystallographic orientations are plotted along IPF-X axis of sample reference system. **a** scatter plot of crystallographic axes of all apatite crystal from carbonatite INH693. **b** scatter plot of crystallographic axes of monazite in all apatite crystal. **c** scatter plot of crystallographic axes of quartz in all apatite crystal. **d** scatter plot of crystallographic axes of calcite in all apatite crystal. Contoured plots (**e, f, g, h**) with contours levels in normalized multiples of uniform distribution where relative high concentrations of axis orientation are reported in dark red. **e** all apatite crystal. **f** monazite inclusions. **g** quartz inclusions. **h** calcite inclusions.

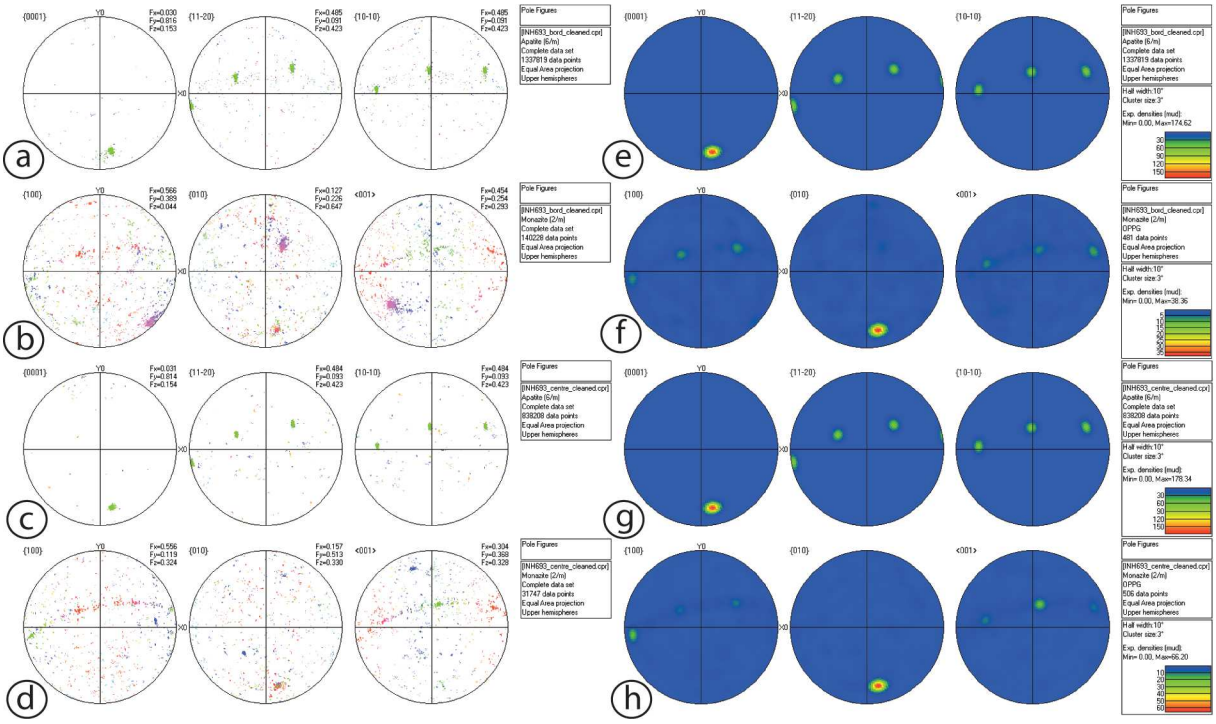

Figure III.13 Apatite-monazite crystallographic preferred orientation in pole figures. Pole figures are generated as equal-area of upper hemisphere stereographic projection of the orientation of three crystallographic axes of all crystals for each phase individually. Crystallographic orientations are plotted along IPF-X axis of sample reference system. **a** scatter plot of crystallographic axes of apatite-rim zone from carbonatite INH693. **b** scatter plot of crystallographic axes of monazite rim grains in apatite-rim crystal. **c** scatter plot of crystallographic axes of apatite in apatite-core crystal. **d** scatter plot of crystallographic axes of monazite inclusions in apatite-core zone. Contoured plots (**e, f, g, h**) with contours levels in normalized multiples of uniform distribution where relative high concentrations of axis orientation are reported in dark red. **e** apatite-rim zone. **f** monazite-rim grains. **g** apatite-core zone. **h** monazite inclusions in apatite-core zone.

III.6. Discussion

Apatites from Ihouhaouene carbonatites are remarkable by their pegmatitic size-grain, their composition and crystallization in a complex magmatic context of immiscibility and hybridization. The Ihouhaouene complex was formed from primary mantle melts generated by variable degrees of melting of carbonated heterogeneous mantle source and records high trace-element diversity. All rock facies show hybrid compositions resulting from the assemblage of minerals crystallized from distinct melt types by the segregation of both cumulus minerals (clinopyroxene, wollastonite, apatite…) and immiscible carbonate melt fractions, as well as in the concomitant chemical evolution of the silicate parental melt (Djeddi et al. 2019).

The REE concentrations in Ihouhaouene carbonatite and syenite are mainly controlled by apatite megacrysts with or without numerous REE-rich inclusions. Inclusion-free apatites are tracer of carbonate-silicate melt composition from which they crystallized, whereas inclusion-bearing apatite record magmatic crystallization and sub-solidus reactions involving possible fluid-rock interactions. REE-Th-rich britholite and monazite-quartz-calcite inclusions in apatites from Ihouhaouene carbonatite complex display chemical and textural variations through all rock facies and attest of REE redistribution and/or enrichment in primary magmatic apatites.

One important observation comparing magmatic inclusion-free apatite and inclusion-bearing apatite (britholite or monazite) is that both apatite types have similar geochemical signature suggesting that all apatites are primary magmatic phases. Si-rich apatites with and without britholite exsolutions have high Nb/Ta (Figure III.14.a) and record the hybrid characteristic of crystals during immiscibility and fractional crystallization. Likewise Si-poor apatites with or without monazite, quartz and calcite inclusions have variable Nb/Ta ratio (low and high ratio, Figure III.14.a), suggesting that they crystallized all from an evolved segregated melt.

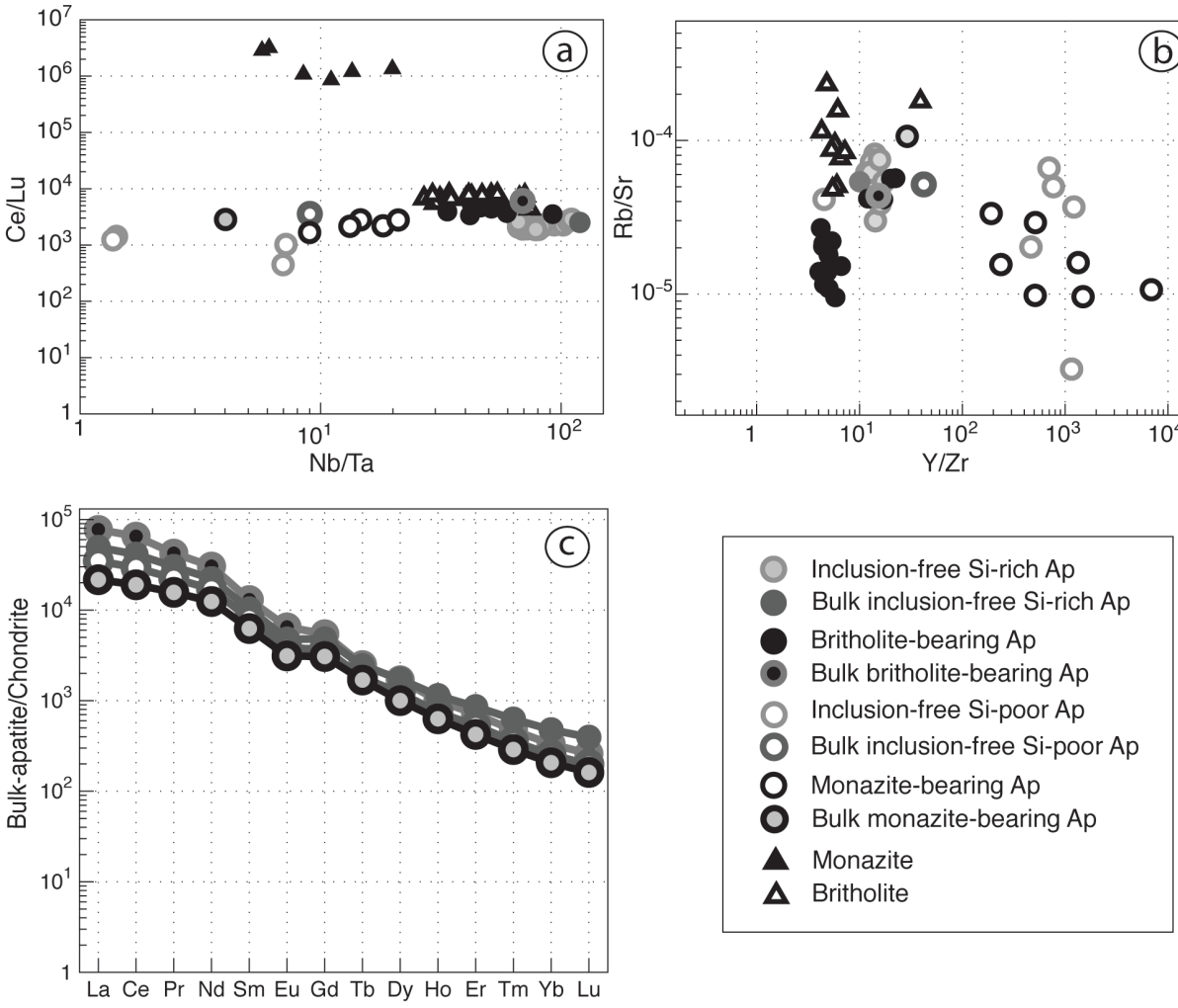

Figure III.14. Trace element compositions of free-inclusion apatites, apatite-britholite and apatite–monazite inclusions from Ihouhaouene carbonatites **a**. REE bulk-rock **b**. Ce/Lu versus Nb/Ta **c**. Rb/Sr versus Y/Zr.

III.6.a. Britholite exsolution in Si-rich apatite

Although apatites may record varying degrees of fluid-rock interaction starting from shortly after crystallization and continuing down to ambient P-T conditions (Harlov, 2018), the presence of inclusion-free apatites in Si-rich carbonatite allows estimation of apatite composition that underwent with little low temperature and fluid re-equilibration. Inclusion-free REE-Si-rich apatites are interpreted as magmatic on account of the absence of typical dissolution-reprecipitation features and their homogeneous composition therefore their high SiO_2 content indicate that they crystallized from a melt with high silica activity at magmatic conditions.

Apatite REE-evolution

The evolution of apatite composition during britholite exsolution can be estimated assuming that inclusion-free Si-rich apatite represents the composition of apatite before exsolution and

comparing in situ apatite composition both inclusion-free and britholite-bearing Si-rich apatites have high concentrations of LREEs, silica and sulphur.

They have close REE bulk apatite patterns (Figure III.14c) with slightly lower LREE in bulk britholite-bearing apatite than in bulk free-inclusion Si-rich apatite probably because of low REE rate in the primary apatite before exsolution. Incorporation of REE into apatite structure can be facilitated by several substitutions (section III.3). Ihouhaouene apatites are SiO_2 and SO_2 rich, inclusion-free Si-rich apatite has highest average SiO_2 content (5 wt.%) compare to britholite-bearing apatite (3.6 wt.%) and don't have Na_2O component owing the fact that apatite/liquid partitioning of REE enhances with increasing SiO_2 content in the magma following the substitution of P, Ca by Si and REE. All apatite analyses (inclusion-free or britholite-bearing) present a stoichiometric composition for the P-sites (6 apfu) including Si- and S- cations and Ca-sites (10 apfu) including REE-cations, calculated for 24 oxygen, indicating that REE compositions are proper during EMP analysis and the substitution mechanism considered for Si-rich apatites is following the equations (figure III.15):

$$2REE^{3+} + \text{—} = 3Ca^{2+} \qquad (1)$$

$$S^{6+} + Si^{4+} = 2P^{5+} \qquad (2)$$

and

$$REE^{3+} + Si^{4+} = Ca^{2+} + P^{5+} \qquad (3)$$

The ideal slope for REE-Si-S incorporation in apatites during the later substitution mechanisms is of (-1) (figures III.15.a). Inclusion-free and britholite-bearing Si-rich apatites are approximately consistent with equation (1) with a slope range between -0.5 and -1.5 (Figure III.15.a). They are completely coherent with equation (2) with a slope of -0.9 to -1 (figure III.15.b). The imperfect fit between measured inclusion-free and britholite-bearing apatite compositions and the ideal slope (-1) for the equation (1) may be assigned to the cation site vacancies and the high REE contents. This charge imbalance is compensated by substitution mechanism of equation (3) (Figure III.15.c). This suggests that Si^{4+} is the main responsible for charge balancing during LREEs structural incorporation in apatites. Inclusion-free apatites have higher Si- content and lower REE- content than britholite-bearing apatites and that suggest higher silica contents than REE contents in the magmatic conditions. Moreover, britholite-bearing apatites have variable to high REE contents 0.3 to 0.8 (apfu) interpreted as REE-enrichment from fluid-rock interaction.

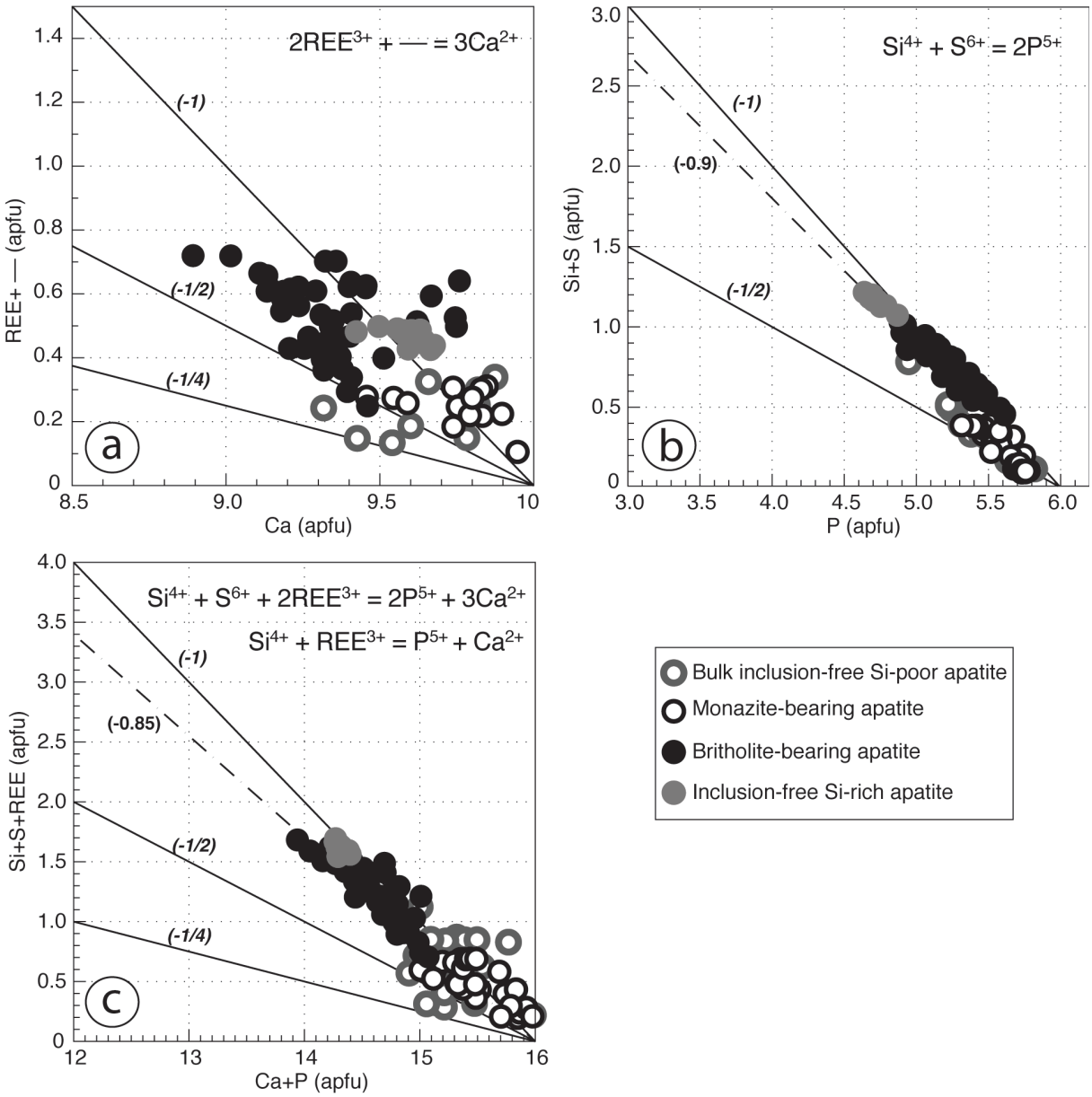

Figure III.15. REE evolution in Si-poor and Si-rich apatites from Ihouhaouene carbonatites. **a.** ∑REE versus Ca (apfu) substitution following equation (1). **b.** Si+S versus P (apfu) substitution following equation (2). **c.** Si+S+REE versus Ca+P (apfu) following equation (3) and sum of equations (1) and (2).

Britholite exsolution

According to the REE and major element content of apatite and britholite, both minerals form a solid solution between fluorapatite and britholite (Hughson *et al*. 1964; Oberti *et al*. 2001; Pan & Fleet, 2002; Ardhaoui *et al*. 2006) (Figures III.3, 4; section III.5). Exsolution reaction can result from decreasing temperature (solvus) (Torró *et al*. 2012) or changing conditions during cooling (e.g. fluid interaction, Uher *et al*. 2015; Zozulya *et al*. 2017).

For Si-rich apatite, crystallization in Si-rich carbonatite and syenite result from complex fractional crystallization and immiscibility processes that lead to hybridization. The very close composition of in situ apatite and bulk Si-rich apatite without and with inclusions (LREE/HREE fractionation (Ce/Lu= 2517 and 6057 respectively, Figure III.14.a) and the high Nb/Ta and Y/Zr ratios (Nb/Ta= 120 and 69 and Y/Zr= 15 and 10 respectively, Figure III.14.a, b) strongly suggest similar crystallization environment and apatite-britholite exsolution can be determined assuming that inclusion-free apatites are representative of magmatic apatite before britholite exsolution.

The variation of composition between apatites is less than 1 apfu for all cationic- sites and then we calculate an average representative composition to write the exchange reaction considering cationic mass balance for britholite and apatite:

Apatite + Fluid

$[(Ca_{9.6}, REE_{0.2})(Si_{0.8}, S_{0.4}, P_{4.8})O_{24}(F_2)] + 4.8\ Ca^{2+} + 4.4\ REE^{3+} + 4.8\ Si^{4+} + 24O^{2-}$ rich fluid =>

Apatite + Britholite

$[(Ca_{9.4}, REE_{0.4})(Si_{0.6}, S_{0.2}, P_{5.2})O_{24}(F_2)] + [(Ca_5, REE_{4.2})(Si_5, P_1)O_{24}(F_2)]$

The exchange reaction considering the variation britholite-bearing apatite composition shows REE-enrichment and slight deficient amount of Si for substitution and local replacement and inter-crystallization of britholite (Figure III.15). Apatite-britholite reaction implies that REE content of the primary apatite (inclusion-free) is not sufficient to allow for the precipitation of the observed amounts of britholite at the expense of apatite caused by REE-bearing fluid. Also, britholite and apatite compositions don't display an intermediate composition as observed for the thorian mineral in Oka (Illimaussaq, Canada). As a consequence, the sub-solidus reaction involved for britholite exsolution can be considered as a solvus and requires the contribution of Si-REE-rich fluid. This is supported by the crystallization of britholite in the same orientation that host-apatite suggesting that britholite-exsolutions are topotactic and precipitate by an oriented fluid reaction (Pan, 1993).

The transportation of these elements into fluids, particularly REE, has been proposed as complexes. Ligands may be CO_3^{2-} (Balshov et al., 1975), PO_4^{3-}, F^-, Cl^- (Mineyev, 1963; Kapustin, 1966; Flynn & Burnham, 1978, Harlov et al., 2002a; Harlov & Forster, 2003). For Si-rich apatite, the high Cl, Th and U in britholite compare to the host apatite corroborate the presence of saline fluid during cooling and re-equilibration at subsolidus conditions.

III.6.b. Apatite and monazite-quartz-calcite inclusions

The REE-Si-poor-apatites are magmatic and crystallized from the segregated CO_2-rich melt from an evolved SiO_2-CO_2-rich melt (Djeddi *et al*. 2019). The low silica and REE content of Si-poor apatites are interpreted as magmatic because of the absence of typical dissolution-reprecipitation features and indicate that they crystallized from a melt with low silica activity at magmatic conditions.

Apatite-REE evolution

The evolution of apatite composition during fluid-rock interaction and monazite-calcite-quartz inclusions precipitation can be estimated assuming that inclusion-free Si-poor apatite represents the composition of apatite before fluid-apatite re-equilibration and comparing in situ apatite composition, both inclusion-free and monazite-bearing Si-poor apatites have low LREEs and silica contents and high sulphur contents (Figure III.15). They have close REE bulk apatite patterns (Figure III.14.c) with slightly lower LREE in bulk monazite-bearing apatite than in bulk free-inclusion Si-poor apatite probably because of fluid leaching or the low REE contents of the primary apatite before fluid-rock interaction.

As seen for Si-rich apatites incorporation of REE into apatite structure can be facilitated by the 1-3 substitution mechanism equations (section III.6.a). Inclusion-free apatites in Ihouhaouene Si-poor carbonatites are SiO_2 poor and SO_2 rich owing the fact that REE apatite/liquid partitioning decrease with decreasing SiO_2 content in the magma.

The ideal slope for REE-Si-S incorporation in apatites during substitution mechanisms (1-3) is of (-1) (figures III.15.c). Inclusion-free and monazite-bearing Si-poor apatites are approximately consistent with equation (1) with a slope between -0.25 and -1.5 (Figure III.15.a). They are completely coherent with equation (2) (Figure III.15.b) with a slope ranges from -0.5 to -1. The imperfect fit between measured inclusion-free and monazite-bearing apatite compositions and the ideal slope (-1) for the equation (1) may be attributed to the cation site vacancies in the Ca-sites because of the low REE contents and the high S cations in P-sites. This charge imbalance is not compensated by substitution mechanism of equation (3) (Figure III.15.c). This suggests that S is the main responsible for charge balancing during LREEs structural incorporation in Si-poor apatites considering the low Si^{4+} in the Si-poor apatite structure. Inclusion-free Si-poor apatites and monazite-bearing apatites have both variable REE contents (0.1-0.4 apfu) with the low content recorded in monazite-bearing apatites (Figure III.15.a) and suggest that REE- rich monazite contents derived at the expense of apatite by local dissolution and mineral replacement at sub-solidus conditions. Moreover, monazite-bearing apatites have slightly lower Si content than inclusion-free Si-poor apatites and suggest apatite Si-leaching probably in favour of quartz precipitation.

Monazite-quartz-calcite crystallization in apatite

The presence of quartz and calcite as inclusions in Si-poor apatite strongly suggests sub-solidus reaction and the presence of Si-CO_2-bearing supergene fluids. Otherwise, the high content of sulfur in monazite (1.7 wt.% S) compared to sulfur content in hosted-apatite and inclusion-free apatites argue for the presence of sulfur-bearing fluid or sulphur transfer from precursor Si-poor apatite (Figure III.3.d, section III.5).

The composition of bulk apatite mineral displays similar REE concentration for apatite without and with inclusions (LREE/HREE fractionation (Ce/Lu= 3575 and 2842 respectively, Figure III.14.a) and the low Nb/Ta and high Y/Zr ratios (Nb/Ta= 9 and 4 and Y/Zr= 42 and 29 respectively, Figure III.14.a, b) infer similar crystallization environment and apatite-monazite-quartz-calcite inclusions can be determined assuming that inclusion-free apatites are representative of magmatic apatite before monazite-quartz-calcite crystallization.

However, Si-poor apatites have a wide range of Nb/Ta and Ce/Lu composition as a signature of magmatic processes (fractional-crystallization and immiscibility from evolved CO_2-Si- rich melts) and that prevent us from going-back to the real composition of each apatite before fluid-interaction.

Although EMP element-map of apatite-monazite crystal displays high Ce and Si concentrations at the rim and the core of apatite crystal and the presence of a partial dissolution/crystallisation at the middle, the homogeneous distribution of monazite-quartz-calcite in apatite crystal suggest that re-equilibration is not only related to apatite dissolution (Pan *et al*. 1993; REF Harlov, 2015) but rather to fluid-assisted re-equilibration.

This is corroborated by homogeneous monazite composition for major and trace element compositions at the rim and the core of apatite. Furthermore, monazite and host apatite and inclusion-free apatite have identical Nb/Ta ratios (Figure III.14.b) suggesting that monazite inclusions precipitation during fluid –assisted re-equilibration doesn't fractionate the Nb/Ta ratio and started from shortly after crystallization at sub-magmatic conditions.

The presence of quartz and calcite with monazite involved high SiO_2 and CO_2 activity during sub-solidus conditions. On account of the lower Si-composition of monazite-bearing apatites than inclusion-free Si-poor apatites we consider fluid leaching and the mineral assemblage can be represented by the following reaction proposed by Pan *et al*. (1993):

apatite (1) + (Ca^{2+}, P^{5+}, C, O^{2-}) in fluid ➔ apatite (2) + monazite+ quartz+ calcite

$[(Ca_{5-x}, REE_x)\ (P_{3-x}, Si_x)O_{12}\ (F, Cl, OH)] + 2(x-y)Ca^{2+} + 2(x-y)P^{5+} + 9(x-y)O^{2-}$ ➔ $[(Ca_{5-y}, REE_y)\ (P_{3-y}, Si_y)O_{12}\ (F, Cl, OH)] + (x-y)\ REEPO_4 + (x-y)\ SiO_2 + (x-y)CaCO_3$, $(x > y)$.

However, according to cationic mass balance between apatite, monazite, quartz and calcite in Si-poor apatite from Ihouahouene, the reaction needs to be adjusted. Following the low proportions (1.48% monazite, 2.47 % calcite, 1.4% quartz, Figure III.10 see results section) of this mineral assemblage in apatite, S and REE contents in monazite can derived from the primary apatite considering the high sulphur contents in Si-poor inclusion-free apatites and the close REE-bulk compositions of Si-poor apatites.

The stoichiometric composition of all apatite analyses (inclusion-free or monazite-bearing) presents a close composition for the P- and Ca-sites. The variation of average composition between apatites is less than 1 apfu for all cationic- sites, thus monazite-quartz-calcite inclusions precipitate essentially from Ca-P-CO_2 sub-magmatic fluids:

Apatite + Fluid

$[(Ca_{9.8}, REE_{0.2})(Si_{0.3}, S_{0.2}, P_{5.4})O_{24}(F_2)] + [0.2\ Ca^{2+} + 0.1\ C^{4-} + 0.1\ P^{5+} + 0.9\ O^{2}]$ fluid =>

Apatite + Monazite + quartz + calcite

$[(Ca_{9.9}, REE_{0.1})(Si_{0.2}, S_{0.1}, P_{5.7})O_{24}(F_2)] + 0.1\ (REE, S)PO_4 + 0.1\ SiO_2 + 0.1\ CaCO_3$

During the exchange reaction Si and REE are preferentially removed out of the apatite and system (Harlov, 2015). The mass transfer of REE, Si and S between apatites assisted by fluid transfer can be sufficient in concentrations for nucleation and inter-crystallization of monazite, quartz and calcite. This is further supported by the crystallization of subhedral monazite elongated (b-axis) parallel to the orientation of host-apatite (c-axis) suggesting an epitaxial relationship and precipitate by an oriented fluid reaction (Pan, 1993; Harlov, 2015). Likewise, the reacted apatites display the same crystallographic orientation over all the crystal suggesting fluid-assisted re-equilibration after a weak dissolution-precipitation at subsolidus conditions.

III.6.c. Fluid-rock interaction and REE enrichment reaction

Rocks Rocks undergo re-equilibration with fluids in various environments rising mineral replacement reactions. Replacement reactions commonly take the form of fluid-aided, coupled dissolution-precipitation and frequently result in pseudomorph formation (Wladyslaw et al., 2016).

The difference in Ihouhaouene apatite REE-composition consists in the fact that they crystallized from Si-rich and Si-poor magmas and the composition of magmatic apatite plays also a key role during subsolidus reaction and re-equilibration and the crystallization of REE-minerals. The REE distribution and bulk-REE patterns recorded by Ihouhaouene Si-rich and Si-poor magmatic apatites are completely coherent with experimental studies of Watson & Green (1981) and Hammouda *et al*. (2010) that explain the increase of REE apatite-melt partitioning with increasing silica activity.

The close spatial association of apatite-britholite and apatite-monazite in Ihouhaouene carbonatite indicates similar cooling environment (T, P) and a strong control of initial apatite

composition on REE-equilibration (Si-rich and Si-poor apatite). The presence of hydrothermal fluid and percolation can considered as local fluid-rock interaction, more or less enriched in Si- and CO_2 related to the silica and carbonate affinity of the Ihouahouene magmatic complex:

- Si-REE-rich apatites crystallized under high magmatic silica activity and further cooling with Cl-Th-REE-rich fluid induced exsolution of britholite and REE-enrichment in apatite, and
- Monazite-quartz-calcite inclusions are formed during S-Si-REE mass transfer by Ca-P-CO_2-rich fluid-assisted and apatite re-equilibration at sub-magmatic conditions.

The volatile components in inclusion-free apatites and inclusion-bearing apatites can be a tracer of temperature at magmatic and sub-magmatic conditions. Britholite and monazite can both crystallize at high temperature conditions. Cl and Th in fluid inducing britholite exsolution indicate an elevated temperature at sub-solidus conditions (Piccoli & Candela, 1994, 2002). The high S-contents in magmatic inclusion-free Si-poor apatite and the rich-S monazite inclusion can be explained by the late stage oxidation of the residual carbonatitic melt and by degassing at magma late-stage and sub-magmatic fluid-rock re-equilibration (Burgisser & Scaillet, 2007). That attests of distinct apatite compositions at magmatic conditions (Si-rich and Si-poor) and different sub-magmatic conditions controlling fluid-rock interaction.

III.6.d. Britholite and monazite: sub-magmatic minerals before REE-oxides crystallization?

The distribution of REE in minerals is a useful geochemical and petrogenetic tracer of igneous crystallization and sub-solidus re-equilibration. The Ihouhaouene alkaline site represents an important step between magmatic and metamorphic processes. The presence of REE-bearing mineral such as britholite and monazite attests of little fluids-rock interaction and re-equilibration during metamorphic episode, whereas most of carbonatite underwent complex and multistage history of REE-deposition and enrichment (e.g. ore-deposits at Bayan Obo and Mountain Pass, Smith *et al*. 2000; Castor, 2008).

In most ore-deposit carbonatite, further sub-solidus reaction and hydrothermal remobilization of trace elements lead to trace element remobilization and crystallization of REE-oxides (Wei *et al*. 2017). The most important REE-mineral is bastnasite, a REE-carbonate mineral ($REECO_3F$), which attests of the presence of LREE-CO_2-F-rich fluids (Wei *et al*. 2017). The Mountain Pass, California (Mariano & Mariano Jr, 2012) and Bayan Obo, China (Smith *et al*. 2000) ore deposits have bastnäsite associated with monazite. These deposits are the two largest sources of cerium, yttrium and other light-rare-earth elements (Smith *et al*. 2000; Castor; 2008; Yang *et al*. 2011; Mariano & Mariano Jr, 2012; Wei *et al*. 2017).

Previous studies have noted variations in the distribution of the REE in LREE-enriched monazite and bastnasite, and attempted to relate this to the formation environment of late-magmatic

and/or hydrothermal origin (Fleischer, 1965; Fleischer, 1978; Fleischer & Altschuler, 1969; Smith *et al*. 2000). Such deposits have also received much attention because of their potential act as indicators of hydrothermal fluid source, chemistry and processes (Smith *et al*. 2017 and references in).

Monazite is a common REE-phosphate associated to apatite as are the result of coupled dissolution–reprecipitation processes during the metasomatic alteration of apatite and can form over a wide P–T range, starting at near-surface pressures and 100 °C (Harlov, 2005; Putnis 2009; Harlov, 2015 and references in). In Ihouhaouene apatites monazite can growth at sub-magmatic high P-T conditions and at low P-T conditions during carbonatite exhumation and fluid-apatite re-equilibration. The REE contents of magmatic Si-poor apatites are high enough to account for the formation of the observed amounts of monazite inclusions.

Only few occurrences of britholite have been reported in the literature. Uher *et al*. (2015) and Giebel *et al*. (2017) reported britholite occurrences in the Palabora carbonatite complex in South Africa as linked to late-magmatic crystallization or sub-solidus alteration of primary minerals (forsterite) by late magmatic to hydrothermal fluids. Britholite is mostly described from nepheline syenites and contact metasomatic deposits and generally forms during hydrothermal processes related to the replacement of apatite or monazite (Budzyń et al. 2011; Uher *et al*. 2015; Zirner *et al*. 2015; Gibel *et al*. 2017). Likewise, britholite has been described as a low-temperature phase (e.g. The Virulando carbonatite, Angola) and formed during late-stage supergene alteration processes (Torró *et al*. 2012). Generally, britholite is assumed to have a late stage to post-magmatic origin for most occurrences (Wall et al. 993; Uher et al. 2015; Gibel *et al*. 2017). In Ihouhaouene carbonatites, britholite exsolutions occur by apatite replacement and the mass-balance considerations imply that the REE content of both precursor apatite and britholite-bearing apatite are high and depend of the silica activity in magmas and at late-crystallization stages. Thus we suggest that the britholite exsolution following several apatite substitutions was caused by late carbonatitic REE-bearing fluid at low P-T sub-magmatic conditions.

Evidences de magmatisme et de métamorphisme contemporains dans les carbonatites et syénites d'Ihouhaouene au Nord-Ouest du terrane de l'In Ouzzal à l'Eburnéen : datations U-Pb in situ effectuées sur apatite et zircon

Ce chapitre inclut une étude géochronologique préliminaire des complexes alcalins d'Ihouhaouene à partir des dations U-Pb in situ sur apatite et zircon dans les carbonatites et les syenites afin de déterminer l'âge de cristallisation de ces roches et comprendre leur mise en place durant l'évènement tectono-métamorphique régional de l'In Ouzzal à l'éburnéen.

U-Pb dating of apatite and zircon in carbonatite and alkaline rock complex (Ihouhaouene, In Ouzzal terrane, Western Hoggar)

A. Djeddi[1,2*], K. Ouzegane[2], F. Parat[1], J.-L. Bodinier[1,3], M. Poujol[4], M. J. R. Alpiste[5], C. Garrido[5], R. Lafay[1]

[1] Géosciences Montpellier, UMR 5243, CC60, Université de Montpellier, Place Eugène Bataillon, 34095 Montpellier cedex 5, France

[2] FSTGAT-USTHB, BP32, El Alia 16111 Bab Ezzouar, Algeria

[3] Geology & Sustainable Mining Program, UM6P, Hay Moulay Rachid, Ben Guerir, Morocco

[4] Géosciences Rennes, UMR CNRS 6118, Université de Rennes 1, OSUR, Campus de Beaulieu, 35042 Rennes Cedex, France

[5] Instituto Andaluz de Ciencias de la Tierra (IACT), CSIC & Universidad de Granada, Avenida de las Palmeras 4,18100 Armilla, Granada, Spain.

*E-mail : asma.djeddi@gm.univ-montp2.fr

Abstract

Apatite and zircon grains from Precambrian carbonatites and syenites from Ihouhaouene (In Ouzzal terrane, NW Hoggar) were studied by geochemical and in-situ isotope methods. Apatite and zircon were identified combining microscopic surveys of thin sections of the carbonatite and syenite rocks (optical microscopy, optical microscopy combined with cathodoluminescence (OM–CL), scanning electron microscopy and EPMA mapping). All apatite studied samples display no evidence for alteration processes caused by late-stage infiltration of fluids. Whereas, zircons show chemical Hf and Y zoning possibly caused by the late-stage carbonatite melts and that result in different changes in the geochemistry and isotope composition of zircon regions. For Ihouhaouene carbonatites, in-altered apatites display different rim and core ages between 1808 and 2020 Ma, respectively and indicate a high diffusion temperatures and slow cooling for carbonatites. All carbonatitic zircons (1941 Ma) are magmatic and their Th/U ratios are high and depend of melt composition and equilibrium with Th-U-rich minerals as apatite and monazite and suggest an intermediate to felsic melt source.

For the 2100 Ma old associated syenites, zircon grains recorded different U-Pb ages between core and rims that couldn't be observe by SEM. The solid state recrystallization of zircon occurred mainly in account of immiscibility-hybridization processes as consequence of combining isotope information from distinct magmatic events and simultaneous granulitic metamorphism in the In Ouzzal and that led to diffusion driven loss and gain of Th and U, high disturbance of the U–Pb system and low CL intensities in such zircon domains. Otherwise, apatites from syenite underwent a late stage Pan-African fluids interaction and recorded the thermic alkaline granites emplacement in Ihouhaouene region at 651 Ma that represent the carbonatite exhumation age previously recognized by fission track.

IV.1. Introduction

Carbonatites are low degree carbonate-rich melts that derived from the mantle. The formation ages of carbonatites span a time period of 3 Ga with an increasing abundance towards more recent times (Tichomirowa et al. 2013; Rukhlov and Bell, 2010). The oldest known carbonatite were formed in the Archaean period in the Tupertalik, western Greenland (Bizzarro *et al*. 2002) whereas the youngest carbonatite is the presently active volcano Oldoinyo Lengai in the East-African Rift system (Dawson, 1962; Bell & Keller, 1995; Baudouin *et al*. 2016).

Most of the known carbonatite occurrences are situated in anorogenic settings related to intracontinental rifting (Xu *et al*. 2014). Collision-related or post-collisional carbonatites as Ihouhaouene carbonatites (In Ouzzal terrane, Western Hoggar, Algeria) are much rarer (Tilton *et al*. 1998; Hou *et al* 2006; Chakhmouradian *et al*. 2008).

The study of isotope systems of such rocks as Ihouhaouene carbonatites supply useful information on the composition of the mantle and his evolution during time, owing to their isotopic characteristics generally inherited from the mantle source on account of the initially high concentrations of Sr and rare-earth elements (REE) in carbonatitic magmas (Nelson et al. 1988; Xu et al. 2014) and their rapid ascent to the surface (Treiman, 1989). Carbonatite melts could cause significant changes to the sub-continental mantle by the carbonatite metasomatism (Dupuy *et al*. 1992). Nevertheless, carbonatite rocks are themselves susceptible to secondary alteration processes that can disturb their primary isotope composition (Deines, 1989; Demeny et al. 2004a; Tichomirowa et al. 2013*;* Xu et al. 2014). They are often affected by alteration processes such as interaction with water fluids (weathering), degassing of CO_2 (Rayleigh fractionation processes) and further sub-solidus re-equilibration processes (Deines, 1989; Demeny et al. 2004a; Tichomirowa et al. 2006; Tichomirowa et al. 2013*;* Xu et al. 2014).

Carbonatites contain several minerals enriched in U and (or) Th such as baddeleyite, monazite, zircon, apatite, zirconolite, perovskite, and pyrochlore that make therefore a precise age determination of these rocks using the U-Pb method (Amelin & Zaitsev, 2002). However, enrichment in U, Th and their decay products causes deviation from the secular radioactive equilibrium in growing minerals that results over time in the excess or deficiency of radiogenic Pb isotopes (Amelin & Zaitsev, 2002).

Ihouhaouene carbonatites are associated to alkaline syenites and only carbonatites were previously dated on zircon and apatite grains by ID- TIMS that record an eburnean age of 2 Ga (Bernard-Griffiths et al. 1988; Allègre *et al*. 1972). The age of syenites is unknown; therefore, our primary objective is to explain both the geochemical and structural relations of the Ihouhaouene alkaline rocks and confirm their Eburnean age (2Ga) by LA-ICPMS on in situ minerals.

At present, we studied apatite and zircon formed as a primary minerals from Precambrian carbonatite complex from Ihouhaouene, In Ouzzal (2 Ga). These carbonatites were partially studied

for their mineral isotope composition (O, C, Rb–Sr, Sm–Nd) and their age (U-Pb on zircon). Their cogenetic origin is always disputed in the literature.

Zircon was chosen for U-Pb investigations because of its physical and chemical resistance to alteration processes (Cherniak & Watson, 2001) and inclusion-free apatites representative of magmatic apatite is the most U-bearing mineral available to date carbonatites when zircon is not present. The aim of U-Pb dating of apatites and zircons from Ihouhaouene carbonatites and syenites is to develop alternative models of carbonatite petrogenesis and magmatic to post magmatic processes in syn-metamorphic orogenic settings that will explain both the structural relations with the associated syenites and granulitic host-rocks and unusual isotopic signatures of the Ihouhaouene rocks. In a broader context, interpretation of the geodynamic evolution of the Ihouhaouene area resulted from isotopic data is important to clarify the tectonic history of In Ouzzal terrane.

IV.2. Geological setting

Ihouhaouene Carbonatites and syenites intrude the In Ouzzal granulite host rocks. The In Ouzzal terrane (Western Hoggar) is an example of Archaean crust (Ferrara & Gravelle, 1966; Lancelot *et al*. 1976; ben Othman *et al*. 1984; Rousseau *et al*. 1995) remobilized during a very-high-temperature metamorphism related to the paleoproterozoic orogeny (2 Ga) (Ferrara & Gravelle, 1966; Allègre & Caby, 1972) and characterized by prograde evolution at high pressures (800–1050ºC at 10–11 kbar) followed by an isothermal decompression (9–5 kbar) (Ouzegane *et al*. 2003) (Table IV-1).

The Ihouhaouene carbonatites and associated syenites have a close field relationship and present a cogenetic relationship from their petrological and geochemical features (Djeddi *et al*. 2019). A geochemical model of their petrogenesis by immiscibility and fractional crystallization and hybridization is developed in the Chapter II (Djeddi *et al*. 2019).

Previously published isotopic studies of Ihouhaouene carbonatites, identified a high Sr and low Nd initial ratios ($^{87}Sr/^{86}Sr \approx 0.709$ and $\varepsilon Nd_{(T)} \approx$ -6.4 to –8.6 with T_{DM} = 3.3 -2.7 Ga) characterized an enriched Archaean source (Bernard-Griffiths et al. 1988; Fourcade et al 1996); The O and C stable isotope data ($\delta^{13}C$ = –3.5 to –9.7 ‰; $\delta^{18}O$ = +7.6 to +15.5 ‰) suggest these features reflect contamination of the hypothetical mantle derived magmatic carbonatites by the Archaean crust (Ouzegane *et al*. 1988).

Few works have been realized on the geochronology of Ihouhaouene carbonatitic complex. The U-Pb hydroxyapatites (2090 Ma; Allègre *et al*. 1972) and zircons (1994± 22–17 Ma; Griffiths *et al*. 1988) ages (ID TIMS) obtained from carbonatites show that the emplacement of syenite-carbonatite complex is syn-Eburnean and is synchronous of granulitic metamorphic event (2000 – 1800 Ma; Ouzegane *et al*. 2003 and references in) (Table IV-1). Ihouhaouene carbonatites were interpreted as syn-granulitic rised up by the upwelling of the asthenospheric mantle during the eburnean (2000-1800 Ma) metamorphism of the In Ouzzal terrane (Ouzegane *et al*. 2003). The apatite

fission-track study of Carpena *et al*. 1988 on apatites from Ihouhaouene carbonatites exposed the low temperature thermal history of the Archaean unit of In Ouzzal and reveals that apatites have recorded the Pan-African orogeny event (500-630 Ma; 100-120ºC) (Table IV-1).

Table IV.1: Summary of previous geochronological and stable isotopes data about the In Ouzzal granulites and Ihouhaouene carbonatites and syenites (Griffiths *et al*. 1988; Ouzegane *et al*. 2003):

Authors	**Method**	**Age**
Granulite		
Ferrara & Gravelle (1966)	Rb-Sr Whole rock isochron Biotites	2995±50 Ma >1830–1910 Ma
Allegre & Caby (1972)	Rb-Sr and K-Ar (minerals)	1860 Ma
Rousseau *et al*. 1995	U-Pb zircons	3500–3100 Ma; 2000 Ma
Lancelot *et al*. 1976	U-Pb zircons	3100–2900 Ma; 2050 Ma
ben Othman *et al*. 1984	Sm-Nd model ages	3473–3123 Ma
Carbonatite		
Allegre *et al*. 1972	U-Pb-Th on hydroxyapatite	2090 Ma
Carpena *et al*. 1988	Apatite Fission-tracks	≈ 600 Ma
Griffiths *et al*. 1988	U-Pb zircons	1994± 22–17 Ma
Carbonatite and syenite		**Isotopes**
Ouzegane *et al*. 1988	C-O on calcite	$\delta^{18}O$ = -7.6 to 10.3‰; $\delta^{13}C$ = -6 to -9.7‰
Bernards-Griffiths *et al*. 1988	Sr-Nd whole rock	εNd(T)= -6.4 to – 8.6; Isr(T) = 0.7097
Fourcade *et al*. 1996	Sr-Nd Whole rock, C-calcite, O- Cpx	εNd(T)= -8.5 ; Isr(T) = 0.7095; $\delta^{18}O$ = 6.9 to 8‰; $\delta^{13}C$ = -3.5 to -9.7‰

IV.3. Instrumentaion and analytical methods

For zircons, we analysed the carbonatitic and syenitic thin sections by scanning electronic microscopy combined with cathodoluminescence (SEM–CL) to identify all zircons with up to 20 μm size on thin section samples. Optical microscopy combined to cathodoluminescence (OM-CL) was applied on apatite in carbonatite and syenite thin sections to understand the CL colours changes caused by alteration processes. Then, in-situ isotope U–Pb analyses from zircons and apatites were performed to characterize both primary and secondary signatures of carbonatite and syenite.

IV.3.a. EPMA in situ zircon analysis for major elements

The major element concentrations in zircons from carbonatite IC2-9A and syenite IC2-6A were measured by electron microprobe (Cameca SX100 at the Microsonde sud, University of Montpellier, France). Operating conditions used are: acceleration voltage of 20 kV, beam current of 100 nA and a beam focalized (1 μm). Background counting time of 10min for all elements: 30 s for each major element and Y, Yb, Hf and 40 s were applied. The internal standards chosen for each

element were: andradite for Ca, Fe and Si, TiO_2 for Ti, $ZrSiO_4$ for Zr, Cl-apatite for P, ThO_2 for Th, $Yb_3Fe_5O_{12}$ for Yb, HfO_2 for Hf, UO_2 for U, enriched glass REE3 for Ce and YIG for Y. Distribution of five major elements (Hf, Si, Th, U, Ce) within zircon crystals was characterized by collecting WDS X-ray element maps with a step size of 0.4 to 3 μ according to the crystal dimensions.

IV.3.b. Apatite U-Pb dating

U-Pb apatite geochronology was performed by laser ablation (LA-ICP-MS) on thick sections at Rennes Geosciences using a ESI NWR193UC Excimer laser inductively coupled to an Agilent 7700x Quadripole plasma mass spectrometer ICP-MS. The detailed analytical procedures are described in the table IV.2. Optical Microscopy Cathodoluminescence (OM-CL) images using a Reliotron CL system equipped with a digital colour camera available at Rennes Geosciences were performed on the analysed apatites in order to verify the homogeneity of the crystals and avoid any inclusion contamination. The analyses consisted of 20s background measurement followed by 60s integration time, then 15 seconds wash-out delay time to clean out the previous sample. A 40 µm ablation beam diameter with 7 Hz repetition rates were used. Instrument and mass calibrations were carried out before each analysis session on the NIST SRM 612 reference glass, inspecting the 238U signal and minimizing the ThO^+/Th^+ ratio (<0.5%). During the ablation analysis, the signals of the masses 43Ca, 204 (Pb + Hg), 206Pb, 207Pb, 208Pb and 238U are acquired. Signal 235U is calculated from 238U based on the ratio 238U/235U=137.88. The apatite standards used as internal references for apatite analyses are Madagascar (ID-TIMS age of 473.5 ± 0.7 Ma, Cochrane *et al*. 2014), Durango (31.44 ± 0.18 Ma, McDowell *et al*. 2005) and McClure (523.51 ± 2.09 Ma, Schoene and Bowring 2006). The data were corrected for U-Pb fractionation and for mass bias by repeated measurements of the Madagascar apatite standard. Durango and McClure apatite standard measurements were treated as external references and used to control the reproducibility and accuracy of corrections. They provided 207Pb corrected ages of 32.27 ± 0.70 Ma (MSWD = 0.44, probability = 0.98) and 527.2 ± 5.6 Ma (MSWD = 0.21, probability = 0.99) during the analyses, respectively. Data processing was performed using Igor Pro Iolite software (Paton *et al*. 2010) with the data reduction scheme VizualAge_UcomPbine set (Chew *et al*. 2014). This data treatment consists of a correction of the common Pb using the 207Pb method for the initial Pb isotope composition specified in the reference values of the Madagascar standard. Thus the fractionation curve 207Pb / 235U is adjusted with a correction of the common Pb based on 207Pb using an initial 207Pb/206Pb value of 0.8681 (Cochrane *et al*. 2014).

Table IV.2: Operating conditions for the LA-ICP-MS apatite analysis

Laboratory & Sample Preparation	
Laboratory name	Géosciences Rennes, UMR CNRS 6118, Rennes, France
Sample type/mineral	Apatite
Sample preparation	Thin sections
Imaging	Optical Microscopy Cathodoluminescence (OM-CL)
Laser ablation system	
Make, Model & type	ESI NWR193UC, Excimer
Ablation cell	ESI NWR TwoVol2
Laser wavelength	193 nm
Pulse width	< 5 ns
Fluence	6 J/cm^2
Repetition rate	5Hz
Spot size	40 μm
Sampling mode / pattern	Single spot
Carrier gas	100% He, Ar make-up gas and N2 (3 ml/mn) combined using in-house smoothing device
Background collection	20 seconds
Ablation duration	60 seconds
Wash-out delay	15 seconds
Cell carrier gas flow (He)	0.75 l/min
ICP-MS Instrument	
Make, Model & type	Agilent 7700x, Q-ICP-MS
Sample introduction	Via conventional tubing
RF power	1350W
Sampler, skimmer cones	Ni
Extraction lenses	X type
Make-up gas flow (Ar)	0.85 l/min
Detection system	Single collector secondary electron multiplier
Data acquisition protocol	Time-resolved analysis
Scanning mode	Peak hopping, one point per peak
Detector mode	Pulse counting, dead time correction applied, and analog mode when signal intensity > ~ 10^6 cps
Masses measured	^{204}(Hg + Pb), ^{206}Pb, ^{207}Pb, ^{208}Pb, ^{232}Th, ^{238}U + ^{43}Ca (Ap)
Integration time per peak	10-30 ms
Sensitivity / Efficiency	23000 cps/ppm Pb (50μm, 10Hz)
Data Processing	
Gas blank	20 seconds on-peak
Calibration strategy	Madagascar apatite standard used as primary reference material, McClure and Durango standards used as secondary reference material (quality control)
Common-Pb correction, composition and uncertainty	No common-Pb correction.
Reference Material info	Madagascar (Cochrane *et al*. 2014) McClure (Schoene & Bowring 2006) Durango (McDowell *et al*. 2005)
Data processing package used	Iolite (Paton *et al*. 2010), VizualAge_UcomPbine (Chew *et al*. 2014) More information on the procedure in Pochon *et al*. 2016
Quality control / Validation	McClure: 526 ± 4 Ma (N=19, MSWD=0.2 ; probability=1.0) Durango: 32 ± 0.6 Ma (N=25, MSWD=0.8 ; probability=0.8)

IV.3.c. Zircon U-Pb dating

Material preparation protocol

Mineral separation procedures were applied to concentrate the zircon crystals using the facilities available at Granada Institute (IACT). All devices are thoroughly cleaned before and after each use to avoid contamination from a previously treated sample. The carbonatite and syenite samples are reduced using a jaw crusher to obtain a powder of a particle size of 250 μm. The powder is sieved for 50 minutes to keep only the material of diameter between 100 and 250 microns. A first stage of concentration of the heavy minerals is carried out using a Wilfley shaking table. The heavier fraction, after being dried, is separated according to the magnetic susceptibility of heavy minerals using a Frantz isodynamic separator. The second step is performed using heavy liquids of bromoform (density of 2.89) and methylene iodide (density of 3.3). Zircons characterized by diamagnetic properties and superior density than 3.3 are examined and carefully handpicked under a binocular microscope on the basis of their quality (absence of micro-fractures, evidence of deterioration and inclusions) and then classified according to their morphology, the development of the crystalline faces and their colour. The selected zircon grains are then embedded in epoxy mounts, grounded and polished on a lap wheel with 6 and 1 mm diamond suspensions successively.

Analytical procedure

Uranium-Pb dating of zircons in carbonatite (IC2-9A) and syenite (IC2-6A) thin sections was performed at the Instituto Andaluz de Ciencias de la Tierra (IACT) (Granada, Spain) using the Laser Ablation ICP-MS. The analyses were acquired using an Excimer laser of 193 nm wavelength coupled to an Agilent 8800 Triple Quadripole ICP-MS multi-collector mass spectrometer. The detailed analytical procedures are described in the table IV.3.

A diameter laser ablation of 15 µm, 10 Hz frequencies and a laser power of 8J/cm^2 were used. The analyte thus produced is transported in a 100% helium gas mixture to the plasma source for ionization. Each analysis consists of an ablation pulse of 30 seconds integration time. The different isotopic masses (204Pb, 206Pb, 207Pb, 208Pb, 232Th, 235U and 238U) are simultaneously measured in static mode with a scan time between 150 ms for 204Pb, 206, 207, 208 and U238, 100 ms for 235U and 232Th and 60 ms for 202Hg using Faraday type detectors. The corrections for isotopic and elementary fractionations as well as for Isoprobe deviation are made from two standards: Zircon 91500 (1065.4 ± 0.3 Ma, Wiedenbeck *et al*. 1995) used as an internal standard and Plesovice (337 ± 0.7 Ma, Slama *et al*, 2008) used as an external standard. The data is processed on Igor Pro Iolite 2.5 software + VisualAge data Reduction scheme (School of Earth Sciences, University of Melbourne). The ages are then derived from the York (1969) linear regression calculations performed using the ISOPLOT version 3 software (Ludwig, 2003).

Table IV.3 Operating conditions for the LA-ICP-MS zircon analysis

Laboratory & Sample Preparation	
Laboratory name	Instituto Andaluz de Ciencias de la Tierra (CSIC-UGR) Petrology, Geochemistry and Geochronology
Sample type/mineral	Zircons
Sample preparation	Thin section
Imaging	CL, EVO15 Zeiss SEM, 10 nA, 8.5mm working distance, 2.6 A Fil I
Laser ablation system	
Make, Model & type	Photon Machines Analyte Excite 193
Ablation cell & volume	Hellex, Double Volume Cell
Laser wavelength (nm)	193 nm
Pulse width (ns)	4 ns
Fluence (J.cm-2)	8 J.cm-2
Repetition rate (Hz)	10 Hz
Ablation duration (secs)	30 secs
Ablation pit depth / ablation rate	N/A
Spot diameter (mm) nominal/actual	15 μ
Sampling mode / pattern	Static spot ablation
Carrier gas	100% He in the cell
Cell carrier gas flow (l/min)	0.9 l/min
ICP-MS Instrument	
Make, Model & type	Agilent 8800 QQQ ICP-MS
Sample introduction	
RF power (W)	1500W
Make-up gas flow (l/min)	0.5 l/min
Detection system	Mixed Faraday-multiple ion counting array
Masses measured	202-207, 235, 238
Integration time per peak/dwell times (ms); quadripole settling time between mass jumps	150 ms for Pb204, 206, 207, 208 and U238 100 ms for U235 and Th232 60 ms for Hg202
Total integration time per output datapoint (secs)	~2.3 secs
Data Processing	
Gas blank	30 second on-peak zero subtracted
Calibration strategy	91500 used as primary reference material, Plesovice used as secondaries/validation
Reference Material info	91500 (Wiedenbeck *et al*. 1995) Plesovice (Slama *et al*, 2008)
Data processing package used / Correction for LIEF	Igor Pro Iolite 2.5 software + VisualAge Data Reduction
Common-Pb correction, composition and uncertainty	No common-Pb correction applied to the data.
Uncertainty level & propagation	Ages are quoted at 2s absolute, propagation is by quadratic addition. Reproducibility and age uncertainty of reference material and common- Pb composition uncertainty, are propagated where appropriate.
Quality control / Validation	Plesovice (337 ± 0.7 Ma)

IV.4. Results

IV.4.a. Apatite in situ U-Pb dating

The free-inclusion apatite samples from Ihouhaouene carbonatite (INH 170) and syenite (IC3-10) are dominated by REE-activated luminescence emission. The CL behaviour of investigated apatites (Figure IV.1) is in accordance with the trace element characteristics of the samples (High LREE, Chapter III).

INH 170 apatite displays the same CL behaviour in all the crystal from the rim to the core. This apatite is coloured in bluish-violet CL (Figure IV.1.a).

Apatite from syenite IC3-10 sample displays different CL colours with high yellow and violet luminescent regions (Figure IV.1. b). CL image of syenites apatite reveals irregular internal structures. High bluish CL inclusions of fluorite are present in K-feldspars in syenite and around apatite crystals in carbonatite.

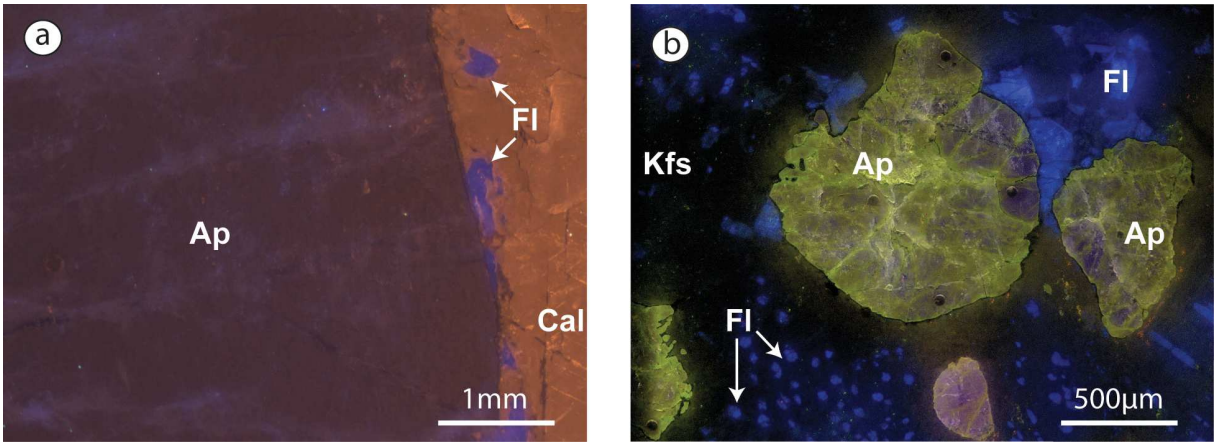

Figure IV. 1. Cathodoluminescence microscopy (CL) images of apatite from **a.** INH170 carbonatite sample showing one-generation apatite with bluish-violet CL colour. **b.** IC3-10 syenite sample showing different apatite yellow and violet CL colours. AP: apatite, Cal: calcite, Fl: fluorite, Kfs: feldspar.

In the Ihouhaouene carbonatites and syenites, U-Pb dating was performed on inclusion-free apatites from carbonatite sample INH 170 and syenite sample IC3-10A. The analytical data are reported in the table IV.4.

Table IV.4 LA-ICP-MS U-Pb geochronological results for apatite from the Ihouhaouene carbonatite and syenite (The $^{207}Pb/^{206}Pb$ and $^{206}Pb/^{238}U$ ages present the corrected ages)

Sample	Th (ppm)	U (ppm)	Pb (ppm)	207Pb/206Pb	±2σ	238U/206Pb	±2σ	207Pb/206Pb Age (Ma)	±2σ	206Pb/238U Age (Ma)	±2σ
INH 170											
INH170_1–b	3027	440	712	0,2229	0,004	2,693	0,189	1808	126	1809	111
INH170_2–c	2764	391	632	0,2113	0,001	2,481	0,172	1995	152	1994	118
INH170_3	2622	362	653	0,2659	0,005	2,272	0,155	2025	142	2030	115
INH170_4	2181	290	526	0,2527	0,002	2,372	0,169	1976	154	1977	122
INH170_5	2585	371	568	0,2054	0,001	2,720	0,192	1833	132	1830	111
INH170_6	2858	391	712	0,2736	0,002	2,482	0,172	1835	144	1832	109
INH170_7	3295	494	716	0,1946	0,002	3,103	0,212	1637	120	1628.5	97
INH170_8	3042	435	904	0,3613	0,003	2,313	0,160	1734	150	1717	104
INH170_10	2920	430	667	0,2137	0,010	3,115	0,233	1588	124	1578	103
INH170_11	2801	413	660	0,2343	0,004	2,762	0,183	1744	106	1735.6	99
INH170_12	2876	376	899	0,4127	0,006	2,069	0,146	1782	118	1759	112
INH170_13	2273	302	536	0,2435	0,002	2,543	0,168	1863	132	1865	108
INH170_14	2364	312	608	0,2988	0,002	2,330	0,163	1888	156	1883	112
INH170_15	2531	357	552	0,1980	0,001	2,782	0,186	1809	126	1807	108
INH170_16	2015	271	492	0,2652	0,006	2,416	0,163	1897	114	1901	109
INH170_17	2208	293	496	0,2144	0,002	2,677	0,186	1842	146	1836	113
INH170_18	2182	303	510	0,2282	0,002	2,639	0,181	1836	136	1830	109
INH170_19	2704	385	950	0,4407	0,003	1,969	0,132	1785	166	1757	101
INH170_20	2825	389	1000,2	0,4468	0,003	1,952	0,130	1782	168	1754	102
INH170_21	2617	358	882	0,4233	0,002	2,050	0,143	1764	160	1741	104
INH170_22	1576	212	424	0,2984	0,002	2,337	0,164	1883	148	1875	111
INH170_23	1619	219	669	0,5106	0,003	1,549	0,106	1980	190	1980	121
INH170_24	2062	283	830	0,5082	0,003	1,637	0,113	1883	180	1861	108
IC3-10											
IC3_10_1	0,8	2,70	3,48	0,7170	0,015	2,665	0,313	-	-	425.6	47
IC3_10_2	2,17	4,75	5,59	0,6804	0,010	2,845	0,267	-	-	510.1	46
IC3_10_3	0,87	2,02	3,32	0,7310	0,014	2,229	0,224	-	-	469.2	44
IC3_10_4	1,83	2,66	4,10	0,6910	0,017	2,387	0,456	-	-	584	107
IC3_10_5	7,47	3,48	6,38	0,7480	0,011	2,179	0,261	-	-	408.3	47
IC3_10_6	0,68	2,35	3,28	0,7040	0,013	2,439	0,232	-	-	521.9	47
IC3_10_7	1,06	3,24	4,35	0,7020	0,011	2,580	0,246	-	-	495.6	46
IC3_10_8	3,46	4,33	5,96	0,7020	0,012	2,623	0,261	-	-	486.8	46
IC3_10_9	6,63	4,16	4,81	0,6650	0,011	3,002	0,288	-	-	523.6	48
IC3_10_10	2,54	3,09	3,97	0,6880	0,013	2,650	0,267	-	-	527.2	51
IC3_10_11	6,35	5,25	5,71	0,6420	0,014	3,146	0,317	-	-	557.6	54
IC3_10_12	2,51	3,61	3,65	0,6590	0,013	3,206	0,329	-	-	501.2	49
IC3_10_13	1,25	3,04	4,32	0,7250	0,012	2,550	0,247	-	-	420.7	39
IC3_10_14	1,16	2,76	4,37	0,7510	0,011	2,305	0,218	-	-	367.7	34
IC3_10_15	2,48	2,94	4,45	0,7330	0,013	2,421	0,276	-	-	417.2	46
IC3_10_16	2,29	2,00	5,81	0,8140	0,012	1,389	0,131	-	-	198.3	18
IC3_10_17	5,01	3,15	6,17	0,7640	0,015	1,996	0,187	-	-	376.0	34
IC3_10_18	33,9	5,18	8,28	0,6850	0,011	2,850	0,317	-	-	494.0	53
IC3_10_19	1,63	2,88	4,73	0,7460	0,012	2,206	0,234	-	-	410.1	41
IC3_10_20	6,02	4,39	5,41	0,6980	0,011	2,807	0,268	-	-	461.3	42
IC3_10_21	3,93	5,27	5,19	0,6470	0,010	3,184	0,324	-	-	538.5	52
IC3_10_22	9,22	7,78	5,83	0,5750	0,010	3,967	0,393	-	-	571.1	53
IC3_10_23	6,09	6,09	6,62	0,6730	0,010	3,078	0,284	-	-	485.9	42

From the carbonatite sample (INH170), twenty-three U-Pb isotopes analyses on five apatite megacrysts (5mm to 1 cm) were carried out. In the Tera Wasserburg diagram, all ellipses are in discordant positions with a relatively high proportion of commun Pb ($^{207}Pb/^{206}Pb$ = 0.198 – 0.508) (Table IV.4). Apatites in carbonatite (INH170) have homogenous composition with no recrystallization evidences (Figure IV.1.a). The $^{207}Pb/^{206}Pb$ corrected ages from center and rim apatite grains ranging between 1744 ± 106 Ma to 2025 ± 142 Ma and 1588 ± 124 Ma to 1976 ± 154 Ma respectively, yield similar ages within the errors (Table IV.4).

Furthermore, the weighted average $^{207}Pb/^{206}Pb$ corrected ages obtained from the center and rim grains yields a age of 1867 ± 88 Ma (MSWD = 2.4, N= 8; Figure IV.2.b) and 1794 ± 57 Ma (MSWD = 2.2, N= 15; Figure IV.2.a) respectively.

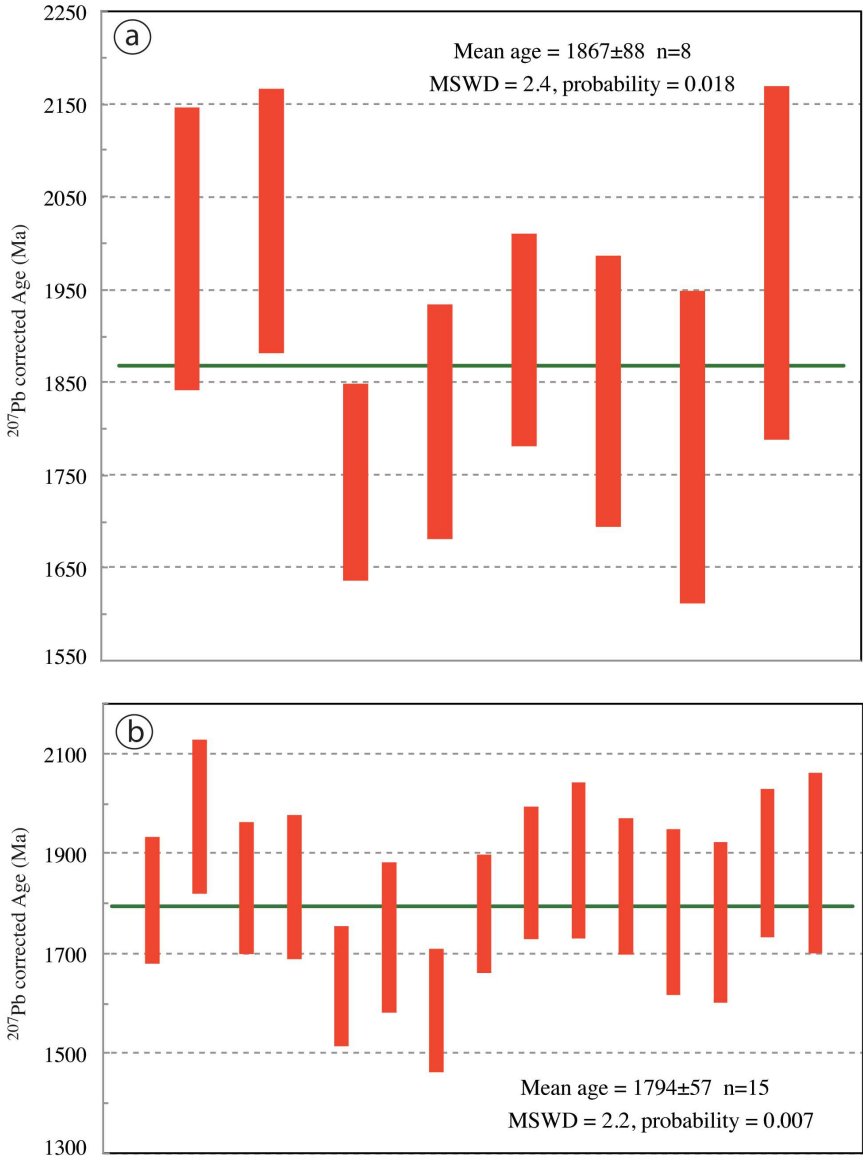

Figure IV.2. The weighted average $^{207}Pb/^{206}Pb$-corrected age diagram of apatites from INH170.carbonatite. **a.** Center apatite grains. **b.** Rim apatite grains. Errors are reported at 2 σ.

The linear regression of data (except excluded data INH170-9) define an intercept age of 1866 ± 68 Ma (MSWD = 1.9; N= 23) with an initial $^{207}Pb/^{206}Pb$ value of 0.8 (Figure IV.3). If the discordia is forced to a $^{207}Pb/^{206}Pb$ value of 0.98 calculated following the terrestrial Pb evolution model of Stacey and Kramers for an age of 1.8 Ga, we obtain a similar and more precise lower intercept date with 2σ error at 1845 ± 38 Ma (MSWD = 1.8, Figure IV.4a). The weighted average $^{207}Pb/^{206}Pb$-corrected ages (calculating using Stacey & Kramers, 1975 terrestrial Pb evolution model) are comparable within error at 1838 ± 42 Ma (MSWD = 1.8; N = 22; Figure IV.4b).

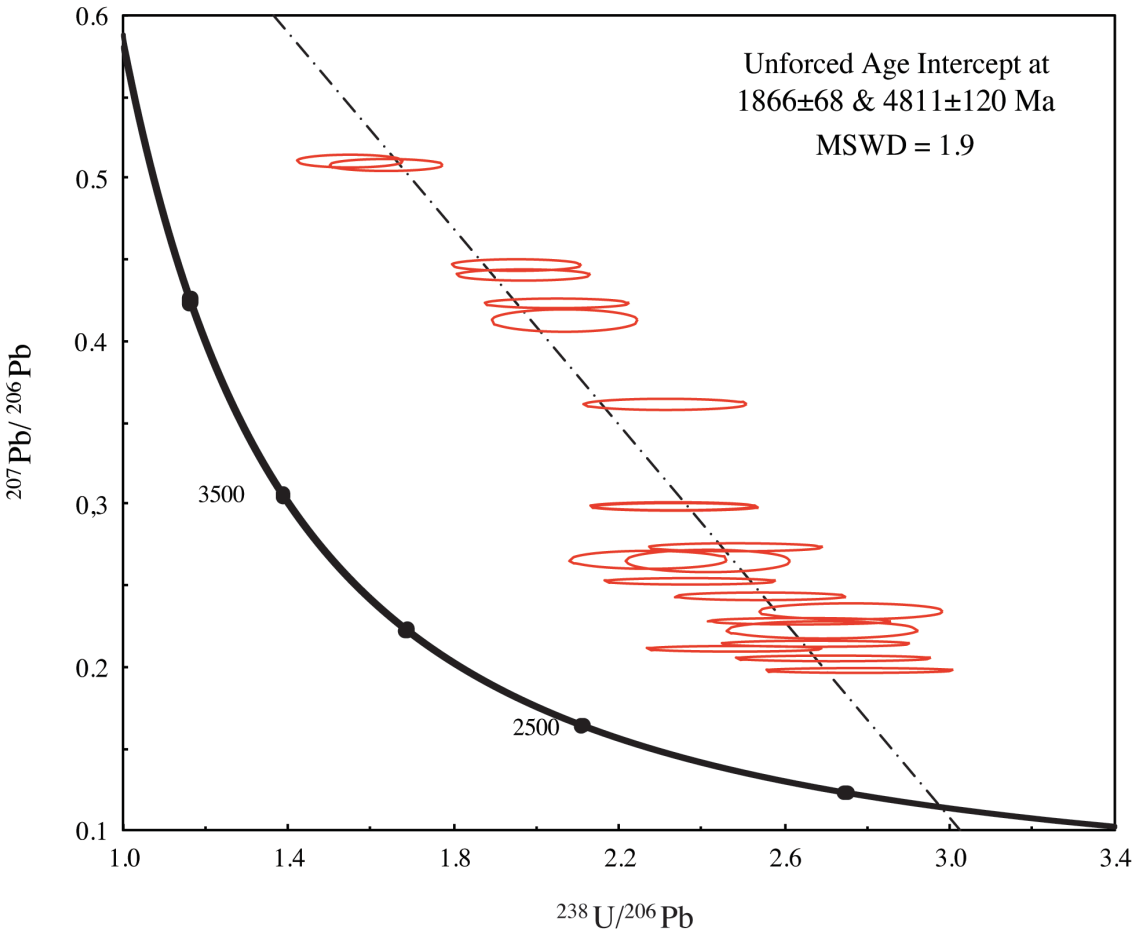

Figure IV.3. The U-Pb Tera-Wasserburg Concordia diagram based on the unforced Intercept age of apatite from the carbonatite INH170. Ellipses and errors are reported at 2 σ.

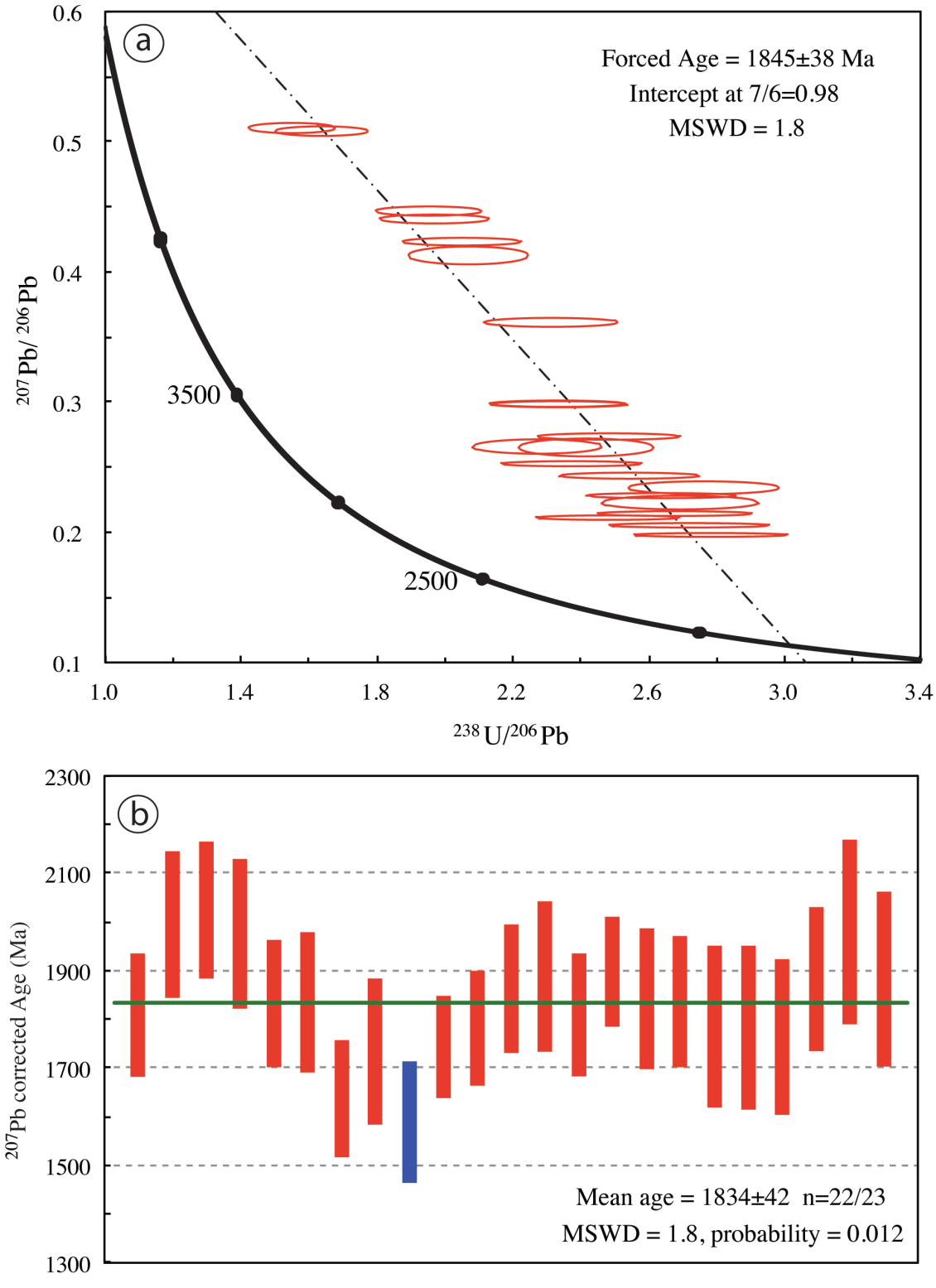

Figure IV.4. The U-Pb Tera-Wasserburg discordia diagram of apatite from carbonatite INH170. **a.** The discordia is calculated with the initial common Pb value forced to $^{207}Pb/^{206}Pb$ of 0.98 calculated following the Pb evolution model of Stacey and Kramers (1975). **b.** Corresponding weighted average $^{207}Pb/^{206}Pb$-corrected age diagram. Ellipses and errors are reported at 2 σ.

Twenty-three U-Pb isotopes analyses from thirteen IC3-10A syenite apatite crystals (300 to 2mm) were performed. They are very discordant with variable and high amounts of common Pb ($^{207}Pb/^{206}Pb$ values between 0.575 – 0.814) (Table IV.4). The unforced age of this apatite is not considered because of the high common Pb in apatites then to obtain the linear regression the age need to be forced following the upper intercept. If the discordia is forced to a $^{207}Pb/^{206}Pb$ value of 0.91 calculated following the terrestrial Pb evolution model of Stacey and Kramers for an age of 600 Ma, we obtain a more precise lower intercept date with 2σ error at 651 ± 51 Ma (MSWD = 0.66, N = 23; Figure IV.5).

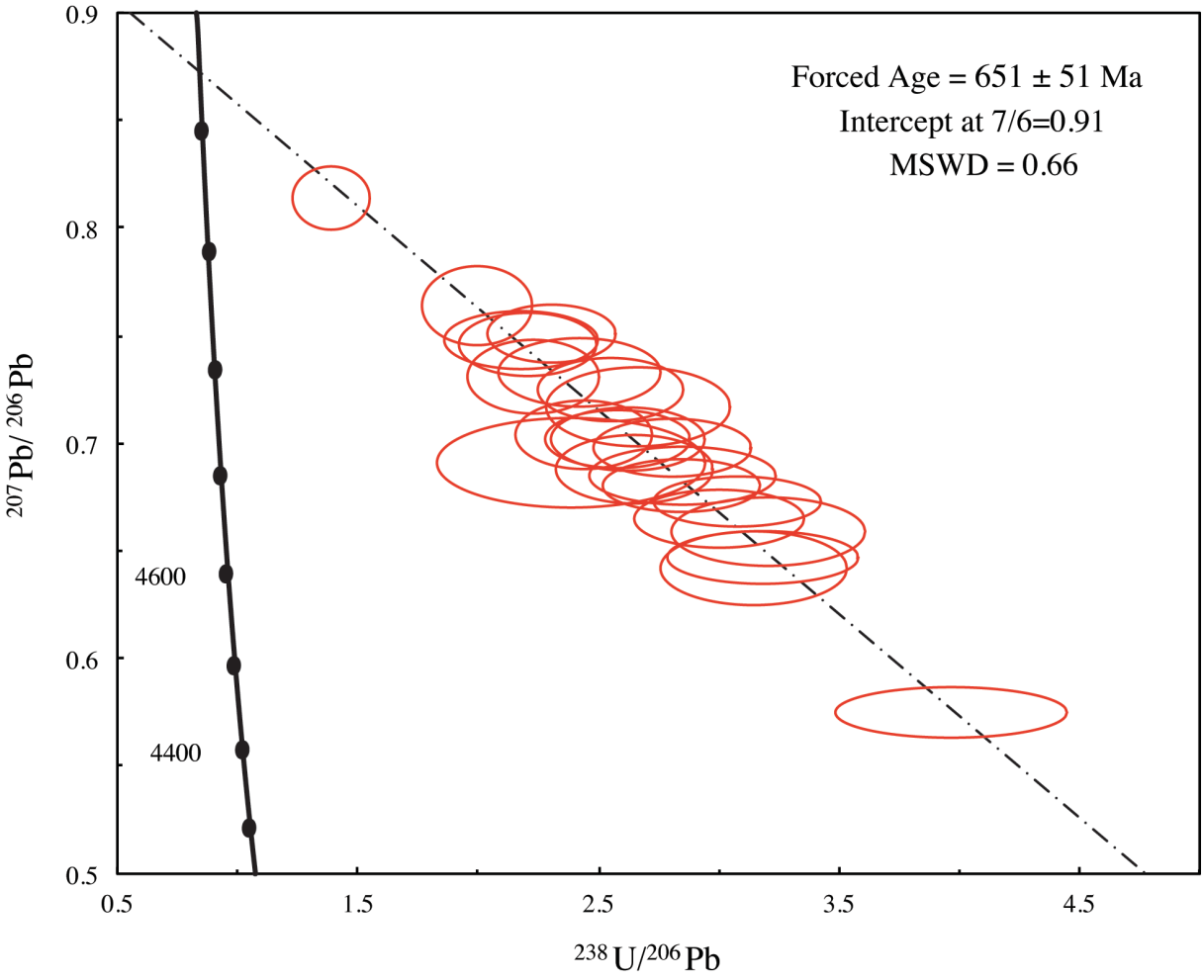

Figure IV.5. The U-Pb Tera-Wasserburg discordia diagram of apatite from syenite IC3-10 based on calculated age with the initial common Pb value forced to $^{207}Pb/^{206}Pb$ of 0.87 following the Pb evolution model of Stacey and Kramers (1975). Ellipses and errors are reported at 2 σ.

IV.4.b. Zircon mineral chemistry

Carbonatite zircon grains (Table IV.5) have homogenous composition with 27.9-31.7 wt.% SiO_2, 66.3-67.7 wt.% ZrO_2 (Figure IV.6a). They display a wide range in HfO_2 contents from 0.35 to 0.61 wt.% and $TiO_2 < 0.01$ wt.% (Figure IV.6b).

In syenite, zircon grains (Table IV.5) have higher HfO_2 of 0.9 to 1.4 wt.% (Figure IV.6) with 28.8-31.4 wt.% SiO_2, 61.9-67.2 wt.% ZrO_2 and $TiO_2 < 0.02$ wt.% (Figure IV.6a and b).

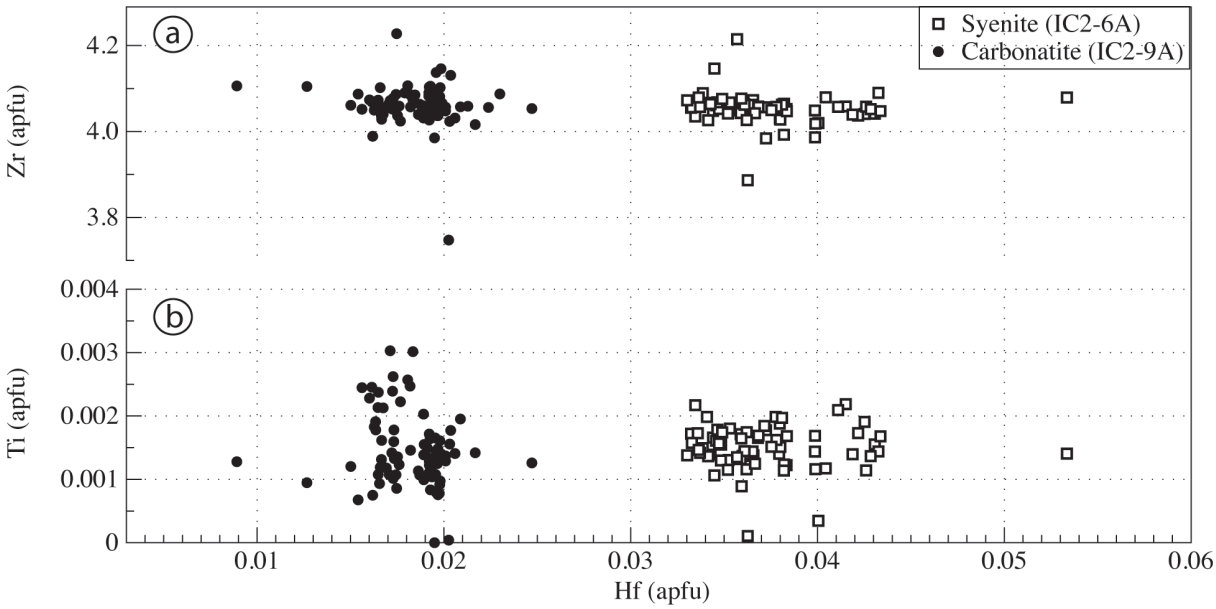

Figure IV. 6. Zircon mineral chemistry from IC2-6A syenite and IC2-9A Si-rich carbonatite samples in molar units. a. Zr versus Hf (a.p.f.u). b. Ti versus Hf (a.p.f.u).

Abundant zircons were observed in Ihouhaouene carbonatite and syenite. Zircon grains are elongated and display prismatic shapes with dominant (100) and (110) crystal faces and surrounded terminations (Figure IV.7). Zircon populations are characterized by a non-systematic zoning (Figures IV.7a-d). EMP quantitative maps display a slight chemical intergrowth zoning in Hf and Y in zircons from syenite (Figures IV.7a and b) (Spear et Pyle, 2002). and concentric zoning in zircons from carbonatite (Figures IV.7c and d) (Zhu and O'Nions, 1999).

Zircon crystals are present in small grains with length ranging from 15 to 200 μm included in K-feldspar (Figures IV.7a, b and c) and in reactional texture around clinopyroxene and garnet and around apatite crystals (Figure IV.7d).

Table IV.5: Representative major element composition of zircon from the Ihouhaouene carbonatite and syenite

Rock type	Si-rich carbonatite														
Sample	IC2-9Ap. Z1.9	IC2-9Ap. Z1.10	IC2-9Ap. Z2.3	IC2-9Ap. Z2.6	IC2-9Ap. Z3.13	IC2-9Ap. Z3.14	IC2-9Ap. Z4.2	IC2-9Ap. Z4.3	IC2-9Ag. Z2.3	IC2-9Ag. Z2.4	IC2-9Ag. Z2.5	IC2-9Ag. Z1.4	IC2-9Ag. Z1.6	IC2-9Ag. Z3.4	IC2-9Ag. Z3.5
Type	Core	Rim	Core	Rim	Core	Middle	Core	Rim	Core	Middle	Rim	Core	Rim	Core	Rim
SiO_2	27.89	30.65	31.48	31.54	31.20	31.40	31.40	31.45	31.37	31.31	31.66	25.46	31.58	31.72	31.56
TiO_2	0.01	0.02	0.02	0.02	0.01	0.02	0.12	0.07	0.02	0.01	0.02	0.00	0.02	0.01	0.01
ZrO_2	64.65	67.96	66.77	67.00	67.38	67.13	67.24	67.07	66.91	66.54	66.16	56.32	66.28	66.61	66.34
FeO	0.02	0.07	0.01	0.01	bdl	bdl	0.04	0.03	0.02	0.03	0.04	0.01	0.05	0.01	0.08
CaO	0.11	0.33	0.01	0.01	0.02	0.01	0.08	0.05	0.02	0.03	0.04	10.27	0.06	0.01	0.04
PbO	bdl	bdl	bdl	bdl	bdl	0.01	0.03	bdl	bdl	bdl	bdl	0.01	bdl	bdl	bdl
UO_2	bdl	bdl	bdl	bdl	bdl	bdl	bdl	bdl	bdl	bdl	bdl	bdl	bdl	bdl	bdl
ThO_2	0.03	bdl	0.12	bdl	0.24	bdl	bdl	0.13	0.24	0.14	0.04	0.18	bdl	bdl	bdl
Y_2O_3	bdl	bdl	0.02	bdl	bdl	bdl	bdl	bdl	bdl	bdl	bdl	bdl	bdl	bdl	0.02
Yb_2O_3	0.07	bdl	bdl	0.04	0.02	bdl	bdl	0.05	0.04	0.04	bdl	bdl	0.02	bdl	0.01
HfO_2	0.46	0.57	0.46	0.59	0.55	0.56	0.56	0.60	0.49	0.69	0.57	0.52	0.58	0.49	0.47
Total	93.24	99.60	98.88	99.21	99.42	99.12	99.48	99.45	99.10	98.80	98.52	92.79	98.58	98.87	98.53
Numbers of ions on the basis of 16O															
Si	3.74	3.82	3.92	3.92	3.88	3.91	3.89	3.90	3.91	3.91	3.95	3.47	3.94	3.89	3.94
Ti	0.001	0.002	0.002	0.002	0.001	0.002	0.011	0.007	0.002	0.001	0.002	-	0.001	0.001	0.001
Zr	4.23	4.13	4.06	4.06	4.09	4.07	4.07	4.06	4.06	4.05	4.02	3.75	4.03	4.09	4.04
Fe^{2+}	0.002	0.007	0.001	0.001	-	-	0.005	0.003	0.002	0.003	0.004	0.002	0.005	0.001	0.001
Ca	0.016	0.044	0.001	0.001	0.003	0.001	0.010	0.006	0.002	0.004	0.005	1.502	0.009	0.004	0.001
Pb	-	-	-	-	-	-	0.001	-	-	-	-	0.001	-	-	-
U	-	-	-	-	-	-	-	-	-	-	-	-	-	-	-
Th	0.001	-	0.003	-	0.007	-	-	0.004	0.007	0.004	0.001	0.006	-	-	-
Y	-	-	0.001	-	-	-	-	-	-	-	-	-	-	-	0.002
Yb	0.003	-	-	0.001	0.001	-	-	0.002	0.001	0.002	-	-	0.001	-	-
Hf	0.02	0.02	0.02	0.02	0.02	0.02	0.02	0.02	0.02	0.02	0.02	0.02	0.02	0.02	0.02
Total	8	8	8	8	8	8	8	8	8	8	8	9	8	8	8

bdl : below detection limit

Table 5: continued

Rock type	**Red syenite**																	
Sample	IC2-6A. Z2.3	IC2-6A. Z2.5	IC2-6A. Z1.3	IC2-6A. Z1.4	IC2-6A. Z3.2	IC2-6A. Z3.3	IC2-6A. Z4.3	IC2-6A. Z4.4	IC2-6A. Z5.4	IC2-6A. Z5.6	IC2-6A. Z6.4	IC2-6A. Z6.5	IC2-6A. Z7.13	IC2-6A. Z7.14	IC2-6A. Z8.2	IC2-6A. Z8.3	IC2-6A. Z9.3	IC2-6A. Z9.6
Type	Core	Rim	Core	Rim	Core	Rim	Core	Rim	Core	Rim	Core	Rim	Core	Middle	Core	Rim	Core	Rim
SiO_2	31.15	31.26	31.16	31.16	31.38	31.14	31.19	31.25	31.48	31.14	31.20	31.19	30.54	30.96	31.38	31.27	31.12	31.15
TiO_2	0.01	0.01	0.02	0.02	0.02	0.01	0.01	0.02	0.02	0.02	0.02	0.01	0.01	0.01	0.01	0.02	0.02	0.01
ZrO_2	66.33	66.48	67.93	66.83	66.12	66.51	66.49	66.67	66.23	66.60	66.59	66.71	66.26	66.37	66.53	66.79	67.05	66.93
FeO	0.04	0.04	0.07	0.05	bdl	0.01	0.13	0.1	bdl	0.01	0.01	0.02	0.09	0.1	0.12	0.05	0.01	0.02
CaO	0.02	0.01	0.16	0.004	0.01	0.01	0.01	0.01	0.01	0.01	0.01	0.01	0.02	bdl	0.01	0.02	bdl	0.01
PbO	0.07	0.14	0.03	0.06	0.02	bdl	0.02	0.03	0.02	0.03	0.05	0.03	0.11	0.14	0.06	0.05	0.05	bdl
UO_2	bdl	0.06	bdl	bdl	bdl	bdl	bdl	bdl	bdl	bdl	bdl	bdl	0.03	0.06	bdl	bdl	bdl	bdl
ThO_2	0.05	bdl	bdl	bdl	0.18	bdl	0.1	0.26	0.13	bdl	bdl	bdl	bdl	0.14	0.04	bdl	bdl	0.10
Y_2O_3	0.01	0.01	0.01	0.03	bdl	bdl	0.01	0.02	0.03	0.04	0.02	0.02	0.01	0.11	0.004	0.01	0.02	0.005
Yb_2O_3	bdl	bdl	0.08	bdl	bdl	0.10	bdl	0.07	0.04	0.01	bdl	bdl	bdl	bdl	bdl	0.10	bdl	bdl
HfO_2	1.06	0.99	1.23	0.99	1.06	1.01	0.98	0.98	1.07	1.02	1.03	1.01	1.48	1.19	1.18	1.06	0.94	0.93
Total	98.75	99.01	100.69	99.15	98.80	98.80	98.93	99.39	99.02	98.88	98.94	99.00	98.56	99.04	99.35	99.36	99.21	99.16
Numbers of ions on the basis of 16O																		
Si	3.90	3.91	3.85	3.89	3.92	3.90	3.90	3.90	3.93	3.90	3.90	3.90	3.86	3.88	3.91	3.90	3.88	3.89
Ti	0.001	0.001	0.001	0.002	0.002	0.001	0.001	0.002	0.002	0.001	0.002	0.001	0.001	0.001	0.001	0.002	0.001	0.001
Zr	4.05	4.05	4.09	4.07	4.03	4.06	4.05	4.05	4.03	4.06	4.06	4.06	4.08	4.06	4.04	4.06	4.08	4.07
Fe^{2+}	0.004	0.004	0.01	0.01	-	0.001	0.01	0.01	-	0.001	0.001	0.002	0.01	0.01	0.01	0.005	0.001	0.002
Ca	0.003	0.001	0.02	0.001	0.001	0.001	0.001	0.002	0.001	0.001	0.001	0.001	0.003	-	0.002	0.002	-	0.001
Pb	0.002	0.005	0.001	0.002	0.001	-	0.001	0.001	0.001	0.001	0.002	0.001	0.004	0.005	0.002	0.002	0.002	-
U	-	0.002	-	-	-	-	-	-	-	-	-	-	0.001	0.002	-	-	-	-
Th	0.001	-	-	-	0.01	-	0.003	0.01	0.004	-	-	-	-	0.004	0.001	-	-	0.003
Y	0.001	-	-	0.002	-	-	0.001	0.00	0.002	0.003	0.001	0.001	0.001	0.01	-	-	0.001	-
Yb	-	-	0.003	-	-	0.004	-	0.00	0.001	-	-	-	-	-	-	0.004	-	-
Hf	0.04	0.04	0.04	0.04	0.04	0.04	0.03	0.03	0.04	0.04	0.04	0.04	0.05	0.04	0.04	0.04	0.03	0.03
Total	8	8	8	8	8	8	8	8	8	8	8	8	8	8	8	8	8	8

bdl : below detection limit

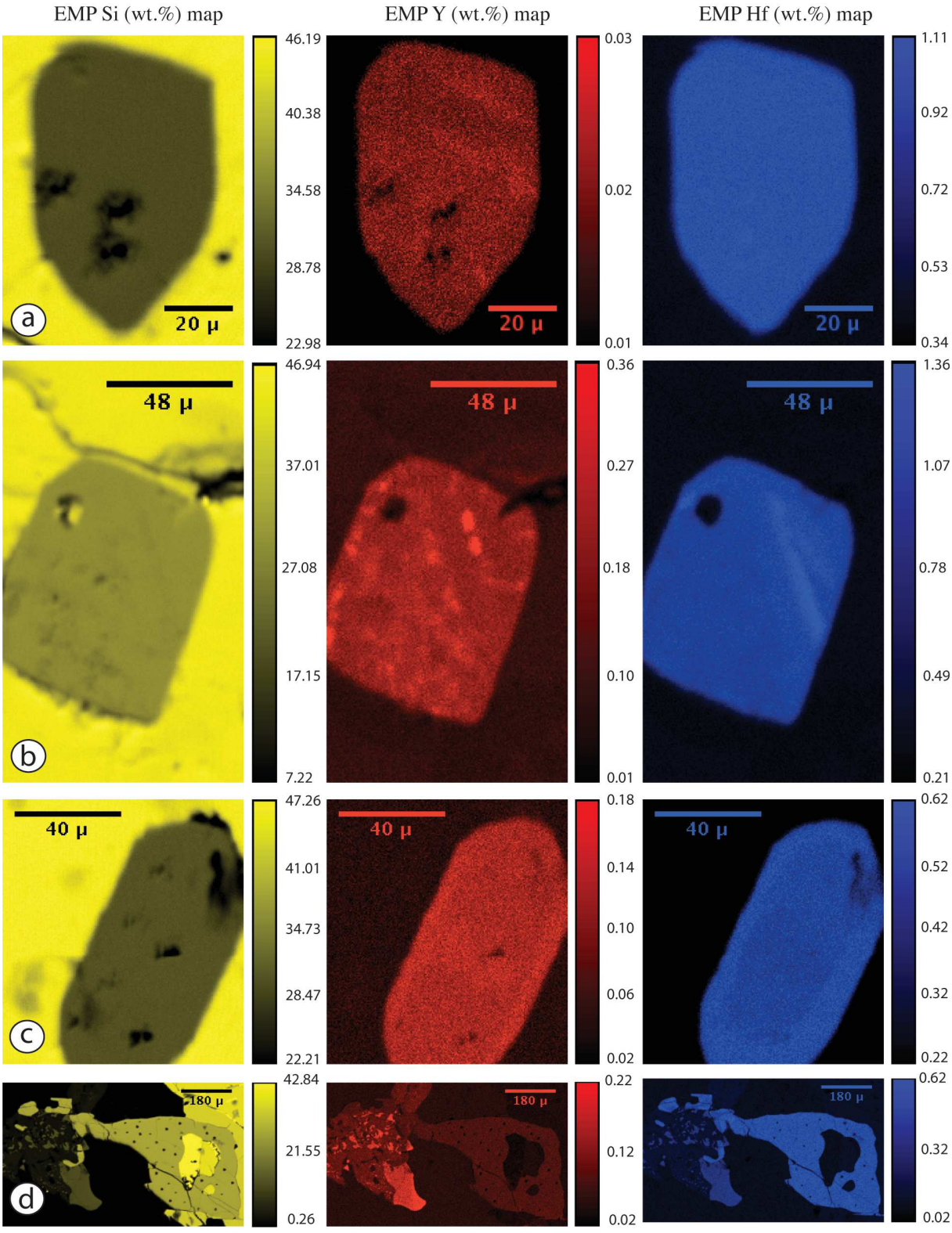

Figure IV. 7. Quantitative EMP mapping for Si, Y and Hf (wt.%) in zircons from samples **(a-b)** IC2-6A red syenite and **(c-d)** IC2-9A Si-rich carbonatite.

IV.4.c. Zircon in situ U-Pb dating

From the IC2-6A syenite zircons (Figure 3 in supplementary material D), fifty-four U-Pb isotopes analyses on twelve zircon grains were carried out (Table IV.6). These analyses are characterized by variable U and Th contents ranging from 96 to 8000 ppm, and from 7.4 to 3980 ppm respectively and associated to low to moderate Th/U ratio bracketed between 0.01 and 0.55 (Table IV.6, Figure IV.8a).

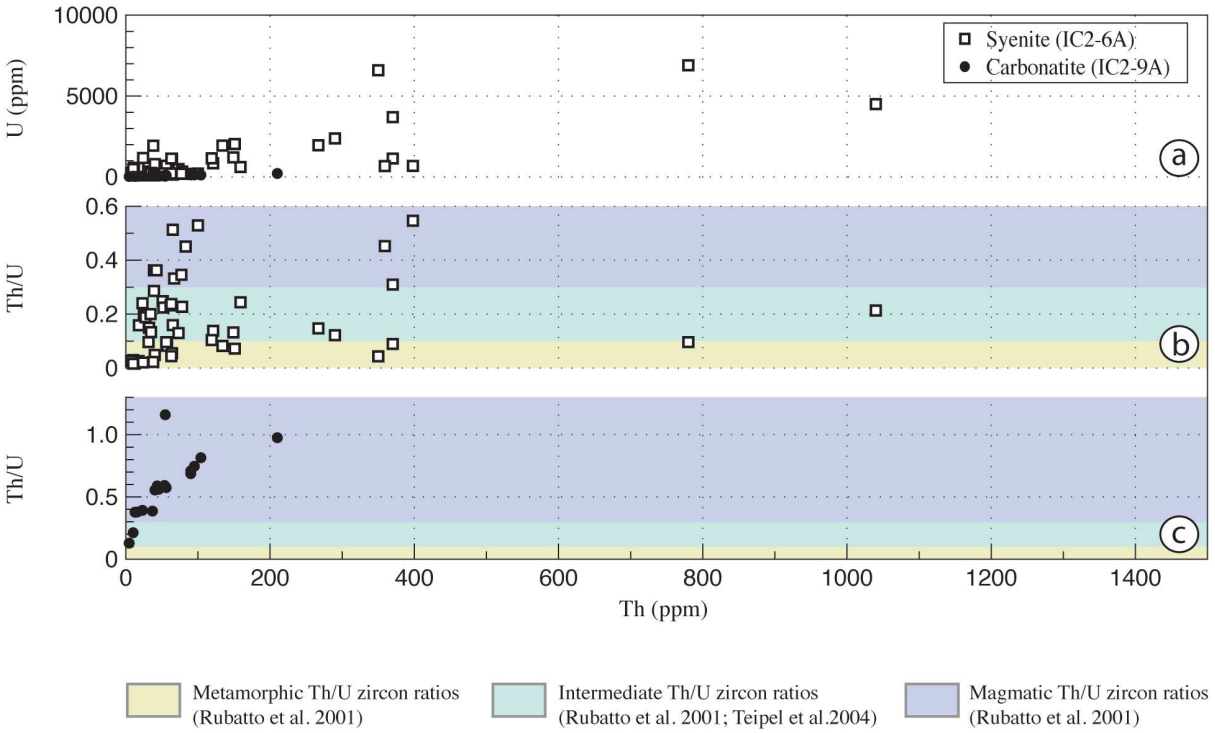

Figure IV. 8. a. U versus Th (ppm) for carbonatite and syenite Zircon samples. Th/U versus Th (ppm) showing the magmatic or metamorphic zircon type following Rubatto *et al*. 2001 and Teipel *et al*. 2004 for **b.** syenite zircons and **c.** carbonatite zircons.

In the Concordia diagram, the ellipses are in concordant to discordant positions (83 to 120 % of concordance ; Table IV.6). The $^{206}Pb/^{238}U$ ages are comprised between 1324 ± 341 Ma and 2699 ± 763 Ma (Table IV.6). The 54 concordant ellipses yield a concordia age of 2162.64 ± 0.8 Ma (MSWD = 21, Figure IV.9a). The weighted mean $^{206}Pb/^{238}U$ age obtained by excluding 18 discordant data affected by Pb loss, yields a similar age within error of 2163.58 ± 0.82 Ma (MSWD = 3.27, Figure IV .9b).

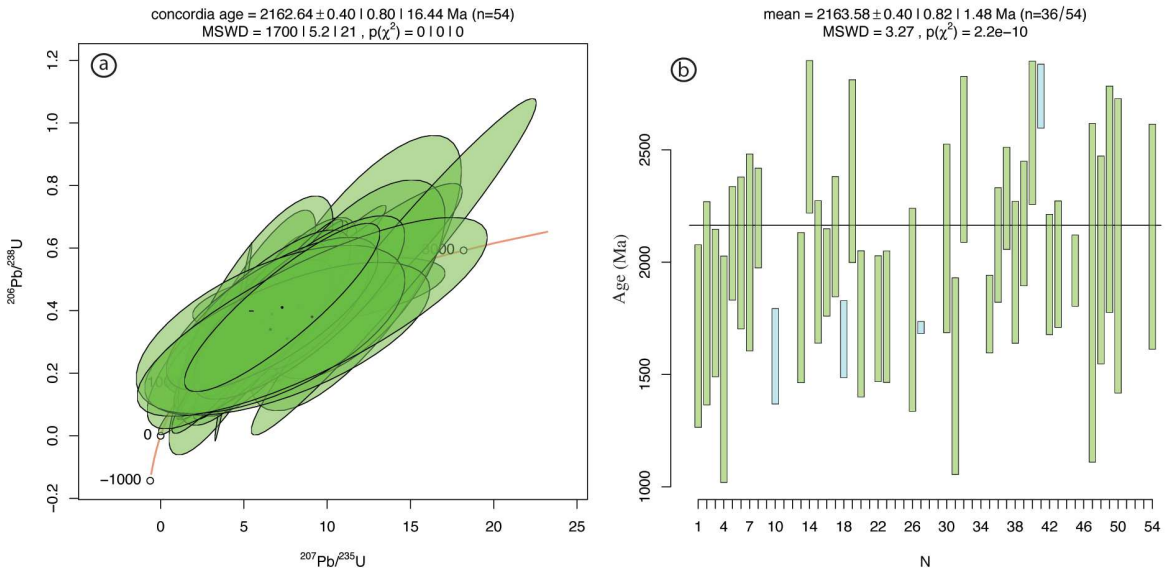

Figure IV. 9. a. U-Pb Concordia diagram based on $^{207}Pb/^{235}U$ and $^{206}Pb/^{238}U$ isotopic ratios measured on zircons from syenite sample IC2-6A by LA-ICP-MS. **b.** Weighted mean age diagram using $^{206}Pb/^{238}U$ calculated ages. Ellipses and errors are reported at 2 σ.

From the IC2-9A carbonatite zircons (Figures 1 and 2 in supplementary material D), eighteen U-Pb isotopes analyses on five zircon grains were performed (Table IV.6). These zircon grains have relatively low U content of 30.2 to 130 ppm, 4.6 to 210 ppm Th and Th/U ratio of 0.1 to 1.16 (Table IV.6, Figure IV.8b). All the data are concordant to sub-concordant (85 to 115 % of concordance) between 1867.4 ± 62.7 Ma and 2020 ± 77.8 Ma and yield a concordia age of 1941.5 ± 27.4 Ma (MSWD = 2.9, N = 18; Figure IV.10a). This age is similar within error with the age 1936.6 ± 42.4 Ma obtained by the weighted average $^{206}Pb/^{238}U$ age (MSWD = 0.56, N = 12; Figure IV.10b).

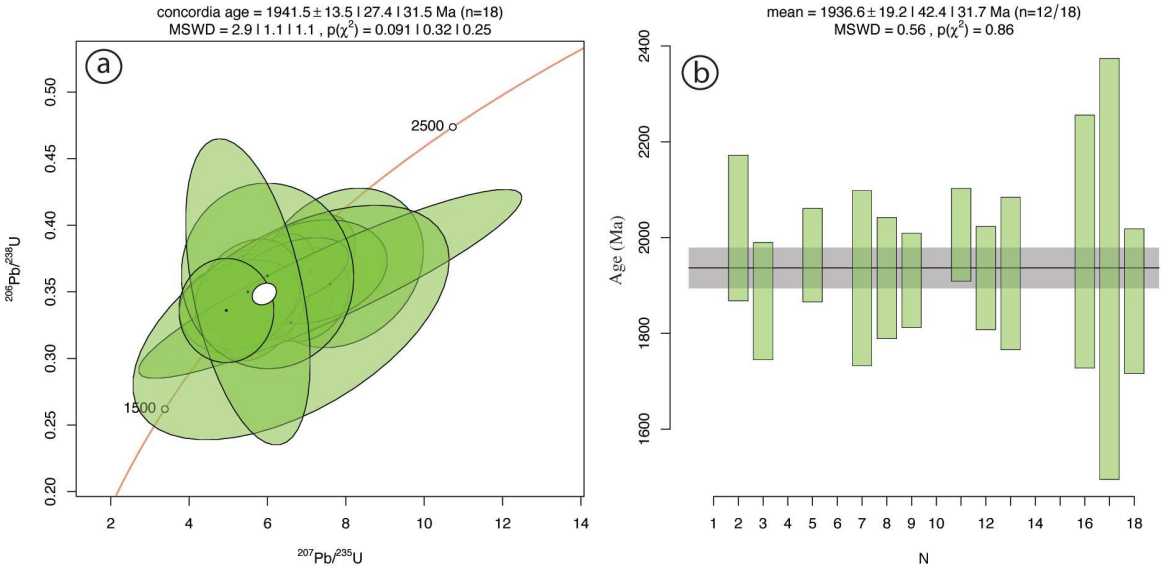

Figure IV. 10. a. U-Pb Concordia diagram based on $^{207}Pb/^{235}U$ and $^{206}Pb/^{238}U$ isotopic ratios measured on zircons from carbonatite sample IC2-9A by LA-ICP-MS. **b.** Weighted mean age diagram using $^{206}Pb/^{238}U$ calculated ages. Ellipses and errors are reported at 2 σ.

Table IV.6: LA-ICP-MS U-Pb geochronological results for zircon from the Ihouhaouene carbonatite and syenite

Sample	Th (ppm)	U (ppm)	Th/U	207Pb/206Pb	±2σ	207Pb/235U	±2σ	206Pb/238U	±2σ	207Pb/206Pb Age (Ma)	±2σ	207Pb/235U Age (Ma)	±2σ	206Pb/238U Age (Ma)	±2σ	Concordia Age (Ma)	±2σ
IC2-9A																	
5105-R-2	53.6	88	0.59	0.1390	0.02	6.470	0.98	0.347	0.03	2167	144	2041.8	66.6	1920.3	59.8	1970.5	47.3
5105-R-3	36.9	94.8	0.39	0.1300	0.02	6.900	1.10	0.368	0.03	2177	128	2098.7	70.7	2020	77.8	2063.3	64.5
5105-R-4	40.3	75.1	0.56	0.1100	0.02	4.940	0.97	0.336	0.03	1743	191	1809.1	82.9	1867.4	62.7	1845.6	49.9
5105-R-5	23	55.8	0.39	0.1510	0.03	7.900	1.70	0.368	0.05	2409	194	2219.7	97.0	2020	115	2131.3	88.0
5105-R-6	210	217	0.98	0.1250	0.02	5.590	0.70	0.356	0.02	1862	126	1914.6	53.9	1963.2	49.9	1940.2	35.7
5105-C-1	90	129	0.71	0.1330	0.02	6.910	0.96	0.348	0.03	2276	129	2099.9	61.6	1925	69.3	2016.9	52.8
5105-C-2	95	130	0.75	0.1300	0.02	6.000	1.00	0.346	0.04	2040	132	1975.8	72.5	1915.5	93.4	1958.6	70.6
5105-C-4	43.5	71.6	0.59	0.1140	0.02	5.800	0.93	0.346	0.03	1979	161	1946.4	69.4	1915.5	64.7	1929.7	46.8
5105-C-5	104	125	0.81	0.1130	0.02	5.470	0.88	0.345	0.02	1880	127	1895.9	69.1	1910.7	50.3	1907.5	48.4
5105-C-6	45.7	80.8	0.56	0.1420	0.03	7.100	1.60	0.365	0.03	2241	193	2124	100	2005.8	75.6	2039.6	68.9
5105-C-7	90	138	0.69	0.1260	0.02	6.600	1.20	0.365	0.02	2113	144	2059.3	80.2	2005.8	49.6	2011.3	49.4
5105-C-9	55.9	99	0.57	0.1160	0.03	5.500	1.10	0.346	0.02	1884	182	1900.6	85.9	1915.5	55.1	1911.5	48.7
5105-C-10	41.2	80	0.56	0.1100	0.02	5.500	1.10	0.348	0.03	1874	180	1900.6	85.9	1925	81.3	1913.5	65.5
5089-R-6	4.6	30.2	0.13	0.1470	0.08	7.600	4.00	0.356	0.06	2400	326	2185	236	1963	138	1816.8	91.0
3922-R-2	54.6	46.6	1.16	0.1490	0.07	6.600	3.30	0.327	0.07	2304	365	2059	220	1824	175	1848	184
3922-C-1	12.7	33.6	0.38	0.1250	0.04	6.000	1.80	0.362	0.06	1959	304	1976	131	1992	135	1983.4	92.9
5373-C-2	15.7	42.8	0.38	0.1090	0.04	5.500	1.30	0.350	0.09	1864	389	1901	102	1935	224	1909.2	70.8
3930-C	10.1	48.3	0.21	0.1070	0.02	4.950	0.99	0.336	0.03	1746	203	1810.8	84.5	1867.4	77.2	1840.9	56.0
IC2-6A																	
2209-R-1	83	195	0.45	0.0880	0.02	4.20	1.10	0.2940	0.05	1690	406	1674	215	1661	269	1671	208
2209-C-1	100	218	0.53	0.1000	0.02	5.00	1.40	0.3460	0.08	1711	399	1819	237	1915	374	1817	231
2209-R-2	65	149	0.51	0.1080	0.02	5.00	1.00	0.3300	0.08	1798	384	1819	169	1838	378	1818	168
2209-C-2	39	96	0.36	0.0910	0.03	3.50	1.30	0.2660	0.05	1537	523	1527	293	1520	270	1523	258
1359-R-1	51	198	0.25	0.1340	0.02	6.90	1.20	0.3940	0.08	2057	199	2099	154	2141	356	2084	129
1359-R-2	31.4	340	0.10	0.1160	0.01	6.50	1.40	0.3760	0.07	2034	204	2046	190	2058	314	2041	173
1359-C-1	65	480	0.16	0.1037	0.01	6.50	1.60	0.3650	0.06	2087	272	2046	217	2006	264	2043	224
1359-C-2	57	660	0.08	0.1630	0.04	7.70	1.00	0.4070	0.10	2192	367	2197	117	2201	444	2196	114
1689-R	159	620	0.24	0.1254	0.01	7.34	0.30	0.3988	0.00	2144.2	71.4	2153.7	36.5	2163.61	0.41	2163.6	0.40
1689-C	267	1960	0.15	0.0953	0.01	3.69	0.82	0.2720	0.07	1594	194	1569	178	1551	375	1581	109
2060-C-1	23.1	101	0.24	0.1300	0.03	7.70	2.10	0.3900	0.10	2266	131	2197	245	2123	464	2259	121
2060-C-2	25	111	0.20	0.1480	0.03	7.50	1.80	0.3880	0.07	2230	300	2173	215	2114	316	2174	220

Table IV.6: continued

Sample	Th (ppm)	U (ppm)	Th/U	207Pb/206Pb	±2σ	207Pb/235U	±2σ	206Pb/238U	±2σ	207Pb/206Pb Age (Ma)	±2σ	207Pb/235U Age (Ma)	±2σ	206Pb/238U Age (Ma)	±2σ	Concordia Age (Ma)	±2σ
IC2-6A																	
2060-C-3	32.1	215	0.15	0.1160	0.02	5.00	1.10	0.3420	0.08	1732	285	1819	186	1896	389	1797	171
2060-R-2	18.1	116	0.16	0.1870	0.04	11.70	2.60	0.5200	0.18	2489	396	2581	208	2699	763	2558	174
2060-R-3	27.1	135	0.19	0.1210	0.02	5.80	1.30	0.3480	0.08	1969	212	1946	194	1925	368	1956	162
1235-C-1	149	1210	0.13	0.1160	0.01	5.80	1.10	0.3500	0.07	1959	130	1946	164	1935	344	1954.1	99.6
1235-C-2	134	1940	0.08	0.1220	0.01	6.70	2.80	0.3700	0.15	2116	144	2073	369	2029	706	2113	137
1235-C-3	121	850	0.14	0.0932	0.01	4.13	0.46	0.2970	0.04	1640	162	1660.3	91.0	1676	174	1657.2	87.9
1235-R-2	370	1140	0.31	0.1420	0.03	9.50	3.10	0.4530	0.05	2370	478	2388	300	2409	213	2405	208
2056-C	290	2380	0.12	0.0948	0.01	4.40	1.10	0.3000	0.07	1738	209	1712	207	1691	362	1725	166
2056-R-2	359	670	0.45	0.0930	0.02	3.28	0.97	0.2280	0.07	1703	405	1476	230	1324	341	1482	244
6478-R-1	10	378	0.03	0.0985	0.01	4.60	1.30	0.3120	0.10	1748	203	1749	236	1751	486	1748	143
6478-R-2	12.4	570	0.02	0.1030	0.02	4.62	0.87	0.3070	0.08	1785	338	1753	157	1726	370	1757	150
6478-C-1	40.1	800	0.05	0.1050	0.01	4.20	1.30	0.2570	0.06	1934	237	1674	254	1474	328	1819	239
6478-C-2	17.5	560	0.03	0.0870	0.02	4.20	1.40	0.2740	0.08	1819	297	1674	273	1561	400	1730	255
1038-R-1	38	1930	0.02	0.1120	0.04	4.90	1.80	0.3300	0.16	1761	456	1802	310	1838	776	1788	231
1038-C-1	350	6600	0.04	0.1020	0.03	4.37	0.46	0.3000	0.13	1726	605	1706.7	87.0	1691	645	1709.0	14.1
1038-R-3	11.3	570	0.02	0.0958	0.01	4.80	1.20	0.2990	0.07	1902	255	1785	210	1686	367	1826	185
1038-C-2	7.4	247	0.03	0.1050	0.02	4.20	1.00	0.3230	0.08	1514	207	1674	195	1804	404	1600	150
1038-R-4	10	490	0.02	0.1290	0.03	6.90	2.00	0.3800	0.13	2121	355	2099	257	2076	607	2106	214
1097-C-1	34.3	157	0.20	0.0920	0.03	3.50	1.10	0.2810	0.08	1433	292	1527	248	1596	398	1492	224
1097-C-2	73	490	0.13	0.1620	0.02	9.80	3.40	0.4400	0.15	2472	214	2416	320	2351	672	2458	189
1097-R-2	42.5	120	0.36	0.1060	0.04	5.70	1.90	0.4000	0.15	1685	440	1931	288	2169	691	1863	261
1368-R-1	23.9	1170	0.02	0.1140	0.01	6.10	2.10	0.3200	0.11	2205	167	1990	300	1790	537	2167	132
1368-C-1	151	2040	0.07	0.0978	0.01	4.50	1.40	0.3000	0.10	1779	114	1731	258	1691	496	1768.9	88.7
1368-C-2	64	1140	0.05	0.1280	0.02	6.60	1.90	0.3700	0.13	2089	216	2059	254	2029	612	2076	131
1365-C-1	780	6900	0.10	0.1330	0.01	8.50	1.80	0.4260	0.07	2284	119	2286	192	2288	316	2284	116
1365-R-2	370	3700	0.09	0.1170	0.01	5.80	2.10	0.3500	0.14	1959	215	1946	314	1935	669	1955	162
1365-C-2	398	680	0.55	0.1240	0.01	7.50	1.20	0.4030	0.04	2164	175	2173	143	2183	198	2172	142
1365-C-3	56	690	0.10	0.1590	0.02	11.70	2.20	0.5000	0.13	2555	339	2581	176	2614	559	2576	163
1367-R-1	34.9	251	0.13	0.1830	0.03	14.00	3.50	0.5400	0.22	2725	286	2750	237	2783	921	2738.7	73.1
1367-C-1	63	1140	0.04	0.1060	0.02	5.70	1.10	0.3440	0.06	1959	165	1931	167	1906	297	1945	137
1367-R-2	119	1150	0.10	0.1130	0.01	6.20	1.50	0.3700	0.10	1979	200	2004	212	2029	471	1991	144

Table IV.6: continued

Sample	Th (ppm)	U (ppm)	Th/U	207Pb/206Pb	±2σ	207Pb/235U	±2σ	206Pb/238U	±2σ	207Pb/206Pb Age (Ma)	±2σ	207Pb/235U Age (Ma)	±2σ	206Pb/238U Age (Ma)	±2σ	Concordia Age (Ma)	±2σ
IC2-6A																	
1008-R-1	1040	4500	0.21	0.1650	0.01	9.30	1.30	0.3840	0.07	2612	178	2368	128	2095	326	2454.6	96.9
1008-C	3400	17500	0.18	0.1092	0.01	6.36	0.83	0.3960	0.06	1903	108	2027	115	2151	263	1962.1	81.3
1008-R-2	3980	15200	0.24	0.1082	0.00	6.81	0.23	0.4270	0.01	1890.3	42.4	2087.0	29.9	2292.2	63.2	2035.2	28.2
2303-R-1	67	189	0.33	0.1330	0.04	5.30	2.50	0.3400	0.13	1849	490	1869	403	1887	625	1863	385
2303-C-1	52	227	0.22	0.1290	0.03	6.20	1.70	0.3580	0.08	2037	335	2004	240	1973	399	2010	236
2303-C-2	78	339	0.23	0.1400	0.02	8.30	2.60	0.4100	0.12	2309	338	2264	284	2215	549	2280	258
2303-R-2	77	206	0.35	0.1160	0.03	6.70	2.60	0.3900	0.10	2023	470	2073	343	2123	464	2073	335
2055-R	30	87.8	0.26	0.1810	0.09	7.60	3.50	0.3100	0.10	2633	587	2185	413	1741	492	1897	616
1354-C-1	62	221	0.23	0.1600	0.05	9.10	4.30	0.3800	0.13	2593	479	2348	432	2076	607	2391	491
1354-C-2	63	217	0.24	0.1100	0.03	7.30	2.40	0.4100	0.11	2086	279	2149	294	2215	503	2113	256

IV.5. Discussion

IV.5.a. U-Pb Apatite dating: Pb diffusion or dissolution-recrystallization

Apatites in carbonatite have violet-bluish CL that is similar to magmatic apatites from alkaline rock complexes (Kempe & Götze, 2002; Tichomirowa *et al*. 2003; Chakhmouradian *et al*, 2008). Instead apatites from syenite sample have yellow CL that is typical of apatites in silicate melts (Tichomirowa *et al*. 2003; Demeny *et al*. 2004b; Karchevsky & Moutte, 2004; Chakhmouradian *et al*, 2008). While the main indicator for yellow CL colour is Mn^{2+}, that of bluish CL is the Eu^{2+} (Tichomirowa *et al*. 2003).

The 207Pb/206Pb corrected ages obtained on five apatite crystals vary between 1588 ± 124 and 2025± 142 Ma. There does not seem to be any relationship between these different ages and the position of analysis in the crystal (rim, center). The weighted average 207Pb/206Pb corrected ages for center and rim grains yields similar ages within the errors of 1867 ± 88 Ma (MSWD = 2.4, N= 8; Figure IV.2.b) and 1794 ± 57 Ma (MSWD = 2.2, N= 15; Figure IV.2.a) respectively, which implies that all these 5 grains record the cooling temperatures at the Eburnean event.

Allègre & Caby (1972) have obtained an age of ~ 2090 Ma on hydroxyapatite and Bernard-Griffiths *et al*. (1988) ~ 2000 Ma on zircon grain. The weighted average $^{207}Pb/^{206}Pb$ corrected age obtained on all rim and center apatites yields an age of 1834 ± 42 Ma (Figure IV.4). This age is recognized as metamorphic age of the In Ouzzal granulitic host rocks with ultra-hot-temperature peak of 1000ºC at 2000 Ma and cooling temperatures of 750ºC at 1800 Ma (Ouzegane *et al*. 2003 and references in). This age of 1834 Ma obtained on the apatites is younger than the ages of 2090 Ma and 1994 ± 22–17 Ma obtained by U/Pb on hydroxyapatite and zircon (Allègre et al. 1972 and Bernard-Griffiths *et al*. 1988) that were interpreted by these authors as the ages of setting up of the syenite-carbonatite complex.

Pb diffusion between the center and rim of carbonatitic apatite grains should be synchronous with the crystallization process. The closure temperatures for Pb in an apatite of 1cm effective diffusion radius for a cooling rate of 10ºC/Ma are 750ºC (Cherniak & Watson 2001), which imply a higher Pb closure temperature in apatite for higher effective diffusion radius. In the In Ouzzal terrane, temperature remains high for a long period, therefore the Ihouhaouene apatites probably have a slow cooling rate and slow mineral diffusion rate.

Apatites in syenite have low and heterogeneous Th concentrations (Table IV.4) compare to the carbonatitic-apatites. They are heterogeneous with obvious crystal growth and Mn-F-fluid interaction, characterized by a smaller grain size compare to apatite in carbonatites.

Ages recorded in apatite grains of syenite IC3-10 are much younger (~ 651 Ma) than the ages of carbonatitic apatites and correspond to the Pan-African event which is well-know in the Hoggar (800- 550 Ma). Therefore, syenites record the thermic event during the emplacement of alkaline granite-plutons (T>450ºC; Haddoum *et al*. 2013) in the Ihouhaouene area given that no Pan-African metamorphism had affected the In Ouzzal terrane rocks because of his refractory behaviour after the granulitic metamorphism (Ouzegane *et al*. 2003; Haddoum *et al*. 2013). A similar Pan-African age has been found by Carpena *et a l*(1988) by fission-track (~ 600 Ma) and suggested an exhumation age of carbonatites at Pan-African.

IV.5.b. U-Pb Zircon dating and growth in carbonatites and syenites

Zoning in Hf and Y have been observed in EMP maps but Pb couldn't be observed in CL zircon images because of its low abundance and the fact that its electronic structure militates against its being a CL activator in zircon (Cherniak & Watson, 2001). The EPMA data presented here, indicate that carbonatitic and syenitic zircons underwent recrystallization caused by infiltration of Si-rich carbonatitic late-stage melts.

Significant differences in geochemical composition of immiscible carbonate-melts and evolution in hybrid system led to different types of zircon recrystallization and isotope compositions of zircon grains in syenites. Hf in zircons is higher in syenite than carbonatite (Figure IV.11) and suggests that Hf increases in zircon with magmatic differentiation (Hoskin & Schaltegger 2003). Thus Hf decreases in carbonatitic zircon grains with high bulk-carbonatite Zr/Hf ratio (Figure IV.8a) and low bulk-carbonatite SiO_2 wt.% contents (Figure IV.11b) and increases in syenitic zircon grains with high-evolved bulk-syenite Zr/Hf ratio (Figure IV.11a) and SiO_2 wt.% contents (Figure IV.11b). HfO_2 values for nepheline-syenite zircon up to 3.3 wt.% have been reported in Belousova *et al*. 2002 and Guo *et al*. 1996.

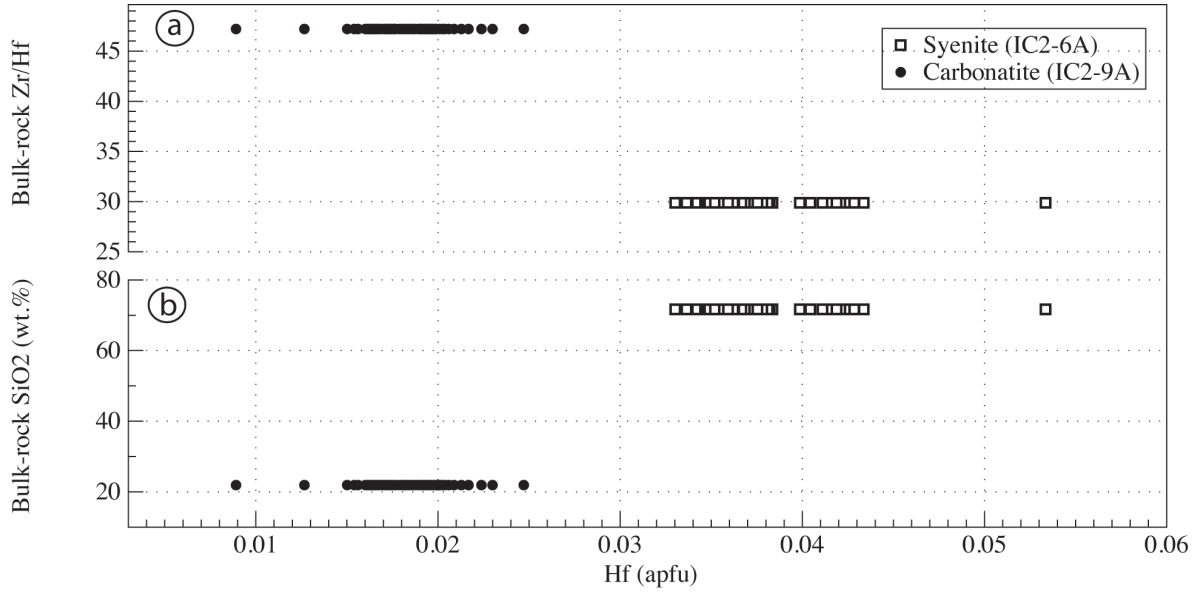

Figure IV. 11. Zircon Hf mineral chemistry variation from IC2-6A syenite and IC2-9A Si-rich carbonatite samples in molar units. **a.** Bulk-rock Zr/Hf versus Hf (a.p.f.u). **b.** Bulk-rock SiO_2 versus Hf (a.p.f.u).

Zircon crystals from Ihouhaouene carbonatites have low U and Th concentrations (U = 30.2-130 ppm and Th = 4.6-210 ppm) compare to zircons from associated syenites (U =96-17500 ppm and Th = 7.4-3980 ppm) (Table IV.6) and that are similar to concentrations in Kimberlitic zircons and significantly lower than other igneous zircons (Hoskin & Schaltegger 2003; Grims *et al*. 2007; Tichomirowa *et al* 2013). The incorporation of Th in zircon is primarily controlled by the availability of Th and U in the system and partitioning with other phases (Rubatto, 2017). The presence of Th-rich minerals as REE-rich apatite, britholite and monazite in carbonatites is the reason for low Th/U in coexisting zircons.

All dated carbonatitic zircons have Th/U ratio >0.1 (Figure IV.12a) and are intermediary to magmatic zircon types (Williams *et al*. 1996; Schaltegger *et al*. 1999; Rubatto *et al*. 2001). Two zircon compositions have Th/U ratio 0.1<Th/U<0.3 as intermediate between metamorphic and magmatic values (Rubatto *et al*. 2001; Hoskin & Schaltegger 2003; Teipel *et al*. 2004) and corresponding Concordia ages are of 1816 ± 91 Ma and 1840.9 ± 56 Ma (Table IV.6) and correspond to the metamorphic ages recorded in the In Ouzzal terrane (Ouzegane *et al*. 2003). The other (N=16) carbonatitic zircons have Th/U > 0.3 and correspond to magmatic zircons types (Rubatto *et al*. 2001; Schaltegger *et al*. 1999; Williams *et al*. 1996). While syenitic zircons have a wide range of Concordia ages with: 18 zircons have Th/U < 0.1 that can be considered as metamorphic zircons (Williams *et al*. 1996; Schaltegger *et al*. 1999; Rubatto *et al*. 2001), 28 syenitic zircons have 0.1<Th/U<0.3 (Figure IV.12b) (Intermediate values between magmatic and metamorphic zircons) and 8 zircons have 0.3<Th/U<0.55 (as magmatic zircons). All of syenitic zircons provide similar large U-Pb ages for all zircon types (Figure IV.12b). However, the Th/U> 0.1 ratios of zircons from carbonatites and syenites

suggest that they crystallized from intermediate to felsic melt source (Linnemann *et al*. 2011) (Figure IV.12).

Hoskin & Schaltegger 2003 recognized igneous zircons with Th/U ratios ≥0.5 and metamorphic zircons with Th/U ratios <0.01. Furthermore, Yakymchuk *et al*. (2018) considered that igneous zircons rarely have Th/U<0.1 and metamorphic zircons in ultra-high temperature granulitic conditions can have values ranging from Th/U< 0.01 to > 10 and that in the presence of Th-rich minerals as monazite and allanite. That suggests that all Th/U ratios from carbonatitic and syenitic zircons cannot be discriminant for a magmatic or metamorphic zircon origin because of the high amounts of Th-rich minerals in the Ihouhaouene alkaline rocks.

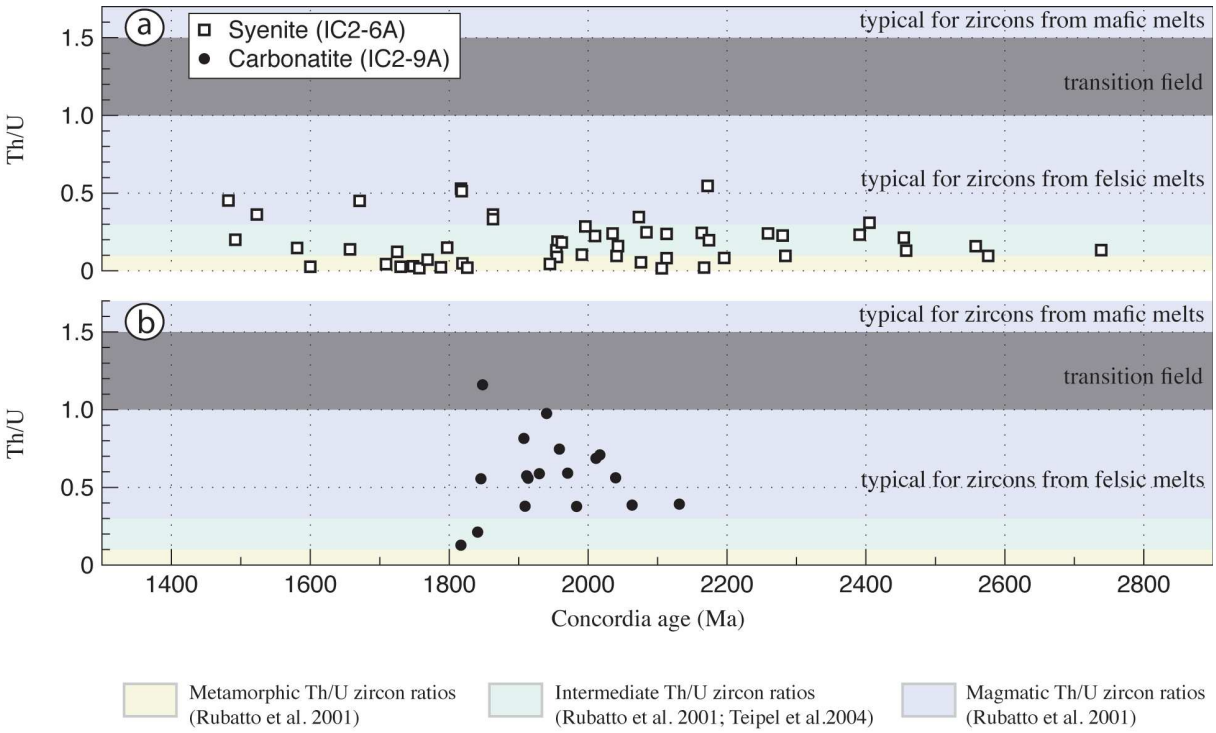

Figure IV. 12. Th/U versus U-Pb ages of Zircons showing the magmatic or metamorphic zircon type following Rubatto *et al*. 2001 and Teipel *et al*. 2004 and the felsic, intermediate or mafic source type for magmatic zircons (Th/U>0.3) following Linnemann *et al*. 2011 for **a.** syenites and **b.** carbonatites.

IV.6. Conclusion and outlook

Apatites from Ihouhaouene carbonatites recorded the metamorphic Eburnean age of the granulitic host rocks of In Ouzzal terrane. This age may be metamorphic and/or magmatic age of carbonatite on account of the homogenous composition of apatites and the lack of crystal growth and fluid interaction features. While the syenite apatites recorded a late fluid-rock interaction at low temperatures during carbonatite and syenite exhumation at Pan-African orogeny. Apatites from carbonatite don't record this low T° event and that could probably be related to their pegmatitic dimensions in different mineralogical nature of calcitic material formed of crystals with strong thermal expansion anisotropy compare to the smaller apatites in syenite, that are surrounded by K-feldspar and clinopyroxene.

Zircons from Ihouhaouene carbonatites have low Th/U ratio values $0.1<Th/U<1.16$ compare to the atypical Th/U zircon ratio from carbonatites (e.g. Zircons from carbonatites from the Kola Peninsula, Russia have Th/U ratios varying up to 9000; Amelin & Zaitsev, 2002). Th/U ratios don't allow us to attribute them a magmatic origin because of the high Th and U contents in carbonatites. In the case they have a magmatic source they may suggest an intermediate to felsic melt source (Hoskin & Schaltegger 2003; Liu *et al*. 2008; Linnemann *et al*. 2011). Magmatic Proterozoic zircons from Hoggar have Th/U ratios higher than 1.5 and derived from mafic magmas (Linnemann *et al*. 2011). Therefore Ihouhaouene carbonatites couldn't arise directly from mantle and the carbonatitic zircon compositions confirm their origin by immiscibility from an evolved CO_2-Si-rich magma. Zircons from Ihouhaouene syenites have intermediate Th/U ratio values $0.1<Th/U<0.55$ (felsic melt source) and different U-Pb Concordia ages. This ion probe analyses disturbance in zircons crystals on thin sections didn't appear in CL images and that could be attributed to mixing as consequence of combining isotope information from distinct fractionation and immiscibility-hybridization episodes during the magmatic event and/or to the inherited zircons of granulitic metamorphism in the In Ouzzal.

That is accurate in the case we consider the analysed zircons in carbonatites as magmatic grains. Although, the crystallization of apatite, monazite, allanite and britholite in carbonatites in magmatic to sub-magmatic environments may influence the Th budget of the rock and the Th/U of equilibrated zircon in magmatic and sub-solidus conditions then the data presented here can not form a discriminant results for the Ihouhaouene carbonatitic magmatic or metamorphic history. The in situ LA-ICP-MS method on thin section facilitates dating high zircon number during an analytical session and allows to determine the position of zircons related to the associated minerals but not the structure and texture of zircon grain as core or rim crystal-region in 3D. Thus, zircons in syenites require more textural study on separated zircon grains to more understand the U/Pb isotopic compositions and relationship to the carbonatitic zircons and the In Ouzzal granulitic host rock.

Acknowledgments:

This work was financially supported by the FP7-PEOPLE-IRSES project MEDYNA (2014–2017) "Maghreb -EU research staff exchange on geodynamics, geohazards, and applied geology in North-west Africa". The help of Françoise Roger gratefully acknowledged. We thank Romain Lafay and Loic Blanchard for their appreciated analytical work and we thank C. Nevado and D. Delmas for their technical assistance.

Discussion

Carbonatite and CO_2-rich alkaline magmas are ideal for monitoring the evolution of the sub-continental upper mantle because they rise up rapidly to the surface (low density and low viscosity) and thus the crustal contamination is reduced.

The edge of carbonatites over oceanic basalts is that they can be used to track the temporal evolution of the mantle over a considerable part of the Earth's history. Carbonatites are present on the continents in significant volumes and occur since Archaean ages (e.g. 2.68 Ga Lac Shortt carbonatite, Quebec). Hence, carbonatites and alkaline magmas are window on deep processes and allow characterization of the nature of deep mantle they derived from and understanding global geochemical and geodynamic cycle. The questions related to carbonatite petrogenesis are:

- Whether carbonatite melts are primary melts derived from carbonatitic mantle source? Or whether they are derived from a carbonated-silicate parent melt by fractional-crystallization and immiscibility?
- What is the relationship between carbonatites and the associated alkaline rocks?
- What is the composition of the CO_2-rich parental melt?
- Are REE in carbonatites from magmatic processes? Or the result of late-enrichment processes?

This thesis carries out some key results to these major questions about the petrogenesis of carbonatites through the detailed petro-geochemical study of the Proterozoic carbonatites and associated syenites of Ihouhaouene area in South Algeria.

Are carbonatites derived from primary carbonated mantle melt or by fractional-crystallization-immiscibility processes? And what is their relation with the associated silicate rocks?

The intra-cratonic Ihouhaouene carbonatites and syenites are silica-saturated, syn-orogenic and form linear intrusive rock outcrops in large shear-zones. They are characterized by the absence of felspathoids and differ from the most typical petrographic environment of intrusive carbonatites in intra-cratonic settings that includes a broad spectrum of silica-undersaturated peralkaline rocks, including melilitolites, foidolites and foid syenites (Chakhmouradian et al, 2008). These types of rocks are not recognized in Ihouhaouene area.

Only few localities reported carbonatites and silica-saturated syenites similar to Ihouhaouene igneous complex, whereas the cogenetic relationship between alkaline rocks and carbonatites have not been studied; Eden Lake in Canada (Chakhmouradian et al. 2008), Murun, Khalyuta, Oshurkovo and numerous other localities in eastern Siberia (Konev et al. 1996; Yarmolyuk et al. 1997; Nikiforov et al. 2003), Mushugai-Khuduk, Bayan Hushuu, Tsogt-ovoo and Ulugei in Mongolia (Samoylov & Kovalenko, 1983), Dalucao and Maoniuping in China (Xu et al. 2003; Hou et al. 2006), Sevathur and Samalpatti in India (Viladkar & Subramanian, 1995; Schleicher et al. 1998), Dunkel'dyk in Tajikistan (Faiziev et al. 1998), Loch Urigill in Scotland (Young et al. 1994), Halpanen and Naantali in Finland (Puustinen & Karhu, 1999; Woodard and Hölttä, 2005), and El Picacho in Mexico (Ramírez Fernández et al. 2000).

The petro-mineralogical and geochemical study of Ihouhaouene igneous complex permits to determine a cogenetic relationship between carbonatites and syenites. Through the structural relationships, the bulk-rock compositions and mineral chemistry of apatite and clinopyroxene in both carbonatites and syenites we highlight important features and similarities of these two rock types:

(1) Ihouhaouene carbonatites and syenites are intimately related. They have close spatial distribution on the field and share the same magmatic mineral assemblages of apatite and clinopyroxene in all rock facies. Whole-rock major- and trace-element compositions of carbonatites and syenites characterize four rock facies as function of silica contents and present a continuous range from continuous range of CO_2 and silica whole-rock compositions from silica-poor carbonatites to silica-rich (red) syenites suggesting a cogenetic evolution from the same parental melt between all rock facies.

(2) Mineral compositions of apatite from Si-rich carbonatites and White syenites have extreme enrichment of LREE and Pb, Th compared to coexisting clinopyroxenes and apatite compositions from Si-poor carbonatites and red syenites. Recalculated liquids in equilibrium with apatite and clinopyroxene from apatite and clinopyroxene in carbonatites and syenites have different subchondritic to superchondritic Nb/Ta ratio (0.8-110; $Nb/Ta_{chondrite}$=18; Sun &

McDonough 1989) suggesting that they crystallized from different carbonate-rich silicate melt and form hybrid mineral aggregates that did not re-equilibrate afterwards:

a- The high LREE and chondritic to superchondritic Nb/Ta ratios in recalculated equilibrium melts from apatite and clinopyroxene in Red syenites are similar to melilititic and nephelinitic compositions and reflect differentiated silicate-melt compositions by fractional crystallization and immiscibility.

b- The high LREE and elevated superchondritic Nb/Ta values in Si-rich carbonatites from Ihouhaouene complex are coherent with Nb/Ta ratios in experimental carbonatites as a result of immiscibility processes from carbonate-rich silicate melts (Koster van Groos & Wyllie 1968; Wyllie & Huang 1975; Freestone & Hamilton 1980; Kjarsgaard & Peterson 1991; Dalton & Wood 1993; Kjarsgaard *et al*. 1995; Mitchell 2009; Novella & Keshav 2010; Brooker & Kjarsgaard 2011; Martin *et al*. 2013).

c- The high superchondritic Nb/Ta values in minerals in white syenites like in Si-rich carbonatites suggest that Nb-Ta compositions were largely disordered in whole rocks compositions by the hybridization process and indicate that apatites in white syenites crystallized from carbonatitic melts.

d- The low LREE and low Nb/Ta values observed in Si-poor carbonatites exclude its origin either as a primary carbonate melt from the mantle or as a segregated carbonate fraction from a primary CO_2-rich silicate melt and require segregation from geochemically evolved silicate melts.

In this scheme, the carbonatite and syenite rock facies reflect the parental melt compositions inherited from complex differentiation stages of carbonated-silicate melt as a result of several steps of fractional crystallization and carbonated melt immiscibility unsettled by hybridization process that we illustrate by the proposed geodynamic model (Figure 8).

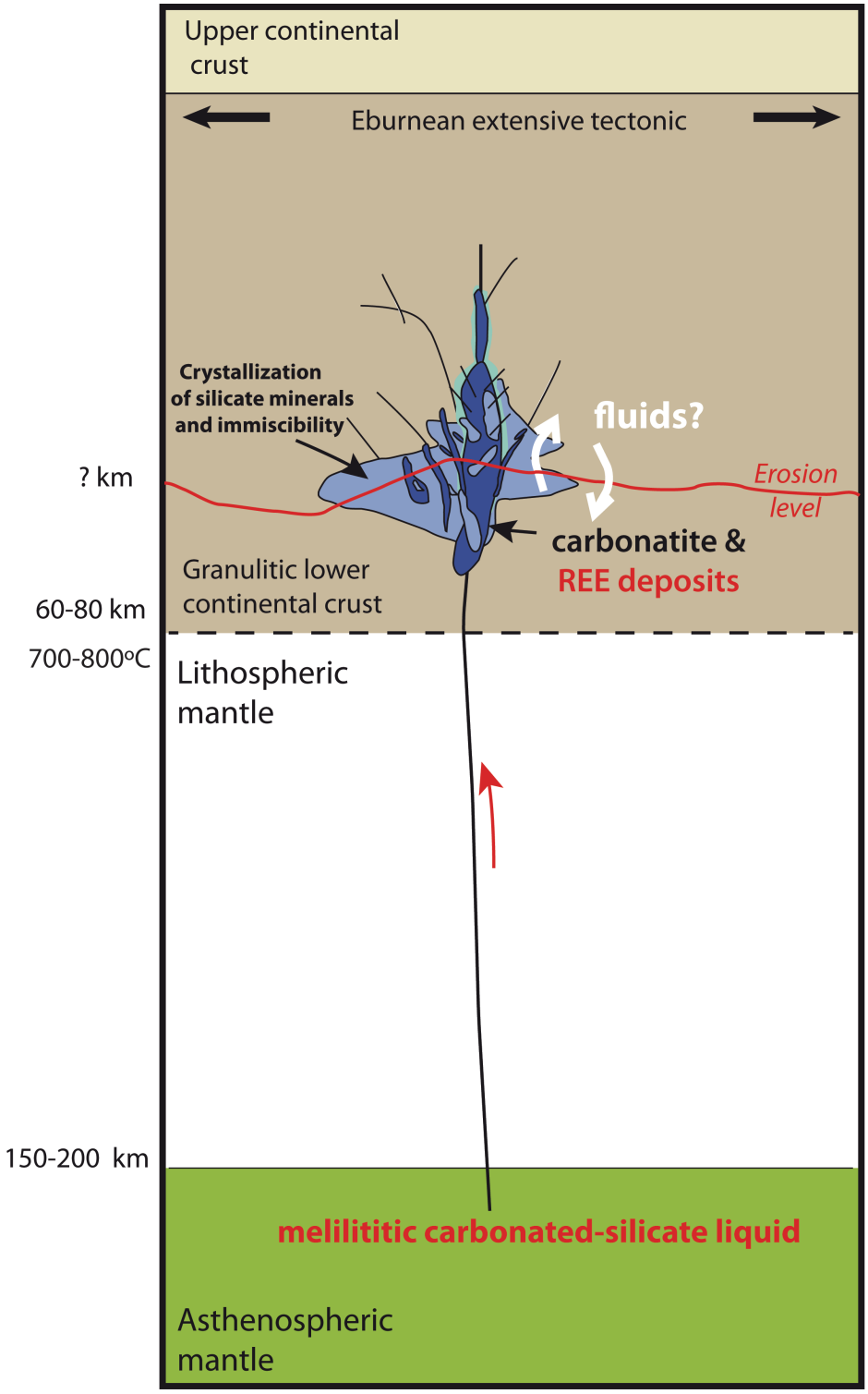

Figure 8. Conceptual representation of the geodynamic emplacement of Ihouhaouene carbonatite and syenite association in the In Ouzzal terrane at the Eburnean tectono-metamorphic period.

What is the composition of the mantle and the carbonated-silicate primary melt they derived from? And which parameters control such Nb/Ta variation in immiscible carbonated melts?

To explain the complex evolution of silicate melts in the Ihouhaouene area and reproduce the melt source compositions, I performed a numerical model (Chapter II) using a stepwise approach integrating two *Rayleigh distillation equations*, alternately. I used the fractional crystallization equation for the mineral (clinopyroxene and apatite) segregation and an equation formally similar to the fractional melting equation (Shaw 1970) for the segregation of immiscible melt fractions.

Ihouhaouene carbonatites with high Nb/Ta are Si-rich and don't have pure carbonatite composition in a silica-undersaturated rock system as in experimental studies. Therefore the choice of partitioning coefficients between carbonate and silicate melts is imperative for the calculation of petrogenetic model. Partition coefficients are considered constant within a given step of melt segregation but they strongly depend of parental melt compositions (Martin *et al*. 2013). To account for the parental melt evolution, I used liquid/liquid partition coefficients deduced from the equilibrium melt compositions calculated in my study (Chapter II).

My results for Ce/Lu vs Nb/Ta behaviour from successive numerical experiment A and B, using a primary melilitite composition (Baudouin *et al*. 2016) as initial parental melt and liquid/liquid partition coefficients inferred from average equilibrium between apatites in Si-rich carbonatites and clinopyroxene in red syenites for model A and from equilibrium between apatites and clinopyroxenes in White syenites for model B suggest that:

- The high Nb/Ta and LREE/HREE apatite equilibrium melts from Si-rich carbonatites represent a poorly evolved magma from low immiscible melt fractions (F).
- The low Nb/Ta and LREE/HREE apatite and clinopyroxene equilibrium melts from red syenites represent segregated silicate melt fraction from a poorly to mildly evolved parental magma.
- Hybridization and mingling of both carbonated immiscible fractions and segregated silico-carbonated melt fractions induce evolved-mixt parental melt with hybrid mineral compositions for evolved immiscibilities.
- The low Nb/Ta and LREE/HREE clinopyroxene equilibrium melts from white syenites represent a segregated carbonated melt from the evolved-mixt magma.
- The low Nb/Ta and High LREE/HREE apatite equilibrium melts from Si-poor carbonatite represent a strongly evolved magma from high immiscible melt fraction (F).

The petrogenetic numerical model of carbonatites and syenites highlight three key parameters among other than hybridization that explain the atypical Nb/Ta compositions and the high REE concentrations observed in Ihouhaouene:

- *Initial melt compositions* control the *coefficient partitioning* behaviour of Nb, Ta and rare earth elements between the segregated carbonate and silicate melts during immiscibility process.

- *The immiscibility rate "F"* strongly controls the REE distribution and Nb/Ta ratio systematics between segregated carbonated and residual silicate-melt fractions.

- *The fractional crystallization rate ("f") after each immiscibility step* controls the REE concentration in the residual silicate-melt fractions and thus the parental melt increments.

The reproduced compositions of Ihouhaouene carbonatites and syenites through the petrogenetic modelling of the complex processes (fractional-crystallization immiscibility and hybridization) suggest that the alkaline complex derived from a carbonated-silicate melt of a melilititic composition.

Dalton and Presnal (1998b) demonstrated experimentally the continuum between carbonatite and silicate melts and denoted the carbonatite-kimberlite transition at the 6 GPa isobar. Moore and Wood (1998) report the carbonatite to melilitite melts transition at the 3 GPa isobar (Hamouda & Keshav, 2015). The silicate melts composition as kimberlitic or melilititic composition can result from melting of the same source and it is a matter of degree of melting (of no more than 1%) and variation of temperature and pressure (Gudfinnsson & Presnall, 2005; Keshav & Gudfinnsson, 2013; Novella *et al*. 2014; Keshav & Hamouda, 2015) and liquid immiscibility at low pressure (~2–2.6 GPa) could be behind silicate and carbonatitic liquids observed in nature.

The high silica contents in Ihouhaouene alkaline complex can be the result of early crustal contamination during magmatic evolution affecting the melilitite magmatic precursor of carbonatites. This contamination event is observed in the uncommon isotopic signatures of $\varepsilon ND_{(T)}$ and $\varepsilon Sr_{(T)}$ (Ouzegane *et al*. 1988; Bernard-Griffiths *et al*. 1988) suggesting an enriched source.

Otherwise calciocarbonatites can be generated through reaction of carbonated melts containing H_2O or other volatiles with depleted harzburgitic or lherzolitic assemblages at low pressures (15 Kbar, 1150ºC) (Dalton and Wood 1993). However, carbonated harzburgitic assemblages would produce more magnesian melts while residual wehrlites are in equilibrium with calcic melts (Dalton and Wood 1993).

Furthermore, the petrogenetic modelling of Ihouhaouene calcic carbonatite and syenite involve immiscibility and fractional crystallization processes at the origin of the carbonated and alkaline segregated melts. Immiscibility of calcio-carbonatites has been observed in experiments of carbonated eclogites melting and on carbonate stability during subduction and show that, in the case carbonates are carried by silica-saturated (tholeiitic) crust, they will not survive transport to depths greater than 300 km (Hammouda & Keshav, 2015). However, In the case of continents, the low Tº gradients tend to stabilize solid carbonates at depths. And then, carbonatitic magmas observed in continental areas, if primary, must be caused by thermal perturbation of regions by carbonated melt metasomatism (mantle plumes?).

The subchondritic to superchondritic Nb/Ta ratio of the modelled equilibrium melts from melilititic (30 wt.% CO_2) and evolved silico-carbonated hybrid parental melts and calculated partitioning coefficients from Ihouhaouene apatites and clinopyroxenes involve partial melting (<1%) of melilitite from carbonated REE-rich mantle and separation of immiscible carbonate melts with low segregation rates less than 1 % (0.01 and 0.08 %) from differentiated silicate melts. The Ihouhaouene carbonatites present evidence for carbon in the Archaean mantle and the question of carbon mass-balance at this period of the Earth's history remains critical.

Are REE in carbonatite from primary melt or the result of late-enrichment processes?

Ihouhaouene carbonatites have high concentrations in rare earth elements (up to 7000*Chondrite) that are essentially controlled by apatite megacrysts and represent one of the most global rare earth resources carbonatite related deposit. The Si-rich and Si-poor carbonatites in Ihouhaouene are characterized by the presence of Si-rich and Si-poor apatites, respectively. Both rock facies have inclusion-free apatites and inclusion-bearing apatites. REE-rich inclusions in Ihouhaouene apatites are britholite exsolutions and monazite-quartz-calcite assemblage that are two of the most important REE minerals.

The petro-geochemical and micro-structural study of apatites and REE-rich britholite exsolutions and monazite inclusions from Ihouhaouene carbonatites allow us to highlight chief features of REE-enrichment processes and determine the fluid compositions at sub-magmatic stage:

(1) Inclusion-free apatites from Ihouhaouene carbonatites are remarkable by their pegmatitic size-grain and present tracer of primary carbonate-silicate melt composition from which they crystallized, whereas inclusion-bearing apatite record sub-solidus reactions involving possible fluid-rock interactions.

(2) REE-Th-rich britholite and monazite-quartz-calcite inclusions in apatites from Ihouhaouene carbonatite complex present chemical and textural variations through all rock facies and attest of different REE- rich fluid-rock re-equilibrations.

(3) Both inclusion-free apatite and inclusion-bearing apatite (britholite or monazite) have similar geochemical Nb/Ta signature suggesting that Nb and Ta do not fractionate during fluid-apatite re-equilibrations and all apatites have magmatic signature.

Therefore, Ihouhaouene apatites record variable degree of fluid-rock interactions. The presence of inclusion-free apatites in Si-rich and Si-poor carbonatites and different apatite mineral-inclusions imply that carbonatites underwent fluid re-equilibration starting from shortly after crystallization and continuing down to ambient P-T conditions.

What is the composition of fluids responsible for REE-britholite exsolution in Si-rich apatites and REE- monazite quartz and calcite inclusions in Si-poor apatites?

The fluid composition in equilibrium with britholite- and monazite-bearing apatites can be addressed, considering the REE-bulk-apatite compositions with and without inclusions in both Si-rich and Si-poor rock facies and compared with the correspondent in-situ compositions:

(1) The REE bulk-apatite composition of free-inclusion apatites from both Si-rich and Si-poor carbonatites have close compositions to their correspondent in-situ apatite composition and have high REE concentrations.

(2) The bulk britholite-bearing Si-rich apatite have slightly higher LREE concentrations than bulk free-inclusion Si-rich apatite owing to the britholite REE rate from fluid import.

(3) Both inclusion-free Si-rich apatites and britholite-bearing apatites have high in-situ REE and SiO_2 (~ 5 wt.%) contents indicating that they crystallized from a melt with high silica activity at magmatic conditions.

(4) The high Cl, Th and U in britholite exsolutions compared to the Si-rich host and inclusion free-apatite corroborate the presence of saline fluid during cooling and re-equilibration at subsolidus conditions.

(5) The bulk monazite-bearing Si-poor apatite have slightly lower LREE composition than bulk free-inclusion Si-rich apatite owing to the apatite-fluid re-equilibration.

(6) The presence of quartz and calcite inclusions with monazite in Si-poor apatite strongly suggests sub-solidus reaction and the presence of Si-CO_2-bearing supergene fluids.

(7) The high content of sulphur (~ 1.7 wt.%) in monazite compare to the low content in hosted-apatite and inclusion-free apatite indicate the presence of sulphur-bearing fluid during re-equilibration at subsolidus conditions or mass transfer in expense of precursor apatites.

These close chemical features of apatites and britholite and monazite-quartz-calcite inclusions are supported by the microstructural texture results on that I carried out on inclusion-bearing apatites by EBSD measurements:

(1) Britholite crystallizes with a-, m- and c- axes in the same orientation that a-, m- and c- axes of host-apatite and britholite orientation rotates as observed for apatite in progressive replacement and crosscut the apatite sub-grains.

(2) Monazite has the b- axis orientation parallel the c axis (0001) orientation of host apatite and the same a- and c- axes orientations follow the a- and m- axes of apatite. Whereas quartz has the same axes orientations than apatite.

Accordingly, to explain the crystallization environment and the rock-fluid interaction and re-equilibration at subsolidus conditions leading to the britholite and monazite-quartz-calcite inclusions in apatites from the Ihouhaouene carbonatites I assumed that inclusion-free apatites are representative of magmatic apatite before britholite exsolution and monazite inclusions. In this case, the exchange reaction for cationic mass balance for both britholite-apatite and monazite-apatite according to two re-equilibration and diffusion reactions indicate that incorporation of REE into apatite structure and britholite exsolution are induced by substitution of P, Ca by Si and Cl-Th-REE-rich fluids during subsolidus conditions. Likewise monazite-quartz and calcite inclusions are formed during S-Ca-P-CO_2-rich fluid-apatite re-equilibration and mineral diffusion.

Therefore, Ihouhaouene apatites record variable degree of fluid-rock interactions. The presence of inclusion-free apatites in Si-rich and Si-poor carbonatites and different topotactic apatite mineral-

inclusions indicate that carbonatites underwent different fluid re-equilibration and oriented fluid reaction starting from shortly after crystallization and continuing down to ambient P-T conditions. Furthermore, the REE-enrichment processes in Ihouhaouene complex reveal an early sub-magmatic stage, that can represent an early stage of the two world's major ore-deposits at Bayan Obo and Mountain Pass, where a multistage history of REE-deposition and enrichment are observed (Figure 9).

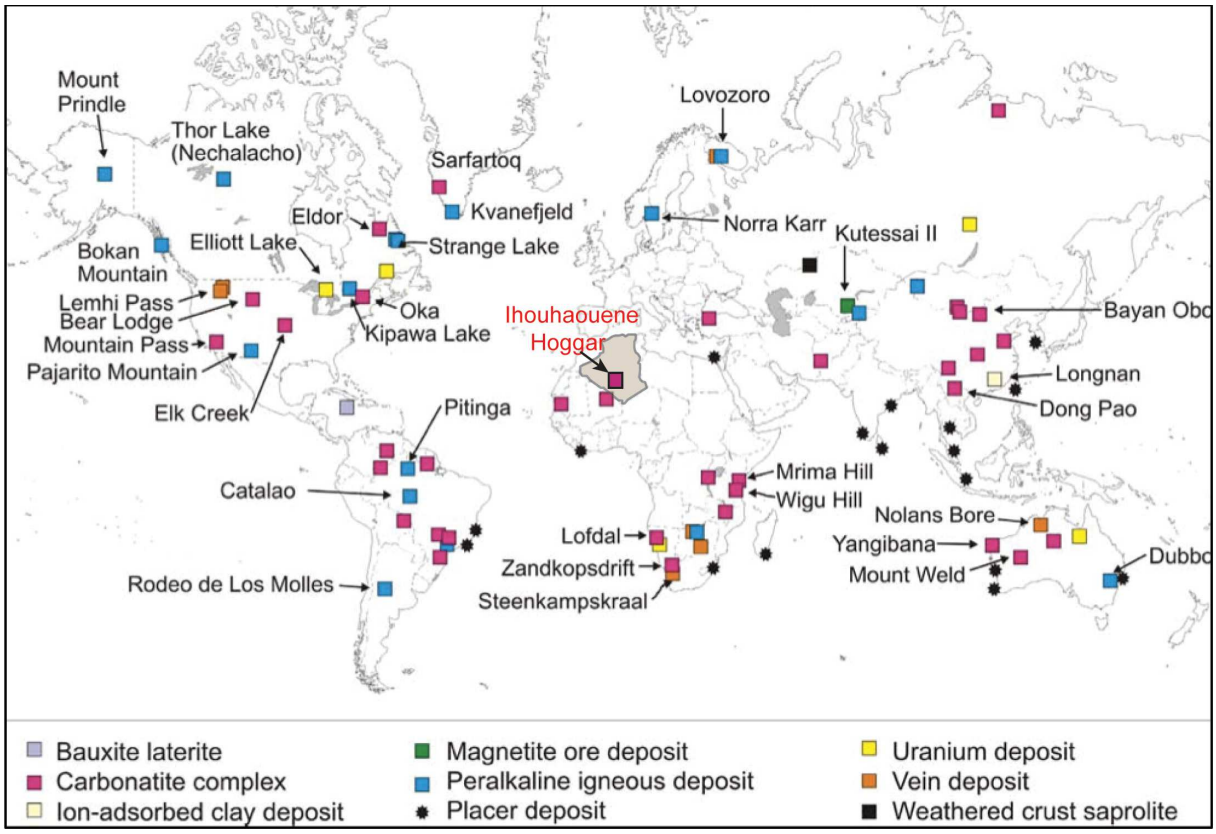

Figure 9. Worldwide map distribution of REE ore deposits (Modified after Mariano, Cox, Hedrick).

Ihouhaouene carbonatite and syenite complex in the regional tectono-metamorphic context

The detailed petro-geochemical results in the first part of my thesis on carbonatites and syenites from Ihouhaouene indicate a cogenetic relationship between these two types of rocks.

Based on the 2090 Ma and 1994 ± 22–17 Ma U-Pb ages obtained previously from apatite and zircon in carbonatite by Allègre et al. (1972) and Bernard-Griffiths et al. (1988), respectively, the alkaline complex of Ihouhaouene was emplaced at the period of transition between the Archaean primitive earth environment and the regional ultra-high-temperature metamorphic event at Eburnean in the In Ouzzal terrane. However, the U-Pb determined age by Bernard-Griffiths et al. (1988) characterizes the age of carbonatites from a single zircon grain, the reason why more detailed geochronological study in my thesis has been performed to confirm and better constrained the relationship between carbonatites and syenites. The age of the Ihouhaouene complex allow us to replace the magmatic occurrence in the regional tectono-metamorphic context of the In Ouzzal terrane.

LA-ICP-MS U-Pb dating on apatites and zircons from Ihouhaouene carbonatite and syenite thin section samples from this study allow to bring up the following ages and open even more questions on the complexity of the emplacement context of carbonatite and syenite rocks of Ihouhaouene:

(1) The apatites in carbonatite sample have homogeneous violet-bluish cathodoluminescence colour by Eu^{2+} indicator and do not have any obvious zoning.
(2) The U-Pb ages from the center to the rim of carbonatitic apatite vary from 1744 ± 106 Ma to 2025 ± 142 Ma and 1588 ± 124 Ma to 1976 ± 154 Ma respectively, suggesting Pb diffusion in the apatite crystal but the weighted average $^{207}Pb/^{206}Pb$ corrected ages obtained to the center and rim grains yields similar ages within errors (1867 ± 88 Ma; 1794 ± 57 Ma, respectively) that correspond to the peak and cooling ages of eburnean ultra high temperature metamorphism in the In Ouzzal terrane.
(3) The apatites in syenite samples have heterogeneous yellow cathodoluminescence colour with obvious crystal recrystallized zones revealed by Mn^{2+} indicator.
(4) The U-Pb Ages recorded in the core and rim of apatites from syenites are much younger ~ 651 Ma, than the carbonatitic ages and correspond to the Pan-African event in the Hoggar (800-550 Ma).

For a cooling rate of 10ºC/Ma, the Pb diffusion in apatite is not effective when the diffusion radius is higher than 1cm and thus the closure temperature is higher than 750ºC (Cherniak & Watson 2001). The In Ouzzal temperatures at 2000 Ma has been estimated at 1100ºC and decreased to 750ºC at 1800 Ma (Ouzegane et al. 2003). This implies that high temperatures remain for a long period of time, and the Ihouhaouene carbonatitic apatites may have recorded In Ouzzal metamorphism over 200 Ma. However the lack of zoning and mineral growth textures in carbonatitic apatite suggests slow cooling and mineral diffusion rates.

In addition, the ages recorded in syenite are Pan-African; a tectonic event characterized by the emplacement of granitic plutons in the In Ouzzal terrane where temperatures were up to 450ºC. These temperatures may result in Pb diffusion in apatite (with a small effective diffusion radius) and apatites are more susceptible to low temperature fluids because of their small apatite grains. A similar age has been found by Carpena *et al*. 1988 by fission-track (~ 600 Ma) and suggested an exhumation age of carbonatites and syenites at Pan-African.

The ages determined on apatite correspond to the Eburnean metamorphic age in the In Ouzzal terrane that don't correspond to the crystallization age obtained by Allègre et al. 1972 at 2090 Ma in carbonatite, that is 90 Ma older than the eburnean peak metamorphism (1100ºC) of In Ouzzal terrane (2000 Ma), suggesting that magmatic intrusion occurred close to or before the 2100-1800

***Ma UHT metamorphism in the In Ouzzal terrane and the crystallization of carbonatites cover all this period. The syenites, on the other hand, recorded an exhumation age at the Pan-African ~* 651 Ma.**

What is the magmatic age of associated syenites?

(1) Zircons in carbonatite and syenite have obvious Hf and Y zoning in the EMP maps. This implies different fluid infiltration in late-stage melts leading to zircon crystal-growth with different isotopic compositions on account of the significant differences in geochemical composition of immiscible carbonate-melts and evolution in hybrid system.
(2) Zircons in syenite have higher Hf contents than zircons in carbonatite suggesting that Hf increases in zircon with magmatic differentiation and corroborate the fact that Hf has high partitioning in the segregated silicate melts from immiscibility process.
(3) Carbonatitic zircons have 0.1<Th/U< 1.16, whereas zircons in syenite have 0.01 <Th/U< 0.55.
(4) The zircon calculated Concordia ages in carbonatites are between 1840 ± 56 Ma and 2131 ± 88 Ma, whereas syenite contains multiple age population of zircons (2738. ± 73 Ma to 1657 ± 87 Ma) where the ages obtained in carbonatite are recorded in syenite zircons.

The period 2100 - 1800 Ma in the In Ouzzal terrane corresponds to the UHT metamorphic events whereas the period between 2700 and 2500 Ma correspond to the Archaean ages of the cratonic in Ouzzal unit. The geodynamic signification of the transition period between 2500 and 2100 Ma in the In Ouzzal correspond to the Archaean-Eburnean transition characterized by a multitude of extension episodes and active shear-zones as observed in the Guinean Archaean domain of the West African Craton that suggest the emplacement of Ihouhaouene carbonatites and syenites in a extensive tectonic and explain their emplacement in shear-zones and the linear magmatic textures of syenites.

The oldest ages recorded in apatites and zircons from carbonatite and syenite in Ihouhaouene reveal crystallization close to or before the UHT metamorphism in In Ouzzal terrane. This suggests crystallization of the alkaline complex may be around 2162 Ma (Concordia age of zircons from syenite) considering the Archaean zircon ages and the late Eburnean zircons as inherited ages. However, the complex geodynamic history of Ihouahouene complex required additional dating (e.g. monazite, allanite, and additional apatite and zircon) to reconstruct accurate magmatic and metamorphic geochronology events.

Conclusion et perspectives

The bulk rock and mineral geochemistry of carbonatites and syenites allow us to determine four rocks facies: Si-rich and Si-poor carbonatites and Red and White syenites. The equilibrium melts compositions of these rock facies have subchondritic to superchondritic Nb/Ta geochemical signatures and reflect different parental melt compositions inherited from previous differentiation stages of carbonated-silicate melt as a result of several steps of carbonated melt immiscibility. These processes are mainly accompanied by hybridization that assemblage crystallized minerals from distinct melt compositions.

All the rock facies have high bulk REE and segregated from a primary CO_2-rich silicate melt that evolved during immiscibility process and form evolved carbonated and silicate melts.

The geochemical model proposed in my thesis explain the subchondritic to superchondritic Nb/Ta ratio equilibrium melts and involve partial melting of carbonated REE-rich mantle and separation of immiscible carbonate melts with low segregation rates less than 1 % (0.01 and 0.08 %) from melilititic and evolved silico-carbonated hybrid parental melts. Hybridization in the atypical Ihouhaouene system induces important variations in coefficient partitioning behaviour of Nb, Ta and rare earth elements between the segregated carbonate and silicate melts during immiscibility process.

The Ihouhaouene immiscible carbonatites and syenites are well preserved and characterized by exceptional occurrence of REE–rich minerals, britholite, monazite, and allanite and thus represent a unique opportunity to trace tardy-magmatic processes and re-equilibration at sub-solidus conditions. More specifically, the enrichment and distribution REE in apatite may represent an early stage before extreme REE-deposition and REE-oxides crystallization (e.g. Bastnasite) link to complex metamorphic events as observed for the two world's major ore-deposits Bayan Obo, Mountain Pass and Mount Weld. The incorporation of REE into apatite structure in Ihouhaouene carbonatites and syenites is assisted by the high silica composition of the alkaline magmas and substitution of P, Ca by Si, REE and from REE-rich fluids during subsolidus conditions. The intrusion of CO_2-rich alkaline magmas beneath the continental craton Hoggar occurred at the beginning of the eburnean (2Ga) tectono-metamorphic event in the In Ouzzal terrane. The alkalinity and volatile rich- character of primary magmas clearly highlights the presence of CO_2-rich lithospheric or asthenospheric mantle beneath the In Ouzzal craton that may be similar to the CO_2-rich mantle beneath all the gathered cratons at the Paleoproterozoic period such: the Siberian craton (Russia), West African craton (Algeria, Morocco and Mauritania), the Kaapvaal craton (South Africa) and the Amazonian craton (Brazil) characterized by several carbonatitic-alkaline complex occurrences. Exhumation of Ihouhaouene continental crust occurred at 651 Ma synchronous to the Pan-African tectono-thermic event and the amalgamation of the several terranes in the Hoggar by the suturation of the oceanic areas between them.

- **Outlook**

The complexity of multistage processes involved during the formation of igneous alkaline complex has led to several open questions that still need to be addressed:

- Origin of deep carbon – composition of deep fluid
  - H_2O in cpx => H_2O in magmas

- Magma transfer from asthenospheric/lithospheric mantle to the crust – alkaline magma = low partial melting.
  - Experimental for phase equilibrium and fractional – crystallization + immiscibility from high SiO_2 and CO_2 melt composition = corroborate the proposed geochemical model.

- Depth of magma intrusions - Metamorphic conditions (P, T, fluid) involved in sub-solidus environment (REE enrichment)
  - P-T modelling of synchronous Ihouhaouene granulites.
  - Experiment for apatite-britholite – determine the solvus as a function of temperature.

- Role of inherited structures during magma genesis and evolution. Age of fluid transfer and mantle metasomatism, contribution of granulitic continental crust, role of tardi-magmatic events on mineral equilibration (e.g. Pan-African events)
  - U-Pb dating monazite, allanite + zircon
  - Hafnium

Références bibliographiques

Adjerid, Z., Ouzegane, Kh, Godard, G. & Kienast, J.R., 2008. First report of ultrahigh-temperature sapphirine + spinel + quartz and orthopyroxene + spinel + quartz parageneses discovered in Al-Mg granulites from the Khanfous area (In Ouzzal metacraton, Hoggar, Algeria). The Boundaries of the West African Craton. Geological Society, London, Special Publications, 297, 147–167.

Adjerid Z, Godard G, Ouzegane K, Kienast JR (2013) Multistage progressive evolution of rare osumilite-bearing assemblages preserved in ultrahigh-temperature granulites from In Ouzzal (Hoggar, Algeria). Journal of Metamorphic Geology 31: 505–524.

Ait Djafer, S., 1996. Relation cristallisation fusion et cheminement pression température dans les migmatites de l'In Ouzzal NW Hoggar. Unpublished Magister, U.S.T.H.B., Alger, Algérie, 188 p., unpublished.

Allègre C J, Caby R, Tatsumoto M (1972) U-Th-Pb systematics of hydroxyapatite intergrowths. Trans Assoc Geol Unions 53 : 556 (Abstract).

Amelin, Y & Zaitsev, A N (2002). Precise geochronology of phoscorites and carbonatites : The critical role of U-series disequilibrium in age interpretations, Geochimica et Cosmochimica Acta 66(13), 2399–2419.

Andrade F.R.D, Möller P, Lüders V, Dulski P, Gilg H.A. (1999) Hydrothermal rare earth elements mineralization in the Barra do Itapirapuã carbonatite, southern Brazil: behaviour of selected trace elements and stable isotopes (C, O) Chem. Geol. (155) pp. 91-113.

Attoum, A., 1983. Etude géologique et structurale des mylonites Panafricaines et des minéralisations aurifères associées dans le secteur de Tirek Hoggar, Algérie. Thèse 3_eme cycle Montpellier, France 1998.

Attoum, A., 1993. Contribution à l'étude des zones de cisaillement panafricaines: tectonique, microtectonique et cinématique des mylonites de Tirek (Hoggar, Algérie). Bull. Serv. Géol. De l'Algérie, 4, 65-87.

Baker MB, Wyllie PJ (1990) Liquid immiscibility in a nephelinite-carbonate system at 25 kbar and implications for carbonatite origin. Nature 346: 168–170.

Baudouin C, Parat F, Denis CMM, Mangasini F (2016) Nephelinite lavas at early stage of rift initiation (Hanang volcano, North Tanzanian Divergence). Contributions to Mineralogy and Petrology 171: 1–20.

Bea F, Montero P, Haissen F, El Archi A (2013). 2.46 Ga kalsilite and nepheline syenites from the Awsard pluton, Reguibat Rise of the West African Craton, Morocco. Generation of extremely K-rich magmas at the Archean–Proterozoic transition Precambrian Research (224) pp 242-254.

Bell K, Keller J (1995) (Eds.), Carbonatite Volcanism: Oldoinyo Lengai and the Petrogenesis of Natrocarbonatites, Springer-Verlag, Berlin 210 pp.

Bell K, Kjarsgaard BA, Simonetti A (1998). Carbonatites - Into the twenty-first century. Journal of Petrology 39: 1839–1845.

Benbatta, A., Bendaoud, A., Cenki-Tok, B., Adjerid, Z., Lacene, K., & Ouzegane, K. (2017). Ternary feldspar thermometry of Paleoproterozoic granulites from In-Ouzzal terrane (Western Hoggar, southern Algeria). Journal of African Earth Sciences, 127, 51–61.

Bendaoud, A., 2008. Pétrologie et Géochimie des séries basiques et ultrabasiques Précambriennes de l'In Ouzzal et du Hoggar Central et leur relation avec l'Encaissant. Thèse de Doctorat U.S.T.H.B., Alger, Algérie (Unpublished).

Ben Othman D, Polv M, Allègre CJ (1984) Nd-Sr isotopic composition of granulites and constraints on the evolution of the lower continental crust. Nature 307 : 51 ~515.

Benyahia, O., 1996. Les granulites à silicates calciques du môle In Ouzzal NW Hoggar: Minéralogie

géochimie et relation de phases. Unpublished Magister, U.S.T.H.B., Alger, Algérie, 110 p.

Bernard-Griffiths J, Peucat JJ, Fourcade S, Kienast JR, Ouzegane K (1988). Origin and evolution of 2 Ga old carbonatite complex (Ihouhaouene, Ahaggar, Algeria): Nd and Sr isotopic evidence. Contributions to Mineralogy and Petrology 100: 339–348.

Bertrand JML, Caby R, Ducrot J, Lancelot JR, Moussine-Pouchkine A, Saadallah A (1978) The late Pan-African intracontinental linear fold belt of the eastern Hoggar (Central Sahara, Algeria): geology, structural development, U/Pb geochronology, tectonic implications for the Hoggar shield. Precambr Res 7, 349–376.

Bizzarro, M., & Stevenson, R. K. (2002). Hf isotope evidence for a hidden mantle reservoir, (9), 771-774.

Boumaza, S., 1996. Pétrologie d'un nodule migmatitique _a saphirine d'In Hihaou In Ouzzal, Hoggar occidental: diffusion chimique et comparaison avec les granulites Al–Mg de l'encaissant. Unpublished Magister, U.S.T.H.B., Alger, Algérie, 200 p.

Bouzid, A., Akacem, N., Hamoudi, M., Ouzegane, K., Abtout, A., and Kienast, J.-R., 2008, Modélisation magnétotellurique de la structure géologique profonde de l'unité granulitique de l'In Ouzzal (Hoggar occidental) [in French with an abridged English version]: Comptes Rendus Geoscience, v. 340, p. 711–722.

Black R, Bonin B, Lameyre J (1985) The structural setting of alkaline ring-complexes J. Afr. Earth Sci., (3) pp. 5-16.

Black R, Latouche L, Liégeois JP, Caby R, Bertrand JM (1994) Pan-African displaced terranes in the Tuareg shield (central Sahara). J. Geol. 22 : 641–644.

Blundy J, Dalton J (2000) Experimental comparison of trace element partitioning between clinopyroxene and melt in carbonate and silicate systems, and implications for mantle metasomatism. Contributions to Mineralogy and Petrology 139: 356–371.

Bonin B, Lameyre J (1978) Réflexions sur la position et l'origine des complexes magmatiques anorogéniques. Bull Soc Géol Fr 7, XX (1): 45–59.

Borodin L S, Pavlenko A S (1974) The role of metasomatic processes in the formation of alkaline rocks H. Sørensen (Ed.), The Alkaline Rocks, Wiley, London, U.K , pp. 515-534.

Bowen, N.L. (1928) The Evolution of the Igneous Rocks. Princeton University Press, Princeton, New Jersey, 332 pp.

Bowden P (1985) The geochemistry and mineralization of alkaline ring complexes in Africa (a review) J. Afric. Earth Sci., (3) pp. 17-39.

Brassinnes, S., Balaganskaya, E., Demaiffe, D., (2005). Magmatic evolution of the differentiated ultramafic, alkaline and carbonatite intrusion of Vuoriyarvi (Kola Peninsula, Russia). A LAICP-MS study of apatite. Lithos 85, 76–92.

Brooker RA, Kjarsgaard BA (2011) Silicate-carbonate liquid immiscibility and phase relations in the system SiO_2-Na_2O-Al_2O_3-CaO-CO_2 at 0.1-2.5 GPa with applications to carbonatite genesis. Journal of Petrology 52: 1281–1305.

Bu¨hn, B., Wall, F., Le Bas, M.J., 2001. Rare-earth element systematic of carbonatitic fluorapatites and their significance for carbonatite magma evolution. Contributions to Mineralogy and Petrology 141, 572–591.

Burke K, Ashwal L D, Webb S J (2003) New way to map old sutures using deformed alkaline rocks and carbonatites. Geology, 31 (5), pp. 391-394.

Burke K, Khan S (2006) Geoinformatic approach to global nepheline syenite and carbonatite distribution: testing a Wilson cycle model Geosphere, 2 (1), pp. 53-60.

Caby, R., 1970. La chaine Pharusienne dans le NW de l'Ahaggar Central Sahara, Algérie: sa place

dans l'orogenèse du Précambrien supérieur en Afrique. Thèse de Doctorat d'Etat, Montpellier, Publication de la Direction des Mines et de la Géologie, Alger, 47, 289 p.

Caby, R., 1996. A review of the In Ouzzal granulitic terrane, Tuareg shield, Algeria: its significance within the Pan-African Trans- Saharan Belt. Journal of Metamorphic Geology 14, 659–666.

Caby, R., Bertrand, J.M., Black, R. (1981). Pan-African ocean in the hoggar-iforas segment, central sahara. In: Kroner, A. (Ed.), Precambrian Plate Tectonics. Elsevier, Amsterdam, pp. 407-433.

Caby R., Andreopoulos-Renaud U., Gravelle M. (1982) Cadre géologique et géochronologie U/Pb sur zircon des batholites précoces dans le segment pan-Africain du Hoggar central (Algérie). Bull Soc Géol Fr 24, 677–684

Caby R., Andreopoulos-Renaud U., Pin C. (1989) Late Proterozoic arc-continent and continent-continent collision in the pan-African trans-Saharan belt of Mali. Can J Earth Sci 26, 1136–1146.

Caby, R., Monié, P., 2003. Neoproterozoic subduction and differential exhumation of western Hoggar (south-west Hoggar, Algeria): new structural, petrological and geochronological evidence. J. Afr. Earth Sci. , 37, 269-293.

Carignan J, Hild P, Mevelle G, Morel J, Yeghicheyan D (2001) Routine Analyses of Trace Elements in Geological Samples using Flow Injection and Low Pressure On-Line Liquid Chromatography Coupled to ICP-MS: A Study of Geochemical Reference Materials BR, DRN, UB-N, AN-G and GH. Geostandards and Geoanalytical Research 25: 187–198.

Carpena J, Kienast JR, Ouzegane K, Jehanno C (1988) Apatites from In Ouzzal carbonatites (N.W. Hoggar): the final thermal history of an Archaean basement. Geol Soc Am Bull 100 (8): 1237-1243.

Castor S.B. (2008) The Mountain Pass rare-earth carbonatite and associated ultrapotassic rocks, California Can. Mineral., 46 pp. 779-806.

Chakhmouradian AR, Mumin AH, Demény A, Elliott B (2008) Postorogenic carbonatites at Eden Lake, Trans-Hudson Orogen (northern Manitoba, Canada): Geological setting, mineralogy and geochemistry. Lithos 103 : 503–526.

Chakhmouradian A.R., Wall F. (2012). Rare earth elements: minerals, mines, magnets (and more). Elements, 8 (2012), pp. 333-340.

Chakhmouradian A.R., Zaitsev A.N. (2012) Rare earth mineralization in igneous rocks: sources and processes. Elements, 8 (2012), pp. 347-353.

Chakhmouradian, A. R., Reguir, E. P., Zaitsev, A. N., Couëslan, C., Xu, C., Mumin, A. H., & Yang, P. (2017). Lithos Apatite in carbonatitic rocks : Compositional variation, zoning, element partitioning and petrogenetic significance, 275, 188–213. lithos.2016.12.037

Chen W, Honghui H, Bai T and Jiang S 2017, Geochemistry of Monazite within Carbonatite Related REE Deposits. Resources 2017, 6(4), 51.

Cherniak, D. J., & Watson, E. B. (2000). Pb diffusion in zircon. Chem. Geol. 172, 5–24.

Chew, D.M., Petrus, J.A., and Kamber, B.S. (2014) U–Pb LA-ICPMS dating using accessory mineral standards with variable common Pb. Chemical Geology, 363, 185–199.

Cochrane, R., Spikings, R.A., Chew, D., Wotzlaw, J.-F., Chiaradia, M., Tyrrell, S., Schaltegger, U., and Van der Lelij, R. (2014) High temperature (>350 °C) thermochronology and mechanisms of Pb loss in apatite. Geochimica et Cosmochimica Acta, 127, 39–56.

Cornu M.N. (2017). Evolution magmatique d'un volcan bouclier océanique avant et après une déstabilisation massive de ses flancs: Fogo, Cap Vert et Tenerife, Canaries. Ph.D. dissertation thesis, Université de Clermont Auvergne. Laboratoire Magmas et Volcans.

Dalton JA, Presnall DC (1998) Carbonatitic melts along the solidus of model lherzolite in the system

CaO-MgO-Al_2O_3-SiO_2-CO_2 from 3 to 7 GPa. Contributions to Mineralogy and Petrology 131: 123–135.

Daly R.A. (1910) – Origin of alkaline rocks. Bull. Geol. Soc. Am., 21, 87-118.

Dasgupta R, Hirschmann MM (2006) Melting in the Earth's deep upper mantle caused by carbon dioxide. Nature 440: 659.

Dasgupta R, Hirschmann MM, Stalker K (2006) Immiscible transition from carbonate-rich to silicaterich melts in the 3 GPa melting interval of eclogite + CO2 and genesis of silica-undersaturated ocean island lavas. Journal of Petrology 47: 647–671.

Dalton JA, Wood BJ (1993) The compositions of primary carbonate melts and their evolution through wallrock reaction in the mantle. Earth and Planetary Science Letters 119: 511–525.

Dawson JB (1962) Bull. Volcanol. 24, 349–88. -(1966) In Carbonatites (O. F. Tuttle and J. Gittins, eds.) Wyllie 15568.

Dawson JB (1998) Peralkaline nephelinite-natrocarbonatite relationships at Oldoinyo Lengai, Tanzania. Journal of Petrology 39: 2077–2094.

Deer WA, Howie RA, Zussman J (1982) Rock-forming minerals, vol1A: Orthosilicates. Longman, New York.

Demaiffe, D. (2008). Le magmatisme alcalin et carbonatitique : synthèse sur la province paléozoïque de Kola (Russie) et caractéristiques générales du massif protérozoïque de Matongo (Burundi). Bull Séances Acad R Sci O-M 54:171–196.

Demeny, A., Sitnikova, M.A., Karchevsky, P.I., 2004a. Stable C and O isotope compositions of carbonatite complexes of the Kola Alkaline Province: phoscorite– carbonatite relationships and source compositions. In: Wall, F., Zaitsev, A. (Eds.), Phoscorites and Carbonatites from Mantle to Mine: The Key Example of the Kola Alkaline Province: The Mineralogical Society Series, 10, pp. 407–431.

Deines, P., 1989. Stable isotope variations in carbonatites. In: Bell, K. (Ed.), Carbonatites — Genesis and Evolution. Unwin Hyman, pp. 301–359.

Djemai, S., 1996. Les pyrigarnites et les granulites alumineuses d'Amesmessa, Môle. In: Ouzzal, Hoggar (Ed.), Relations de phases et déformation. Thèse de Magister U.S.T.H.B., Alger, Algérie, p. 210 (Unpublished).

Djemai, S., Hammid, H., Bendaoud, A., Ouzegane, K., Kienast, J.-R., 2009. Les séries archéennes d'Amesmessa (ouest Hoggar) remobilisées au Protérozoïque: cartographie, évolution tectonique et cheminement P-T. Bull. du Serv. Géologique Natl. 20 (1), 1-27.

Drareni, A., Ouzegane, K., Bendaoud, A., 2007. L'archéen du Hoggar : Géochronologie et evolution géodynamique. Bull du Serv Géol National, Vol. 18, 103-126.

Drüppel K, Hoefs J, Okrusch M (2004) Fenitizing Processes Induced by Ferrocarbonatite Magmatism at Swartbooisdrif, NW Namibia. Journal of Petrology 46: 377–406.

Dupuy, C., Liotard, J.M., Dostal, J., 1992. Zr/Hf fractionation in intraplate basaltic rocks: carbonatite metasomatism in the mantle source. Geochimica et Cosmochimica Acta 56, 2417–2423.

English KL, Redfern J, Bertotti G, English JM, Cherif RY (2017) Intraplate uplift: new constraints on the Hoggar dome from the Illizi basin (Algeria). Basin Res 29:377–393.

Eriksson, SC, Fourie, PJ, De Jager, DH 1985A cumulate origin for the minerals in clinopyroxenites of the Phalaborwa ComplexTrans Geol Soc S Africa 88207214.

Ewart A, Griffin WL (1994) Application of proton-microprobe data to trace-element partitioning in volcanic rocks. Chemical Geology 117: 251–284.

Ferkous, K., Leblanc, M., 1995. Gold mineralization in the West Hoggar shear zone, Algeria. Mineral. Deposita 30, 221-224.

Ferrara G, Gravelle M (1966) Radiometric ages from Western Ahaggar (Sahara) suggesting an eastern limit for the West African Craton. Earth Planet Sci Lett 1:319-324.

Fourcade S, Kienast JR, Ouzegane K (1996) Metasomatic effects related to channelled fluid streaming through deep crust: Fenites and associated carbonatites (In Ouzzal Proterozoic granulites, Hoggar, Algeria). Journal of Metamorphic Geology 14: 763–781.

Freestone IC, Hamilton DL (1980) The role of liquid immiscibility in the genesis of carbonatites – An experimental study. Contributions to Mineralogy and Petrology 73: 105–117.

Gittins J (1979) Problems inherent in the application of calcite-dolomite geothermometry to carbonatites Contrib. Mineral. Petrol., 69, pp. 1-4

Gittins J, Harmer RE (1997) What is ferrocarbonatite? A revised classification. Journal of African Earth Sciences 25: 159–168.

Gittins J, Jago BC (1998) Differentiation of natrocarbonatite magma at Oldoinyo Lengai volcano, Tanzania. Mineralogical Magazine 62: 759–768.

Green TH, Adam J, Sie SH (1992) Trace Element Partitioning Between Silicate Minerals and Carbonatite at 25 kbar and Application to Mantle Metasomatism. Mineralogy and Petrology 46: 179–184.

Griffin WL, Powell WJ, Pearson NJ, O'Reilly SY (2008) GLITTER: data reduction software for laser ablation ICP-MS. Laser ablation-ICP-MS in the earth sciences. Mineralogical Association of Canada Short Course Series 40: 204–207.

Grimes, C.B., John, B.E., Kelemen, P.B., Mazdab, F.K., Wooden, J.L., Cheadle, M.J., Hanghoi, K., Schwartz, J.J., 2007. Trace element chemistry of zircons from oceanic crust: a method for distinguishing detrital zircon provenance. Geology 35, 643–646.

Gudfinnsson GH, Presnall DC (2005) Continuous gradations among primary carbonatitic, kimberlitic, melilititic, basaltic, picritic, and komatiitic melts in equilibrium with garnet lherzolite at 3-8 GPa. Journal of Petrology 46: 1645–1659.

Guiraud M, Kienast JR, Ouzegane K (1996) Corundum–quartz bearing assemblage in the Ihouhaouene area In Ouzzal, Algeria. Journal of Metamorphic Geology 14: 755–761.

Guo J, O'Reilly SY, Griffin WL (1996) Zircon inclusions in corundum megacrysts: I. Trace element geochemistry and clues to the origin of corundum megacrysts in alkali basalts. Geochim Cosmochim Acta 60:2347-2363.

Haddoum, H., 1992. Etude structurale des terrains archéens du môle In Ouzzal Hoggar occidental, Algérie. Thèse de Doctorat d'état U.S.T.H.B, Alger, Algérie, p. 214.

Haddoum, H., Choukroune, P., Peucat, J.J., 1994. Structural evolution of the precambrian In ouzzal massif, central sahara, Algeria. Precambrian Res. 65, 155-166.

Haddoum, H., Mokri, M., Ouzegane, K., & Ait-djaffer, S. (2013). Extrusion du bloc In Ouzzal vers le Nord (Hoggar Occidental, Algérie): Conséquence d'un poinçonnement panafricain Extrusion de l'In Ouzzal vers le Nord (Hoggar occidental, Algérie): une conséquence d'un poinçonnement panafricain, (December 2014).

Hamilton DL, Bedson P, Esson J (1989) The behaviour of trace elements in the evolution of carbonatites. In Carbonatites, Genesis and Evolution (ed. K. Bell), Unwin and Hyman, __ 405-427.

Hammouda T, Chantel J, Devidal JL (2010) Apatite solubility in carbonatitic liquids and trace element partitioning between apatite and carbonatite at high pressure. Geochimica et Cosmochimica Acta 74: 7220–7235.

Harlov D.E (2015) Apatite and fluids: a fingerprint for metasomatic processes Elements, 11, pp. 171-

176.

Harlov, D. E. (2018). Apatite : A Fingerprint for Metasomatic Processes, (November), 171–176. Elements.11.3.171.

Harrison T.M, Watson E.B (1984) The behavior of apatite during crustal anatexis: Equilibrium and kinetic considerations Geochim. Cosmochim. Acta, (48) pp. 1467-1477.

Hatch G.P. (2012). Dynamics in the global market for rare earths. Elements, 8 (2012), pp. 341-346.

Heinrich, E. W. (1966). The Geology of Carbonatites. Rand McNally, Chicago.

Herz N (1977) Timing of spreading in the South Atlantic: Information from Brazilian alkalic rocks. GSA Bulletin 88 (1): 101-112.

Hogarth, D.D., Hartree, R., Loop, S. and Solberg, T.N. (1985) Rare-earth element minerals in four carbonatites near Gatineau, Quebec. Amer. Mineral., 70, 1135–42.

Holm PM, Wilson JR, Christensen BP, Hansen L, Hansen SL, Hein KM, Mortensen AK, Pedersen R, Plesner S, Runge MK (2006) Sampling the Cape Verde mantle plume: evolution of melt composition on Santo Antão, Cape Verde Islands. Journal of Petrology 47: 145-189.

Hornig-Kjarsgaard I., (1998) Rare earth elements in sövitic carbonatites and their mineral phases J. Petrol., (39) pp. 2105-2121.

Hoskin P.W.O and Ireland T.R. (2000) Rare earth element chemistry of zircon and its use as a provenance indicator. Geology 28 (7): 627-630.

Hoskin, P.W.O., Schaltegger, U., 2003. The composition of zircon and igneous and metamorphic petrogenesis. Reviews in Mineralogy and Geochemistry 53, 27–62.

Hou Z. Q., Tian S. H., Yuan Z. X., Xie Y. L., Yin S. P., Yi L. S., Fei H. C. and Yang Z. M. (2006) The Himalayan collision zone carbonatites in western Sichuan, SW China: petrogenesis, mantle source and tectonic implication. Earth Planet. Sci. Lett. 244, 234–250.

Hughes J.M & Rakovan. J.F. (2015) Structurally robust, chemically diverse: apatite and apatite supergroup minerals. Elements, 11, pp. 165-170.

Humphries M. Rare Earth Elements: the Global Supply Chain (2013) (CRS Report for Congress, Congressional Research Service Report R41347, Washington, USA) p. 27.

Jones JH, Walker D, Pickett DA, Murrell MT, Beattie P (1995) Experimental investigations of the partitioning of Nb, Mo, Ba, Ce, Pb, Ra, Th, Pa, and U between immiscible carbonate and silicate liquids. Geochimica et Cosmochimica Acta 59: 1307–1320.

Karchevsky, P.I., Moutte, J., 2004. The phoscorite–carbonatite complex Vuoriyarvi, northern Karelia. In: Wall, F., Zaitsev, A. (Eds.), Phoscorites and Carbonatites from Mantle to Mine: The Key Example of the Kola Alkaline Province: The Mineralogical Society Series, 10, pp. 163–199.

Kempe, U., Götze, J., 2002. Cathodoluminescence (CL) behaviour and crystal chemistry of apatite from rare-metal deposits. Mineralogical Magazine 66, 151–172.

Kienast JR, Ouzegane K (1987) Polymetamorphic A1, Mg-rich granulites with orthopyroxene - sillimanite and sapphirine parageneses in Archaean rocks from Hoggar, Algeria. In: Wiley J (ed) African geology reviews.

Kim Y. Koecke B. Fiege B. Simon A. Becker U. (2017) An ab-initio study of the energetics and geometry of sulfide, sulfite and sulfate incorporation in apatite; the thermodinamic basis for using this system as an oxybarometer Am. Min., (102) pp. 1646-1656.

Kjarsgaard B, Peterson T (1991) Nephelinite-carbonatite liquid immiscibility at Shombole volcano, East Africa: Petrographic and experimental evidence. Mineralogy and Petrology 43: 293–314.

Kjarsgaard BA, Hamilton DL, Peterson TD (1995) Peralkaline Nephelinite/Carbonatite Liquid Immiscibility: Comparison of Phase Compositions in Experiments and Natural Lavas from

Oldoinyo Lengai. In : Bell K, Keller J (eds) Carbonatites Volcanism–Oldoinyo Lengai and Petrogenesis of Natrocarbonatites. IAVCEI Proceedings in Volcanology 4: 163–190.

Klemme S, van der Laan SR, Foley SF, Günther D (1995) Experimentally determined trace and minor element partitioning between climopyroxene and carbonatite melt under upper mantle conditions. Earth and Planetary Science Letters 133: 439–448.

Konecke B. Fiege A. Simon A. Parat F. Stechern A (2017). Co-variability of S6+, S4+, and S2– in apatite as a function of oxidation state: Implications for a new oxybarometer. Am. Min., (102) pp. 548-557.

Koster Van Grogs AF, Wyllie, P.J. (1966) American Journal of Science. 264, 234–55.

Koster van Groos AF, Wyllie PJ (1968) Liquid immiscibility in the join $NaAlSi_3O_8$ –Na_2CO_3–H_2O. American Journal of Science 266: 932–967.

Kresten P (1988) The chemistry of fenitization : examples from Fen, Norway. Chemical Geology 68: 329–349.

Lancelot, J.R., Vitrac, A., Allegre, C.J., 1976. Uranium and lead isotopic dating with grain-by grain zircon analysis: a study of a complex geological history with a single rock. Earth and Planetary Science Letters 29, 357–366.

Lapin AV, Ploshko VV (1988) Rock-association and morphological types of carbonatite and their geotectonic environments. Int. Geol. Rev., 30: 390-396.

Larsen LM (1979) Distribution of REE and other trace elements between phynocrysts and peralkaline undersaturated magmas, explified by rocks from the Gardar igneous province, South Greenland. Lithos 12: 303–315.

Le Bas, M. J. and Handley, C. D. (1979) Variation in apatite composition in ijolitic and carbonatitic igneous rocks. Nature, 279, 54–56.

Liégeois JP 2019. A New Synthetic Geological Map of the Tuareg Shield: An Overview of Its Global Structure and Geological Evolution. In: Bendaoud A, Hamimi Z, Hamoudi M, Djemai S, Zoheir B (eds) The geology of the Arab world—an overview. Springer Geology, Switzerland, pp 83–107.

Liégeois JP, Black R, Navez J, Latouche L (1994) Early and late Pan-African orogenies in the Aïr assembly of terranes (Tuareg Shield, Niger). Precambr Res 67:59–88.

Liégeois JP, Latouche L, Boughrara M, Navez J, Guiraud M (2003) The LATEA metacraton (Central Hoggar, Tuareg shield, Algeria): behaviour of an old passive margin during the Pan-African orogeny. Journal of African Earth Sciences 37: 161–190.

Liégeois JP, Benhallou A, Azzouni-Sekkal A, Yahiaoui R, Bonin B (2005) The Hoggar swell and volcanism: reactivation of the Precambrian Tuareg shield during Alpine convergence and west African Cenozoic volcanism. In: Foulger GR, Natland JH, Presnall DC, Anderson DL (eds) Plates, plumes and paradigms, vol 388. Geological Society of America special paper, pp 379–400.

Lelubre M (1952) Recherches sur la géologie de l'Ahaggar central et occidental (Sahara central). Bull Serv Carte Geol Algérie 22:2 vol

Le Maitre RW, Bateman P, Dubek A, Keller J, Lameyre J, Le Bas MJ, Sabine PA, Schmid R, Sørensen H, Streckeisen A, Woolley AR, Zanettin B (1989) A Classification of Igneous Rocks and Glossary of Terms: Recommendations of the International Union of Geological Sciences Subcommission on the Systematics of Igneous Rocks, Blackwell, Oxford, p. 193 and Wall Chart.

Le Maitre R.W. (Ed.) (2002). Igneous Rocks: A Classification and Glossary of Terms (2^{nd} edition), Cambridge University Press.

Lancelot JR, Vitrac A, All6gre CJ (1975) Uranium and lead isotopic dating with grain-by-grain zircon

analysis: a study of complex geological history with a single rock. Earth Planet Sci Lett 29 : 357-366.

Linnemann, U., Ouzegane, K., Drareni, A., Hofmann, M., Becker, S., Gärtner, A., & Sagawe, A. (2011). Lithos Sands of West Gondwana : An archive of secular magmatism and plate interactions — A case study from the Cambro-Ordovician section of the Tassili Ouan Ahaggar (Algerian Sahara) using U – Pb – LA-ICP-MS detrital zircon ages. LITHOS, 123(1–4), 188–203.

Louaradi D. (1994) Étude isotopique (C, O) et microthermométrique (inclusions fluides et vitreuses) des magmas alcalins et carbonatitiques du rift est-Africain et de la presqu'ile de Kola. Ph.D. dissertation thesis, Univ. Paris VII.

Ludwig, K.R., 2003. Isoplot 3.00. In: Berkeley Geochronology Center Special Publication 4, 70 pp.

Mahood GA, Stimac JA (1990) Trace-element partitioning in pantellerites and trachytes. Geochimica et Cosmochimica Acta 54: 2257–2276.

Mariano A.N, and Mariano A.N, Jr (2012) Rare earth mining and exploration in North America: Elements, v. 8, p. 369–376.

Martins T, Couëslan CG, Böhm CO (2011) The Burntwood Lake alkali-feldspar syenite revisited, west-central Manitoba (part of NTS 63N8). Report of Activities, 79–85.

Martin LHJ, Schmidt MW, Mattsson HB, Guenther D (2013) Element Partitioning between Immiscible Carbonatite and Silicate Melts for Dry and H2O-bearing Systems at 1-3 GPa. Journal of Petrology 54: 2301–2338.

McConnell, 1973. The substitution of SiO^{4-} and SO^{4-} groups for po4-groups in the apatite structure. The American Mineralogist, 977–986.

McCubbin F.M. Jones R.H. (2015) Extraterrestrial apatite: planetary geochemistry to astrobiology Elements, 11 (3) pp. 183-188.

McDowell, F.W., McIntosh, W.C., and Farley, K.A. (2005) A precise 40Ar–39Ar reference age for the Durango apatite (U–Th)/He and fission-track dating standard. Chemical Geology, 214, 249–263.

Mitchell R.H. (2005) Carbonatites and Carbonatites and Carbonatites. Canadian Mineralogist, v.43, pp.2049–2068.

Mitchell RH (2009) Peralkaline nephelinite-natrocarbonatite immiscibility and carbonatite assimilation at Oldoinyo Lengai, Tanzania. Contributions to Mineralogy and Petrology 158: 589–598.

Möller P. (1989). REE(Y), Nb, and Ta enrichment in pegmatites and carbonatite–alkalic rock complexes ; O Möller, P Cerny, F Saupé (Eds.), Lanthanides, Tantalum and Niobium, Springer, Berlin.

Montero P, Haissen F, Mouttaqi A, Molina J F, Errami A, Sadki O, Cambeses A, Bea F (2016). Contrasting SHRIMP U–Pb zircon ages of two carbonatite complexes from the peri-cratonic terranes of the Reguibat Shield: Implications for the lateral extension of the West African Craton. Gondwna Reaserch (38) pp 238-250.

Mouri, H., Guiraud, M., Hensen, B.J., 1996. Petrology of phlogopite– sapphirine—bearing Al–Mg granulites from Ihouhaouene Mole In Ouzzal-Hoggar Algeria: an example of phlogopite stable at high temperature. Journal of metamorphic Geology 14, 725– 738.

Nash W.P. (1972). Mineralogy and petrology of the Iron Hill carbonatite complex, Colorado Bull Geol. Soc. Am., (83) pp. 1361-1382.

Nelson D. R., Chivas A. R., Chappell B. W. and McCulloch M. T. (1988) Geochemical and isotopic systematic in carbonatites and implications for the evolution of ocean-island sources. Geochim. Cosmochim. Acta 52, 1–17.

Novella D, Keshav S (2010) Silicate melt–carbonatite liquid immiscibility reconsidered in the system $CaO–MgOAl_2O3–SiO_2–CO_2$ at 2–3 GPa. (Conference Abstract.) France: EMPG XIII, Toulouse.

Oberti R, Ottolini L, Della Ventura G, Parodi GC (2001) On the symmetry and crystal chemistry of britholite: New structural and microanalytical data. American Mineralogist 86 1066–1075.

Ouzegane K (1987) Les granulites Al–Mg et les carbonatites dans la série de l'In Ouzzal, NW Hoggar, Algérie. Thèse d'état, Paris VII, France, p. 433.

Ouzegane K, Fourcade S, Kienast J, Javoy M (1988) New carbonatite complexes in the Archaean In'Ouzzal nucleus (Ahaggar, Algeria): Mineralogical and Geochemical data. Contributions to Mineralogy and Petrology 98: 277–292.

Ouzegane, K., Kienast, J.R., 1996. Nature et _evolution des séries métamorphiques de très haute température de l'Unité Granulitique de l'In Ouzzal Ouest Hoggar. Bull. Serv. Géologique de l'Algérie 7, 133-157.

Ouzegane K, Kienast JR, Bendaoud A, Drareni A (2003) A review of Archaean and Paleoproterozoic evolution of the In Ouzzal granulitic terrane (Western Hoggar, Algeria). Journal of African Earth Sciences 37: 207–227.

Pan, Y., & Fleet, M. E. (2002). Compositions of the Apatite-Group Minerals : Substitution Mechanisms and Controlling Factors. 48.2.

Paquette, J.L., Piro, J.L., Devidal, J.L., Bosse, V., Didier, A., Sanac, S., Abdelnour, Y., 2014. Sensitivity enhancement in LA-ICP-MS by N2 addition to carrier gas: application to radiometric dating of U–Th-bearing minerals. Agilent ICPMS J. 58.

Paton, C., Woodhead, J.D., Hellstrom, J.C., Hergt, J.M., Greig, A., and Maas, R. (2010) Improved laser ablation U-Pb zircon geochronology through robust downhole fractionation correction. Geochemistry, Geophysics, Geosystems, 11, Q0AA06.

Pasero M. Kampf A.R. Ferraris C. Pekov I.V. Rakovan J. White T.J. (2010). Nomenclature of the apatite supergroup minerals. European Journal of Mineralogy, 22 pp. 163-179.

Pecora WT (1962), Carbonatite problem in the Beapaw Mountains, in Engle, A. E. J., James, H. L., and Leonard, B. F., eds., Petrologic studies : A volume in honor of A. F. Buddington : Geological Society of America, p. 38-104.

Pekov I.V. , Pasero M., Yaskovskaya A.N. , Chukanov N.V. , Puscharovsky D.Yu., Merlino S. bkova, N.V. Z, Kononkova, N.N. , Men'shikov Y.P. , Zadov A.E (2007). Fluorcalciobritholite, (Ca,REE)5[(Si, P)O4]3 F, a new mineral: description and crystal chemistry European Journal of Mineralogy, (19) pp. 95-103.

Peucat, J.J., Bernard-Giffiths, J., Ouzegane, K. Haddoum, H., Kienast, J.R., 1991. Behaviour of Sr, Nd, Pb isotopic systems during a high temperature granulite metamorphism. Terra Astracts, 3, EUG, Strasbourg.

Peucat J.J., Capdevila R, Drareni A, Choukroune P, Fanning M, Bernard-Griffiths J, Fourcade S (1996) Major and trace element geochemistry and isotope Sr, Nd, Pb, O systematics of an Archaean basement involved in a 2.0 Ga VHT 1000ºC metamorphic event: In Ouzzal massif, Hoggar, Algeria. Journal of Metamorphic Geology 14: 667–692.

Piccoli P M and Candela P A 2002 Apatite in igneous systems; In: Phosphates (reviews in mineralogy and geochemistry) (eds) Kohn M J, Rakovan J and Hughes J M, Miner. Soc. America and Geochem. Soc., Washington, 48 255–292.

Prowatke S, Klemme S (2006) Trace element partitioning between apatite and silicate melts. Geochimica et Cosmochimica Acta 70: 4513–4527.

Prud'homme N. (1990) Caracterisation petrographique et geochimique de la carbonatite et de la syénite de la mine Lac Shortt, Petrographic and geochemical characterization of the

carbonatite and of the syenite of the Shortt Lake Mine, Canada. (M.Sc Thesis). Université du Québec à Chicoutimi.

Rakovan, J. (2002). Growth and Surface Properties of Apatite ; In: Phosphates (reviews in mineralogy and geochemistry) (eds) Kohn M J, Rakovan J and Hughes J M, Miner. Soc. America and Geochem. Soc., Washington, 48 3-86.

Riker J.M. Cashman K.V. Kauahikaua J.P. Montierth C.M (2009). The length of channelised lava flows: insight from the 1859 eruption of Mauna Loa Volcano, Hawaii. J. Volcanol. Geotherm. Res., (183) pp. 139-156.

Romanchev BP, Sokolov SV (1980) Liquation in the production and geochemistry of rocks in carbonatite complexes. Geochem Int 16:125–135.

Rougier S, Missenard Y, Gautheron C, Barbarand J, Zeyen H, Pinna R, Liégeois JP, Bonin B, Ouabadi A, Derder MEM, Frizon de Lamotte D (2013) Eocene exhumation of the Tuareg Shield (Sahara, Africa). Geology 41:615–618.

Rousseau D, All6gre CJ, Caby R, Lancelot J (1975) Formation et ~volution de la formation catazonale In'Ouzzal etudi6e par les m6thodes Rb-Sr et U-Pb. 3 R6union Ann Sci Terre, Montpellier, pp 326 (Abstract).

Rubatto, D., Gebauer, D., & Compagnoni, R. (1999). Dating of eclogite-facies zircons : the age of Alpine metamorphism in the Sesia – Lanzo Zone (Western Alps), 167, 141–158.

Rubatto, D. (2001). Zircon trace element geochemistry : partitioning with garnet and the link between U – Pb ages and metamorphism, 184, 123–138.

Rubatto D, 2017. Zircon: The Metamorphic Mineral. Reviews in Mineralogy and Geochemistry (2017) 83 (1): 261-295.

Rukhlov, A. S., & Bell, K. (2010). Geochronology of carbonatites from the Canadian and Baltic Shields, and the Canadian Cordillera : clues to mantle evolution, 11–54.

Saha A, Ray J, Ganguly S, Chatterjee N (2011) Occurrence of melanite garnet in syenite and ijolite – melteigite rocks of Samchampi – Samteran alkaline complex, Mikir Hills , Northeastern India. Current Science 101: 1-10.

Schaltegger U, Fanning CM, Gu¨nther D, Maurin JC, Schulmann K, Gebauer D (1999) Growth, annealing and recrystallization of zircon and preservation of monazite in high-grade metamorphism: conventional and in-situ U-Pb isotope, cathodoluminescence and microchemical evidence. Contrib Mineral Petrol 134:186-201.

Schoene, B., and Bowring, S.A. (2006) U–Pb systematics of the McClure Mountain syenite: Thermochronological constraints on the age of the $^{40}Ar/^{39}Ar$ standard MMhb. Contributions to Mineralogy and Petrology, 151, 615–630.

Semiani A., 1995. Métallogénie de la zone de cisaillement aurifère est-ouzzalienne: structure, pétrologie et géochimie des gisements d'or de Tirek-Amessmessa (Hoggar occidental, Algérie). Thèse de Doctorat, Université de Rennes 1, France, 285p.

Shaw DM (1970) Trace element fractionation during anatexis. Geochimica et Cosmochimica Acta 34: 237–243.

Sláma J, Košler J, Condon D J, Crowley JL, Gerdes A, Hanchar J M, Horstwood M S A, Morris G A, Nasdala L, Norberg N, Schaltegger U, Schoene B, Tubrett M N, Whitehouse M J (2008). Plešovice zircon — A new natural reference material for U–Pb and Hf isotopic microanalysis, Chemical Geology 249, 1–35.

Spear, F. S. & Pyle, J. M., 2002. Apatite, monazite and xenotime in metamorphic rocks. Reviews in Mineralogy, 48, 293–335.

Stacey, J.S., Kramers, J.D., 1975. Approximation of terrestrial lead isotopic evolution by a two-stage model. Earth and Planetary Science Letters 26, 207–221.

Stoppa F, Rosatelli G, Wall F, Jeffries T (2005) Geochemistry of carbonatite-silicate pairs in nature: A case history from Central Italy. Lithos 85: 26–47.

Streckeisen A (1974) Classification and nomenclature of plutonic rocks recommendations of the IUGS subcommission on the systematics of Igneous Rocks. Geologische Rundschau 63: 773–786.

Sun S –s, McDonough WF (1989) Chemical and isotopic systematics of oceanic basalts: implications for mantle composition and processes. Geological Society, London, Special Publications 42: 313–345.

Sweeney RJ, Green DH, Sie SH (1992) Trace and minor element partitioning between garnet and amphibole and carbonatitic melt. Earth Planet Sci Lett 113:1–14.

Teipel U, Eichhorn R, Loth G, Rohrmuller J, Holl R, Kennedy A (2004). U-Pb SHRIMP and Nd isotopic data from the western Bohemian Massif (Bayerischer Wald, Germany): Implications for Upper Vendian and Lower Ordovician magmatism, 782–801.

Tichomirowa, M., Whitehouse, M. J., Gerdes, A., Götze, J., Schulz, B., & Belyatsky, B. V. (2013). Different zircon recrystallization types in carbonatites caused by magma mixing : Evidence from U – Pb dating , trace element and isotope composition (Hf and O) of zircons from two Precambrian carbonatites from Fennoscandia. Chemical Geology, 353, 173–198.

Tilton G. R., Bryce J. G. and Mateen A. (1998) Pb–Sr–Nd isotope data from 30 and 300 Ma collision zone carbonatites in northwest Pakistan. J. Petrol. 39, 1855–1874.

Treiman A. H. (1989) Carbonatites magma: properties and processes. In Carbonatites: Genesis and Evolution (ed. K. Bell). Unwin Hyman, London, pp. 89–104.

Van Achterbergh, E., Ryan, C., Jackson, S., Griffin, W., 2001. Data reduction software for LA-ICP MS. In: Sylvester P. (Ed), Laser Ablation-ICPMS in the Earth Sciences. Mineral Assoc Can Short Course Handbook 29, 239–243.

Van Straaten P (1989) Nature and structural relationships of carbonatites from Southwest and West Tanzania. In: Bell K (ed) Carbonatites—genesis and evolution. Unwin Hyman, Boston, pp. 177–199.

Veksler I V, Petibon C, Jenner GA, Dorfman AM, Dingwell DB (1998) Trace element partitioning in immiscible silicate-carbonate liquid systems: An initial experimental study using a centrifuge autoclave. Journal of Petrology 39: 2095–2104.

Vernet M, Marin L, Boulmier S, Lhomme J, Demange JC (1987) Dosage du fluor et du chlore dans les matériaux géologiques y compris les échantillons hyperalumineux. Analusis 15(9):490–498.

Verwoerd W J (1993) Update on carbonatites of South Africa and Namibia. South African Journal of Geology. 96(3),75-95.

Walter A-V (1991) Caractérisation minéralogique et géochimique de l'altération de la carbonatite de Juquiá (S.P. Brésil). Comportement des terres rares dans les minéraux phosphatés. Thèse d'université, Université d'Aix-Marseille III, France.

Watson EB, Green TH (1981) Apatite liquid partition coefficients for the rare earth elements and strontium. Earth Planet Sci Lett 56: 405–421.

Webster, J. D., & Piccoli, P. M. (2018). Magmatic Apatite : A Powerful, Yet Deceptive , Mineral, (November), 177–182. Elements.11.3.177.

Weidendorfer D, Schmidt MW, Mattsson HB (2016) Fractional crystallization of Si-undersaturated alkaline magmas leading to unmixing of carbonatites on Brava Island (Cape Verde) and a general model of carbonatite genesis in alkaline magma suites. Contributions to Mineralogy and Petrology 171: 1–29.

Wendlandt, R.F., Harrison, W.J. (1979). Rare earth partitioning between immiscible carbonate and silicate liquids and CO_2 vapour; results and implications for the formation of light rare earthenriched rocks. Contrib. Mineral. Petrol. 69, 409 – 419.

Wiedenbeck M, Alle P, Corfu F, Griffin W.L, Meier M, Oberli F, Von A. Quadt, J.C. Roddick, W. Spiegel Three natural zircon standards for U–Th–Pb, Lu–Hf, trace element and REE analyses Geostandards Newsletter, 19 (1995), pp. 1-24.

Williams IS, Buick IS, Cartwright I (1996) An extended episode of early Mesoproterozoic fluid flow in the Reynolds Range, central Australia. J Metamor Geol 14:29-47.

Woolley AR (1989) The spatial and temporal distribution of carbonatites. In: Bell K (ed) Carbonatites: nomenclature, average chemical composition. Unwin Hyman, Boston.

Woolley AR, Kempe DRC (1989) Carbonatites: nomenclature, average chemical compositions, and element distribution, In Carbonatites, Genesis and Evolution (ed. K. Bell), Unwin and Hyman 1-14.

Wyllie PJ, Huang WL (1975) Peridotite, Kimberlite and carbonatite explained in the system CaO-MgO- SiO_2-CO_2. Geology 3: 621–624.

Wyllie PJ, Lee WJ (1998) Model system controls on conditions for formation of magnesiocarbonatite and calciocarbonatite magmas from the mantle. Journal of Petrology 39: 1885–1893.

Xu, C., Chakhmouradian, A. R., Taylor, R. N., Kynicky, J., Li, W., Song, W., & Fletcher, I. R. (2014). ScienceDirect Origin of carbonatites in the South Qinling orogen : Implications for crustal recycling and timing of collision between the South and North China Blocks. Geochimica et Cosmochimica Acta, 143, 189–206.

Yakymchuk, C., Kirkland, C. L., & Clark, C. (2018). Th / U ratios in metamorphic zircon. Metamorph Geol. 2018; 36: 715–737.

York, D., 1969. Least-squares fitting of a straight line with correlated errors. Earth Planet. Sci. Lett., 5, 320-324.

Zhu, X.K. and O'Nions, R.K., 1999, Zonation of monazite in metamorphic rocks and its implications for high temperature thermochronology: a case study from the Lewisian terrain: Earth Planet. Sci. Lett., V. 171, 209–220.

Annexes

Annexe A – Relations de terrain et minéraux des carbonatites et syénites d'Ihouhaouene
Annexe B – Modélisation géochimique des processus magmatiques
Annexe C – Les monazites et britholites dans les carbonatites d'Ihouhaouene
Annexe D – Les datations U-Pb sur apatite et zircons dans le complexe d'Ihouhaouene

Annexe A

Relations de terrain et minéraux des carbonatites et syénites d'Ihouhaouene (Chapitre I)

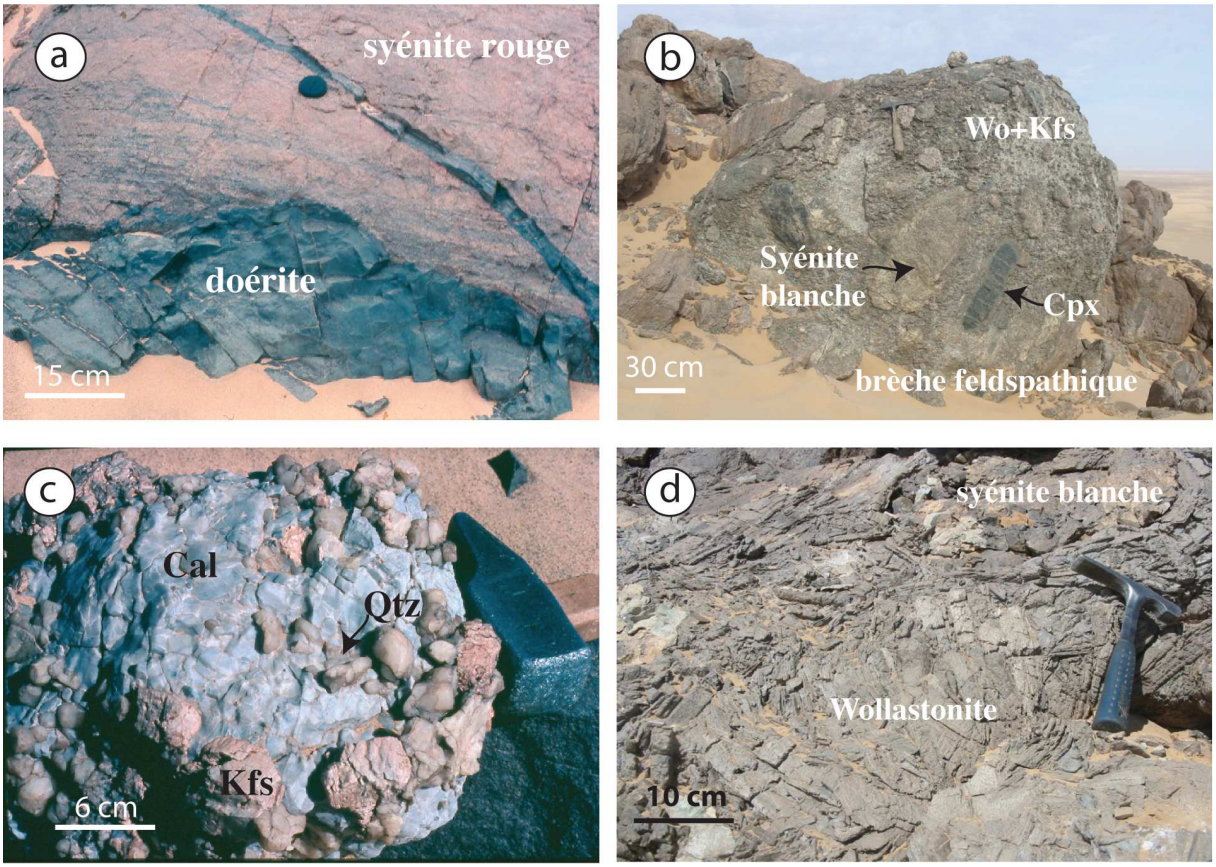

Figure 1 : **a** dyke de Dolérite recoupant une syénite rouge. **b** affleurement de breche feldspatique dans le Nord Wadi Tirahart. **c** Pegmatite de quartz- calcite dans l'Oued Ihouhaouene. **d** Un niveau de wollastonite dans la syenite blanche du Sud Wadi Tirahart.

Table 1 composition des carbonatites et syénites d'Ihouhaouene

Echantillon	Centre	Type pétrographique	Textures	Minéraux													Remarque
				Ap	Brith	Mnz	Cal	Alla	Cpx	Qtz	FK	Sph	Wo	Am	oxy	autre	
IC1-1A	Oued Ihouhaouene	pegmatite de syénite	pegmatitique					X	X	X	X	?					Contact Sy- pegm
IC1-1B										X	X						pegmatite
IC1-2A		carbonatite	pegmatitique	X			X	X	X	X	X						Contacte carbonatite-pegmatite
IC1-2B				X			X		X	X	X						
IC1-2C				X			X		X	X	X		?		X		
IC1-3A		carbonatite	pegmatitique	X			X	X	X	X			X				
IC1-3B				X			X		X	X	X		X		X	Fl	Fluorite dans FK ?
IC1-3C		contact carb + pegmatite	pegmatitique								X						
IC1-3D		feldspath pegmatitique	pegmatitique					X	X		X						Petits cristaux de Cpx+All
IC1-3E											X						
IC1-3F								X	X	X	X						Fk altéré
IC1-3G								X	X	X	X						
IC1-4A		Carbonatite bréchique	grenue à grains fins	X			X	X	X								
IC1-4B				X			X	X	X						X		Cpx altéré
IC1-4C				X			X	X	X	X	X						contact avec syenite
IC1-5A		Carb+Syenite	grenue	X			X	X	X	X							
IC1-5B		Carb+Syenite	grenue	X			X	X	X	X	X						
IC1-7A		Dolerite	grenue						X		X						plagio
IC1-11		filon de quartz	grenue							X							Filon de quartz
IC1-12A		Syenite rouge	grenue	X				X	X	X	X	X					Minéral doré?
IC1-12		Carbonatite bréchique	grenue	X	X		X		X		X		?			Gt	FK altéré
IC1-12E		Carb+Syenite	grenue	X	X		X	X	X	X	X	X				Gt	
IC1-12D			grenue	X	X		X	X	X	X	X					Gt	
IC1-12B			grenue	X			X	X	X	X	X	X				Fl ?	
IC1-12C			grenue	X			X	X	X	X	X	X					
IC1-13		Syénite blanche	grenue	X				X	X	X	X	X					Ap en inclusion dans Cpx
IC1-13B		pegmatite de syénite	grenue					X	X	X	X	X					

Echantillon	Centre	Type pétrographique	Textures	Minéraux													Remarque
				Ap	Brith	Mnz	Cal	Alla	Cpx	Qtz	FK	Sph	Wo	Am	oxy	autre	
IC1-14	Oued Ihouhaouene	quartzite	grenue							X	X			?	X		
IC1-17A		pegmatite de syénite	grenue							X	X				X		Pas de Cpx
IC1-17B		pegmatite de syénite	grenue							X	X				X		Beaucoup d'oxyde
IC1-24a		Syenite rouge	grenue	X				X	X	X	X	X			X		petites apatites
IC1-24B				X					X	X	X					Gt	très altérée
IC2-3A	Wadi Tirahart Sud	Leptynite	grano-blastique							X	X				X	Gt	+Micas
IC2-3B		Leptynite								X	X				X	Gt	+Micas
IC2-5A		cumulats pyroxéniques	grenue	X				X	X		X	?		X	X		+Micas
IC2-5B				X				X	X			?		X	X		+Micas
IC2-7A		pegmatite de syénite	grenue	X					X	X	X			?	X		Cpx déstabilisé
IC2-7B		pegmatite de syénite	grenue	X				X	X	X	X			?	X		+Micas
IC2-9A		Carb bréchique	grenue porphyroide	X	X		X	X	X	X	X		X			Gt	
IC2-9B				X	X		X	X	X	X	X		X			Gt	
IC2-9C		Carb + syenite		X	X		X	X	X	X	X		X		X	Gt	inclusion de syenite dans la carbonatite
IC2-10A		Carb + Syenite	grenue				X	?	X		X		X		X	Gt	
IC2-10B		Carb + Syenite	grenue	X	X				X		X	X	X		X	Gt	
IC2-10C		Carb + Syenite	grenue				X				X	X	X		X	Gt	des FK en points triples
IC2-11A		carbonatite	pegmatitique	X	X		X	X	X		X	X	X			Gt	inclusion de syenite dans la carbonatite
IC2-11B		Carb + Syenite	pegmatitique	X	X		X		X		X	X	X				
IC2-11C		Carb + Syenite	pegmatitique	X	X		X		X		X	X	X				
IC2-11D		Carb + Syenite	pegmatitique	X	X		X		X	X	X	X	X			Gt	Qtz autour du Cpx
IC2-15A		Syénite rouge	grenue	X				X	X	X	X			?	X		Petits cristaux d'apatite sans inclusions
IC2-15B		Syénite + dolérite	grenue	X					X	X	X			?	X		
IC2-20A		Carb bréchique	grenue	X			X	X	X		X						allanite rouge dans les fissures d'apatite
IC2-20B				X			X	X	X		X						cumulats de Cpx
IC2-21		carbonatite	pegmatitique	X	X		X	X	X								allanite rouge dans les fissures d'apatite
IC2-27A		Syénite blanche	grenue	X	X		X		X	X	X		X				
IC2-27B				X	X		X		X	X	X		X				

Table 1 (suite) composition des carbonatites et syénites d'Ihouhaouene

Echantillon	Centre	Type pétrographique	Textures	Minéraux													Remarque
				Ap	Brith	Mnz	Cal	Alla	Cpx	Qtz	FK	Sph	Wo	Am	oxy	autre	
IC3-1A	Wadi Tirahart Nord	Carb bréchique	grenue	X		X	X	X	X			X		?	X		Contact Sy- pegm
IC3-1B				X		X	X	X	X	X	X	X		?	X		(fluides tardifs ?)
IC3-1C				X		X	X	X	X	X		X		?	X		
IC3-2A		contact Carb - syenite	grenue	X			X		X		X			?	X		
IC3-2B		Carb		X			X	X	X		X	X		?			
IC3-4		Syénite rouge	grenue litée	X		X			X		X			?	X		Mineraux allongés et non-déformés
IC3-5		Carbonatite	pegmatitique	X		?	X	X	X		X				X		
IC3-7A		Carbonatite	pegmatitique	X		?	X	X	X								apatites à coeurs limpides
IC3-7B		Carbonatite	pegmatitique	X		?	X	X	X								
IC3-12		Carb + syénite	grenue	X		X	X	X	X								all+Mnz en inclusions
IC3-15A		Carb bréchique	grenue	X		?	X	X	X		X						
IC3-15B				X		?	X	X	X		X	X				Gt?	Minéral doré?
IC3-15C		contact Carb - syenite	grenue	X		X	X	X	X		X	?				Gt?	Minéral doré? Sph?
IC3-17		Carbonatite bréchique	grenue	X		?	X	X	X								Minéraux fins
IC3-18		Syénite blanche	grenue	X				X	X	X	X	X		X	X	Gt?	Minéral doré?
IC3-19A		Carbonatite	pegmatitique	X	X		X	X	X		X	X					carbonatite en poche
IC3-19B		contact Carb - syenite	grenue	X	X		X	X	X		X	X					
IC3-20		Carbonatite	pegmatitique	X		X	X	X	X						X		
IC3-21A		Carbonatite	pegmatitique	X			X	X									
IC3-21B		Carbonatite	pegmatitique	X			X	X	X		X	X					
IC3-10		Syénite blanche	grenue	X		?		X	X	X	X			X	X		
IC3-12B		Syénite blanche	grenue	X	X		X	X	X	X	X	X	X			Gt	Minéral doré?

Table 1 (suite) composition des carbonatites et syénites d'Ihouhaouene

Table 2 Les carbonatites d'Ihouhaouene utilisés des travaux antérieurs

		Centre 1 (Oued Ihouhaouene)													
N° d'Echantillon		158	160	170 + C	181	185	351	375	440	444	455	458	538	IHO 2	171
C I (bréchiques)	RT	-	-	+	+	-	-	-	-	+	-	+	-	-	-
	Réf	-	ouz	ouz, Jullien 2016	ouz	-	ouz	ouz	ouz	ouz/griff	-	ouz/griff	ouz	-	Ouz
	Lame	+	-	+	-	+	-	-	-	+	+	+	-	+	+
	Ech	-	-	+	-	-	-	+	+	-	-	+	-	-	-
	EPMA	-	cpx, amph	ap, cpx, wol, gt	ap,all,	-	-	-	-	-	-	all,	-	-	ap,all,
	isotope	-	C, O (in cal)	-	C, O (in cal)	-	C, O (in cal)	C, O (in cal)	C, O (in cal)	-	-	C, O (in cal)	C, O (in cal)	-	C, O (in cal)
	REE	-	-	+	ap rose	-	-	-	-	+	-	+	-	-	cpx, ap
	traces	-	-	ap, cpx, wol,	calcite	-	calcite	calcite	calcite	calcite	-	calcite	calcite	-	-

N° d'Echantillon		355	453	457(a, b, c)	907	952			354	356	371
C II (pegmatitiques)	RT										
	Réf		ouz	ouz					ouz	ouz	ouz
	Lame	+		+	+	+					
	Ech			+		+	C III (veines de calcite)		+	+	
	EPMA			cpx, amph							
	isotope		C, O (in cal)	C, O (in cal)					C, O (in cal)	C, O (in cal)	C, O (in cal)
	REE										
	traces									calcite	

Table 2 (suite)

		Centre 3 (Tirahart Nord)													
N° d'Echantillon		3,13	3,15	3,19	3,22	3,25	3,32	3,34	3,6	642	686	687	866	867	
C I (bréchiques)	RT			+		+	+	+							
	Réf	Frd	Frd, soraya	Frd, soraya		Frd, soraya	Frd	Frd, soraya		anal2016	soraya ? Sy				
	Lame	+	+	+	+	+	+	+	+	+	+	+	+	+	
	Ech									poudre					
	EPMA		cpx, fk, all	amph, fk, cal, sph		cal		all, fk , amph		ap					
	isotope	C, O (in cal)	C, O (in cal)	C, O (in cal), Rb/Sr, Sm/Nd		C, O (in cal)	C, O (in cal), Rb/Sr, Sm/Nd	C, O (in cal)							
	REE			Rb, Sr, sm Nd			Rb, Sr, sm Nd								

N° d'Echantillon		3,9	3,12	3,14	3,20	3,23	3,28	3,30	3,31	3,33	690 (a,b,c)	693	694	864	911
C II (pegmatitiques)	RT														
	Réf			Frd, master				soraya	soraya	Frd, soraya, master		soraya, master, anal2016	Jullien		
	Lame	+	+	+	+	+	+	+	+	+	+	+	+	+	+
	Ech	poudre											+		
	EPMA			brith, ap				sph, amph	cal, ap	ap, monz, brith, ap		monz, monz, monz, ap			
	isotope			C, O (in cal)			C, O (in cal)			C, O (in cal)					

N° d'Echantillon		3,1	3,3	3,26	3,4	3,8	639
C III (veines de calcite)	RT						
	Réf	Frd	Frd, master, soraya	Frd			
	Lame	+	+	+	+	+	+
	Ech				+		
	EPMA		brith, ap, monz, ap				
	isotope	C, O (in cal)	C, O (in cal)	C, O (in cal)			

Table 2 (suite)

Centre 2 (Tirahart Sud)					
N° d'Echantillon		545		604	603
C I (bréchiques)	RT	+	C II (pegmatitiques)		
	Réf	griff		ouz, anal2016	ouz
	Lame	+		+	+
	Ech				
	EPMA			ap, brith, ap	brith
	isotope				
	REE	+			

Annexe B

Modélisation géochimique des processus magmatiques (Chapitre II)

Table 1 Representative major element whole-rock compositions of granulitic basement and cumulats in syenites

Rock type	**S.P**	**S.P**	**D**	**G**	**L**	**S.P**	**L**	**L**	**SK**	**M**	**M**	**L**	**N**	**S.P**	**S.C**	**S.C**	**D**
Localization						**OI**									**SWT**		
Sample	IC1-1	IC1-3	IC1-7a	IC1-9	IC1-10	IC1-13B	IC1-14	IC1-17	IC1-20B	IC1-20	Tih1-a	IC2-3	IC2-6B	IC2-7	IC2-15	IC2-15S	IC2-16
SiO_2 (wt%)	64,68	64,87	53,69	53,75	87,08	63,36	75,66	75,65	47,04	13,23	24,55	75,10	48,94	63,09	61,63	65,68	46,90
Al_2O_3	18,97	19,08	16,73	23,95	9,49	17,48	13,13	12,92	13,02	2,64	1,75	13,57	10,15	19,77	12,95	12,67	13,56
Fe_2O_3	0,34	0,19	10,21	14,41	0,52	1,01	1,32	1,38	2,59	4,46	1,32	0,88	6,92	0,74	9,52	8,39	16,62
MnO	b.d	b.d	0,17	0,14	b.d	0,04	0,03	0,03	0,42	0,59	0,74	0,02	0,32	b.d	0,16	0,11	0,25
MgO	0,21	0,04	5,47	3,04	0,11	0,40	0,27	0,18	9,51	15,14	0,96	0,19	8,13	0,3	1,57	0,95	4,22
CaO	0,68	0,35	8,71	0,45	0,09	2,01	1,29	0,93	21,94	32,35	46,51	0,91	20,62	1,45	4,07	3,40	8,52
Na_2O	3,51	2,41	2,99	0,43	0,26	2,15	3,05	2,67	1,26	b.d	0,14	2,34	1,44	3,37	2,78	2,80	3,28
K2O	10,75	12,56	1,03	2,3	2,12	11,89	4,89	5,61	0,43	0,47	0,42	6,52	0,6	10,1	3,89	3,81	1,3
TiO_2	b.d	b.d	0,81	0,86	0,18	0,88	0,22	0,2	0,09	0,09	0,07	0,08	0,39	0,06	1,49	1,19	3,06
P_2O_5	b.d	b.d	0,27	b.d	b.d	b.d	b.d	b.d	0,15	b.d	b.d	0,10	b.d	0,31	0,59	0,42	0,62
LOI	0,34	0,27	0,33	0,52	1,13	0,83	0,80	0,85	2,43	30,67	24,15	0,73	1,52	0,98	0,94	0,66	1,74
Total	99,48	99,76	100,38	99,86	100,98	100,06	100,67	100,42	98,89	99,64	100,60	100,4	99,02	100,17	99,57	100,06	100,06
CO_2	0,0	0,11	0,09	0,02	0,05	0,23	0,20	0,17	1,88	25,49	21,13	0,04	0,90	0,17	0,07	0,03	0,08
F	0,006	0,003	0,058	0,003	0,002	0,044	0,008	0,007	0,022	0,064	0,008	0,002	0,036	0,024	0,084	0,058	0,10
S	<0,01	<0,01	0,05	0,01	<0,01	<0,01	<0,01	0,01	0,25	0,03	<0,01	0,01	0,19	<0,01	0,06	<0,01	0,04
Cl (ppm)	66	49	76	93	51	115	130	38	940	510	78	44	460	240	275	440	1870
Mg#	0,72	0,45	0,68	0,46	0,46	0,61	0,45	0,34	0,94	0,93	0,74	0,46	0,82	0,62	0,40	0,31	0,50
$(N+K)_{ox}/Al_{ox}$	0,8	0,78	0,24	0,11	0,25	0,8	0,6	0,64	0,13	-	0,32	0,65	0,20	0,68	0,52	0,52	0,34

Mg# = $Mg/(Mg+Fe_{tot})$

OI: Oued Ihouhauene; SWT: South Wadi Tirahart; NWT: North Wadi Tirahart

S.P: syenitic pegmatite; S.C: Syenitic cumulats; D: dolerite; L: leptynite; G: granulite Al-Fe; M: marble; SK: skarn; Q: quartzite; G.Q: garnet quartzit; AN: anorthosite; N: norite;

Table 1 Continued

Rock type	**Q**	**M**	**P**	**G.Q**	**AN**	**L**
Localization	**SWT**		**NWT**			
Sample	IC2-30	IC2-22	IC3-A1	IC3-A2	IC3-D	IC3-E
SiO_2 (wt%)	99,21	12,35	49,85	65,33	49,07	78,02
Al_2O_3	0,42	1,78	3,40	10,55	24,66	12,43
Fe_2O_3	0,11	3,92	12,15	7,10	3,17	0,46
MnO	b.d	1,04	11,26	12,0	0,15	b.d
MgO	b.d	19,49	9,29	1,49	2,82	0,23
CaO	0,03	28,46	13,24	3,77	12,35	1,18
Na_2O	b.d	b.d	0,18	b.d	3,39	3,27
K2O	0,08	b.d	b.d	b.d	1,54	3,71
TiO_2	0,05	0,05	0,15	0,14	0,04	0,04
P_2O_5	b.d	b.d	b.d	0,13	0,36	b.d
LOI	0,3	31,73	0,2	-0,03	2,84	0,67
Total	100,21	98,82	99,72	100,47	100,38	100,01
CO_2	<0,01	25,79	0,24	0,07	0,03	0,05
F	<0,002	0,004	0,01	0,01	0,09	0,003
S	<0,01	<0,01	<0,01	<0,01	<0,01	<0,01
Cl (ppm)	42	370	150	110	235	195
Mg#	-	0,95	0,75	0,45	0,78	0,66
$(N+K)_{ox}/Al_{ox}$	-	-	-	-	0,2	0,56

Mg# = $Mg/(Mg+Fe_{tot})$

OI: Oued Ihouhauene; SWT: South Wadi Tirahart; NWT: North Wadi Tirahart

S.P: syenitic pegmatite; S.C: Syenitic cumulats; D: dolerite; L: leptynite; G: granulite Al-Fe; M: marble; SK: skarn; Q: quartzite; G.Q: garnet quartzit; AN: anorthosite; N: norite

Table 2 Representative trace element whole-rock compositions of granulitic basement and cumulats in syenites

Rock type	**S.P**	**S.P**	**D**	**G**	**L**	**S.P**	**L**	**L**	**SK**	**M**	**M**	**L**	**N**	**S.P**	**S.C**	**S.C**	**D**
Localization						**OI**									**SWT**		
Sample	IC1-1	IC1-3	IC1-7a	IC1-9	IC1-10	IC1-13B	IC1-14	IC1-17	IC1-20B	IC1-20	Tih1-a	IC2-3	IC2-6B	IC2-7	IC2-15	IC2-15S	IC2-16
Cs (ppm)	2,6	1,85	0,29	0,26	0,25	1,18	0,10	0,04	0,38	1,62	0,13	0,29	0,9	0,47	0,22	0,29	0,62
Rb	440	397	21,46	68,2	47,79	368	76,67	57,23	19,74	28,57	11,48	196	27,21	179	63,8	77,45	47,25
Ba	7704	4844	591	914	473	4164	1792	2221	306	440	270	516	284	5354	3581	2066	1204
Th	80,1	0,37	6,59	18,56	7,17	44,49	24,44	9,98	27,38	23,04	2,13	94,18	26,13	74,07	21,8	26,59	4,13
U	3,87	0,12	1,52	9,55	0,52	10,78	0,67	0,41	3,35	3,26	0,32	11,61	6,92	2,88	2,08	4,92	5,85
Nb	1,74	0,34	56,26	78,45	3,78	799	4,52	5,26	8,32	20,9	2,02	9,96	56,19	7,31	213	189	489
Ta	0,14	0,01	3,67	4,01	0,32	69,03	0,16	0,26	38,64	16,96	0,23	0,59	3,84	0,61	13,84	11,06	31,91
La	51,6	18,68	31,1	52,41	33,91	98,72	126	90,68	11,57	52,89	33,66	37,28	63,52	96,58	99,95	98,09	52,6
Ce	82,25	23,74	62,89	87,29	43,25	277	178	145	19,99	84,85	54,87	59,84	157	143	183	188	105
Pb	1,68	90,72	0,13	0,27	13,67	1,16	33,42	26,08	0,08	0,14	13,96	0,82	0,11	0,7	0,3	0,31	0,28
Pr	7,35	2,1	7,2	9,02	5,58	39,3	15,51	14,17	2,24	8,04	5,38	5,64	19,71	13,85	21,66	21,21	12,41
Sr	3173	3164	361	140	43,02	1523	296	260	1319	1017	131	160	911	2355	334	273	472
Nd	22,12	6,4	28,41	33,1	19,58	166	45,24	45,01	8,15	26,59	17,55	17,55	78,31	48,24	86,67	83,52	50,04
Zr	1,73	0,55	106	49	77,29	49,5	150	77,64	26,06	19,11	8,55	93,2	135	4,06	23,62	14,53	278
Hf	0,08	0,01	3,06	1,49	3,11	2,16	5,49	3,17	0,78	0,72	0,39	3,72	4,97	0,19	1,09	0,6	7,62
Sm	2,34	0,83	5,32	6,81	2,81	32,61	4,57	5,34	1,55	3,95	2,61	2,83	14,09	6,38	15,97	15,44	9,96
Eu	1,34	1,13	1,46	1,69	0,81	7,46	1,36	1,68	0,43	1,02	0,47	0,93	2,99	4,54	3,78	3,57	2,92
Gd	1,26	0,51	5,02	6,98	1,98	20,75	2,46	3,25	1,39	3	2	2,31	9,53	3,63	14,51	13,7	9,49
Tb	0,11	0,05	0,76	1,12	0,20	2,34	0,28	0,37	0,21	0,38	0,26	0,37	1,1	0,36	2,11	1,97	1,39
Dy	0,43	0,24	4,61	6,99	0,89	10,04	1,35	1,86	1,3	1,99	1,35	2,27	4,82	1,44	12,32	11,32	8,05
Y	1,65	1,18	24,38	39,12	3,87	35,9	5,76	7,87	6,53	11,45	7,11	14,27	18,93	5,61	60,76	57,75	38,68
Ho	0,06	0,04	0,95	1,45	0,15	1,40	0,24	0,34	0,24	0,37	0,25	0,48	0,73	0,20	2,43	2,21	1,54
Er	0,14	0,08	2,64	4	0,34	2,87	0,65	0,9	0,68	0,98	0,63	1,41	1,69	0,44	6,61	5,9	4,1
Tm	0,02	0,01	0,39	0,6	0,05	0,32	0,09	0,13	0,11	0,15	0,09	0,22	0,23	0,05	0,95	0,83	0,56
Yb	0,09	0,05	2,48	3,77	0,31	1,56	0,61	0,86	0,76	0,97	0,55	1,45	1,43	0,26	5,9	5,13	3,54
Lu	0,02	0,01	0,37	0,55	0,05	0,18	0,09	0,13	0,12	0,14	0,08	0,2	0,22	0,03	0,87	0,75	0,51
Eu/Eu*	0,78	1,73	0,28	0,25	0,34	0,29	0,41	0,4	0,29	0,3	0,21	0,36	0,26	0,94	0,25	0,25	0,3
Nb/Ta	12,69	51,02	15,35	19,55	11,71	11,57	27,78	20,56	0,22	1,23	8,71	16,74	14,64	12,02	15,4	17,12	15,31
Zr/Hf	22,34	94,23	34,49	33,05	24,86	22,88	27,3	24,53	33,52	26,66	21,85	25,04	27,18	21,52	21,68	24,02	36,41

Mg# = Mg/(Mg+Fe_{tot})

OI: Oued Ihouhauene; SWT: South Wadi Tirahart; NWT: North Wadi Tirahart

S.P: syenitic pegmatite; S.C: Syenitic cumulats; D: dolerite; L: leptynite; G: granulite Al-Fe; M: marble; SK: skarn; Q: quartzite; G.Q: garnet quartzit; AN: anorthosite; N: norite

Table 2 Continued

Rock type	**Q**	**M**	**P**	**G.Q**	**AN**	**L**
Localization	**SWT**		**NWT**			
Sample	IC2-30	IC2-22	IC3-A1	IC3-A2	IC3-D	IC3-E
Cs (ppm)	0,01	0,01	0,05	0,03	0,29	0,06
Rb	2,17	0,05	0,49	0,28	46,08	43,67
Ba	25,07	11,84	2,94	28,89	328	1394
Th	0,7	1,25	2,96	1,87	7,99	15,08
U	0,98	0,14	15,71	16,19	3,67	2,34
Nb	3,67	2,23	5,09	2,1	30,83	0,43
Ta	0,24	0,47	2,37	0,22	2,86	0,08
La	4,73	5,63	20,39	18,56	11,02	34
Ce	7,20	10,47	60,07	35,60	17,11	42,27
Pb	0,01	0,002	0,01	0,003	0,09	0,14
Pr	0,89	1,29	7,79	4,05	1,63	3,57
Sr	3,39	30,6	26,9	8,73	302	406
Nd	2,93	5,06	29,08	15,21	5,04	10,45
Zr	11,78	30,5	28,19	17,35	12,22	56,69
Hf	0,37	0,9	1,3	0,55	0,44	1,73
Sm	0,38	1,11	5,45	4,99	0,81	1,07
Eu	0,08	0,25	0,3	0,41	0,34	1,33
Gd	0,24	1,29	4,35	7,75	0,66	0,58
Tb	0,03	0,21	0,76	1,44	0,1	0,06
Dy	0,14	1,43	4,93	8,59	0,59	0,21
Y	0,65	10,34	28,23	45,18	3,2	1,07
Ho	0,02	0,32	1,01	1,49	0,12	0,04
Er	0,06	0,98	2,8	3,54	0,31	0,11
Tm	0,01	0,15	0,40	0,45	0,05	0,02
Yb	0,05	1	2,43	2,51	0,31	0,12
Lu	0,01	0,16	0,33	0,3	0,05	0,02
Eu/Eu*	0,25	0,21	0,06	0,07	0,47	1,69
Nb/Ta	15,06	4,75	2,14	9,46	10,79	5,67
Zr/Hf	31,42	32,93	21,21	31,36	27,80	32,75

Mg# = Mg/(Mg+Fe_{tot})

OI: Oued Ihouhauene; SWT: South Wadi Tirahart; NWT: North Wadi Tirahart

S.P: syenitic pegmatite; S.C: Syenitic cumulats; D: dolerite; L: leptynite; G: granulite Al-Fe; M: marble; SK: skarn; Q: quartzite; G.Q: garnet quartzit; AN: anorthosite; N: norite

Table II.6 Representative major element composition of minerals (**Supplementary data B1**)

Rock type	**Carb**	**Sy**	**Sy**	**Carb**	**Carb**
Sample	IC1-4B.13	IC3-4.1	IC3-4.2	Inh545.26	IC2-9A.22
Mineral	Kfs	Kfs	Ab	Gt	Gt
Type	Core	Core	Core	rim	rim
SiO2	62,86	63,43	68,01	38,04	35,81
TiO2	0,02	0,03	-	0,16	0,69
Al2O3	18,1	18,01	19,53	9,67	4,42
Fe2O3	0,1	0,19	0,02	16,67	24,62
MnO	-	0,001	0,01	0,51	0,37
MgO	-	0,01	0,002	0,03	0,03
CaO	0,002	0,04	0,05	34,89	33,34
Na2O	0,24	0,2	11,67	-	0,03
K2O	17,24	17,3	0,23	0,01	-
P2O5	-	-	-	-	-
Cr2O3	-	0,01	-	0,03	-
NiO	-	-	-		
La2O3	-	-	-	-	-
Ce2O3	-	-	-	-	-
Pr2O3	-	-	-	-	-
Nd2O3	-	-	-	-	-
Sm2O3	-	-	-	-	-
Gd2O3	-	-	-	-	-
Dy2O3	-	-	-	-	-
Y2O3	-	-	-	-	-
ThO2	-	-	-	-	-
SO2	-	-	-	-	-
F	-	-	-	-	-
Cl	-	-	-	-	-
Total	98,57	99,22	99,52	101,85	101,95
Numbers of ions on the basis of	***8O***			***12O***	
Si	2,97	2,98	2,99	3,14	3,13
Ti	-	-	-	0,01	0,05
Al	1,01	1	1,01	0,94	0,46
Fe3+	0,004	0,01	0,001	1,08	1,67
Fe2+	-	-	-	0,07	0,14
Mn	-	-	-	0,04	0,03
Ni	-	-	-	-	-
Mg	-	-	-	0,003	0,003
Ca	0,0001	0,002	0,003	3,09	3,13
Na	0,02	0,02	0,99	0,001	-
K	1,04	1,04	0,01	0,001	-
P	-	-	-	-	-
Cr	-	-	-	0,002	-
La	-	-	-	-	-
Ce	-	-	-	-	-
Pr	-	-	-	-	-
Nd	-	-	-	-	-
Pm	-	-	-	-	-
Sm	-	-	-	-	-
Eu	-	-	-	-	-
Gd	-	-	-	-	-
Tb	-	-	-	-	-
Dy	-	-	-	-	-
Y	-	-	-	-	-
Th	-	-	-	-	-
S	-	-	-	-	-
F	-	-	-	-	-
Cl	-	-	-	-	-
Total	5,05	5,04	5,01	8,38	8,59
An	0,01	0,21	0,25		
Ab	2,08	1,70	98,47		
Or	97,91	98,09	1,27		
Alm				1,71	2,74
Pyr				0,08	0,07
Spess				0,83	0,55
Gross				72,18	63,05
Andr				25,2	33,59

Kfs: K-feldspar, Ab: Albite, Gt: Garnet, Cal: Calcite, Wo:Wollastonite, Aln: Alanite, Sph: Sphene, Br: Britholite

Table II.6 Continued

Rock type	Sy	Sy	Carb	Sy	Carb
Sample	IC2-27B.44	IC1-4B.27	INH 545.25	IC2-27B.25	IC2-9A.16
Mineral	Gt	Cal	Cal	Wo	Wo
Type	rim	Core	Core	Core	Core
SiO2	36,26	0,01	0,11	50,62	50,83
TiO2	0,53	0,01	0,03	0,01	0,02
Al2O3	5,55	0,01	0,04	0,01	0,01
Fe2O3	23,06	0,15	0,04	0,27	0,46
MnO	0,49	0,19	0,02	0,66	0,57
MgO	0,03	0,16	-	-	0,004
CaO	33,75	57,59	55,65	47,8	47,62
Na2O	0,01	0,01	0,02	0,02	0,002
K2O	0,004	-	0,03	0,002	-
P2O5	-	-	-	-	-
Cr2O3	-	0,001	0,02	-	-
NiO		0,02	-	0,02	0,01
La2O3	-	-	-	-	-
Ce2O3	-	-	-	-	-
Pr2O3	-	-	-	-	-
Nd2O3	-	-	-	-	-
Sm2O3	-	-	-	-	-
Gd2O3	-	-	-	-	-
Dy2O3	-	-	-	-	-
Y2O3	-	-	-	-	-
ThO2	-	-	-	-	-
SO2	-	-	-	-	-
F	-	-	-	-	-
Cl	-	-	-	-	-
Total	102,17	58,14	55,96	99,41	99,53
Numbers of ions on the basis of		***3O***		***6O***	
Si	3,13	0,0002	0,002	0,99	0,99
Ti	0,03	0,0001	0,0004	0,0002	0,0003
Al	0,56	0,0001	0,0008	0,0001	0,0003
Fe3+	1,56	-	-	-	-
Fe2+	0,11	0,002	0,0005	0,004	0,01
Mn	0,04	0,003	0,0003	0,01	0,01
Ni	-	0,0002	-	0,0003	0,0002
Mg	0,003	0,004	-	-	0,0001
Ca	3,12	0,99	0,99	1	1
Na	-	0,0003	0,001	0,001	0,0001
K	-	-	0,001	-	-
P	-	-	-	-	-
Cr	-	-	0,0002	-	-
La	-	-	-	-	-
Ce	-	-	-	-	-
Pr	-	-	-	-	-
Nd	-	-	-	-	-
Pm	-	-	-	-	-
Sm	-	-	-	-	-
Eu	-	-	-	-	-
Gd	-	-	-	-	-
Tb	-	-	-	-	-
Dy	-	-	-	-	-
Y	-	-	-	-	-
Th	-	-	-	-	-
S	-	-	-	-	-
F	-	-	-	-	-
Cl	-	-	-	-	-
Total	8,55	1	1	2,01	2,01
An					
Ab					
Or					
Alm	2,24				
Pyr	0,07				
Spess	0,74				
Gross	64,69				
Andr	32,29				

Kfs: K-feldspar, Ab: Albite, Gt: Garnet, Cal: Calcite, Wo:Wollastonite, Aln: Alanite, Sph: Sphene, Br: Britholite

Table II.6 Continued

Rock type	**Carb**	**Carb**	**Carb**	**Sy**	**Sy**
Sample	INH 458.24	INH 642. 29	IC2-9A.41	INH 3.24.5	IC1-24A.34
Mineral	Aln	Sph	Br	Br	Mt
Type	Core	Core	Core	Core	Core
SiO2	32,92	29,82	20,29	20,12	0,09
TiO2	-	34,23	-	-	0,11
Al2O3	15,05	3,08	-	-	0,04
Fe2O3	12,21	1,40	0,03	-	93,99
MnO	0,05	0,06	-	-	0,07
MgO	1,53	0,05	-	-	0,01
CaO	13,51	27,18	16,6	19,1	0,01
Na2O	0,03	0,01	0,08	0,06	-
K2O	0,01	-	0,004	0,01	0,004
P2O5	0,01	-	3,73	2,6	-
Cr2O3	0,15	-	-	-	0,024
NiO	0,02	0,01	-	-	0,02
La2O3	5,37	-	10,47	9,16	-
Ce2O3	11,06	-	23,76	23,14	-
Pr2O3	0,87	-	2,02	2,11	-
Nd2O3	3,43	-	9,49	9,99	-
Sm2O3	0,25	-	2,93	3,18	-
Gd2O3	0,10	-	0,72	0,74	-
Dy2O3	-	-	0,13	0,19	-
Y2O3	<0.001	-	0,99	0,99	-
ThO2	0,03	-	2,67	2,42	-
SO2	-	-	0,20	0,24	-
F	0,39	-	1,63	1,76	-
Cl	0,005	-	0,34	0,23	-
Total	96,97	95,84	94,82	97,07	101,32
Numbers of ions on the basis of	***13O***	***5O***	***24O***		***4O***
Si	3,02	4	5,34	5,33	0,003
Ti	-	3,45	-	-	0,003
Al	1,63	0,49	-	-	0,002
Fe3+	0,37	-	-	-	1,98
Fe2+	0,57	0,16	0,01	-	1
Mn	0,004	0,01	-	-	0,002
Ni	-	0,001	-	-	-
Mg	0,21	0,01	-	-	-
Ca	1,33	3,91	4,68	5,42	-
Na	-	0,003	0,04	0,03	-
K	-	-	0,001	0,005	-
P	-	-	0,83	0,58	-
Cr	-	-	-	-	-
La	0,18	-	1,02	0,89	-
Ce	0,37	-	2,29	2,24	-
Pr	0,03	-	0,19	0,2	-
Nd	0,11	-	0,89	0,94	-
Pm	-	-	-	-	-
Sm	0,01	-	0,27	0,29	-
Eu	-	-	-	-	-
Gd	-	-	0,06	0,06	-
Tb	-	-	-	-	-
Dy	-	-	0,01	0,02	-
Y	-	-	0,14	0,14	-
Th	-	-	0,16	0,15	-
S	-	-	0,05	0,06	-
F	0,11	-	1,36	1,48	-
Cl	-	-	0,15	0,1	-
Total	7,95	12.02	17,49	17,94	3
An					
Ab					
Or					
Alm					
Pyr					
Spess					
Gross					
Andr					

Kfs: K-feldspar, Ab: Albite, Gt: Garnet, Cal: Calcite, Wo:Wollastonite, Aln: Alanite, Sph: Sphene, Br: Britholite

Supplementary Data B2

Table 1 Calculated partition coefficient in model A

	Sample	Rb	Sr	Y	Zr
Recalculated liquids in equilibrium with apatite from Si-rich carbonatites	INH170	0.24	8443	619	78.39
	INH170	0.22	8786	613	79.00
	INH170	0.22	8474	610	79.61
	INH170	0.20	9393	601	80.21
	INH170	0.20	9065	542	80.82
	INH170	0.20	9278	599	81.42
	INH170	0.21	8768	658	82.03
	INH170	0.17	8136	543	82.64
	INH170	0.20	10446	636	83.24
	INH170	0.20	8679	604	83.85
	INH170	0.21	8481	618	84.45
	INH170	0.18	8548	606	85.06
	INH170	0.25	9713	751	85.67
	IC1-2C	0.14	11761	765	74.76
	IC1-2C	0.11	10817	602	75.36
	IC1-2C	0.06	11246	437	75.97
	IC1-2C	0.18	9565	737	76.58
	IC1-2C	0.15	11032	684	77.18
	IC2-9A	0.23	11724	963	85.18
	IC2-9A	0.16	11495	739	77.42
	IC2-9A	0.22	11491	1235	98.71
	IC2-9A	0.16	10823	839	124.13
Recalculated liquids in equilibrium with Cpx from Red syenites	INH159	46.94	637	19	108.51
	INH159	54.24	448	17	58.04
	INH159	3.14	826	16	211.57
	INH159	3.18	801	14	212.34
	INH159	2.31	576	19	136.85
	IC3-4	16.29	2080	162	109.02
	IC3-4	38.29	1877	146	99.49
	IC3-4	2.34	1715	159	115.62
	IC3-4	3.41	1931	168	117.96
	IC3-4	1.94	2093	119	149.02
	IC3-4	1.74	1358	115	116.09
average composition	**Carbonatite liquid**	0.19	9826	682	83.26
	Syenite liquid	15.80	1304	87	130.41
Partition coefficient	**D = SL / CL**	**84.75**	**0.13**	**0.13**	**1.57**

kd: Cpx equilibrium liquid in red syenit (SL) / apatite equilibrium liquid in carbonatite (CL)

Standard deviation CL	0.04	1262	165.97	10.47
Standard deviation SL	20.44	656.21	68.70	46.26

Table 1 Continued

	Sample	Nb	Ba	La	Ce
recalculated liquids in equilibrium with apatite from Si-rich carbonatites	INH170	45.80	0.90	6812	9753
	INH170	46.00	0.60	6805	9878
	INH170	43.30	0.69	6622	9522
	INH170	42.00	0.78	7350	11042
	INH170	39.20	1.59	6882	10165
	INH170	42.50	0.51	7421	11107
	INH170	47.20	0.76	7428	10740
	INH170	40.90	0.75	6463	9716
	INH170	26.70	1.02	8068	11967
	INH170	45.10	0.94	7007	10305
	INH170	47.60	0.93	6604	9682
	INH170	43.70	0.74	6717	9723
	INH170	43.40	1.11	8280	11947
	IC1-2C	33.00	0.90	11374	17100
	IC1-2C	48.30	0.92	8195	12308
	IC1-2C	22.41	0.36	6253	9514
	IC1-2C	33.10	0.73	8926	14494
	IC1-2C	25.41	0.90	8918	13946
	IC2-9A	27.49	15.54	13387	24569
	IC2-9A	19.93	1.92	9181	16902
	IC2-9A	17.84	3.33	19001	33859
	IC2-9A	25.22	2.18	11204	20527
recalculated liquids in equilibrium with Cpx from Red syenites	INH159	7.16	134.17	27.09	58.14
	INH159	11.16	116.67	17.74	43.52
	INH159	0.45	12.25	36.49	77.73
	INH159	0.06	1.00	43.01	87.49
	INH159	0.81	8.54	26.05	59.69
	IC3-4	10.12	32.79	122.36	407.14
	IC3-4	23.44	224.58	189.83	450.04
	IC3-4	5.60	-	165.61	502.16
	IC3-4	6.23	5.96	149.73	448.49
	IC3-4	9.20	2.58	253.78	637.66
	IC3-4	3.82	1.13	135.03	408.54
average composition	**Carbonatite liquid**	36.64	1.73	8586	13580
	Syenite liquid	7.10	53.97	106.07	289.15
Partition coefficient	**D = SL / CL**	**0.19**	**31.15**	**0.01**	**0.02**

kd: Cpx equilibrium liquid in red syenit (SL) / apatite equilibrium liquid in carbonatite (CL)

Standard deviation CL	10.09	3.15	2963.25	6019
Standard deviation SL	6.66	77.65	80.41	223.16

Table 1 Continued

	Sample	Pr	Sm	Eu	Gd
recalculated liquids in equilibrium with apatite from Si-rich carbonatites	INH170	952	476	76.41	339.68
	INH170	951	460	73.44	316.05
	INH170	920	451	71.99	316.85
	INH170	1040	468	77.76	323.04
	INH170	968	428	71.69	303.13
	INH170	1048	469	77.66	323.87
	INH170	1040	500	81.15	358.67
	INH170	920	417	69.31	286.63
	INH170	1131	500	82.27	339.98
	INH170	1007	476	77.18	328.06
	INH170	949	469	74.72	327.05
	INH170	950	461	72.81	318.87
	INH170	1168	565	89.76	386.25
	IC1-2C	1543	605	105.67	356.88
	IC1-2C	1142	476	81.51	289.16
	IC1-2C	866	374	63.85	222.06
	IC1-2C	1362	566	98.15	337.99
	IC1-2C	1273	557	95.47	332.14
	IC2-9A	2158	959	182.87	569.53
	IC2-9A	1531	701	134.26	414.58
	IC2-9A	2998	1289	240.45	750.34
	IC2-9A	1886	801	156.58	470.50
recalculated liquids in equilibrium with Cpx from Red syenites	INH159	7.67	7.70	1.81	7.74
	INH159	5.72	7.46	1.48	7.56
	INH159	9.29	7.26	1.93	5.75
	INH159	9.91	7.26	1.76	5.71
	INH159	7.67	7.67	2.02	6.30
	IC3-4	61.87	70.01	16.71	60.10
	IC3-4	60.47	61.64	14.84	53.07
	IC3-4	69.57	70.82	17.38	58.88
	IC3-4	64.50	72.09	17.55	60.99
	IC3-4	80.80	64.90	16.51	50.81
	IC3-4	56.20	55.74	14.02	43.12
average composition	**Carbonatite liquid**	1264	566.80	97.95	364.15
	Syenite liquid	39.43	39.32	9.64	32.73
Partition coefficient	**D = SL / CL**	**0.03**	**0.07**	**0.10**	**0.09**

kd: Cpx equilibrium liquid in red syenit (SL) / apatite equilibrium liquid in carbonatite (CL)

Standard deviation CL	510.94	210.23	43.66	110.58
Standard deviation SL	30.68	30.83	7.57	25.49

Table 1 Continued

	Sample	Dy	Yb	Lu	Hf	Ta	Pb
recalculated liquids in equilibrium with apatite from Si-rich carbonatites	INH170	130.77	26.62	3.22	1.16	0.47	406.58
	INH170	125.89	24.71	3.02	1.11	0.49	313.59
	INH170	125.47	26.08	3.19	1.02	0.40	360.92
	INH170	126.25	26.22	3.20	0.82	0.44	291.48
	INH170	116.22	23.88	2.84	0.87	0.34	314.20
	INH170	127.01	26.07	3.14	0.73	0.38	280.86
	INH170	142.66	29.66	3.61	1.08	0.42	407.16
	INH170	111.83	22.85	2.71	0.91	0.31	378.22
	INH170	130.16	27.44	3.34	0.54	0.19	368.28
	INH170	128.61	25.98	3.12	1.15	0.39	463.09
	INH170	130.22	25.96	3.17	1.22	0.47	468.50
	INH170	127.54	25.93	3.16	1.17	0.41	335.73
	INH170	159.05	32.85	4.03	0.91	0.40	329.28
	IC1-2C	151.26	32.69	3.83	0.71	0.13	475.78
	IC1-2C	123.49	25.72	3.05	1.12	0.52	615.72
	IC1-2C	90.96	16.97	1.97	0.15	0.04	386.56
	IC1-2C	144.66	29.53	3.47	0.83	0.22	569.20
	IC1-2C	140.79	26.49	3.11	0.08	0.16	512.70
	IC2-9A	217.33	36.57	4.43	0.52	0.21	805.25
	IC2-9A	159.30	27.27	3.19	0.53	0.34	428.86
	IC2-9A	283.87	46.16	5.48	0.66	0.38	917.05
	IC2-9A	176.89	30.85	3.53	0.80	0.30	571.13
recalculated liquids in equilibrium with Cpx from Red syenites	INH159	4.61	1.60	0.24	6.20	0.21	55.88
	INH159	4.29	1.18	0.17	4.15	0.68	99.31
	INH159	3.14	1.66	0.23	9.44	0.05	43.92
	INH159	2.86	1.48	0.19	9.29	0.06	44.31
	INH159	3.63	1.77	0.21	6.53	0.06	35.29
	IC3-4	36.58	7.74	0.67	3.08	0.22	56.47
	IC3-4	33.09	7.03	0.57	2.88	0.66	78.92
	IC3-4	35.35	8.09	0.68	3.20	0.15	55.98
	IC3-4	38.23	8.56	0.72	3.33	0.21	57.35
	IC3-4	27.19	6.49	0.55	4.13	0.57	68.63
	IC3-4	25.29	5.66	0.50	3.26	0.06	43.73
average composition	**Carbonatite liquid**	144.10	28.02	3.35	0.82	0.34	454.55
	Syenite liquid	19.48	4.66	0.43	5.05	0.27	58.16
Partition coefficient	**D = SL / CL**	**0.14**	**0.17**	**0.13**	**6.13**	**0.79**	**0.13**

kd: Cpx equilibrium liquid in red syenit (SL) / apatite equilibrium liquid in carbonatite (CL)

Standard deviation CL	40.20	5.65	0.68	0.32	0.13	162.09
Standard deviation SL	15.56	3.09	0.22	2.46	0.25	18.37

Table 2 Calculated partition coefficient in model B

	Sample	Rb	Sr	Y	Zr	Nb	Ba	La	Ce	Pr
recalculated liquids in equilibrium with apatite from White syenite	IC2-27B	86.00	1011.42	165.90	3508.33	993.64	13.17	327.24	836.78	102.69
	IC2-27B	114.00	984.00	100.25	3532.14	121.82	12.08	258.87	676.10	83.86
recalculated liquids in equilibrium with Cpx from White Syenite	IC2-27B	0.20	121.12	2.17	47.74	0.39	3.40	3.56	9.85	1.17
	IC2-27B	0.02	118.68	0.46	31.32	0.00	0.50	0.60	1.56	0.18
	IC2-27B	0.28	1160.52	2.65	357.96	0.02	8.88	5.52	13.84	1.49
	IC2-27B	27.06	1182.72	1.16	108.30	0.09	2038.33	4.72	8.67	0.81
	IC2-27B	0.28	1390.16	58.35	1310.00	57.80	36.71	156.72	414.56	47.12
average composition	**Carbonatite liquid**	100.00	997.71	133.07	3520.24	557.73	12.63	293.05	756.44	93.27
	Syenite liquid	5.57	794.64	12.96	371.06	11.66	417.56	34.23	89.70	10.15
Partition coefficient	**D = SL / CL**	**0.06**	**0.80**	**0.10**	**0.11**	**0.02**	**33.07**	**0.12**	**0.12**	**0.11**

kd: Cpx equilibrium liquid in white syenit (SL) / apatite equilibrium liquid in white syenite (CL). bd below detection limit

Standard deviation CL	19.80	19.38	46.42	16.84	616.47	0.77	48.34	113.62	13.32
Standard deviation SL	12.01	622.43	25.39	541.01	25.79	906.15	68.50	181.66	20.67

Table 2 Continued

	Sample	Sm	Eu	Gd	Dy	Yb	Lu	Hf	Ta	Pb
recalculated liquids in equilibrium with apatite from White syenite	IC2-27B	62.39	bd	48.46	10.79	3.50	0.95	16.50	3.70	105.82
	IC2-27B	51.73	bd	39.01	7.76	1.85	0.53	-	0.77	53.42
recalculated liquids in equilibrium with Cpx from White Syenite	IC2-27B	1.06	0.28	0.83	0.45	0.29	0.04	0.63	0.07	4.24
	IC2-27B	0.13	0.03	0.09	0.06	0.22	0.03	0.41	0.00	3.38
	IC2-27B	0.94	0.24	0.60	0.33	2.40	0.37	4.68	0.02	34.12
	IC2-27B	0.46	0.11	0.24	0.16	0.56	0.14	1.96	0.03	131.27
	IC2-27B	36.31	9.19	25.91	13.84	3.75	0.37	15.62	0.40	39.51
average composition	**Carbonatite liquid**	57.06	-	43.73	9.27	2.67	0.74	16.50	2.23	79.62
	Syenite liquid	7.78	1.97	5.53	2.97	1.45	0.19	4.66	0.11	42.50
Partition coefficient	**D = SL / CL**	**0.14**	**-**	**0.13**	**0.32**	**0.54**	**0.26**	**0.28**	**0.05**	**0.53**

kd: Cpx equilibrium liquid in white syenit (SL) / apatite equilibrium liquid in white syenite (CL). bd below detection limit

Standard deviation CL	7.53	-	6.69	2.15	1.17	0.30	-	2.07	37.06
Standard deviation SL	15.95	4.04	11.40	6.08	1.57	0.17	6.36	0.17	52.33

Table 3 Output trace element composition of crystal crystallization and immiscibility model A

		Ce	Lu	Nb	Ta	Rb	Sr	Y	Zr	Ce/Lu	Nb/Ta	Rb/Sr	Y/Zr
50% Cpx	**X %**	0.5	0.5	0.5	0.5	0.5	0.5	0.5	0.5	-	-	-	-
Partition coefficient minerals	**D**	0.23	0.70	0.01	0.02	0.01	0.13	0.33	0.12	-	-	-	-
Melilitite (Baudouin et al. 2016)	**C0**	111	0.14	78.3	4.8	64.7	853	13.1	168	**793**	**16.31**	**0.08**	**0.08**
	D sil/carb	**0.02**	**0.13**	**0.19**	**0.79**	**84.75**	**0.13**	**0.13**	**1.57**				

Cliq: Composition of initial liquid after each fractional crystallization and immiscibility

		f	Ce	Lu	Nb	Ta	Rb	Sr	Y	Zr	Ce/Lu	Nb/Ta	Rb/Sr	Y/Zr
FC1	**Cliq**	0.55	176	0	141	9	117	1439	20	285	**1051**	**16.3**	**0.08**	**0.07**
FC2	**Cliq**	0.5	189	0	269	17	235	2472	29	527	**982**	**15.8**	**0.10**	**0.06**
FC3	**Cliq**	0.45	211	0	565	37	524	4624	46	1070	**928**	**15.1**	**0.11**	**0.04**
FC4	**Cliq**	0.4	245	0	1327	92	1317	9527	78	2413	**890**	**14.5**	**0.14**	**0.03**
FC5	**Cliq**	0.35	302	0	3543	256	3777	21917	144	6123	**874**	**13.8**	**0.17**	**0.02**

Csill: composition of sillicate liquid after each immiscibility; Ccarb: composition of carbonate liquid after each immiscibility

		F	Ce	Lu	Nb	Ta	Rb	Sr	Y	Zr	Ce/Lu	Nb/Ta	Rb/Sr	Y/Zr
Immiscib1	**Ccarb**	0.01	5208	1	700	11	1	10156	144	182	**4269**	**64.0**	**0.0001**	**0.79**
	Csill	0.01	111	0	136	9	118	1348	18	286	**709**	**15.7**	**0.09**	**0.06**
Immiscib2	**Ccarb**	0.011	5345	1	1325	22	3	17328	212	338	**3836**	**61.4**	**0.0002**	**0.63**
	Csill	0.011	114	0	257	17	238	2299	27	529	**637**	**15.1**	**0.10**	**0.05**
Immiscib3	**Ccarb**	0.012	5679	2	2772	47	6	32204	333	686	**3483**	**58.8**	**0.0002**	**0.49**
	Csill	0.012	121	0	537	37	531	4273	42	1075	**578**	**14.4**	**0.12**	**0.04**
Immiscib4	**Ccarb**	0.013	6308	2	6488	116	16	65912	562	1548	**3212**	**56.0**	**0.0002**	**0.36**
	Csill	0.013	134	0	1257	91	1334	8747	71	2424	**533**	**13.8**	**0.15**	**0.03**
Immiscib5	**Ccarb**	0.014	7412	2	6119	115	16	60110	510	1556	**4154**	**53.0**	**0.0003**	**0.33**
	Csill	0.014	158	0	3341	255	3830	19987	131	6154	**503**	**13.1**	**0.19**	**0.02**

Table 4 Output trace element composition of mixt parental liquid of model B

	Ce	Lu	Nb	Ta	Rb	Sr	Y	Zr
X %	0.5	0.5	0.5	0.5	0.5	0.5	0.5	0.5
D1	0.045	0.115	0.05	0.075	0.002	0.04	0.15	0.24
C0	**7412**	**1.78**	**6119**	**115**	**16**	**60110**	**510**	**1556**
CA	**158**	**0.31**	**3341**	**255**	**3830**	**19987**	**131**	**6154**
CA/C0	0.02	0.18	0.55	2.21	240.00	0.33	0.26	3.96
r	0.2	0.2	0.2	0.2	0.2	0.2	0.2	0.2

	F	Ce	Lu	Nb	Ta	Rb	Sr	Y	Zr	Ce/Lu	Nb/Ta	Rb/Sr	Y/Zr
Cliq	0.9	8192	1.96	6846	134	124	66992	560	1843	**4176**	**51.09**	**0.002**	**0.30**
C0	1	7412	1.78	6119	115	15.96	60110	510	1556	**4154**	**53.03**	**0.00**	**0.33**

C0: calculated liquid from immiscibility 5 from model A

CA: calculated liquid from immiscibility 5 from model A

r: rate of mingling; X: 50% cpx

D1: Partition coefficient of minerals

Cliq : mixt liquid composition after 0.1% of Cpx crystallization as parental liquid for model B

Table 5 Output trace element composition of crystal crystallization and immiscibility model B

		Ce	Lu	Nb	Ta	Rb	Sr	Y	Zr	Ce/Lu	Nb/Ta	Rb/Sr	Y/Zr
50% Cpx	**X %**	0.5	0.5	0.5	0.5	0.5	0.5	0.5	0.5	-	-	-	-
Partition coefficient minerals	**D**	0.229	0.7	0.0125	0.016	0.0085	0.125	0.33	0.1175	-	-	-	-
Calculated mixt liquid	**C0**	8192	1.96	6846	134	124	66992	560	1843	**4176**	**51.09**	**0.002**	**0.30**
	D sil/carb	**0.12**	**0.26**	**0.02**	**0.05**	**0.06**	**0.80**	**0.10**	**0.11**				

Cliq: Composition of initial liquid after each fractional crystallization and immiscibility

		f	Ce	Lu	Nb	Ta	Rb	Sr	Y	Zr	Ce/Lu	Nb/Ta	Rb/Sr	Y/Zr
CF1	**Cliq**	0.95	8522	1.99	7202	141	131	70067	579	1928	**4278**	**51.10**	**0.00**	**0.30**
CF2	**Cliq**	0.96	4732	1.58	151	27.10	33.05	71084	275	985	**2988**	**5.58**	**0.00**	**0.28**
CF3	**Cliq**	0.97	4496	1.55	97.26	22.78	28.72	72817	256	929	**2896**	**4.27**	**0.00**	**0.28**
CF4	**Cliq**	0.98	4238	1.52	61.98	18.96	24.71	73925	236	869	**2793**	**3.27**	**0.00**	**0.27**
CF5	**Cliq**	0.99	3963	1.48	39.10	15.62	21.04	74387	216	805	**2682**	**2.50**	**0.00**	**0.27**

Csill: composition of sillicate liquid after each immiscibility; Ccarb: composition of carbonate liquid after each immiscibility

		F	Ce	Lu	Nb	Ta	Rb	Sr	Y	Zr	Ce/Lu	Nb/Ta	Rb/Sr	Y/Zr
Immiscib1	**Ccarb**	0.08	38670	6.10	6941	553	570	86118	2746	9015	**6341**	**12.54**	**0.0066**	**0.30**
	Csill	0.08	4585	1.56	145.13	26.03	31.74	68590	267.42	950	**2931**	**5.58**	**0.0005**	**0.28**
Immiscib2	**Ccarb**	0.01	37033	6.00	4514	470	501	89021	2571	8582	**6176**	**9.61**	**0.0056**	**0.30**
	Csill	0.01	4391	1.54	94.38	22.11	27.87	70902	250.39	905	**2855**	**4.27**	**0.0004**	**0.28**
Immiscib3	**Ccarb**	0.01	35184	5.88	2906	395	435	91190	2391	8095	**5986**	**7.36**	**0.0048**	**0.30**
	Csill	0.01	4172	1.51	60.75	18.58	24.22	72630	232.82	853	**2767**	**3.27**	**0.0003**	**0.27**
Immiscib4	**Ccarb**	0.01	33164	5.74	1851	329	374	92579	2208	7567	**5774**	**5.63**	**0.0040**	**0.29**
	Csill	0.01	3933	1.47	38.71	15.46	20.84	73735	215.00	798	**2669**	**2.50**	**0.0003**	**0.27**
Immiscib5	**Ccarb**	0.01	31016	5.58	1156	268	316	92341	2012	6948	**5560**	**4.31**	**0.0034**	**0.29**
	Csill	0.01	3678	1.44	24.42	12.74	17.75	74196	197.20	739	**2562**	**1.92**	**0.0002**	**0.27**

Supplementary Data B2 illustration

P-T-X conditions of the chosen experimental studies:

The compositions of equilibrium melt calculated from clinopyroxene and apatite REE and trace elements are determined from experimental partition coefficients (mineral/melt) that obey the Henry's Law and concentrations are function of the intensity of the process.

We chose partition coefficient between:

- *Carbonatite and apatite* from Hammouda *et al*. 2010; experiments performed at 4-6 GPa and 1200 to 1380ºC with calcic carbonatitic liquids, calcite + #785 Fluorapatite free of REE inclusion from Ihouahouene (In Ouzzal) and #798 Durango apatite from Young et al., 1969.
- *Carbonatite and clinopyroxene* from (i) Klemme *et al*., 1995 at upper mantle conditions of 20-22 kbar and 1050 to 1100ºC; performed with 30 wt.% silicate phases and 70 wt.% natural carbonates prepared from natural mantle minerals from Kilborne Hole, New Mexico, natural carbonatite from Kaiserstuhl, Germany sedimentary carbonates, calcite-dolomite and siderite from the Mineralogisches museum universitat Gottingen. And from (ii) Green *et al*., 1992 at 25 kbar and 1000ºC, performed with carbonate-peridotitic composition of: 70% dolomitic carbonatite from Wallace and Green, 1988 and 30% Hawaiian pyrolite + trace elements +SiO_2+Al_2O_3.
- *Silica-rich melt and apatite* from (i) Mahood & Stimac 1990 performed in trachyte (apatite sample 231) and from (ii) Prowatke & Klemme 2006 performed at 1 GPa and 1250ºC in andesite (apatite sample 61B).
- *Silica-rich melt and clinopyroxene* from (i) Larsen 1979 and (ii) Mahood & Stimac 1990 both experiments performed in trachytic composition; and (iii) Blundy & Dalton 2000 Kd's in diopside albite dolomite system.

- The average of apatite and clinopyroxene equilibrium recalculated liquids is used to calculate the partition coefficient between silicate and carbonate melts for numerical modelling explained in supplementary data B2.

Supplementary data B2:

The model illustrates the immiscibility-fractional crystallization processes from a silicate-carbonate-rich parental melt. For this numerical modelling we used:

- A stepwise approach combining two Rayleigh distillation equations, alternately: the fractional crystallization equation for the mineral (clinopyroxene) segregation and an equation formally similar to the fractional melting equation (Shaw, 1979) for the segregation of immiscible melt fractions (supplementary data B2).

- Liquid/liquid partition coefficients deduced from the equilibrium melt compositions calculated in our study. Partition coefficients are considered constant within a given step of melt segregation but they are allowed to vary to account for changes in parental melt compositions.

- The residual melt proportion ("f") and the immiscible melt fraction ("F") after each increment of fractional crystallization and immiscible melt segregation, respectively. The aim of our numerical experiments was merely to assess the ability of the crystal fractionation–melt segregation model to account for the Ce/Lu and Nb/Ta variations within a reasonable range of *f* and *F* values.

Model A

- The parental melt composition is a melilitite (Baudouin *et al*. 2016).
- The extracted melt rate "F" is of 0.01
- The liquid/liquid partition coefficient is calculated from: clinopyroxene equilibrium liquid from red syenites / apatite equilibrium liquid from Si-rich carbonatites.

Model B

- The parental melt composition is a mixt liquid of a segregated melts from the second immiscibility of the model A. The mingling is calculated from the carbonate liquid and 20% of silicate liquid. Solely this modelling explains the compositions of the white syenites.
- The extracted melt rate "F" is 0.08 (rate that allows decreasing Nb/Ta in segregated liquids) for the first immiscibility and 0.01 for the following immiscibilities.
- The liquid/liquid partition coefficient is calculated from: clinopyroxene equilibrium liquid from white syenites / apatite equilibrium liquid from white syenites.

Schematic illustration of model A and B

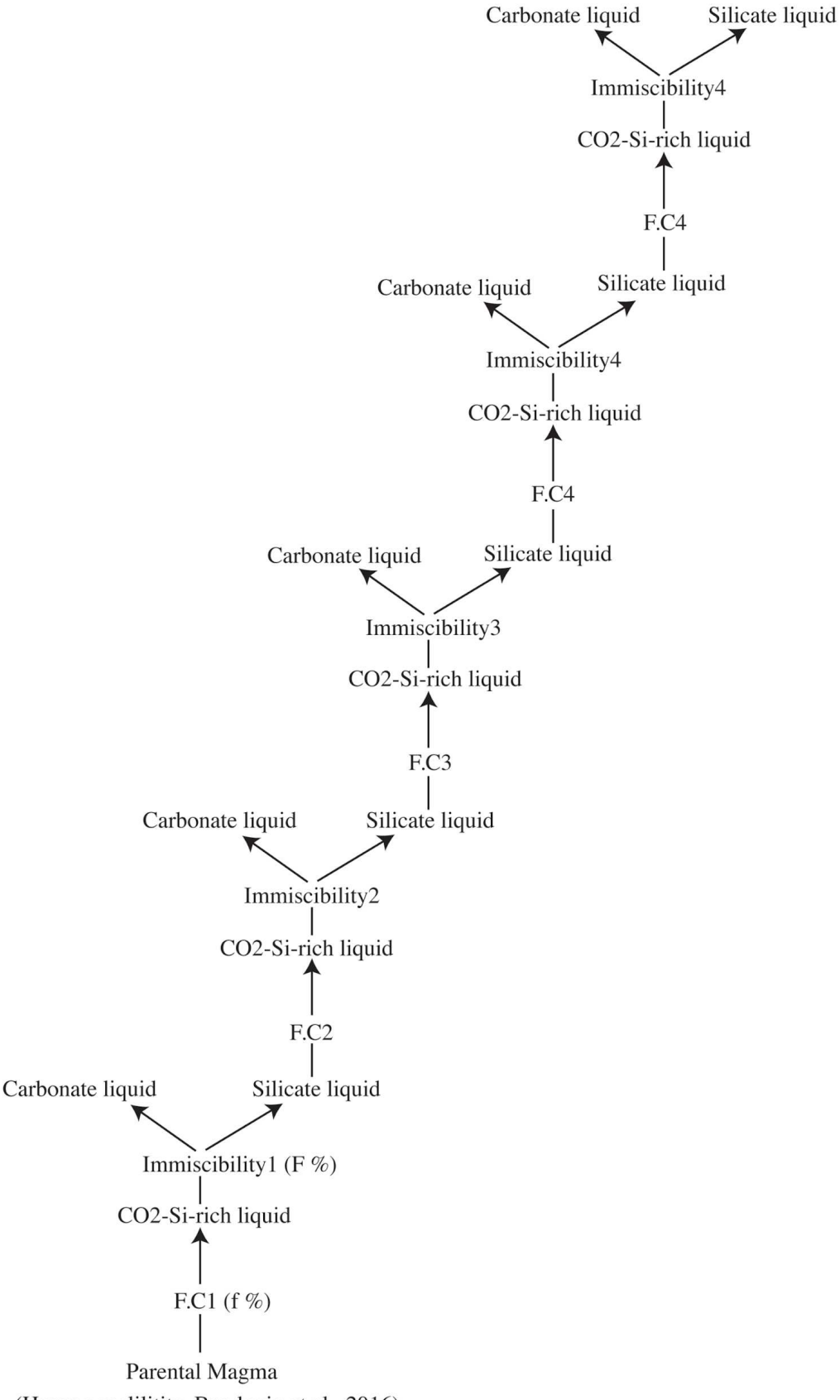

(Hanang melilitite, Baudouin et al., 2016) Model A

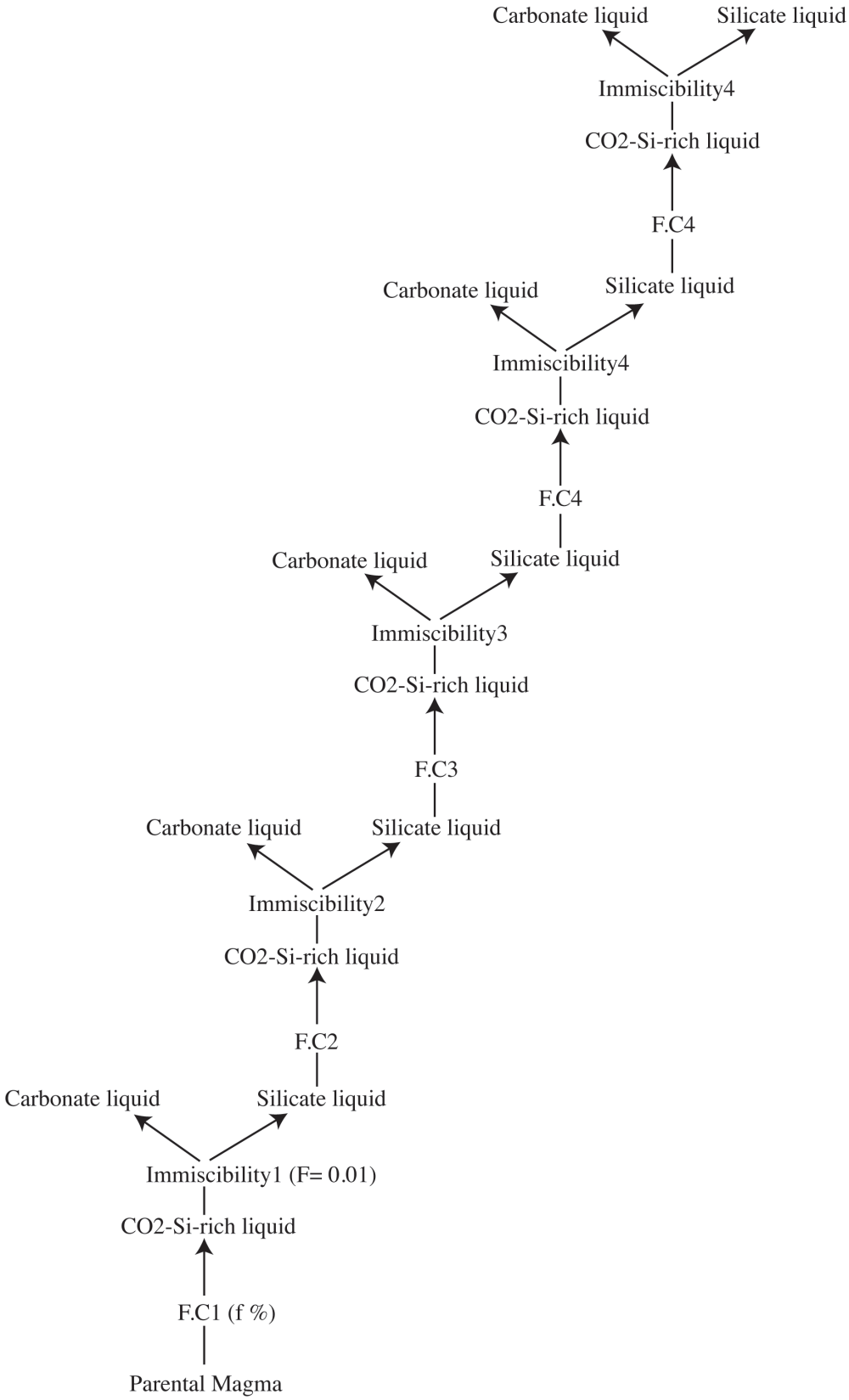

(mingling of carbonate liquid and 20 % of silicate liquid-issue from immiscibility 5 in the numerical model A)

Model B

Annexe C

Les monazites et britholites dans les carbonatites d'Ihouhaouene (Chapitre III)

Table 1 Representative major element composition of inclusion-free apatite

Rock type	**Si-poor carbonatite**				**Si-rich carbonatite**			
Sample	INH642.2	INH642.7	INH642.10	INH642.15	INH170.4	INH170.6	INH170.8	INH170.12
Type	Rim	Core	Rim	Rim	Core	Core	Middle	Rim
SiO_2	1,50	1,85	2,46	0,66	4,91	5,05	5,23	4,95
Fe_2O_3	-	-	0,01	0,00	0,00	-	0,02	-
CaO	51,01	53,23	54,61	58,02	50,41	50,44	50,07	49,09
Na_2O	-	-	0,02	0,00	0,00	-	0,00	-
K_2O	-	-	-	-	0,00	0,00	0,00	-
P_2O_5	36,17	37,38	35,29	42,05	31,43	31,03	30,52	31,33
La_2O_3	0,66	0,95	1,13	0,22	1,40	1,38	1,61	1,63
Ce_2O_3	1,89	2,31	2,78	0,73	3,15	3,23	3,55	3,59
Pr_2O_3	0,19	0,21	0,23	0,11	0,31	0,32	0,36	0,36
Nd_2O_3	0,91	1,03	1,13	0,54	1,31	1,33	1,46	1,46
Sm_2O_3	0,12	0,15	0,12	0,08	0,16	0,19	0,21	0,18
Gd_2O_3	0,09	0,10	0,11	0,07	0,09	0,14	0,12	0,13
Dy_2O_3	0,01	0,01	0,01	0,01	0,04	0,02	0,01	0,05
Lu_2O_3								
Y_2O_3	0,14	0,13	0,14	0,11	0,22	0,22	0,25	0,25
SrO	-	-	-	-	0	-	0,00	0,02
ThO_2	0,02	0,06	0,12	0,00	0,24	0,24	0,23	0,25
SO_2	0,23	0,11	0,41	0,05	1,76	1,55	1,64	1,41
F	4,86	5,16	3,69	3,40	4,59	4,50	4,53	4,33
Cl	0,00	0,00	0,00	0,00	0,03	0,05	0,05	0,04
Total	97,80	102,7	102,24	106,04	100,06	99,68	99,84	99,07
∑ REEox	3,85	4,75	5,50	1,75	6,47	6,60	7,31	7,41
Numbers of ions on the basis of 24O								
Si	0,27	0,32	0,43	0,11	0,87	0,90	0,94	0,89
Fe^{2+}	-	-	0,00	0	0	-	0,00	-
Ca	9,82	9,82	10,26	10,16	9,59	9,68	9,63	9,50
Na	-	-	0,01	0	0	-	0	-
K	-	-	-	0	0,00	0,00	0,00	-
P	5,50	5,45	5,24	5,82	4,73	4,70	4,64	4,79
La	0,04	0,06	0,07	0,01	0,09	0,09	0,11	0,11
Ce	0,12	0,15	0,18	0,04	0,21	0,21	0,23	0,24
Pr	0,01	0,01	0,01	0,01	0,02	0,02	0,02	0,02
Nd	0,06	0,06	0,07	0,03	0,08	0,08	0,09	0,09
Sm	0,01	0,01	0,01	0,00	0,01	0,01	0,01	0,01
Gd	0,01	0,01	0,01	0,00	0,01	0,01	0,01	0,01
Dy	0,00	0,00	0,00	0,00	0,00	0,00	0,00	0,00
Lu	-	-	-	-	-	-	-	-
Sr	-	-	-	0	0	-	0	0,00
Y	0,01	0,01	0,01	0,01	0,02	0,02	0,02	0,02
Th	0,00	0,00	0,00	0,00	0,01	0,01	0,01	0,01
S	0,04	0,02	0,07	0,01	0,29	0,26	0,28	0,24
F	2,76	2,81	2,05	1,76	2,58	2,55	2,57	2,47
Cl	0,00	0,00	0,00	0,00	0,01	0,02	0,02	0,01
Total	18,65	18,72	18,42	17,97	18,52	18,57	18,58	18,42

Ap: Apatite

All the apatite data are on the attached CD

Table 2 Representative trace element composition of apatite

Rock type	**Si-poor carbonatite**										
Sample	IC1-4B.35	IC1-4B.34	INH 642	INH 642	INH 694	INH 694.6	C3-9	INH693.1	INH693.2	INH693.3	INH693.6
Mineral	Ap	Ap	Ap	Ap	Ap	Ap	Ap	Ap	Ap	Ap	Ap
Type			Bulk		Bulk		Bulk				
Sc	0,05	0,22	-	-	-	-	-	0,61	0,40	0,66	0,43
Ti	48,81	39,16	-	-	-	-	-	-	-	-	-
V	4,68	5,18	-	-	-	-	-	10,71	6,96	6,62	5,86
Rb	0,02	0,12	0,24	-	0,10	-	0,32	0,21	0,18	0,07	0,08
Sr	5858	5980	4641	-	5588	125	2961	6189	6030	6868	7035
Y	524	738	1171	-	804	106	848	1321	1067	639	723
Zr	0,45	1,59	27,80	-	14,80	-	29,12	6,92	2,08	0,43	0,11
Nb	0,01	0,03	0,18	-	2,41	-	1,27	0,25	0,10	0,16	0,14
Ba	3,01	1,80	98,62	-	43,16	-	37,23	14,11	1,23	1,41	0,60
La	1149	932	8230	4043	3523	2427	5128	2604	1358	1522	1212
Ce	3514	3430	17977	9856	8572	5608	11631	11716	6516	5460	5320
Pr	488	537	2124	909	1083	710	1489	1649	1090	828	831
Nd	2219	2600	7962	435	4302	3202	5804	7166	4897	3637	3884
Sm	427	547	1226	630	741	428	956	1172	1037	709	685
Eu	82,12	110	221	-	140,79	-	181	290	245	130	143
Gd	305	392	763	448	491	415	631	767	695	474	441
Tb	30,20	41,10	67,27	-	45,18	-	63,23	76,06	73,23	46,49	49,29
Dy	135	184	308	24	209	0	254	310	299	191	204
Ho	18,42	25,83	42,30	-	28,97	-	35,68	43,72	42,04	25,52	27,06
Er	37,95	53,41	87,61	-	60,50	-	70,13	83,62	80,02	47,68	52,58
Tm	3,84	5,60	9,07	-	6,37	-	7,36	8,13	8,33	4,95	5,37
Yb	21,02	29,17	42,88	-	30,65	-	35,10	37,39	35,77	23,69	24,92
Lu	2,48	3,36	5,03	-	3,66	-	4,09	4,19	3,90	2,49	2,76
Hf	0,04	0,05	0,14	-	0,05	-	0,18	0,08	0,06	0,02	0,01
Ta	0,01	0,00	0,02	-	0,14	-	0,31	0,02	0,01	0,01	b.d.
Pb	36,29	35,76	94,30	-	74,70	-	74,25	58,68	21,21	24,64	14,99
Th	53	75	1060	-	896	110	1312	419	103	64	21
U	2,49	5,12	49,86	-	50,42	-	92,85	11,54	8,03	2,32	6,31
Nb/Ta	1,42	7,18	9,02	-	17,64	-	4,02	14,65	9,00	18,18	-
Zr/Hf	12,61	30,58	199	-	272	-	162,39	87,59	34,67	22,18	7,55
Ce/Lu	1419	1021	3575	-	2342	-	2842	2796	1671	2193	1928
Rb/Sr	0,00	0,00	0,00	-	0,00	0,00	0,00	0,00	0,00	0,00	0,00
Y/Zr	1155	464	42,13	-	54,30	-	29,1	190,8	513,1	1492,3	6883

b.d.: below detection

Table 2 continued

Rock type	**Si-rich carbonatite**									
Sample	IC2-9A.48	IC2-9A.49	IC2-9A.39	IC2-9A.46	170.A	170.A	170.A	INH 604	INH604.49	INH604.49
Mineral	Ap	Ap	Ap	Ap	Ap	Ap	Ap	Ap	Ap	Ap
Type					Bulk			Bulk		
Sc	0,41	0,48	0,68	1,15	-	1,36	1,35	-	0,74	1,18
Ti	22,32	18,44	18,23	17,67	-	68,79	68,81	-	-	-
V	25,27	9,26	10,1	22,16	-	20,72	21,17	-	30,32	26,9
Rb	0,351	0,252	0,346	0,24	0,30	0,36	0,34	0,24	0,08	0,13
Sr	6214	6092	6090	5736	5539	4475	4656	5530	8616	8485
Y	2841	2179	3643	2476	1870	1828	1808	1708	1434	1318
Zr	141	128	163	205	186	129	130	112	247	199
Nb	2,749	1,993	1,784	2,522	6,68	4,58	4,6	9,50	16,95	11,2
Ba	25,02	3,09	5,36	3,51	6,35	1,457	0,971	3265	1,31	2,48
La	19143	13129	27171	16022	11667	9741	9732	18343	9882	9572
Ce	45945	31606	63315	38386	25213	18237	18472	39928	22424	21853
Pr	4812	3415	6685	4206	2874	2124	2120	4025	2489	2373
Nd	18825	13568	25552	15685	10353	8693	8669	14233	9322	8969
Sm	2706	1977	3635	2260	1573	1343	1297	1990	1373	1316
Eu	527	387	692	451	277	220	212	377	255	225
Gd	1737	1264	2289	1435	986	1036	964	1122	861	803
Tb	164	120	211	134	90,99	96,71	91,86	93,10	77,12	71,62
Dy	687	503	897	559	439	413	398	430	332	308
Ho	95,22	70,29	122	77,74	64,32	61,07	58,02	56,72	45,45	41,16
Er	194	142	247	155	142	132	123	117	88	81
Tm	20,91	15,4	26,76	17,08	15,94	15,08	14,15	12	9,06	8,15
Yb	108	80,73	137	91,33	81,10	78,8	73,13	56,22	45,87	38,49
Lu	13,02	9,39	16,1	10,38	10,02	9,47	8,89	6,59	5,07	4,45
Hf	0,869	0,89	1,11	1,33	1,48	1,93	1,86	0,59	1,04	1,04
Ta	0,03	0,05	0,05	0,04	0,06	0,07	0,07	0,14	0,33	0,22
Pb	515	274	587	366	298	260	201	355	155	97
Th	3047	2044	4732	2083	1825	1513	1455	2085	1172	652
U	496	294	818	344	271	166	159	276	92	86
Nb/Ta	92,25	41,78	33,66	59,48	120	69,29	66,57	69	51,36	51,85
Zr/Hf	162	144	147	154	126	67,02	70,08	189	238	191
Ce/Lu	3529	3366	3933	3698	2517	1926	2078	6057	4423	4911
Rb/Sr	0,00	0,00	0,00	0,00	0,00	0,00	0,00	0	0,00	0,00
Y/Zr	20,2	17,1	22,4	12,1	10,04	14,1	13,9	15,3	5,8	6,6

b.d.: below detection

Table III.1 Representative major element composition of apatite with britholite

Rock type	**Carbonatite**							
Sample	INH 604.44	INH 604.49	INH 604.54	INH 604a.8	INH 604a.3	INH 545.36	INH 545.13	IC2-9A.54
Mineral	Ap	Ap	Ap	Ap	Ap	Ap	Ap	Ap
Type	Core	Core	Rim	Core	Core	Core	Core	Core
SiO2	3.21	3.02	4.60	2.53	5.10	3.35	5.99	2.45
Fe2O3	-	-	-	0.12	0.00	0.00	-	-
MnO	-	-	-	-	-	-	-	-
CaO	50.2	50.2	47.8	51.5	46.3	48.6	48.4	52.4
Na2O	-	-	-	0.01	0.09	0.00	0.01	-
K2O	0.01	0.01	0.00	0.01	0.02	0.01	0.00	0.00
P2O5	37.2	37.1	33.5	34.1	33.4	30.6	29.8	37.0
La2O3	1.32	1.23	1.78	0.93	2.40	2.24	2.36	0.81
Ce2O3	3.11	2.92	4.14	2.59	6.13	5.27	5.73	2.08
Pr2O3	0.27	0.27	0.41	0.19	0.48	0.48	0.53	0.17
Nd2O3	1.43	1.38	1.87	1.11	2.36	2.03	2.23	1.03
Sm2O3	0.42	0.40	0.55	0.31	0.73	0.23	0.26	0.28
Gd2O3	0.11	0.09	0.14	0.08	0.18	0.19	0.21	0.14
Dy2O3	0.00	0.01	0.01	0.02	0.02	0.06	0.03	-
Lu2O3	0.01	0.03	0.03	0.01	0.00	-	-	-
Y2O3	0.13	0.12	0.17	0.10	0.20	0.25	0.32	0.12
SrO	0.11	0.11	0.08	-	-	0.29	0.38	-
ThO2	0.08	0.19	0.27	0.14	0.37	0.28	0.33	0.09
SO2	0.57	0.56	0.72	0.56	0.74	1.16	1.36	0.68
F	4.13	3.82	4.09	3.17	2.86	3.69	4.36	4.36
Cl	0.17	0.32	0.26	0.06	0.13	0.02	0.04	0.04
Total	102.5	101.7	100.5	97.5	101.5	98.8	102.3	101.7
∑ REEox	6.79	6.46	9.08	5.34	12.51	10.74	11.67	4.63
Numbers of ions on the basis of 24O								
Si	0.55	0.52	0.41	0.46	0.92	1.03	1.08	0.42
Fe2+	-	-	-	0.02	0.00	-	-	-
Mn	-	-	-	-	-	-	-	-
Ca	9.25	9.33	9.97	10.09	8.93	9.43	9.33	9.68
Na	-	-	-	0.00	0.03	0.00	0.01	-
K	0.00	0.00	0.00	0.00	0.00	0.00	0.00	0.00
P	5.42	5.45	5.25	5.28	5.09	4.69	4.54	5.40
La	0.08	0.08	0.07	0.06	0.16	0.15	0.16	0.05
Ce	0.20	0.19	0.17	0.17	0.40	0.35	0.38	0.13
Pr	0.02	0.02	0.01	0.01	0.03	0.03	0.03	0.01
Nd	0.09	0.09	0.07	0.07	0.15	0.13	0.14	0.06
Sm	0.02	0.02	0.01	0.02	0.05	0.01	0.02	0.02
Gd	0.01	0.01	0.01	0.01	0.01	0.01	0.01	0.01
Dy	0.00	0.00	0.00	0.00	0.00	0.00	0.00	-
Lu	0.00	0.00	-	0.00	0.00	-	-	-
Sr	0.01	0.01	-	-	-	0.03	0.04	-
Y	0.01	0.01	0.01	0.01	0.02	0.02	0.03	0.01
Th	0.00	0.01	0.00	0.01	0.02	0.01	0.01	0.00
S	0.09	0.09	0.08	0.10	0.12	0.20	0.23	0.11
F	2.25	2.10	2.57	1.83	1.63	2.11	2.48	2.37
Cl	0.05	0.09	0.00	0.02	0.04	0.01	0.01	0.01
Total	18	18	19	18	18	18	18	18

Table III.1 Continued

Rock type	Carbonatite				Syenite			
Sample	IC2-9A.49	IC1-12.13	INH 455.5	INH 158.2	INH 3.24 .8	INH 3.24 .6	IC2-27B.	IC2-27B.
Mineral Type	Ap Core	Ap Core	Ap Core	Ap Core	Ap Core	Ap Core	Ap Core	Ap Core
SiO2	4.85	3.00	2.84	2.09	2.56	3.49	2.56	3.49
Fe2O3	-	-	-	0.00	-	-	-	-
MnO	-	-	-	0.01	-	-	-	-
CaO	48.3	51.8	51.1	48.9	53.8	51.8	53.8	51.8
Na2O	-	-	0.04	-	0.00	0.01	0.00	0.01
K2O	0.00	-	-	0.01	0.00	0.01	0.00	0.01
P2O5	31.9	35.4	37.3	35.3	37.9	33.4	37.9	33.4
La2O3	1.86	1.11	1.41	0.91	0.78	1.44	0.78	1.44
Ce2O3	4.83	2.54	2.93	1.67	2.12	3.84	2.12	3.84
Pr2O3	0.45	0.29	0.35	0.17	0.25	0.38	0.25	0.38
Nd2O3	2.32	1.31	1.53	0.90	1.14	1.72	1.14	1.72
Sm2O3	0.64	0.35	0.44	0.25	0.30	0.52	0.30	0.52
Gd2O3	0.17	0.10	0.17	0.05	0.16	0.10	0.16	0.10
Dy2O3	0.10	0.06	0.01	-	0.05	0.02	0.05	0.02
Lu2O3	0.01	-	-	-	-	-	-	-
Y2O3	0.30	0.16	0.20	0.10	0.15	0.15	0.15	0.15
SrO	-	-	-	0.07	-	-	-	-
ThO2	0.36	0.04	0.10	0.06	0.16	0.39	0.16	0.39
SO2	0.89	0.83	0.36	0.41	0.60	0.77	0.60	0.77
F	4.12	4.06	4.34	4.63	3.91	4.16	3.91	4.16
Cl	0.03	0.02	0.05	0.04	0.02	0.01	0.02	0.01
Total	101.1	101.1	103.2	95.7	102.2	103.8	102.2	103.8
∑ REEox	10.69	5.92	7.05	4.06	4.95	8.16	4.95	8.16
Numbers of ions on the basis of 24O								
Si	0.87	0.52	0.49	0.38	0.43	0.62	0.43	0.62
Fe2+	-	-	-	0.00	-	-	-	-
Mn	-	-	-	0.00	-	-	-	-
Ca	9.35	9.72	9.42	9.59	9.75	9.84	9.75	9.84
Na	-	-	0.01	-	0.00	0.01	0.00	0.01
K	0.00	-	-	0.00	0.00	0.00	0.00	0.00
P	4.87	5.25	5.42	5.47	5.43	5.01	5.43	5.01
La	0.12	0.07	0.09	0.06	0.05	0.09	0.05	0.09
Ce	0.32	0.16	0.18	0.11	0.13	0.25	0.13	0.25
Pr	0.03	0.02	0.02	0.01	0.02	0.02	0.02	0.02
Nd	0.15	0.08	0.09	0.06	0.07	0.11	0.07	0.11
Sm	0.04	0.02	0.03	0.02	0.02	0.03	0.02	0.03
Gd	0.01	0.01	0.01	0.00	0.01	0.01	0.01	0.01
Dy	0.01	0.00	0.00	-	0.00	0.00	0.00	0.00
Lu	-	-	-	-	-	-	-	-
Sr	-	-	-	0.01	-	-	-	-
Y	0.03	0.01	0.02	0.01	0.01	0.01	0.01	0.01
Th	0.01	0.00	0.00	0.00	0.01	0.02	0.01	0.02
S	0.15	0.14	0.06	0.07	0.10	0.13	0.10	0.13
F	2.35	2.25	2.36	2.68	2.09	2.33	2.09	2.33
Cl	0.01	0.01	0.01	0.01	0.00	0.00	0.00	0.00
Total	18	18	18	18	18	18	18	18

Table III.2 Representative major element composition of britholite

Rock type	**Carbonatite**						
Sample	INH 604.23	INH 604.25	INH 604.29	INH 604a.12	INH 604a.16	INH604.b.22	Inh604a.2
Mineral	Bri	Bri	Bri	Bri	Bri	Bri	Bri
Type	I.G	L	I.G	I.G	I.G	L	L
SiO2	17.61	15.13	19.01	16.83	19.20	9.76	25.96
Fe2O3	-	-	-	-	-	-	2.27
MnO	-	-	-	-	-	-	-
CaO	18.49	26.35	18.62	22.26	18.08	34.35	11.62
Na2O	0.02	0.05	0.08	0.09	-	-	0.02
K2O	0.01	0.01	0.01	0.05	0.00	0.01	0.01
P2O5	6.82	12.91	6.31	9.16	5.11	24.24	0.18
La2O3	10.32	8.43	10.16	9.06	10.92	5.88	9.44
Ce2O3	22.87	19.06	23.78	22.83	26.76	15.84	25.51
Pr2O3	1.81	1.58	1.96	1.70	2.02	1.30	2.21
Nd2O3	8.77	7.74	9.33	8.29	9.59	5.59	11.00
Sm2O3	2.74	2.44	3.03	2.43	2.88	2.05	1.36
Gd2O3	0.53	0.54	0.62	0.63	0.66	0.34	1.00
Dy2O3	0.13	0.11	0.16	0.12	0.21	0.08	0.22
Lu2O3	-	-	-	-	-	0.02	-
Y2O3	0.73	0.70	0.82	0.78	0.95	0.48	0.01
SrO	-	-	-	-	-	-	1.65
ThO2	1.99	2.16	1.54	2.44	1.23	0.83	-
SO2	0.30	0.39	0.31	0.24	0.15	0.47	0.03
F	1.69	2.07	1.66	1.42	1.63	2.72	1.41
Cl	0.37	0.41	0.69	0.31	0.29	0.19	0.18
Total	95.19	100.06	98.11	98.64	99.69	102.97	94.08
∑ REEox	47.89	40.58	49.87	45.85	54.00	31.10	50.74
Numbers of ions on the basis of 24O							
Si	0.55	0.52	0.41	0.46	0.92	1.94	6.97
Fe2+	-	-	-	0.02	0.00	-	0.51
Mn	-	-	-	-	-	-	-
Ca	9.25	9.33	9.97	10.09	8.93	7.30	3.34
Na	-	-	-	0.00	0.03	-	0.01
K	0.00	0.00	0.00	0.00	0.00	0.00	0.01
P	5.42	5.45	5.25	5.28	5.09	4.07	0.04
La	0.08	0.08	0.07	0.06	0.16	0.43	0.93
Ce	0.20	0.19	0.17	0.17	0.40	1.15	2.51
Pr	0.02	0.02	0.01	0.01	0.03	0.09	0.22
Nd	0.09	0.09	0.07	0.07	0.15	0.40	1.05
Sm	0.02	0.02	0.01	0.02	0.05	0.14	0.13
Gd	0.01	0.01	0.01	0.01	0.01	0.02	0.09
Dy	0.00	0.00	0.00	0.00	0.00	0.00	0.02
Lu	0.00	0.00	-	0.00	0.00	0.00	-
Sr	0.01	0.01	-	-	-	-	0.26
Y	0.01	0.01	0.01	0.01	0.02	0.05	0.00
Th	0.00	0.01	0.00	0.01	0.02	0.04	-
S	0.09	0.09	0.08	0.10	0.12	0.09	0.01
F	2.25	2.10	2.57	1.83	1.63	1.83	1.71
Cl	0.05	0.09	0.00	0.02	0.04	0.06	0.08
Total	18	18	19	18	18	18	18

I.G: Irregular shape grain; L: lamellar

Table III.2 Continued

Rock type	**Carbonatite**						
Sample	INH 545.36	INH 545.13	IC2-9A.54	IC2-9A.49	IC1-12.13	INH 455.5	INH 158.2
Mineral	Bri	Bri	Bri	Bri	Bri	Bri	Bri
Type	I.G	I.G	I.G	I.G	L	L	L
SiO2	3.35	5.99	2.45	4.85	3.00	2.84	2.09
Fe2O3	0.00	-	-	-	-	-	0.00
MnO	-	-	-	-	-	-	0.01
CaO	48.63	48.39	52.40	48.32	51.81	51.13	48.94
Na2O	0.00	0.01	-	-	-	0.04	-
K2O	0.01	0.00	0.00	0.00	-	-	0.01
P2O5	30.60	29.80	37.01	31.87	35.43	37.27	35.34
La2O3	2.24	2.36	0.81	1.86	1.11	1.41	0.91
Ce2O3	5.27	5.73	2.08	4.83	2.54	2.93	1.67
Pr2O3	0.48	0.53	0.17	0.45	0.29	0.35	0.17
Nd2O3	2.03	2.23	1.03	2.32	1.31	1.53	0.90
Sm2O3	0.23	0.26	0.28	0.64	0.35	0.44	0.25
Gd2O3	0.19	0.21	0.14	0.17	0.10	0.17	0.05
Dy2O3	0.06	0.03	-	0.10	0.06	0.01	-
Lu2O3	-	-	-	0.01	-	-	-
Y2O3	0.25	0.32	0.12	0.30	0.16	0.20	0.10
SrO	0.29	0.38	-	-	-	-	0.07
ThO2	0.28	0.33	0.09	0.36	0.04	0.10	0.06
SO2	1.16	1.36	0.68	0.89	0.83	0.36	0.41
F	3.69	4.36	4.36	4.12	4.06	4.34	4.63
Cl	0.02	0.04	0.04	0.03	0.02	0.05	0.04
Total	98.78	102.33	101.65	101.12	101.10	103.19	95.66
∑ REEox	10.74	11.67	4.63	10.69	5.92	7.05	4.06
Numbers of ions on the basis of 24O							
Si	1.03	1.08	0.42	0.87	0.52	0.49	0.38
Fe2+	-	-	-	-	-	-	0.00
Mn	-	-	-	-	-	-	0.00
Ca	9.43	9.33	9.68	9.35	9.72	9.42	9.59
Na	0.00	0.01	-	-	-	0.01	-
K	0.00	0.00	0.00	0.00	-	-	0.00
P	4.69	4.54	5.40	4.87	5.25	5.42	5.47
La	0.15	0.16	0.05	0.12	0.07	0.09	0.06
Ce	0.35	0.38	0.13	0.32	0.16	0.18	0.11
Pr	0.03	0.03	0.01	0.03	0.02	0.02	0.01
Nd	0.13	0.14	0.06	0.15	0.08	0.09	0.06
Sm	0.01	0.02	0.02	0.04	0.02	0.03	0.02
Gd	0.01	0.01	0.01	0.01	0.01	0.01	0.00
Dy	0.00	0.00	-	0.01	0.00	0.00	-
Lu	-	-	-	-	-	-	-
Sr	0.03	0.04	-	-	-	-	0.01
Y	0.02	0.03	0.01	0.03	0.01	0.02	0.01
Th	0.01	0.01	0.00	0.01	0.00	0.00	0.00
S	0.20	0.23	0.11	0.15	0.14	0.06	0.07
F	2.11	2.48	2.37	2.35	2.25	2.36	2.68
Cl	0.01	0.01	0.01	0.01	0.01	0.01	0.01
Total	18	18	18	18	18	18	18

I.G: Irregular shape grain; L: lamellar

Table III.2 Continued

Rock type	**Syenite**			
Sample	INH 3.24 .8	INH 3.24 .6	IC2-27B .8	IC2-27B .9
Mineral	Bri	Bri	Bri	Bri
Type	I.G	I.G	I.G	I.G
SiO2	2.56	3.49	2.56	3.49
Fe2O3	-	-	-	-
MnO	-	-	-	-
CaO	53.76	51.81	53.76	51.81
Na2O	0.00	0.01	0.00	0.01
K2O	0.00	0.01	0.00	0.01
P2O5	37.88	33.40	37.88	33.40
La2O3	0.78	1.44	0.78	1.44
Ce2O3	2.12	3.84	2.12	3.84
Pr2O3	0.25	0.38	0.25	0.38
Nd2O3	1.14	1.72	1.14	1.72
Sm2O3	0.30	0.52	0.30	0.52
Gd2O3	0.16	0.10	0.16	0.10
Dy2O3	0.05	0.02	0.05	0.02
Lu2O3	-	-	-	-
Y2O3	0.15	0.15	0.15	0.15
SrO	-	-	-	-
ThO2	0.16	0.39	0.16	0.39
SO2	0.60	0.77	0.60	0.77
F	3.91	4.16	3.91	4.16
Cl	0.02	0.01	0.02	0.01
Total	102.16	103.8	102.2	103.8
∑ REEox	4.95	8.16	4.95	8.16
Numbers of ions on the basis of 24O				
Si	0.43	0.62	0.43	0.62
Fe2+	-	-	-	-
Mn	-	-	-	-
Ca	9.75	9.84	9.75	9.84
Na	0.00	0.01	0.00	0.01
K	0.00	0.00	0.00	0.00
P	5.43	5.01	5.43	5.01
La	0.05	0.09	0.05	0.09
Ce	0.13	0.25	0.13	0.25
Pr	0.02	0.02	0.02	0.02
Nd	0.07	0.11	0.07	0.11
Sm	0.02	0.03	0.02	0.03
Gd	0.01	0.01	0.01	0.01
Dy	0.00	0.00	0.00	0.00
Lu	-	-	-	-
Sr	-	-	-	-
Y	0.01	0.01	0.01	0.01
Th	0.01	0.02	0.01	0.02
S	0.10	0.13	0.10	0.13
F	2.09	2.33	2.09	2.33
Cl	0.00	0.00	0.00	0.00
Total	18	18	18	18

I.G: Irregular shape grain; L: lamellar

Table III.3 Representative major element composition of apatite with monazite inclusions

Rock type	**Si-poor carbonatite**									
Sample	INH 693.1	INH 693.2	INH 693.3	INH 693.4	INH 693.5	INH 693.6	INH 693.7	INH 3.33 .23	INH 3.33 .25	INH 3.33 .26
Mineral	Ap	Ap	Ap	Ap	Ap	Ap	Ap	Ap	Ap	Ap
Type	Rim	Midd	Core	Core	Midd	Rim	Rim	Rim	Core	Rim
SiO2	1.84	0.54	0.48	1.09	0.65	1.78	1.81	1.43	0.97	1.48
Fe2O3	-	0.00	-	0.01	0.00	-	-	-	-	0.00
MnO	-	-	-	-	-	-	0.00	-	-	-
CaO	53.49	55.58	56.06	55.23	56.20	53.99	53.74	53.22	54.28	53.34
Na2O	0.19	0.10	0.09	0.05	0.05	0.17	0.16	0.32	0.14	0.17
K2O	-	-	-	-	0.00	0.00	-	0.00	0.00	-
P2O5	36.73	40.25	40.43	39.21	39.63	36.64	35.53	38.00	39.09	37.97
La2O3	0.53	0.19	0.18	0.38	0.19	0.68	0.63	0.31	0.28	0.37
Ce2O3	1.94	0.77	0.67	1.48	0.82	2.17	2.09	1.48	1.28	1.69
Pr2O3	0.24	0.08	0.08	0.17	0.14	0.24	0.23	0.20	0.18	0.26
Nd2O3	1.39	0.55	0.50	0.85	0.62	1.24	1.30	1.22	0.86	1.33
Sm2O3	0.39	0.17	0.14	0.24	0.18	0.36	0.36	0.35	0.24	0.35
Gd2O3	0.22	0.09	0.07	0.13	0.03	0.13	0.09	0.24	0.07	0.16
Dy2O3	0.08	0.04	0.02	0.05	0.01	0.04	0.01	0.04	0.01	0.07
Lu2O3	0.03	0.01	0.01	0.02	0.02	0.02	-	-	0.02	-
Y2O3	0.31	0.02	0.04	0.07	0.07	0.11	0.17	0.24	0.08	0.22
SrO	-	-	-	-	-	-	-	-	-	-
ThO2	0.08	0.03	0.00	0.01	-	0.11	0.07	0.10	0.03	0.07
SO2	0.39	0.09	0.10	0.04	0.06	0.46	0.41	0.40	0.18	0.20
F	3.99	3.83	4.26	3.94	4.37	4.08	4.22	3.93	4.37	3.95
Cl	0.05	0.02	0.03	0.03	0.02	0.04	0.05	0.04	0.03	0.02
Total	101.9	102.4	103.2	103.0	103.1	102.2	100.9	101.5	102.1	101.7
∑ REEox	5.11	1.92	1.72	3.39	2.07	5.00	4.88	4.07	3.02	4.46
Numbers of ions on the basis of 24O										
Si	0.32	0.09	0.08	0.19	0.11	0.31	0.32	0.25	0.17	0.26
Fe2+	-	0.00	-	0.00	0.00	-	-	-	-	0.00
Mn	-	-	-	-	-	-	0.00	-	-	-
Ca	9.98	10.10	10.10	10.08	10.19	10.05	10.18	9.87	9.94	9.91
Na	0.07	0.03	0.03	0.02	0.02	0.06	0.05	0.11	0.05	0.06
K	-	-	-	-	0.00	0.00	-	0.00	0.00	-
P	5.42	5.78	5.75	5.66	5.68	5.39	5.31	5.57	5.66	5.57
La	0.03	0.01	0.01	0.02	0.01	0.04	0.04	0.02	0.02	0.02
Ce	0.12	0.05	0.04	0.09	0.05	0.14	0.14	0.09	0.08	0.11
Pr	0.01	0.00	0.00	0.01	0.01	0.02	0.01	0.01	0.01	0.02
Nd	0.09	0.03	0.03	0.05	0.04	0.08	0.08	0.08	0.05	0.08
Sm	0.02	0.01	0.01	0.01	0.01	0.02	0.02	0.02	0.01	0.02
Gd	0.01	0.01	0.00	0.01	0.00	0.01	0.01	0.01	0.00	0.01
Dy	0.00	0.00	0.00	0.00	0.00	0.00	0.00	0.00	0.00	0.00
Lu	0.00	0.00	0.00	0.00	0.00	0.00	-	-	0.00	-
Sr	-	-	-	-	-	-	-	-	-	-
Y	0.03	0.00	0.00	0.01	0.01	0.01	0.02	0.02	0.01	0.02
Th	0.00	0.00	0.00	0.00	-	0.00	0.00	0.00	0.00	0.00
S	0.06	0.01	0.02	0.01	0.01	0.08	0.07	0.06	0.03	0.03
F	2.20	2.06	2.26	2.12	2.34	2.24	2.36	2.15	2.36	2.16
Cl	0.02	0.01	0.01	0.01	0.01	0.01	0.01	0.01	0.01	0.01
Total	18	18	18	18	18	18	19	18	18	18

Table III.4 Representative major element composition of monazite

Rock type	Si-poor carbonatite						
Sample	INH 693.14	INH 693.17	INH 693.18	INH 693.19	INH 693.20	INH 693.27	INH 693.29
Mineral	Mnz	Mnz	Mnz	Mnz	Mnz	Mnz	Mnz
Type	Rg	Rg	Rg	Rg	Rg	Incl	Incl
SiO2	1.37	0.74	1.21	1.28	1.27	0.72	1.23
Fe2O3	-	-	-	-	-	-	-
CaO	0.31	0.29	0.30	0.36	0.37	0.34	0.36
Na2O	-	-	-	-	-	-	-
K2O	-	-	0.00	-	0.00	-	-
P2O5	26.91	28.26	26.91	26.37	26.60	28.47	28.57
La2O3	22.02	20.51	20.81	21.08	21.36	20.86	22.52
Ce2O3	34.61	34.88	34.70	34.68	34.42	35.30	34.54
Pr2O3	1.77	1.95	1.94	1.89	1.83	1.87	1.63
Nd2O3	7.56	8.72	8.53	8.35	8.14	8.27	7.36
Sm2O3	2.56	2.75	2.79	2.66	2.56	2.38	2.31
Gd2O3	0.07	0.23	0.17	0.14	0.09	0.11	0.14
Dy2O3	-	0.01	-	0.01	-	-	-
Lu2O3	0.02	-	-	-	0.01	-	0.00
Y2O3	-	0.00	-	-	0.01	-	-
SrO	0.06	0.09	0.06	0.07	0.07	0.12	0.09
ThO2	0.41	0.10	0.08	0.05	0.15	0.21	0.26
SO2	1.39	0.86	1.28	1.41	1.41	0.77	1.28
F	0.53	0.55	0.50	0.45	0.47	0.49	0.52
Cl	0.01	0.01	0.01	0.01	0.02	0.01	0.01
Total	99.59	99.96	99.31	98.83	98.79	99.91	100.8
Σ REEox	68.60	69.06	68.94	68.81	68.43	68.78	68.50
Numbers of ions on the basis of 24O							
Si	0.35	0.19	0.31	0.33	0.33	0.18	0.30
Fe2+	-	-	-	-	-	-	-
Ca	0.08	0.08	0.08	0.10	0.10	0.09	0.10
Na	-	-	-	-	-	-	-
K	-	-	0.00	-	0.00	-	-
P	5.77	6.05	5.81	5.74	5.77	6.09	5.97
La	2.06	1.91	1.96	2.00	2.02	1.94	2.05
Ce	3.21	3.23	3.24	3.26	3.23	3.27	3.12
Pr	0.16	0.18	0.18	0.18	0.17	0.17	0.15
Nd	0.68	0.79	0.78	0.77	0.74	0.75	0.65
Sm	0.22	0.24	0.25	0.24	0.23	0.21	0.20
Gd	0.01	0.02	0.01	0.01	0.01	0.01	0.01
Dy	-	0.00	-	0.00	-	-	-
Lu	0.00	-	-	-	0.00	-	0.00
Sr	0.01	0.01	0.01	0.01	0.01	0.02	0.01
Y	-	0.00	-	-	0.00	-	-
Th	0.02	0.01	0.00	0.00	0.01	0.01	0.01
S	0.33	0.20	0.31	0.34	0.34	0.18	0.30
F	0.42	0.44	0.41	0.37	0.38	0.39	0.40
Cl	0.00	0.00	0.00	0.01	0.01	0.01	0.00
Total	13	13	13	13	13	13	13

Inc: inclusion; Rg: Rim grain

Table III.4 Continued

Rock type	Si-poor carbonatite						
Sample	INH 3.33 .1	INH 3.33 .3	INH 3.33 .12	INH 3.33 .13	INH 3.33 .28	INH 3.33 .29	INH 3.33 .27
Mineral	Mnz	Mnz	Mnz	Mnz	Mnz	Mnz	Tho
Type	Rg	Rg	Incl	Incl	Incl	Incl	Incl
SiO2	0.96	1.34	1.97	1.72	0.78	1.17	13.82
Fe2O3	-	-	0.32	-	-	-	-
CaO	0.28	0.28	1.29	0.27	0.20	0.30	0.44
Na2O	-	-	-	-	-	-	0.30
K2O	-	-	0.00	0.00	-	0.00	0.02
P2O5	28.07	27.35	25.34	27.35	29.16	28.04	7.29
La2O3	17.40	16.78	18.56	18.99	15.43	18.46	4.37
Ce2O3	35.74	33.86	33.05	33.58	35.03	33.93	9.37
Pr2O3	2.32	2.27	1.91	2.02	2.59	2.07	0.62
Nd2O3	9.95	10.22	8.38	8.51	11.40	9.11	2.97
Sm2O3	2.96	2.91	2.61	2.69	3.19	2.88	0.93
Gd2O3	0.12	0.21	0.13	0.20	0.24	0.23	0.27
Dy2O3	0.01	-	-	0.01	-	-	-
Lu2O3	-	-	0.01	-	-	-	-
Y2O3	0.01	0.03	0.03	0.02	-	-	0.48
SrO	0.05	0.08	0.04	0.07	0.06	0.07	0.05
ThO2	0.90	3.08	2.75	3.00	1.77	2.19	50.11
SO2	0.78	0.67	1.17	0.93	0.32	0.78	0.23
F	0.47	0.46	0.47	0.56	0.42	0.40	0.17
Cl	0.01	0.01	0.01	0.01	0.01	0.01	0.02
Total	100	99.56	98.06	99.92	100.6	99.65	91.45
Σ REEox	68.50	66.28	64.67	66.00	67.88	66.69	19.01
Numbers of ions on the basis of 24O							
Si	0.24	0.35	0.51	0.44	0.20	0.30	4.60
Fe2+	-	-	0.07	-	-	-	-
Ca	0.08	0.08	0.36	0.07	0.05	0.08	0.16
Na	-	-	-	-	-	-	0.20
K	-	-	0.00	0.00	-	0.00	0.01
P	6.03	5.95	5.58	5.86	6.23	6.03	2.06
La	1.63	1.59	1.78	1.77	1.44	1.73	0.54
Ce	3.32	3.19	3.15	3.11	3.24	3.16	1.14
Pr	0.21	0.21	0.18	0.19	0.24	0.19	0.08
Nd	0.90	0.94	0.78	0.77	1.03	0.83	0.35
Sm	0.26	0.26	0.23	0.23	0.28	0.25	0.11
Gd	0.01	0.02	0.01	0.02	0.02	0.02	0.03
Dy	0.00	-	-	0.00	-	-	-
Lu	-	-	0.00	-	-	-	-
Sr	0.01	0.01	0.01	0.01	0.01	0.01	0.01
Y	0.00	0.00	0.00	0.00	-	-	0.08
Th	0.05	0.18	0.16	0.17	0.10	0.13	3.80
S	0.19	0.16	0.29	0.22	0.08	0.19	0.07
F	0.38	0.38	0.39	0.45	0.33	0.32	0.17
Cl	0.00	0.01	0.00	0.01	0.00	0.00	0.01
Total	13	13	14	13	13	13	13

Table III.5 Representative trace element composition of REE-inclusions

Rock type					
Sample	INH545.9	INH545.10	INH545.11	INH693.36	INH693.38
Mineral	Bri	Bri	Bri	Mnz	Mnz
Type	I.G	L	L	Rg	Rg
Sc	0,47	1,67	1,04	0,12	0,03
Ti	b.d.	29	b.d.		
V	2,92	8,12	3,50	3,70	4,42
Rb	1,31	2,36	1,87	0,10	b.d.
Sr	4088	7970	3588	373	191,93
Y	7157	11969	9543	181	24,93
Zr	277	597	268	2,15	0,16
Nb	1,86	5,72	1,96	0,08	0,01
Ba	8,11	41,96	30,11	2,10	0,67
La	89229	136963	86859	35727	19652
Ce	178743	268806	200929	40074	23259
Pr	17557	28060	20172	3681	2001
Nd	62403	99857	73405	11890	5433
Sm	8161	12929	10238	1372	336
Eu	1448	2312	1866	166	40,05
Gd	4891	7789	6294	476	106
Tb	442	717	582	25,90	5,02
Dy	1895	3066	2531	67,41	11,80
Ho	255	416	337	4,84	0,96
Er	517	851	681	6,09	1,12
Tm	55,72	92,68	73,84	0,29	0,06
Yb	304	512	399	1,21	0,19
Lu	33,03	55,20	42,56	0,06	0,01
Hf	1,99	5,10	2,32	0,04	b.d.
Ta	0,03	0,15	0,05	b.d.	0,00
Pb	1651	3348	2535	25,08	29,04
Th	8060	11781	6292	107,38	155,77
U	2343	3229	1841	2,83	1,95
Nb/Ta	54,71	37,63	42,61	-	-
Zr/Hf	139	117	116	58,11	-
Ce/Lu	5412	4870	4721	720753	3186179
Rb/Sr	0,00	0,00	0,00	0,00	-
Y/Zr	25,81	20,05	35,60	84,17	156,79

b.d.: below detection **I.G: Irregular shape grain; L: lamellar; Rg: Rim grain**

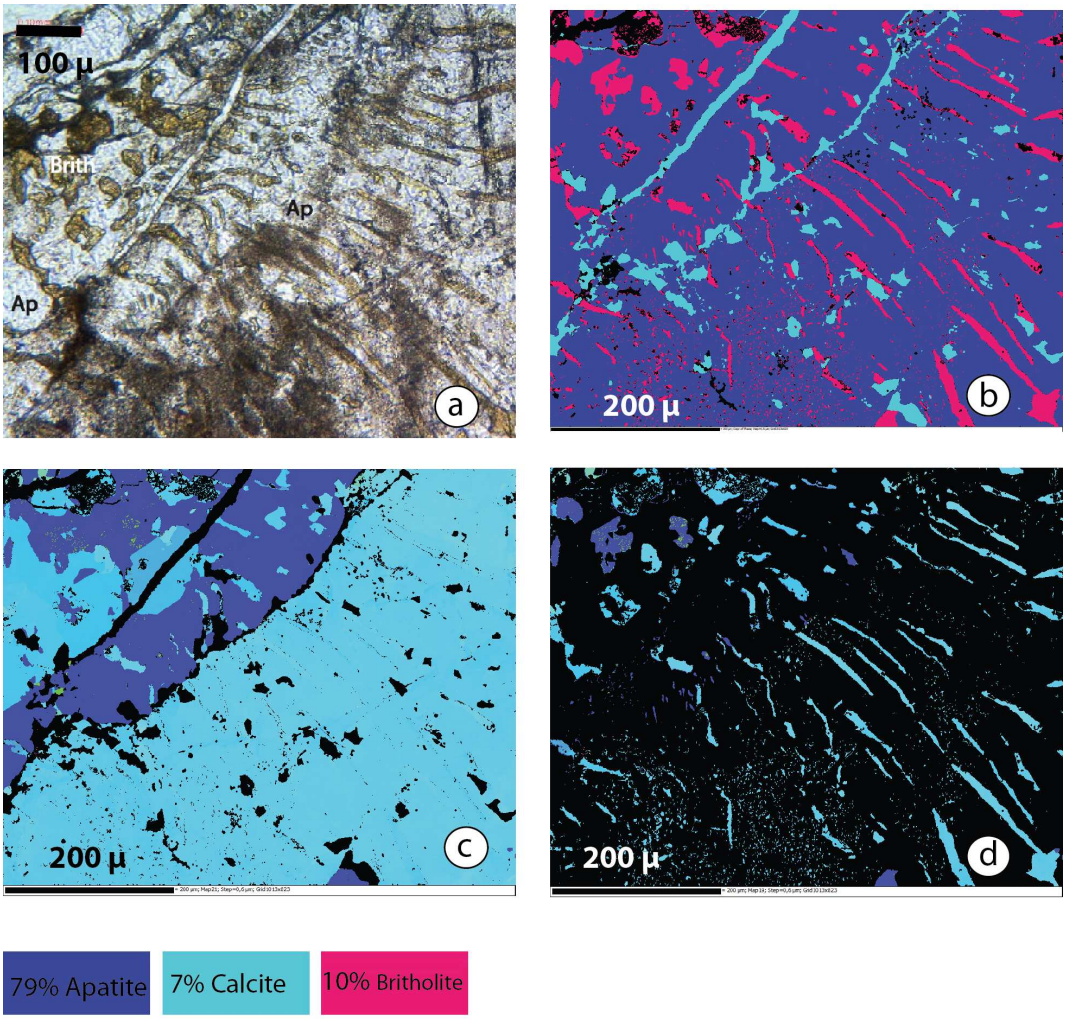

Figure 1 **a** Apatite-britholite en LPNA. **b** Carte de chimie. **c** carte d'orientation de l'apatite et exsolutions de britholites selon l'axe IPFX. **d** orientation IPFX de la britholite

FSD Mixed Image

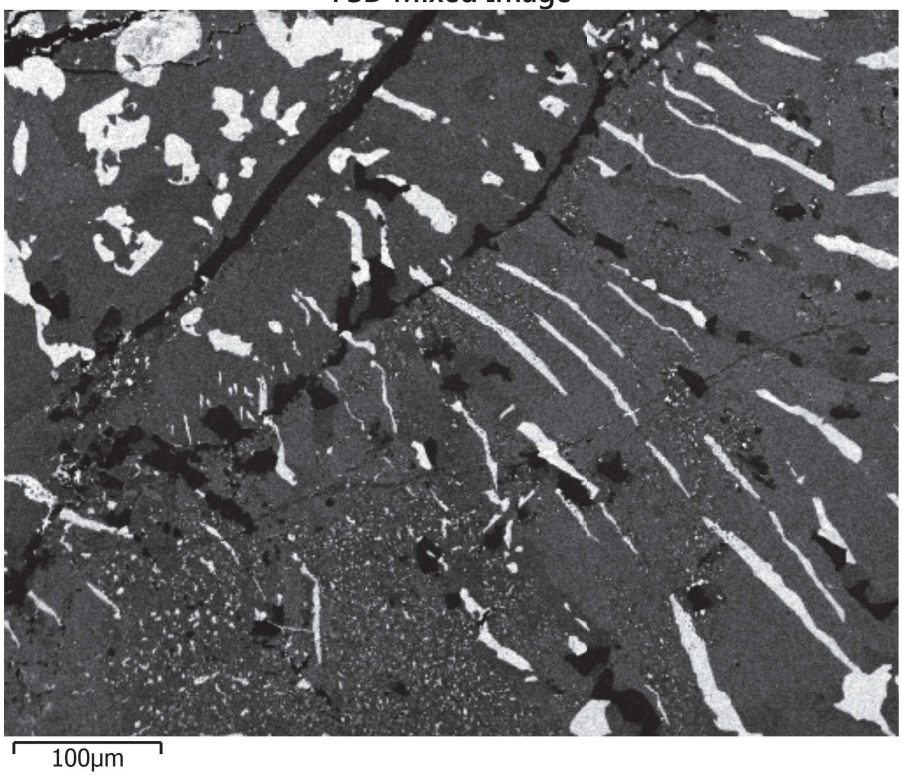

Settings

Accelerating Voltage	17.00 kV
Specimen Tilt (degrees)	70.00 °
Hit Rate	83.39 %
Reanalysis Hit Rate	83.39 %
Speed of Acquisition	63.03 Hz

Phases for Acquisition

Phase	a	b	c	Alpha	Beta	Gamma	Space Group	Database
Apatite	9.41 Å	9.41 Å	6.91 Å	90.00 °	90.00 °	120.00 °	176	AM
Britholite	9.68 Å	9.68 Å	7.07 Å	90.00 °	90.00 °	120.00 °	173	ICSD
Britholite	9.39 Å	9.39 Å	6.90 Å	90.00 °	90.00 °	120.00 °	176	ICSD
Deloneite (Ce)	9.51 Å	9.51 Å	7.01 Å	90.00 °	90.00 °	120.00 °	143	ICSD
Fluorcaphite	9.49 Å	9.49 Å	7.00 Å	90.00 °	90.00 °	120.00 °	173	ICSD
Calcite	4.99 Å	4.99 Å	17.06 Å	90.00 °	90.00 °	120.00 °	0	HKL
Britholite	9.55 Å	9.55 Å	6.99 Å	90.00 °	90.00 °	120.00 °	173	ICSD
Britholite (Ce)	9.70 Å	9.70 Å	7.13 Å	90.00 °	90.00 °	120.00 °	173	ICSD
Britholite (Ce)	9.63 Å	9.63 Å	7.06 Å	90.00 °	90.00 °	120.00 °	173	ICSD
Apatite	9.39 Å	9.39 Å	6.90 Å	90.00 °	90.00 °	120.00 °	176	AM
Apatite	9.40 Å	9.40 Å	6.89 Å	90.00 °	90.00 °	120.00 °	176	AM
Apatite	9.46 Å	9.46 Å	6.88 Å	90.00 °	90.00 °	120.00 °	176	ICSD
Apatite	9.45 Å	9.45 Å	6.88 Å	90.00 °	90.00 °	120.00 °	176	ICSD
Apatite	9.46 Å	9.46 Å	6.88 Å	90.00 °	90.00 °	120.00 °	176	ICSD
Apatite	9.46 Å	9.46 Å	6.88 Å	90.00 °	90.00 °	120.00 °	176	ICSD

Image EBSD en superposition 6

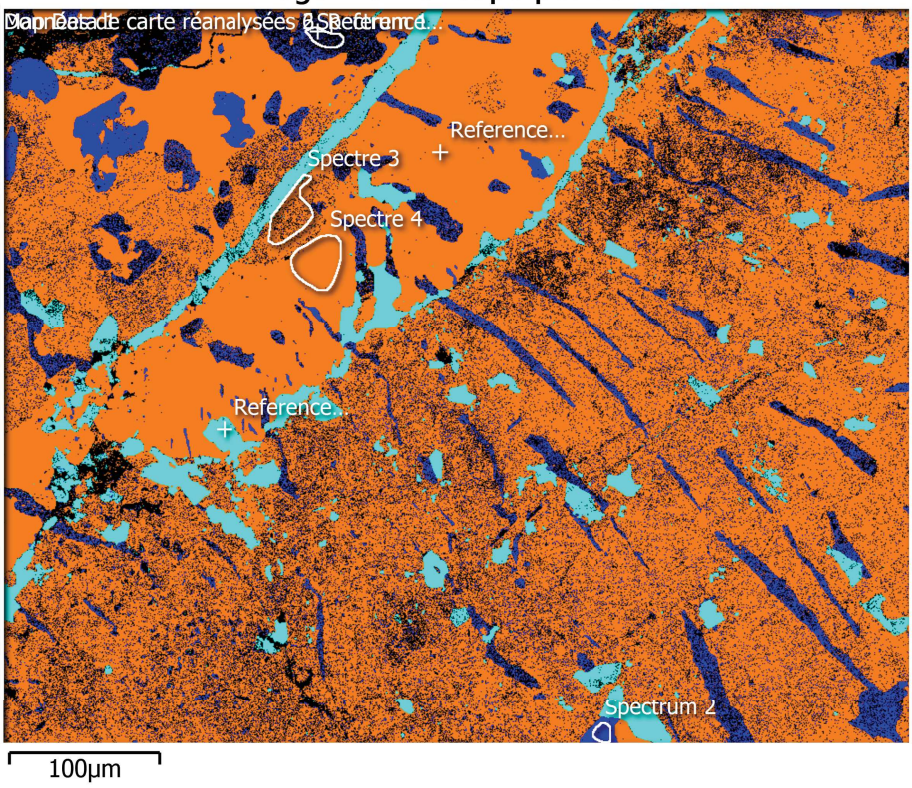

Ca Kα1

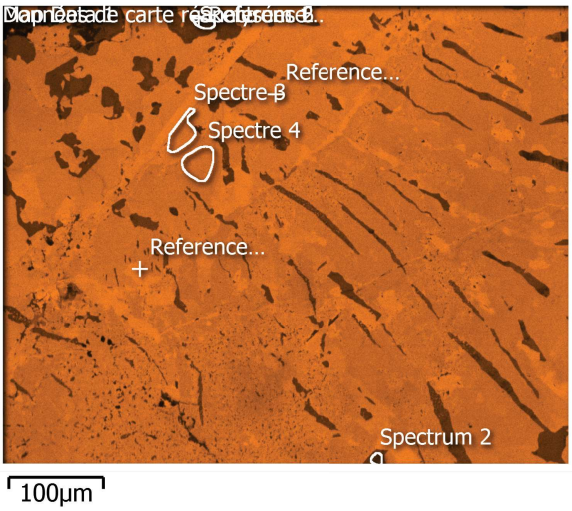

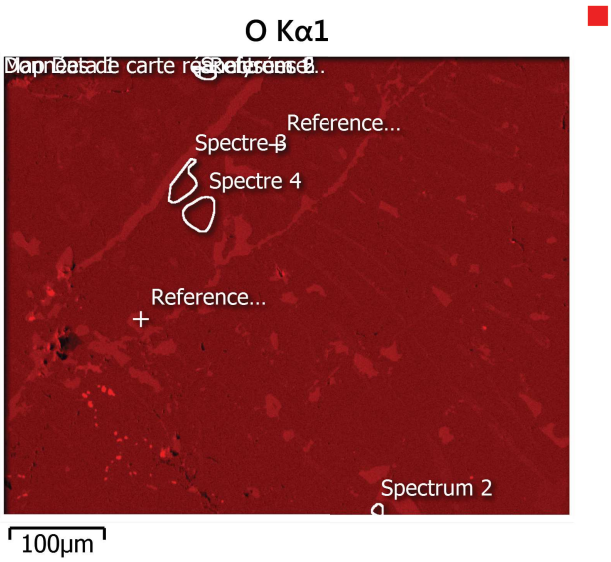
O Kα1
Reference...
Spectre-β
Spectre 4
Reference...
Spectrum 2
100µm

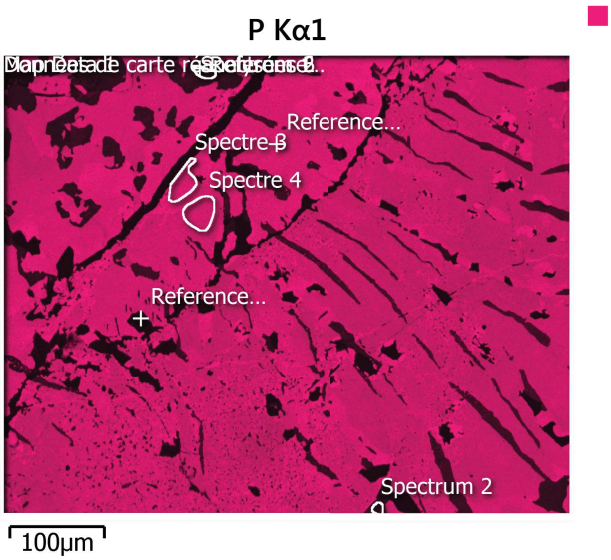
P Kα1
Reference...
Spectre-β
Spectre 4
Reference...
Spectrum 2
100µm

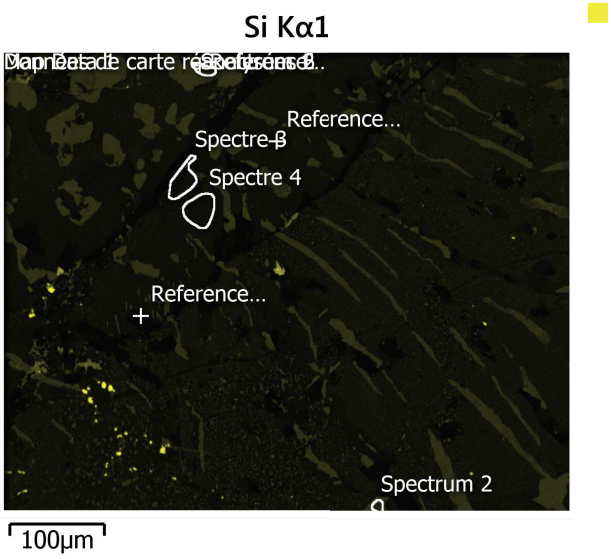
Si Kα1
Reference...
Spectre-β
Spectre 4
Reference...
Spectrum 2
100µm

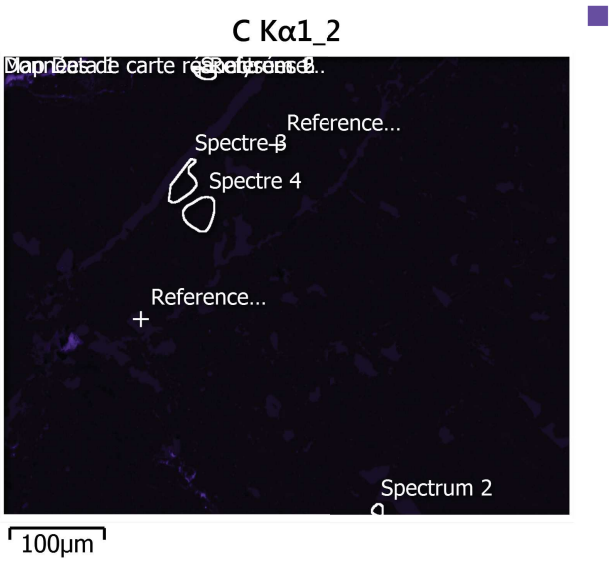
C Kα1_2
Reference...
Spectre-β
Spectre 4
Reference...
Spectrum 2
100µm

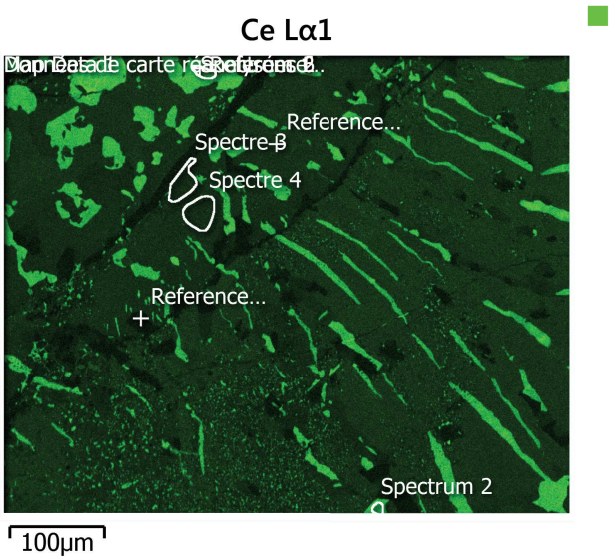
Ce Lα1
Reference...
Spectre-β
Spectre 4
Reference...
Spectrum 2
100µm

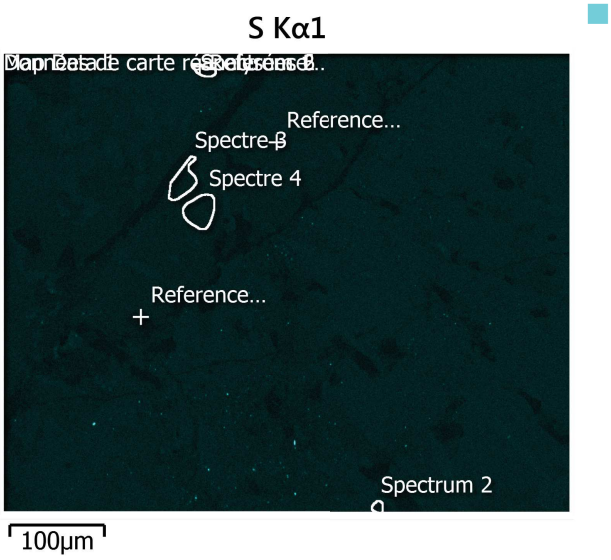
S Kα1
Reference...
Spectre-β
Spectre 4
Reference...
Spectrum 2
100µm

Al Kα1

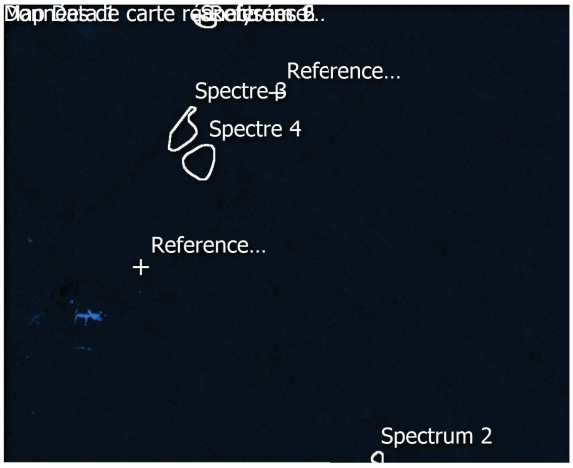

Nd Lα1

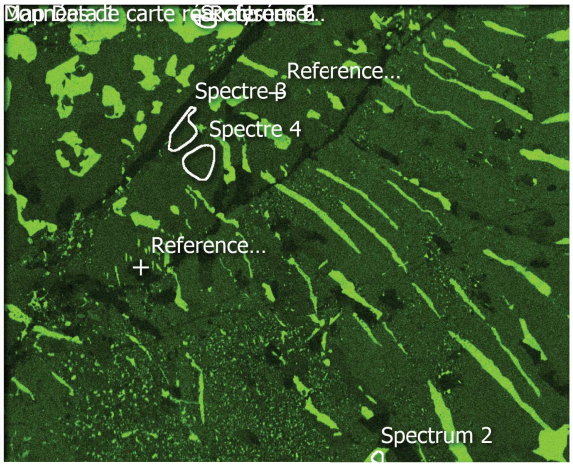

Cl Kα1

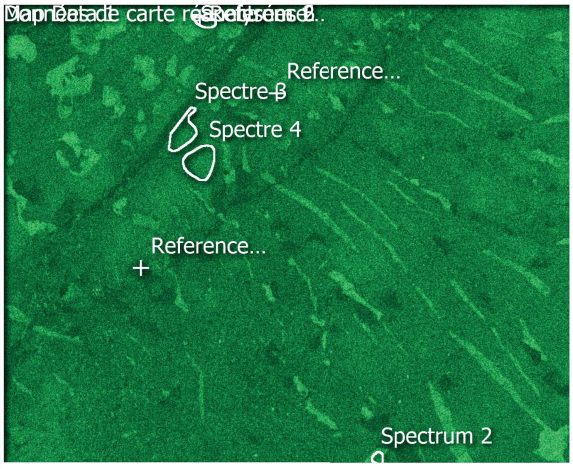

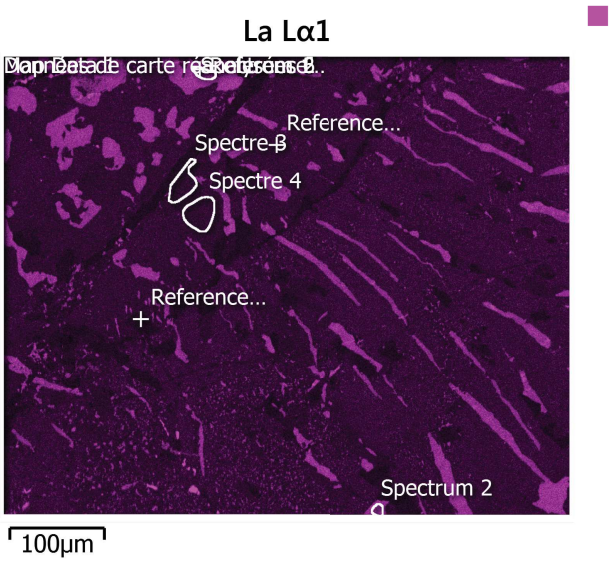
La Lα1
Reference...
Spectre 3
Spectre 4
Reference...
Spectrum 2
100µm

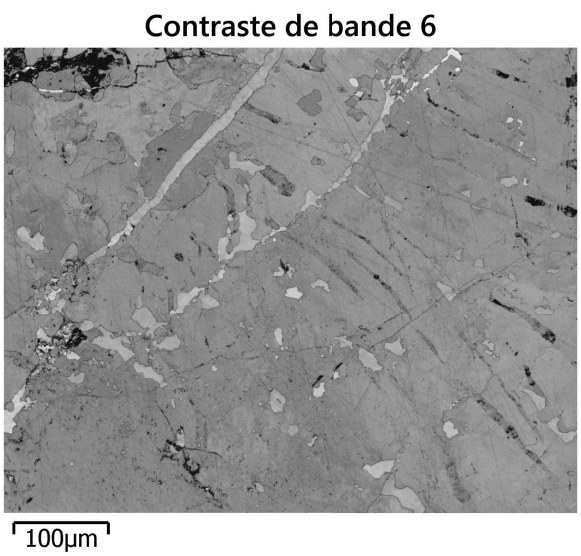
Contraste de bande 6
BC
100µm

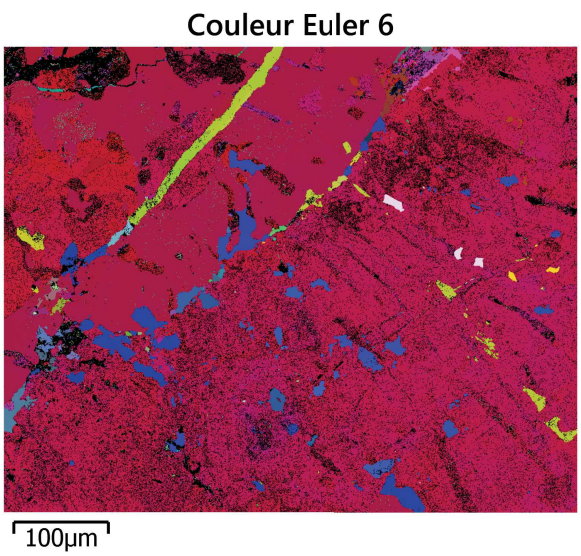
Couleur Euler 6
ϕ1
Φ
ϕ2
100µm

Couleur IPF Z 6

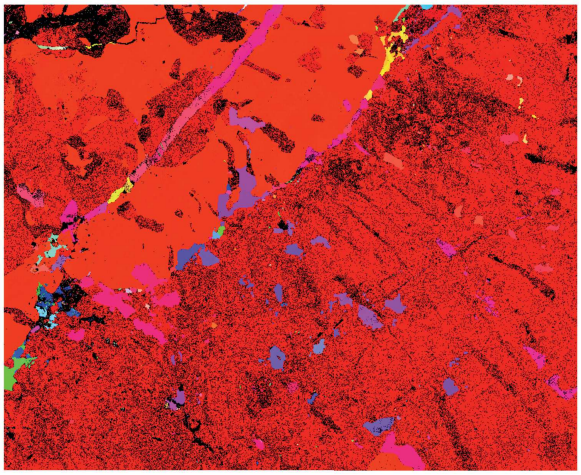

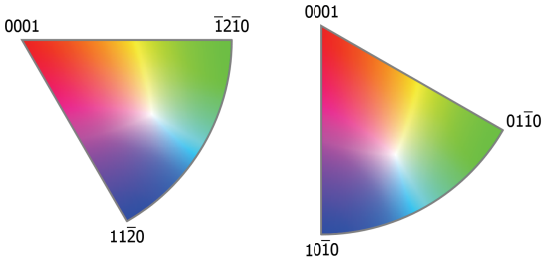

Couleur IPF Y 6

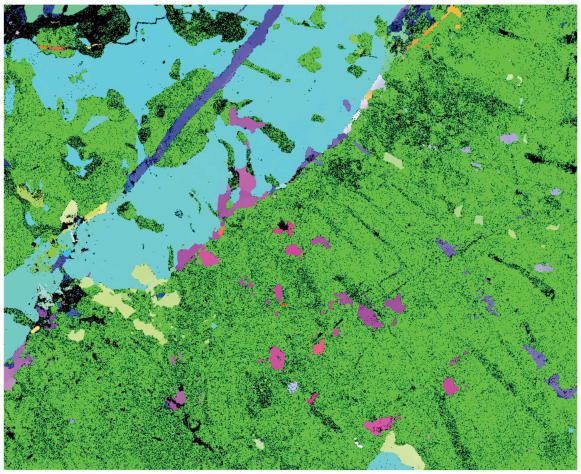

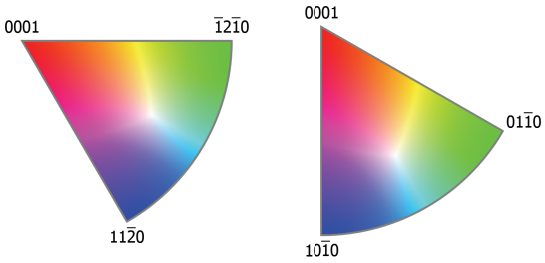

Couleur IPF X 6

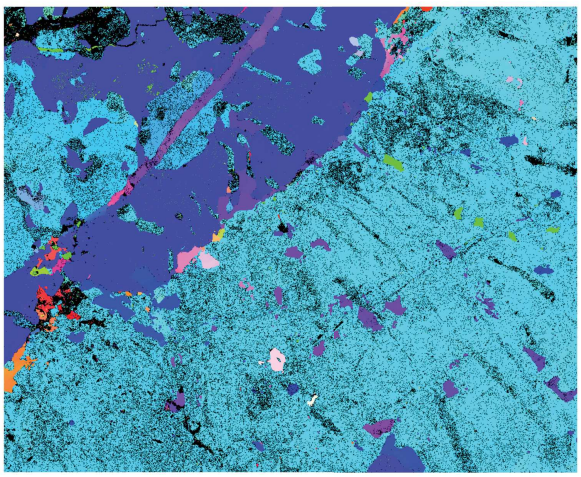

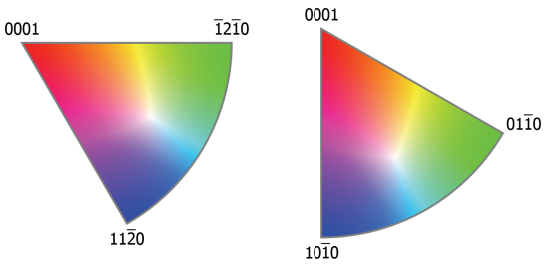

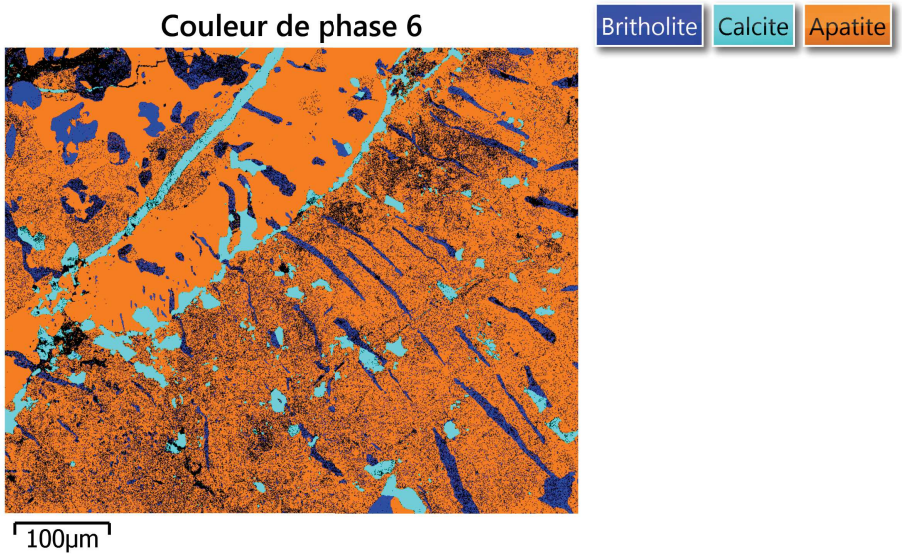

Phase Fraction

Phase Name	Phase Fraction (%)	Phase Count	Mean Band Contrast	Standard Deviation Band Contrast	Min Band Contrast	Max Band Contrast	Mean MAD	Standard Deviation MAD	Min MAD	Max MAD
Britholite	9.05	75420	142.10	18.26	35.00	215.00	0.50	0.14	0.16	1.98
Calcite	6.41	53470	175.08	22.75	35.00	247.00	0.51	0.18	0.18	1.99
Apatite	67.93	566338	151.41	12.31	28.00	230.00	0.46	0.11	0.12	2.00
Zero Solutions	16.61	138471	135.12	30.65	0.00	255.00				
Phase Name	Reanalysis Fraction (%)	Reanalysis Count	Mean Band Contrast	Standard Deviation Band Contrast	Min Band Contrast	Max Band Contrast	Mean MAD	Standard Deviation MAD	Min MAD	Max MAD
Britholite	9.05	75420	142.10	18.26	35.00	215.00	0.50	0.14	0.16	1.98
Calcite	6.41	53470	175.08	22.75	35.00	247.00	0.51	0.18	0.18	1.99
Apatite	67.93	566338	151.41	12.31	28.00	230.00	0.46	0.11	0.12	2.00
Zero Solutions	16.61	138471	135.12	30.65	0.00	255.00				

Annexe D

Les datations U-Pb sur apatite et sur zircon dans le complexe d'Ihouhaouene (Chapitre IV)

Table 1: Representative major element composition of zircon from the Ihouhaouene carbonatite and syenite

Rock type	Si-rich Carbonatite										
Sample	IC2-9Ap. Z1.1	IC2-9Ap. Z1.2	IC2-9Ap. Z1.3	IC2-9Ap. Z1.4	IC2-9Ap. Z1.5	IC2-9Ap. Z1.6	IC2-9Ap. Z1.7	IC2-9Ap. Z1.8	IC2-9Ap. Z1.9	IC2-9Ap. Z1.10	IC2-9Ap. Z1.11
Type	Rim	Middle	Core	Middle	Rim	Middle	Rim	Rim	Core	Rim	Rim
SiO2	31.52	31.15	31.16	31.07	30.72	31.32	31.62	31.73	27.89	30.65	31.36
TiO2	0.01	0.01	0.01	0.01	0.01	0.01	0.02	0.01	0.01	0.02	0.02
ZrO2	67.10	67.11	67.64	67.52	66.88	66.65	66.19	67.35	64.65	67.96	66.73
FeO	0.02	-	b.d.	0.01	0.01	0.01	0.01	0.02	0.02	0.07	0.02
CaO	0.12	0.06	0.06	0.09	0.21	0.07	0.07	0.10	0.11	0.33	0.11
PbO	-	-	-	-	-	-	-	-	-	-	0.03
UO2	-	-	-	-	-	-	-	-	-	-	-
ThO2	-	-	-	0.03	b.d.	-	-	-	0.03	-	0.01
Y2O3	0.02	0.03	-	b.d.	0.02	0.04	-	-	-	-	-
Yb2O3	0.05	0.03	-	-	b.d.	0.05	0.03	0.07	0.07	-	0.01
HfO2	0.47	0.43	0.47	0.36	0.25	0.42	0.47	0.49	0.46	0.57	0.49
Total	99.31	98.81	99.34	99.09	98.10	98.58	98.41	99.78	93.24	99.60	98.77
Numbers of ions on the basis of 16O											
Si	3.91	3.89	3.88	3.87	3.87	3.91	3.95	3.92	3.74	3.82	3.91
Ti	0.001	0.001	0.001	0.001	0.001	0.001	0.002	0.001	0.001	0.002	0.002
Zr	4.06	4.09	4.10	4.10	4.11	4.06	4.03	4.05	4.23	4.13	4.06
Fe2+	0.002	-	-	0.001	0.001	0.001	0.001	0.002	0.002	0.007	0.002
Ca	0.016	0.008	0.008	0.012	0.028	0.010	0.010	0.013	0.016	0.044	0.015
Th	-	-	-	0.001	-	-	-	-	0.001	-	0.001
Y	0.001	0.002	-	-	-	0.003	-	-	-	-	-
Yb	0.002	0.001	-	-	0.000	0.002	0.001	0.003	0.003	-	0.000
Hf	0.02	0.02	0.02	0.01	0.01	0.02	0.02	0.02	0.02	0.02	0.02
Total	8	8	8	8	8	8	8	8	8	8	8

b.d. :below deection

Table 1: Continued

Rock type	Si-rich Carbonatite										
Sample	IC2-9Ap. Z2.1	IC2-9Ap. Z2.2	IC2-9Ap. Z2.3	IC2-9Ap. Z2.4	IC2-9Ap. Z2.5	IC2-9Ap. Z2.6	IC2-9Ap. Z3.2	IC2-9Ap. Z3.3	IC2-9Ap. Z3.4	IC2-9Ap. Z3.5	IC2-9Ap. Z3.6
Type	Rim	Middle	Core	Middle	Rim	Rim	Rim	Rim	Rim	Rim	Middle
SiO2	31.53	31.48	31.48	31.51	31.55	31.54	30.50	31.27	31.54	31.47	31.58
TiO2	0.02	0.02	0.02	0.01	0.01	0.02	0.02	0.01	0.02	0.01	0.01
ZrO2	66.91	67.22	66.77	67.12	66.96	67.00	67.85	66.60	66.19	66.65	66.57
FeO	0.02	b.d.	0.01	0.01	0.01	0.01	0.30	0.10	0.10	0.05	0.06
CaO	0.01	0.02	0.01	0.01	b.d.	0.01	0.17	0.02	0.02	0.03	0.03
PbO	-	-	-	-	0.01	-	-	b.d.	0.01	-	0.01
UO2	-	-	-	-	-	-	-	-	-	-	-
ThO2	-	0.21	0.12	-	-	-	-	-	0.03	-	-
Y2O3	-	-	0.02	-	-	-	-	-	-	-	-
Yb2O3	-	-	-	-	0.03	0.04	-	-	-	0.05	0.17
HfO2	0.51	0.49	0.46	0.48	0.57	0.59	0.55	0.54	0.53	0.53	0.52
Total	99.00	99.43	98.88	99.15	99.14	99.21	99.39	98.54	98.44	98.79	98.96
Numbers of ions on the basis of 16O											
Si	3.92	3.91	3.92	3.91	3.92	3.92	3.81	3.91	3.94	3.92	3.93
Ti	0.001	0.001	0.002	0.001	0.001	0.002	0.001	0.001	0.002	0.001	0.001
Zr	4.06	4.07	4.06	4.07	4.06	4.06	4.14	4.06	4.03	4.05	4.04
Fe2+	0.002	0.000	0.001	0.001	0.001	0.001	0.031	0.010	0.010	0.005	0.006
Ca	0.002	0.003	0.001	0.002	-	0.001	0.023	0.003	0.003	0.003	0.004
Th	-	0.006	0.003	-	-	-	-	-	0.001	-	-
Y	-	-	0.001	-	-	-	-	-	-	-	-
Yb	-	-	-	-	0.001	0.001	-	-	-	0.002	0.006
Hf	0.02	0.02	0.02	0.02	0.02	0.02	0.02	0.02	0.02	0.02	0.02
Total	8	8	8	8	8	8	8	8	8	8	8

b.d. :below deection

Table 1: Continued

Rock type	Si-rich Carbonatite										
Sample	IC2-9Ap. Z3.7	IC2-9Ap. Z3.8	IC2-9Ap. Z3.9	IC2-9Ap. Z3.10	IC2-9Ap. Z3.11	IC2-9Ap. Z3.12	IC2-9Ap. Z3.13	IC2-9Ap. Z3.14	IC2-9Ap. Z3.15	IC2-9Ap. Z3.16	IC2-9Ap. Z3.17
Type	Middle	Rim	Rim	Rim	Rim	Rim	Core	Middle	Line1	Line1	Line1
SiO2	31.40	31.69	31.70	31.45	31.08	31.30	31.20	31.40	31.03	30.76	31.16
TiO2	0.01	0.02	0.01	0.01	0.01	0.01	0.01	0.02	0.01	0.02	0.01
ZrO2	66.66	66.90	67.00	67.07	67.53	67.33	67.38	67.13	67.56	68.41	67.68
FeO	0.05	0.05	0.02	0.01	0.01	0.01	b.d.	b.d.	0.01	0.01	b.d.
CaO	0.06	0.02	0.03	0.07	0.04	0.03	0.02	0.01	0.03	0.09	0.03
PbO	0.01	-	0.01	-	-	0.01	-	0.01	-	b.d.	-
UO2	-	-	-	-	-	-	-	-	-	-	-
ThO2	0.01	-	-	0.33	0.06	0.12	0.24	-	0.15	0.05	-
Y2O3	-	-	-	-	-	-	-	-	-	-	-
Yb2O3	-	-	-	-	0.01	0.08	0.02	0.01	-	0.05	-
HfO2	0.55	0.54	0.57	0.55	0.56	0.55	0.55	0.56	0.54	0.56	0.54
Total	98.75	99.22	99.33	99.48	99.30	99.43	99.42	99.13	99.32	99.95	99.42
Numbers of ions on the basis of 16O											
Si	3.92	3.93	3.93	3.90	3.87	3.89	3.88	3.91	3.87	3.82	3.87
Ti	0.001	0.001	0.001	0.001	0.001	0.001	0.001	0.002	0.001	0.001	0.001
Zr	4.06	4.05	4.05	4.06	4.10	4.08	4.09	4.07	4.11	4.15	4.10
Fe2+	0.005	0.005	0.002	0.001	0.001	0.001	-	-	0.001	0.001	-
Ca	0.008	0.003	0.004	0.009	0.005	0.004	0.003	0.001	0.003	0.011	0.004
Th	-	-	-	0.009	0.002	0.003	0.007	-	0.004	0.001	-
Y	-	-	-	-	-	-	-	-	-	-	-
Yb	-	-	-	-	0.000	0.003	0.001	0.000	-	0.002	-
Hf	0.02	0.02	0.02	0.02	0.02	0.02	0.02	0.02	0.02	0.02	0.02
Total	8	8	8	8	8	8	8	8	8	8	8

b.d. :below deection

Table 1: Continued

Rock type	Si-rich Carbonatite										
Sample	IC2-9Ap. Z3.18	IC2-9Ap. Z3.19	IC2-9Ap. Z3.20	IC2-9Ap. Z3.21	IC2-9Ap. Z3.22	IC2-9Ap. Z3.23	IC2-9Ap. Z3.24	IC2-9Ap. Z3.25	IC2-9Ap. Z3.26	IC2-9Ap. Z3.27	IC2-9Ap. Z3.28
Type	Line1	Line1	Line1	Line1	Line1	Line1	Line1	Line1	Line1	Line1	Line1
SiO2	31.26	30.92	31.27	31.16	31.22	31.46	31.56	31.64	31.43	31.42	31.41
TiO2	0.01	0.01	0.01	0.01	0.01	0.01	0.02	0.01	0.01	0.01	0.02
ZrO2	67.61	67.02	66.83	67.04	67.02	67.12	66.89	66.76	66.80	66.88	66.54
FeO	0.01	0.01	-	b.d.	0.01	0.01	0.01	0.01	0.01	0.01	0.02
CaO	0.04	0.10	0.01	0.02	0.03	0.01	0.01	0.01	0.01	0.01	0.02
PbO	0.01	-	b.d.	-	-	-	0.03	-	-	-	b.d.
UO2	-	-	-	-	-	-	-	-	-	-	-
ThO2	0.08	-	0.11	0.07	0.05	-	0.22	-	-	-	-
Y2O3	-	-	-	-	-	-	-	-	-	-	-
Yb2O3	-	0.06	0.05	0.03	-	0.04	-	-	0.05	-	-
HfO2	0.54	0.55	0.54	0.54	0.55	0.55	0.53	0.55	0.53	0.53	0.55
Total	99.56	98.69	98.83	98.86	98.89	99.20	99.27	98.98	98.85	98.86	98.55
Numbers of ions on the basis of 16O											
Si	3.88	3.87	3.91	3.89	3.90	3.91	3.92	3.93	3.92	3.92	3.92
Ti	0.001	0.001	0.001	0.001	0.001	0.001	0.002	0.001	0.001	0.001	0.002
Zr	4.09	4.09	4.07	4.08	4.08	4.07	4.05	4.05	4.06	4.06	4.05
Fe2+	0.001	0.001	-	-	0.001	0.001	0.001	0.001	0.001	0.001	0.002
Ca	0.006	0.014	0.002	0.002	0.004	0.002	0.001	0.002	0.002	0.002	0.003
Th	0.002	-	0.003	0.002	0.001	-	0.006	-	-	-	-
Y	-	-	-	-	-	-	-	-	-	-	-
Yb	-	0.002	0.002	0.001	-	0.001	-	-	0.002	-	-
Hf	0.02	0.02	0.02	0.02	0.02	0.02	0.02	0.02	0.02	0.02	0.02
Total	8	8	8	8	8	8	8	8	8	8	8

b.d. :below deection

Table 1: Continued

Rock type	Si-rich Carbonatite										
Sample	IC2-9Ap. Z3.29	IC2-9Ap. Z3.30	IC2-9Ap. Z3.31	IC2-9Ap. Z3.32	IC2-9Ap. Z3.33	IC2-9Ap. Z4.1	IC2-9Ap. Z4.2	IC2-9Ap. Z4.3	IC2-9Ap. Z4.4	IC2-9Ap. Z5.1	IC2-9Ap. Z5.2
Type	Line1	Line1	Line1	Line1	Line1	Rim	Core	Rim	Rim	Line1	Line1
SiO2	31.37	31.37	31.69	31.74	31.82	31.03	31.40	31.45	30.98	31.08	31.16
TiO2	-	0.01	0.02	0.01	0.02	1.37	0.12	0.07	0.47	0.11	0.05
ZrO2	64.85	66.94	66.85	66.78	66.36	65.88	67.24	67.07	66.32	67.38	67.28
FeO	0.36	0.03	0.04	0.06	0.12	0.11	0.04	0.03	0.07	0.02	0.01
CaO	0.33	0.02	0.02	0.03	0.04	1.03	0.08	0.05	0.49	0.08	0.03
PbO	b.d.	0.01	-	b.d.	-	-	0.03	0.01	-	b.d.	-
UO2	-	-	-	-	-	-	-	-	-	-	-
ThO2	-	-	0.15	0.03	0.03	0.07	-	0.13	-	0.19	-
Y2O3	-	-	-	-	-	-	-	-	-	-	-
Yb2O3	-	0.06	-	0.02	0.04	-	-	0.05	-	0.03	-
HfO2	0.54	0.54	0.54	0.55	0.61	0.53	0.56	0.60	0.54	0.65	0.50
Total	97.45	98.98	99.30	99.23	99.02	100.04	99.48	99.46	98.86	99.53	99.04
Numbers of ions on the basis of 16O											
Si	3.95	3.91	3.93	3.94	3.95	3.82	3.89	3.90	3.87	3.87	3.88
Ti	-	0.001	0.002	0.001	0.001	0.127	0.011	0.007	0.044	0.010	0.005
Zr	3.99	4.07	4.04	4.04	4.02	3.96	4.07	4.06	4.03	4.09	4.09
Fe2+	0.037	0.003	0.004	0.006	0.012	0.012	0.005	0.003	0.007	0.002	0.001
Ca	0.045	0.003	0.002	0.004	0.005	0.136	0.010	0.006	0.065	0.010	0.005
Th	-	-	0.004	0.001	0.001	0.002	-	0.004	-	0.006	-
Y	-	-	-	-	-	-	-	-	-	-	-
Yb	-	0.002	-	0.001	0.001	-	-	0.002	-	0.001	-
Hf	0.02	0.02	0.02	0.02	0.02	0.02	0.02	0.02	0.02	0.02	0.02
Total	8	8	8	8	8	8	8	8	8	8	8

b.d. :below deection

Table 1: Continued

Rock type	Si-rich Carbonatite										
Sample	IC2-9Ap. Z5.3	IC2-9Ap. Z5.4	IC2-9Ap. Z5.5	IC2-9Ap. Z5.6	IC2-9Ap. Z5.7	IC2-9Ap. Z5.8	IC2-9Ap. Z5.9	IC2-9Ap. Z5.10	IC2-9Ap. Z5.11	IC2-9Ap. Z5.1	IC2-9Ap. Z5.2
Type	Line1	Line1	Line1	Line1	Line1	Line1	Line1	Line1	Line1	Line2	Line2
SiO2	31.29	31.59	31.69	31.42	31.37	31.46	31.60	31.66	31.83	31.17	31.49
TiO2	0.03	0.03	0.03	0.02	0.02	0.03	0.03	0.02	0.02	0.03	0.03
ZrO2	66.98	67.07	67.19	67.07	67.19	67.12	66.92	66.95	66.62	68.03	67.52
FeO	b.d.	0.01	0.01	0.01	0.02	0.02	0.01	0.01	0.01	0.03	b.d.
CaO	0.03	0.03	0.05	0.03	0.04	0.03	0.03	0.04	0.10	0.20	0.06
PbO	-	b.d.	-	b.d.	-	b.d.	0.01	b.d.	b.d.	0.01	b.d.
UO2	-	-	-	-	-	-	-	-	-	-	-
ThO2	0.14	0.08	0.04	-	0.11	0.03	0.02	0.01	0.01	-	0.03
Y2O3	0.01	-	-	b.d.	0.02	0.01	-	0.01	-	-	b.d.
Yb2O3	-	0.03	0.13	0.06	-	0.04	0.08	-	-	-	0.10
HfO2	0.48	0.49	0.49	0.46	0.45	0.47	0.44	0.46	0.54	0.51	0.52
Total	98.95	99.32	99.62	99.08	99.22	99.20	99.13	99.16	99.12	99.98	99.74
Numbers of ions on the basis of 16O											
Si	3.90	3.92	3.92	3.91	3.90	3.91	3.92	3.93	3.95	3.86	3.90
Ti	0.003	0.003	0.002	0.002	0.002	0.002	0.002	0.002	0.002	0.003	0.003
Zr	4.07	4.06	4.05	4.07	4.07	4.07	4.05	4.05	4.03	4.11	4.07
Fe2+	-	0.001	0.001	0.001	0.002	0.002	0.001	0.001	0.001	0.003	0.000
Ca	0.004	0.004	0.007	0.005	0.005	0.004	0.004	0.006	0.013	0.026	0.008
Th	0.004	0.002	0.001	-	0.003	0.001	0.001	0.000	0.000	-	0.001
Y	0.001	-	-	0.000	0.002	0.001	-	0.001	-	-	-
Yb	-	0.001	0.005	0.002	-	0.002	0.003	-	-	-	0.004
Hf	0.02	0.02	0.02	0.02	0.02	0.02	0.02	0.02	0.02	0.02	0.02
Total	8	8	8	8	8	8	8	8	8	8	8

b.d. :below deection

Table 1: Continued

Rock type	Si-rich Carbonatite										
Sample	IC2-9Ap. Z5.3	IC2-9Ap. Z5.4	IC2-9Ap. Z5.5	IC2-9Ap. Z5.6	IC2-9Ap. Z5.7	IC2-9Ap. Z5.8	IC2-9Ap. Z5.9	IC2-9Ap. Z5.10	IC2-9Ag. Z2.1	IC2-9Ag. Z2.2	IC2-9Ag. Z2.3
Type	Line2	Line2	Line2	Line2	Line2	Line2	Line2	Line2	Rim	Middle	Core
SiO2	31.24	29.50	31.46	31.40	31.27	30.62	31.52	31.03	31.34	31.24	31.37
TiO2	0.03	0.02	0.02	0.02	0.03	0.04	0.07	0.08	0.01	0.01	0.02
ZrO2	67.33	63.89	66.20	67.06	66.75	65.11	66.84	66.92	67.72	66.95	66.91
FeO	b.d.	b.d.	0.01	0.01	b.d.	0.01	0.01	0.02	0.05	0.03	0.02
CaO	0.05	2.09	0.03	0.02	0.02	0.04	0.05	0.04	0.08	0.01	0.02
PbO	-	0.02	b.d.	0.01	-	0.01	0.01	-	-	b.d.	b.d.
UO2	-	-	-	-	-	-	-	-	-	-	-
ThO2	-	-	-	0.04	0.06	0.03	0.06	0.01	-	-	0.24
Y2O3	-	b.d.	-	-	-	-	-	-	-	-	-
Yb2O3	0.07	-	-	-	-	0.02	-	-	-	-	0.04
HfO2	0.51	0.48	0.47	0.46	0.45	0.61	0.54	0.52	0.54	0.48	0.49
Total	99.23	96.00	98.19	99.02	98.58	96.50	99.09	98.61	99.75	98.73	99.10
Numbers of ions on the basis of 16O											
Si	3.89	3.81	3.94	3.91	3.91	3.91	3.92	3.88	3.88	3.90	3.91
Ti	0.002	0.002	0.002	0.002	0.002	0.004	0.006	0.007	0.001	0.001	0.002
Zr	4.09	4.02	4.04	4.07	4.07	4.06	4.05	4.08	4.09	4.08	4.06
Fe2+	0.000	0.000	0.001	0.001	0.000	0.001	0.001	0.002	0.005	0.003	0.002
Ca	0.007	0.289	0.004	0.003	0.003	0.005	0.006	0.006	0.010	0.001	0.002
Th	-	-	-	0.001	0.002	0.001	0.002	-	-	-	0.007
Y	-	-	-	-	-	-	-	-	-	-	-
Yb	0.003	-	-	-	-	0.001	-	-	-	-	0.001
Hf	0.02	0.02	0.02	0.02	0.02	0.02	0.02	0.02	0.02	0.02	0.02
Total	8	8	8	8	8	8	8	8	8	8	8

b.d. :below deection

Table 1: Continued

Rock type	Si-rich Carbonatite										
Sample	IC2-9Ag. Z2.4	IC2-9Ag. Z2.5	IC2-9Ag. Z2.1	IC2-9Ag. Z2	IC2-9Ag. Z2.2	IC2-9Ag. Z3	IC2-9Ag. Z2.3	IC2-9Ag. Z4	IC2-9Ag. Z2.4	IC2-9Ag. Z5	IC2-9Ag. Z2.5
Type	Middle	Rim	Line3	Line3	Line3	Line3	Line3	Line3	Line3	Line3	Line3
SiO2	31.31	31.66	31.44	31.29	31.31	30.77	30.38	31.42	31.32	31.27	29.92
TiO2	0.01	0.02	0.01	0.01	0.01	0.01	0.01	0.01	0.01	0.01	0.01
ZrO2	66.54	66.16	66.42	67.00	66.81	67.16	64.98	66.60	67.02	67.15	65.87
FeO	0.03	0.04	0.02	0.02	0.01	0.02	0.01	0.01	0.00	0.01	0.01
CaO	0.03	0.04	0.02	0.02	0.01	0.02	0.03	0.01	0.01	0.01	0.04
PbO	-	-	-	0.02	-	0.01	-	-	-	-	0.01
UO2	-	-	-	-	-	-	-	-	-	-	-
ThO2	0.14	0.04	-	-	0.06	-	-	-	-	0.06	0.01
Y2O3	-	-	-	-	-	-	-	-	-	-	0.01
Yb2O3	0.04	-	-	-	0.01	0.04	0.05	-	0.01	0.12	-
HfO2	0.69	0.57	0.60	0.61	0.56	0.53	0.52	0.54	0.53	0.53	0.49
Total	98.80	98.52	98.52	98.97	98.82	98.56	96.00	98.60	98.92	99.19	96.37
Numbers of ions on the basis of 16O											
Si	3.91	3.95	3.93	3.90	3.91	3.86	3.90	3.92	3.90	3.90	3.85
Ti	0.001	0.002	0.001	0.001	0.001	0.001	0.001	0.001	0.001	0.001	0.001
Zr	4.05	4.02	4.05	4.07	4.07	4.11	4.07	4.06	4.07	4.08	4.13
Fe2+	0.003	0.004	0.003	0.002	0.001	0.002	0.001	0.001	0.000	0.001	0.001
Ca	0.004	0.005	0.003	0.003	0.002	0.002	0.003	0.001	0.002	0.002	0.005
Th	0.004	0.001	-	-	0.002	-	-	-	-	0.002	-
Y	-	-	-	-	-	-	-	-	-	-	-
Yb	0.002	-	-	-	-	0.002	0.002	-	0.001	0.004	-
Hf	0.02	0.02	0.02	0.02	0.02	0.02	0.02	0.02	0.02	0.02	0.02
Total	8	8	8	8	8	8	8	8	8	8	8

b.d. :below deection

Table 1: Continued

Rock type	Si-rich Carbonatite										
Sample	IC2-9Ag. Z6	IC2-9Ag. Z2.6	IC2-9Ag. Z7	IC2-9Ag. Z2.7	IC2-9Ag. Z8	IC2-9Ag. Z2.8	IC2-9Ag. Z9	IC2-9Ag. Z2.9	IC2-9Ag. Z10	IC2-9Ag. Z2.10	IC2-9Ag. Z11
Type	Line3	Line3	Line3	Line3	Line3	Line3	Line3	Line3	Line3	Line3	Line3
SiO2	31.62	31.37	31.30	31.24	30.09	31.21	30.79	28.58	29.57	30.89	31.40
TiO2	0.01	0.01	0.01	0.01	0.01	0.01	0.01	0.01	0.01	0.01	0.01
ZrO2	66.68	66.80	66.94	66.96	67.15	66.17	65.29	63.39	64.88	66.53	66.73
FeO	0.01	0.01	b.d.	b.d.	0.01	b.d.	0.01	0.01	0.01	0.01	0.01
CaO	0.01	0.01	0.01	0.01	0.04	0.04	0.13	0.40	0.36	0.08	0.01
PbO	0.02	-	0.03	b.d.	-	0.02	b.d.	b.d.	0.01	-	0.01
UO2	-	-	-	-	-	-	-	-	-	-	-
ThO2	-	0.13	-	-	-	-	-	0.12	-	-	-
Y2O3	0.00	0.02	-	-	-	-	-	-	-	-	-
Yb2O3	0.16	0.03	-	0.07	0.02	0.06	0.03	-	-	-	-
HfO2	0.48	0.47	0.48	0.50	0.47	0.50	0.51	0.47	0.54	0.60	0.61
Total	99.00	98.88	98.80	98.82	97.82	98.02	96.79	93.00	95.40	98.13	98.80
Numbers of ions on the basis of 16O											
Si	3.93	3.91	3.91	3.90	3.82	3.92	3.92	3.82	3.84	3.89	3.92
Ti	0.001	0.001	0.001	0.001	0.001	0.001	0.001	0.001	0.001	0.001	0.001
Zr	4.04	4.06	4.07	4.08	4.16	4.05	4.05	4.13	4.11	4.08	4.06
Fe2+	0.001	0.001	0.000	0.000	0.001	0.000	0.001	0.001	0.001	0.001	0.001
Ca	0.001	0.002	0.001	0.001	0.005	0.005	0.018	0.057	0.050	0.011	0.001
Th	-	0.004	-	-	-	-	-	0.004	-	-	-
Y	-	0.001	-	-	-	-	-	-	-	-	-
Yb	0.006	0.001	-	0.003	0.001	0.002	0.001	-	-	-	-
Hf	0.02	0.02	0.02	0.02	0.02	0.02	0.02	0.02	0.02	0.02	0.02
Total	8	8	8	8	8	8	8	8	8	8	8

b.d. :below deection

Table 1: Continued

Rock type	Si-rich Carbonatite										
Sample	IC2-9Ag. Z3.1	IC2-9Ag. Z3.2	IC2-9Ag. Z3.3	IC2-9Ag. Z3.4	IC2-9Ag. Z3.5	IC2-9Ag. Z3.6	IC2-9Ag. Z3.7	IC2-9Ag. Z3.8	IC2-9Ag. Z3.9	IC2-9Ag. Z3.10	IC2-9Ag. Z3.11
Type	Line4	Line4	Line4	Line4	Line4	Line4	Line4	Line4	Line4	Line4	Line4
SiO2	32.21	31.97	31.96	31.59	31.43	31.32	31.34	31.39	31.59	31.19	30.99
TiO2	0.01	0.01	0.01	0.01	0.00	0.01	0.01	0.00	0.01	0.01	0.00
ZrO2	66.31	66.77	66.74	66.67	66.51	66.48	66.37	66.23	66.23	66.80	65.23
FeO	0.02	0.01	0.01	0.01	0.01	0.02	0.01	0.01	0.01	0.01	0.03
CaO	0.10	0.05	0.04	0.03	0.03	0.02	0.03	0.01	0.02	0.03	0.17
PbO	0.01	0.02	-	0.01	-	0.02	0.02	-	0.01	-	0.05
UO2	-	-	-	-	-	-	-	-	-	-	-
ThO2	-	0.07	0.24	0.06	0.28	-	0.07	0.17	0.13	0.03	-
Y2O3	-	-	-	-	-	-	-	-	-	-	0.09
Yb2O3	b.d.	0.08	-	-	0.01	-	-	-	-	-	0.06
HfO2	0.61	0.60	0.56	0.57	0.57	0.56	0.58	0.55	0.56	0.56	0.54
Total	99.29	99.61	99.60	98.96	98.86	98.44	98.42	98.41	98.57	98.64	97.27
Numbers of ions on the basis of 16O											
Si	3.98	3.95	3.95	3.93	3.92	3.92	3.92	3.93	3.94	3.90	3.93
Ti	0.001	0.001	0.001	0.001	0.000	0.001	0.001	0.000	0.001	0.001	0.000
Zr	3.99	4.02	4.02	4.04	4.05	4.06	4.05	4.04	4.03	4.07	4.03
Fe2+	0.002	0.001	0.001	0.001	0.001	0.002	0.001	0.001	0.001	0.001	0.003
Ca	0.013	0.007	0.006	0.004	0.004	0.003	0.004	0.001	0.002	0.003	0.023
Th	-	0.002	0.007	0.002	0.008	-	0.002	0.005	0.004	0.001	-
Y	-	-	-	-	-	-	-	-	-	-	0.006
Yb	-	0.003	-	-	-	-	-	-	-	-	0.002
Hf	0.02	0.02	0.02	0.02	0.02	0.02	0.02	0.02	0.02	0.02	0.02
Total	8	8	8	8	8	8	8	8	8	8	8

b.d. :below deection

Table 1: Continued

Rock type	Si-rich Carbonatite										
Sample	IC2-9Ag. Z3.12	IC2-9Ag. Z3.13	IC2-9Ag. Z3.14	IC2-9Ag. Z3.15	IC2-9Ag. Z3.16	IC2-9Ag. Z3.17	IC2-9Ag. Z3.18	IC2-9Ag. Z3.19	IC2-9Ag. Z3.20	IC2-9Ag. Z1.1	IC2-9Ag. Z1.2
Type	Line4	Line4	Line4	Line4	Line4	Line4	Line4	Line4	Line4	Rim	Middle
SiO2	31.17	31.20	31.38	31.17	30.94	31.14	31.08	31.22	31.27	31.52	31.38
TiO2	0.01	0.01	0.01	0.01	0.01	0.01	0.01	0.01	0.01	0.01	0.01
ZrO2	66.89	66.55	66.80	66.46	66.55	66.65	66.87	66.77	66.86	67.08	67.14
FeO	0.01	0.01	0.01	0.13	b.d.	b.d.	b.d.	0.01	b.d.	0.10	0.03
CaO	0.01	0.04	0.00	0.02	0.05	0.02	0.02	0.03	0.03	0.05	0.02
PbO	0.02	0.02	-	-	0.01	0.01	-	0.01	b.d.	-	-
UO2	-	-	-	-	-	-	-	-	-	-	-
ThO2	0.04	0.07	-	0.16	-	-	0.09	0.08	0.07	-	-
Y2O3	-	-	-	-	-	-	-	-	-	-	-
Yb2O3	0.03	-	-	0.04	-	0.08	-	-	-	0.05	0.05
HfO2	0.55	0.57	0.54	0.58	0.58	0.56	0.58	0.57	0.58	0.50	0.46
Total	98.76	98.50	98.76	98.58	98.16	98.50	98.64	98.72	98.84	99.30	99.10
Numbers of ions on the basis of 16O											
Si	3.90	3.91	3.92	3.91	3.89	3.90	3.89	3.90	3.90	3.91	3.90
Ti	0.001	0.001	0.001	0.001	0.001	0.001	0.001	0.001	0.001	0.001	0.001
Zr	4.08	4.06	4.06	4.06	4.08	4.07	4.08	4.07	4.07	4.06	4.07
Fe2+	0.001	0.001	0.001	0.014	-	-	-	0.001	-	0.01	0.004
Ca	0.002	0.006	0.001	0.002	0.006	0.003	0.002	0.004	0.004	0.007	0.003
Th	0.001	0.002	-	0.004	-	-	0.003	0.002	0.002	-	-
Y	-	-	-	-	-	-	-	-	-	-	-
Yb	0.001	-	-	0.001	-	0.003	-	-	-	0.002	0.002
Hf	0.02	0.02	0.02	0.02	0.02	0.02	0.02	0.02	0.02	0.02	0.02
Total	8	8	8	8	8	8	8	8	8	8	8

b.d. :below deection

Table 1: Continued

Rock type	Si-rich Carbonatite									
Sample	IC2-9Ag. Z1.3	IC2-9Ag. Z1.4	IC2-9Ag. Z1.5	IC2-9Ag. Z1.6	IC2-9Ag. Z3.1	IC2-9Ag. Z3.2	IC2-9Ag. Z3.3	IC2-9Ag. Z3.4	IC2-9Ag. Z3.5	IC2-9Ag. Z3.6
Type	Rim	Core	Middle	Rim	Rim	Core	Rim	Core	Rim	Rim
SiO2	31.20	25.46	31.24	31.58	31.71	31.57	31.37	31.72	31.56	31.98
TiO2	0.02	b.d.	0.01	0.02	0.01	0.01	0.01	0.01	0.01	0.01
ZrO2	67.23	56.32	67.14	66.28	66.63	66.85	67.60	66.61	66.34	65.69
FeO	0.03	0.01	0.02	0.05	-	b.d.	0.01	0.01	0.08	0.12
CaO	0.10	10.27	0.04	0.06	0.04	0.01	0.03	0.01	0.04	0.07
PbO	-	0.01	b.d.	-	-	b.d.	-	0.01	-	-
UO2	-	-	-	-	-	-	-	-	-	-
ThO2	-	0.18	-	-	-	-	-	-	-	-
Y2O3	-	-	-	-	-	-	-	-	0.02	-
Yb2O3	-	-	-	0.02	-	-	0.11	-	0.01	-
HfO2	0.55	0.52	0.56	0.58	0.56	0.48	0.49	0.49	0.47	0.46
Total	99.12	92.79	99.00	98.58	98.94	98.92	99.63	98.87	98.53	98.32
Numbers of ions on the basis of 16O										
Si	3.89	3.47	3.89	3.94	3.94	3.93	3.89	3.94	3.94	3.98
Ti	0.001	0.000	0.001	0.001	0.001	0.001	0.001	0.001	0.001	0.001
Zr	4.08	3.75	4.08	4.03	4.04	4.05	4.09	4.04	4.04	3.99
Fe2+	0.003	0.002	0.002	0.005	-	-	0.001	0.001	0.008	0.012
Ca	0.013	1.502	0.005	0.009	0.005	0.001	0.004	0.001	0.005	0.010
Th	-	0.006	-	-	-	-	-	-	-	-
Y	-	-	-	-	-	-	-	-	0.002	-
Yb	-	-	-	0.001	-	-	0.004	-	-	-
Hf	0.02	0.02	0.02	0.02	0.02	0.02	0.02	0.02	0.02	0.02
Total	8	9	8	8	8	8	8	8	8	8

b.d. :below deection

Table 1: Continued

Rock type	Red Syenite										
Sample	IC2-6A. Z2.1	IC2-6A. Z2.2	IC2-6A. Z2.3	IC2-6A. Z2.4	IC2-6A. Z2.5	IC2-6A. Z1.1	IC2-6A. Z1.2	IC2-6A. Z1.3	IC2-6A. Z1.4	IC2-6A. Z3.1	IC2-6A. Z3.2
Type	Rim	mant	core	core	Rim	Rim	core	core	Rim	Rim	core
SiO2	31.29	31.23	31.15	31.08	31.26	31.33	31.12	31.16	31.16	31.09	31.38
TiO2	0.02	0.02	0.01	0.02	0.01	0.02	0.02	0.02	0.02	0.02	0.02
ZrO2	66.36	66.29	66.33	65.95	66.48	66.60	64.38	67.93	66.83	66.38	66.12
FeO	0.03	0.02	0.04	0.04	0.04	0.08	0.07	0.07	0.05	0.01	b.d.
CaO	0.01	0.02	0.02	0.01	0.01	0.01	0.29	0.16	b.d.	0.01	0.01
PbO	0.10	0.13	0.07	0.33	0.14	0.07	0.04	0.03	0.06	-	0.02
UO2	-	0.01	-	0.54	0.06	-	-	-	-	-	-
ThO2	0.08	-	0.05	-	-	0.07	0.06	-	-	-	0.18
Y2O3	-	0.02	0.01	0.12	0.01	0.04	0.03	0.01	0.03	-	b.d.
Yb2O3	b.d.	0.11	-	b.d.	b.d.	0.01	b.d.	0.08	-	0.01	-
HfO2	1.19	1.21	1.06	0.93	0.99	0.97	1.03	1.23	0.99	0.97	1.06
Total	99.09	99.06	98.75	99.02	99.00	99.20	97.03	100.69	99.14	98.49	98.80
Numbers of ions on the basis of 16O											
Si	3.91	3.91	3.90	3.90	3.91	3.91	3.95	3.85	3.89	3.90	3.92
Ti	0.002	0.002	0.001	0.002	0.001	0.002	0.002	0.001	0.002	0.002	0.002
Zr	4.04	4.04	4.05	4.03	4.05	4.05	3.98	4.09	4.07	4.06	4.03
Fe2+	0.003	0.002	0.004	0.005	0.004	0.009	0.007	0.007	0.005	0.001	-
Ca	0.002	0.003	0.003	0.001	0.001	0.002	0.040	0.021	0.001	0.002	0.001
Th	0.002	-	0.001	-	-	0.002	0.002	-	-	-	0.005
Y	-	0.001	0.001	0.008	0.001	0.003	0.002	0.000	0.002	-	-
Yb	-	0.004	-	-	-	-	-	0.003	-	-	-
Hf	0.04	0.04	0.04	0.03	0.04	0.03	0.04	0.04	0.04	0.03	0.04
Total	8	8	8	8	8	8	8	8	8	8	8

b.d. :below deection

Table 1: Continued

Rock type	Red Syenite										
Sample	IC2-6A. Z3.3	IC2-6A. Z3.4	IC2-6A. Z3.5	IC2-6A. Z4.1	IC2-6A. Z4.2	IC2-6A. Z4.3	IC2-6A. Z4.4	IC2-6A. Z4.5	IC2-6A. Z4.6	IC2-6A. Z5.1	IC2-6A. Z5.2
Type	Rim	mant	Rim	Rim	mant	core	Rim	core	Rim	Rim	Rim
SiO2	31.14	31.18	31.22	31.09	31.34	31.19	31.25	31.15	31.20	31.22	31.11
TiO2	0.01	0.02	0.02	0.02	0.02	0.01	0.02	0.02	0.01	0.02	0.01
ZrO2	66.51	66.59	66.37	66.67	66.95	66.49	66.67	66.80	66.81	66.55	66.87
FeO	0.01	0.01	0.01	0.06	0.20	0.13	0.08	0.04	0.02	0.01	0.00
CaO	0.01	0.01	0.02	0.01	0.01	0.01	0.01	0.01	0.01	b.d.	0.02
PbO	b.d.	0.02	0.02	0.04	0.07	0.02	0.03	0.05	0.04	0.02	0.03
UO2	-	-	-	-	-	-	-	-	-	-	-
ThO2	-	0.03	-	-	0.11	0.09	0.26	-	-	-	0.02
Y2O3	-	-	0.01	0.03	0.02	0.01	0.02	0.04	0.02	-	-
Yb2O3	0.10	-	-	0.06	0.02	-	0.07	-	0.08	-	0.03
HfO2	1.01	0.97	1.00	0.95	0.94	0.98	0.98	0.97	1.01	1.04	1.03
Total	98.80	98.83	98.68	98.92	99.67	98.93	99.39	99.08	99.19	98.87	99.11
Numbers of ions on the basis of 16O											
Si	3.90	3.90	3.91	3.89	3.89	3.90	3.90	3.89	3.89	3.90	3.89
Ti	0.001	0.002	0.002	0.002	0.002	0.001	0.002	0.002	0.001	0.002	0.001
Zr	4.06	4.06	4.05	4.07	4.06	4.05	4.05	4.07	4.06	4.06	4.07
Fe2+	0.001	0.001	0.001	0.007	0.021	0.014	0.008	0.004	0.002	0.001	0.000
Ca	0.001	0.002	0.003	0.001	0.001	0.001	0.002	0.001	0.001	0.001	0.002
Th	-	0.001	-	-	0.003	0.003	0.007	-	-	-	-
Y	-	-	0.001	0.002	0.002	0.001	0.002	0.003	0.001	-	-
Yb	0.004	-	-	0.002	0.001	-	0.003	-	0.003	-	0.001
Hf	0.04	0.03	0.04	0.03	0.03	0.03	0.03	0.03	0.04	0.04	0.04
Total	8	8	8	8	8	8	8	8	8	8	8

b.d. :below deection

Table 1: Continued

Rock type	Red Syenite										
Sample	IC2-6A. Z5.3	IC2-6A. Z5.4	IC2-6A. Z5.5	IC2-6A. Z5.6	IC2-6A. Z5.7	IC2-6A. Z6.1	IC2-6A. Z6.2	IC2-6A. Z6.3	IC2-6A. Z6.4	IC2-6A. Z6.5	IC2-6A. Z6.6
Type	Middle	Core	Middle	Rim	Rim	Rim	Middle	Core	Core	Rim	Rim
SiO2	31.34	31.48	31.17	31.14	31.07	30.99	31.16	31.34	31.20	31.19	31.09
TiO2	0.01	0.02	0.01	0.02	0.01	0.01	0.02	0.01	0.02	0.01	0.02
ZrO2	66.51	66.23	66.35	66.60	66.58	69.17	67.15	66.71	66.59	66.71	66.31
FeO	b.d.	-	0.02	0.01	0.02	0.02	0.01	0.01	0.01	0.02	0.01
CaO	b.d.	0.01	0.02	0.01	0.05	0.01	0.02	b.d.	0.01	0.01	b.d.
PbO	0.01	0.02	0.02	0.03	0.02	0.05	0.02	0.02	0.05	0.03	0.03
UO2	-	-	-	-	-	-	-	-	-	-	-
ThO2	0.13	0.13	-	-	-	0.12	0.15	-	-	-	0.02
Y2O3	-	0.03	b.d.	0.04	0.02	0.01	0.02	0.01	0.02	0.02	0.02
Yb2O3	0.02	0.04	-	0.01	-	0.05	-	0.03	-	-	-
HfO2	1.03	1.07	1.07	1.02	1.07	0.98	0.98	1.01	1.03	1.01	1.03
Total	99.05	99.02	98.66	98.88	98.84	101.41	99.53	99.13	98.94	99.00	98.53
Numbers of ions on the basis of 16O											
Si	3.91	3.93	3.90	3.90	3.89	3.81	3.88	3.91	3.90	3.90	3.90
Ti	0.001	0.002	0.001	0.001	0.001	0.001	0.002	0.001	0.002	0.001	0.002
Zr	4.05	4.03	4.05	4.06	4.06	4.15	4.08	4.05	4.06	4.06	4.06
Fe2+	0.000	-	0.002	0.001	0.002	0.002	0.001	0.001	0.001	0.002	0.002
Ca	0.000	0.001	0.003	0.001	0.006	0.001	0.002	-	0.001	0.001	-
Th	0.004	0.004	-	-	-	0.003	0.004	-	-	-	0.001
Y	-	0.002	-	0.003	0.001	0.001	0.001	-	0.001	0.001	0.001
Yb	0.001	0.001	-	-	-	0.002	-	0.001	-	-	-
Hf	0.04	0.04	0.04	0.04	0.04	0.03	0.03	0.04	0.04	0.04	0.04
Total	8	8	8	8	8	8	8	8	8	8	8

b.d. :below deection

Table 1: Continued

Rock type	Red Syenite										
Sample	IC2-6A. Z7.1	IC2-6A. Z7.2	IC2-6A. Z7.3	IC2-6A. Z7.4	IC2-6A. Z7.5	IC2-6A. Z7.6	IC2-6A. Z7.7	IC2-6A. Z7.8	IC2-6A. Z7.9	IC2-6A. Z7.10	IC2-6A. Z7.11
Type	Rim	Core	Rim	Rim	Rim	Middle	Core	Rim	Rim	Rim	Rim
SiO2	31.36	31.33	31.27	31.61	30.89	31.12	30.60	29.60	31.19	30.36	31.00
TiO2	0.02	0.02	0.02	0.01	0.01	0.02	0.02	0.00	0.02	0.00	0.01
ZrO2	66.80	66.26	66.42	67.03	66.09	66.21	65.86	62.92	66.69	61.95	66.34
FeO	0.02	0.02	0.02	0.03	0.13	0.05	0.14	0.28	0.06	0.95	0.07
CaO	0.01	0.02	0.02	0.07	0.24	0.02	0.10	0.42	0.00	1.40	0.01
PbO	0.04	0.06	-	0.01	0.08	0.04	0.21	0.22	0.08	0.13	-
UO2	-	-	-	-	-	-	0.17	0.21	-	-	-
ThO2	-	-	-	-	0.12	-	0.13	-	-	-	-
Y2O3	0.02	-	-	0.05	0.30	-	0.10	0.13	-	0.35	b.d.
Yb2O3	-	-	0.07	0.03	0.15	0.01	-	0.01	0.08	0.10	0.05
HfO2	1.06	1.18	1.08	1.04	0.98	1.21	1.15	1.07	1.15	0.99	0.96
Total	99.31	98.89	98.90	99.88	98.99	98.69	98.48	94.86	99.28	96.22	98.44
Numbers of ions on the basis of 16O											
Si	3.90	3.92	3.91	3.91	3.87	3.90	3.87	3.88	3.89	3.91	3.89
Ti	0.002	0.002	0.002	0.001	0.001	0.002	0.002	0.000	0.002	0.000	0.001
Zr	4.05	4.04	4.05	4.04	4.04	4.05	4.06	4.02	4.06	3.89	4.06
Fe2+	0.002	0.002	0.002	0.003	0.014	0.006	0.015	0.031	0.007	0.102	0.007
Ca	0.001	0.003	0.003	0.010	0.033	0.003	0.014	0.059	-	0.194	0.002
Th	-	-	-	-	0.003	-	0.004	-	-	-	-
Y	0.001	-	-	0.003	0.020	-	0.007	0.009	-	0.024	-
Yb	-	-	0.003	0.001	0.006	0.000	-	0.001	0.003	0.004	0.002
Hf	0.04	0.04	0.04	0.04	0.04	0.04	0.04	0.04	0.04	0.04	0.03
Total	8	8	8	8	8	8	8	8	8	8	8

b.d. :below deection

Table 1: Continued

Rock type	Red Syenite										
Sample	IC2-6A. Z7.12	IC2-6A. Z7.13	IC2-6A. Z7.14	IC2-6A. Z7.15	IC2-6A. Z7.16	IC2-6A. Z10.1	IC2-6A. Z10.2	IC2-6A. Z10.3	IC2-6A. Z10.4	IC2-6A. Z10.5	IC2-6A. Z8.1
Type	Middle	Core	Middle	Rim	Rim	Rim	Core	Rim	Rim	Core	Rim
SiO2	30.96	30.54	30.96	31.05	30.72	31.39	28.86	30.98	30.79	31.23	31.14
TiO2	0.01	0.01	0.01	0.02	0.01	0.01	0.02	0.02	0.01	0.02	0.02
ZrO2	67.11	66.26	66.37	66.42	64.93	66.60	63.05	67.21	65.90	66.78	66.80
FeO	0.10	0.09	0.06	0.08	1.25	0.09	0.47	0.09	0.08	0.05	0.11
CaO	0.03	0.02	b.d.	0.02	0.14	0.01	2.60	0.04	0.02	0.03	0.04
PbO	0.15	0.11	0.14	-	0.13	0.04	0.16	0.01	0.15	0.01	0.10
UO2	0.02	0.03	0.06	-	0.00	-	0.44	-	0.18	-	-
ThO2	0.11	-	0.14	-	0.29	0.12	-	-	-	-	-
Y2O3	0.05	0.01	0.11	-	0.11	-	0.12	b.d.	0.10	-	0.04
Yb2O3	0.09	-	-	-	0.07	0.06	0.08	0.02	0.09	-	0.03
HfO2	1.14	1.48	1.19	0.94	1.06	1.01	1.08	0.95	1.19	1.01	1.07
Total	99.76	98.56	99.04	98.52	98.72	99.34	96.87	99.34	98.51	99.12	99.35
Numbers of ions on the basis of 16O											
Si	3.86	3.86	3.88	3.90	3.87	3.91	3.74	3.87	3.88	3.90	3.88
Ti	0.001	0.001	0.001	0.002	0.001	0.001	0.002	0.001	0.001	0.001	0.002
Zr	4.08	4.08	4.06	4.06	3.99	4.04	3.99	4.09	4.05	4.06	4.06
Fe2+	0.010	0.010	0.006	0.008	0.132	0.010	0.051	0.010	0.008	0.005	0.012
Ca	0.004	0.003	-	0.002	0.019	0.002	0.361	0.006	0.003	0.003	0.005
Th	0.003	-	0.004	-	0.008	0.003	-	-	-	-	-
Y	0.003	0.001	0.007	-	0.007	-	0.008	-	0.007	-	0.003
Yb	0.003	-	-	-	0.003	0.002	0.003	0.001	0.003	-	0.001
Hf	0.04	0.05	0.04	0.03	0.04	0.04	0.04	0.03	0.04	0.04	0.04
Total	8	8	8	8	8	8	8	8	8	8	8

b.d. :below deection

Table 1: Continued

Rock type	Red Syenite										
Sample	IC2-6A. Z8.2	IC2-6A. Z8.3	IC2-6A. Z8.4	IC2-6A. Z8.5	IC2-6A. Z8.6	IC2-6A. Z8.7	IC2-6A. Z8.8	IC2-6A. Z8.9	IC2-6A. Z9.1	IC2-6A. Z9.2	IC2-6A. Z9.3
Type	Core	Rim	Rim	Rim	Rim	Core	Rim	Rim	Rim	Middle	Core
SiO2	31.38	31.27	31.10	31.19	31.51	31.59	31.30	31.26	31.28	30.05	31.12
TiO2	0.01	0.02	0.02	0.02	0.01	0.01	0.02	0.02	0.02	0.01	0.02
ZrO2	66.53	66.79	65.53	66.40	66.45	66.22	66.73	66.48	66.66	69.39	67.05
FeO	0.12	0.05	0.10	0.10	0.26	0.13	0.07	0.08	0.02	0.02	0.01
CaO	0.01	0.02	0.06	0.01	0.01	0.01	0.01	0.01	0.01	0.02	b.d.
PbO	0.06	0.05	0.07	0.05	0.01	0.02	0.07	0.03	0.02	0.05	0.05
UO2	-	-	-	-	-	-	-	-	-	-	-
ThO2	0.04	-	-	0.07	0.29	0.07	0.05	-	0.06	-	-
Y2O3	b.d.	0.01	0.08	-	-	-	b.d.	-	-	0.01	0.02
Yb2O3	-	0.10	0.04	-	-	0.01	-	-	0.01	0.05	-
HfO2	1.18	1.06	1.01	1.05	0.96	1.12	0.94	1.12	0.95	1.00	0.94
Total	99.35	99.36	98.00	98.89	99.51	99.18	99.19	98.99	99.01	100.59	99.21
Numbers of ions on the basis of 16O											
Si	3.91	3.90	3.92	3.90	3.92	3.93	3.90	3.90	3.90	3.74	3.88
Ti	0.001	0.002	0.002	0.002	0.001	0.001	0.002	0.001	0.001	0.001	0.001
Zr	4.04	4.06	4.03	4.05	4.03	4.02	4.06	4.05	4.06	4.21	4.08
Fe2+	0.012	0.005	0.011	0.010	0.027	0.013	0.008	0.008	0.002	0.002	0.001
Ca	0.002	0.002	0.008	0.001	0.001	0.001	0.002	0.001	0.001	0.002	-
Th	0.001	-	-	0.002	0.008	0.002	0.001	-	0.002	-	-
Y	-	-	0.005	-	-	-	-	-	-	0.001	0.001
Yb	-	0.004	0.001	-	-	-	-	-	-	0.002	-
Hf	0.04	0.04	0.04	0.04	0.03	0.04	0.03	0.04	0.03	0.04	0.03
Total	8	8	8	8	8	8	8	8	8	8	8

b.d. :below deection

Table 1: Continued

Rock type	Red Syenite										
Sample	IC2-6A. Z9.5	IC2-6A. Z9.6	IC2-6A-Z9.1	IC2-6A-Z9.2	IC2-6A-Z9.3	IC2-6A-Z9.4	IC2-6A-Z9.5	IC2-6A-Z9.6	IC2-6A-Z9.7	IC2-6A-Z9.8	IC2-6A-Z9.9
Type	Middle	Rim	Line5	Line5	Line5	Line5	Line5	Line5	Line5	Line5	Line5
SiO2	31.03	31.15	31.57	31.68	31.44	31.41	31.27	31.30	31.27	31.32	31.28
TiO2	0.02	0.01	0.01	0.02	0.02	0.02	0.01	0.01	0.02	0.02	0.01
ZrO2	66.83	66.93	65.63	65.60	65.39	65.40	64.99	65.43	65.23	65.65	65.56
FeO	0.01	0.02	0.02	0.02	0.02	0.01	0.01	0.01	0.01	0.01	0.01
CaO	0.01	0.01	0.01	0.01	0.01	0.02	0.01	0.01	0.01	0.01	0.01
PbO	b.d.	-	b.d.	0.00	0.03	0.04	0.02	0.01	0.04	0.03	0.02
UO2	-	-	-	-	-	-	-	-	-	-	-
ThO2	-	0.10	0.16	-	-	b.d.	0.02	0.05	-	0.04	0.07
Y2O3	-	b.d.	b.d.	-	-	-	-	-	0.01	0.01	0.01
Yb2O3	0.08	-	-	-	-	0.09	-	-	0.01	0.12	-
HfO2	1.01	0.93	1.00	1.03	1.04	1.05	1.03	1.02	1.01	1.02	1.00
Total	98.99	99.15	98.47	98.39	97.97	98.07	97.39	97.87	97.65	98.23	98.01
Numbers of ions on the basis of 16O											
Si	3.88	3.89	3.95	3.96	3.95	3.95	3.95	3.94	3.95	3.93	3.94
Ti	0.002	0.001	0.001	0.002	0.002	0.002	0.001	0.001	0.002	0.001	0.001
Zr	4.08	4.07	4.01	4.00	4.01	4.01	4.01	4.02	4.01	4.02	4.02
Fe2+	0.002	0.002	0.002	0.002	0.002	0.001	0.001	0.001	0.001	0.001	0.001
Ca	0.002	0.001	0.002	0.001	0.002	0.003	0.001	0.001	0.001	0.001	0.001
Th	-	0.003	0.005	-	-	-	0.001	0.001	-	0.001	0.002
Y	-	-	-	-	-	-	-	-	-	0.000	0.001
Yb	0.003	-	-	-	-	0.003	-	-	-	0.005	-
Hf	0.04	0.03	0.04	0.04	0.04	0.04	0.04	0.04	0.04	0.04	0.04
Total	8	8	8	8	8	8	8	8	8	8	8

b.d. :below deection

Table 1: Continued

Rock type	Red Syenite										
Sample	IC2-6A-Z9.10	IC2-6A-Z9.11	IC2-6A-Z9.12	IC2-6A-Z9.13	IC2-6A-Z9.14	IC2-6A-Z9.15	IC2-6A-Z9.16	IC2-6A-Z9.17	IC2-6A-Z9.18	IC2-6A-Z9.19	IC2-6A-Z9.20
Type	Line5	Line5	Line5	Line5	Line5	Line5	Line5	Line5	Line5	Line5	Line5
SiO2	31.29	31.16	31.09	30.87	27.65	25.44	26.81	25.73	26.23	24.71	24.68
TiO2	0.02	0.02	0.02	0.01	0.02	0.03	0.29	0.04	0.01	0.01	0.04
ZrO2	65.66	65.64	65.52	65.77	67.00	61.97	59.32	63.26	65.03	65.95	51.14
FeO	0.01	0.01	0.01	0.01	0.01	0.02	0.03	0.01	0.01	0.01	0.02
CaO	0.01	0.01	0.01	b.d.	0.01	0.05	0.09	0.05	0.04	0.07	0.18
PbO	0.03	0.05	0.04	0.04	0.05	0.04	0.04	0.03	0.03	-	0.01
UO2	-	-	-	-	-	-	-	-	-	-	-
ThO2	-	0.08	0.05	0.10	0.05	0.17	-	0.13	0.22	0.18	-
Y2O3	0.02	b.d.	0.01	0.02	0.03	0.01	0.01	0.01	-	0.01	0.02
Yb2O3	0.14	-	b.d.	-	0.13	0.07	0.08	0.10	0.09	-	-
HfO2	0.99	0.98	0.98	0.99	1.04	1.01	1.01	1.07	1.11	1.06	0.97
Total	98.18	97.97	97.76	97.84	96.04	88.83	87.69	90.45	92.79	92.05	77.09
Numbers of ions on the basis of 16O											
Si	3.93	3.93	3.93	3.90	3.64	3.63	3.81	3.61	3.60	3.45	3.95
Ti	0.002	0.002	0.002	0.001	0.002	0.003	0.031	0.004	0.001	0.001	0.005
Zr	4.02	4.03	4.03	4.05	4.31	4.31	4.11	4.33	4.35	4.49	3.99
Fe2+	0.001	0.001	0.001	0.001	0.001	0.002	0.003	0.002	0.001	0.001	0.003
Ca	0.001	0.001	0.001	0.001	0.001	0.007	0.013	0.007	0.007	0.011	0.032
Th	-	0.002	0.001	0.003	0.002	0.005	-	0.004	0.007	0.006	-
Y	0.002	-	0.001	0.002	0.002	0.001	0.001	0.001	-	-	0.001
Yb	0.005	-	-	-	0.005	0.003	0.003	0.004	0.004	-	-
Hf	0.04	0.04	0.04	0.04	0.04	0.04	0.04	0.04	0.04	0.04	0.04
Total	8	8	8	8	8	8	8	8	8	8	8

b.d. :below deection

Table 1: Continued

Rock type	Red Syenite										
Sample	IC2-6A-Z9.21	IC2-6A-Z9.22	IC2-6A-Z9.23	IC2-6A-Z9.24	IC2-6A-Z2.1	IC2-6A-Z2.2	IC2-6A-Z2.3	IC2-6A-Z2.4	IC2-6A-Z2.5	IC2-6A-Z2.6	IC2-6A-Z2.7
Type	Line5	Line5	Line5	Line5	Line6	Line6	Line6	Line6	Line6	Line6	Line6
SiO2	28.06	31.29	31.62	31.36	31.55	31.37	31.33	31.37	31.20	30.14	29.60
TiO2	0.13	0.02	0.01	0.01	0.02	0.01	0.02	0.01	0.02	0.02	0.02
ZrO2	63.06	64.24	65.19	65.06	64.92	64.30	64.26	65.38	65.61	65.36	65.68
FeO	0.03	0.02	0.02	0.01	0.03	0.08	0.04	0.02	0.01	0.05	0.05
CaO	0.07	0.01	b.d.	b.d.	0.03	0.10	0.04	0.01	0.03	0.17	0.15
PbO	0.02	0.04	0.02	0.01	0.08	0.07	0.19	0.07	0.07	0.15	0.22
UO2	-	-	-	-	-	-	0.11	-	-	0.07	0.31
ThO2	0.13	-	-	-	0.03	-	0.07	0.16	-	-	0.03
Y2O3	0.02	-	0.01	b.d.	-	0.05	0.05	0.01	b.d.	0.06	0.06
Yb2O3	-	0.01	-	0.01	0.02	-	0.02	-	0.08	0.06	0.12
HfO2	1.07	1.01	1.00	1.00	1.36	1.31	1.37	1.12	1.09	1.06	0.99
Total	92.61	96.66	97.90	97.50	98.06	97.41	97.56	98.17	98.14	97.16	97.23
Numbers of ions on the basis of 16O											
Si	3.79	3.98	3.97	3.96	3.97	3.97	3.97	3.94	3.93	3.86	3.81
Ti	0.013	0.002	0.001	0.001	0.002	0.001	0.002	0.001	0.002	0.002	0.002
Zr	4.15	3.98	3.99	4.00	3.98	3.97	3.97	4.01	4.03	4.08	4.12
Fe2+	0.003	0.002	0.002	0.002	0.003	0.009	0.004	0.002	0.001	0.005	0.005
Ca	0.010	0.002	0.000	0.001	0.004	0.014	0.006	0.001	0.003	0.024	0.021
Th	0.004	-	-	-	0.001	-	0.002	0.005	-	-	0.001
Y	0.001	-	0.001	-	-	0.004	0.003	0.001	-	0.004	0.004
Yb	-	-	-	-	0.001	-	0.001	-	0.003	0.002	0.005
Hf	0.04	0.04	0.04	0.04	0.05	0.05	0.05	0.04	0.04	0.04	0.04
Total	8	8	8	8	8	8	8	8	8	8	8

b.d. :below deection

Table 1: Continued

Rock type	Red Syenite												
Sample	IC2-6A-Z2.8	IC2-6A-Z2.9	IC2-6A-Z2.10	IC2-6A-Z2.11	IC2-6A-Z2.12	IC2-6A-Z2.13	IC2-6A-Z2.14	IC2-6A-Z2.15	IC2-6A-Z2.16	IC2-6A-Z2.17	IC2-6A-Z2.18	IC2-6A-Z2.19	IC2-6A-Z2.20
Type	Line6	Line6	Line6	Line6	Line6	Line6	Line6	Line6	Line6	Line6	Line6	Line6	Line6
SiO2	24.90	26.04	30.79	30.18	29.35	28.64	30.92	31.61	31.19	31.40	31.93	30.73	32.05
TiO2	0.03	0.02	0.01	0.02	0.02	0.02	0.01	0.01	0.01	0.01	0.02	0.00	0.03
ZrO2	63.96	61.20	66.12	66.22	66.06	66.25	63.88	66.37	66.60	66.62	66.68	61.65	64.04
FeO	0.06	0.07	0.03	0.03	0.05	0.17	0.05	0.04	0.05	0.06	0.06	0.21	0.17
CaO	0.48	0.29	0.02	0.04	0.09	0.81	0.37	0.02	0.03	0.01	0.03	0.51	0.29
PbO	0.19	0.18	0.27	0.27	0.26	0.13	0.06	0.04	0.10	0.14	0.08	0.30	0.06
UO2	0.34	0.12	0.30	0.38	0.39	-	-	-	-	0.02	-	0.28	-
ThO2	0.17	-	-	-	0.12	0.22	0.04	0.17	-	0.01	-	0.08	0.02
Y2O3	0.06	0.05	0.08	0.08	0.07	0.02	b.d.	-	0.05	0.04	0.02	0.36	0.36
Yb2O3	0.05	0.03	0.06	0.08	0.07	-	0.08	-	0.04	0.06	0.08	0.05	0.01
HfO2	0.98	1.03	1.00	0.96	0.96	0.99	1.04	1.02	1.01	0.97	0.98	0.95	0.99
Total	91.25	89.04	98.68	98.28	97.48	97.27	96.48	99.30	99.10	99.37	99.90	95.38	98.18
Numbers of ions on the basis of 16O													
Si	3.50	3.69	3.88	3.83	3.78	3.71	3.95	3.93	3.90	3.91	3.94	3.98	4.01
Ti	0.003	0.002	0.001	0.002	0.002	0.001	0.001	0.001	0.001	0.001	0.002	-	0.002
Zr	4.39	4.23	4.06	4.10	4.15	4.18	3.98	4.02	4.06	4.04	4.01	3.90	3.90
Fe2+	0.008	0.008	0.003	0.004	0.005	0.018	0.005	0.004	0.005	0.006	0.006	0.023	0.018
Ca	0.073	0.044	0.002	0.005	0.013	0.112	0.051	0.003	0.003	0.002	0.004	0.070	0.038
Th	0.005	-	-	-	0.003	0.007	0.001	0.005	-	-	-	0.002	0.001
Y	0.005	0.004	0.005	0.005	0.005	0.001	-	-	0.003	0.003	0.002	0.025	0.024
Yb	0.002	0.001	0.002	0.003	0.003	-	0.003	-	0.001	0.002	0.003	0.002	-
Hf	0.04	0.04	0.04	0.03	0.04	0.04	0.04	0.04	0.04	0.03	0.03	0.04	0.04
Total	8	8	8	8	8	8	8	8	8	8	8	8	8

b.d. :below deection

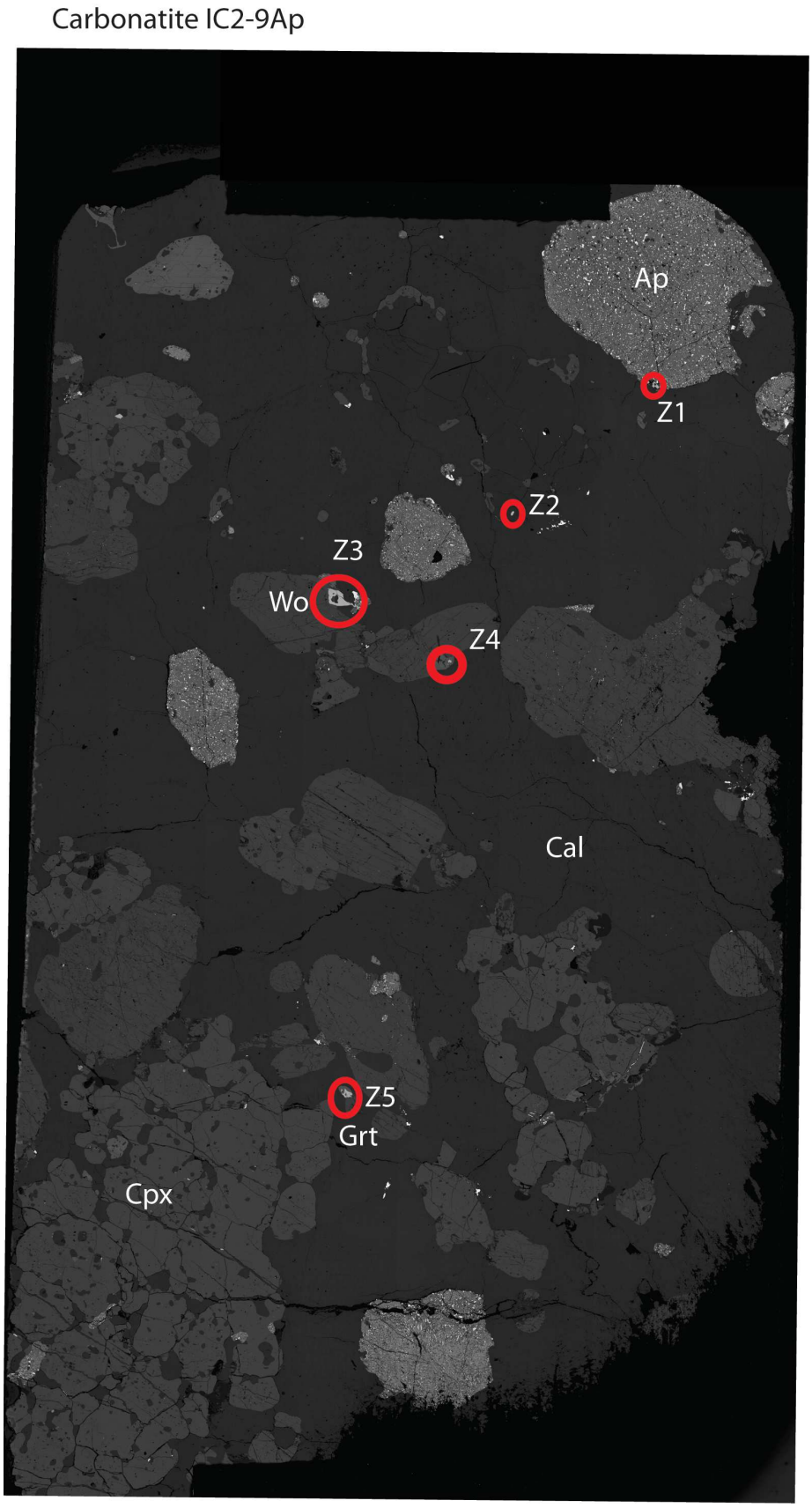

Figure 1 Image MEB-CL de la lame de carbonatite IC2-9Ap et position des zircons analysés

Carbonatite IC2-9Ag

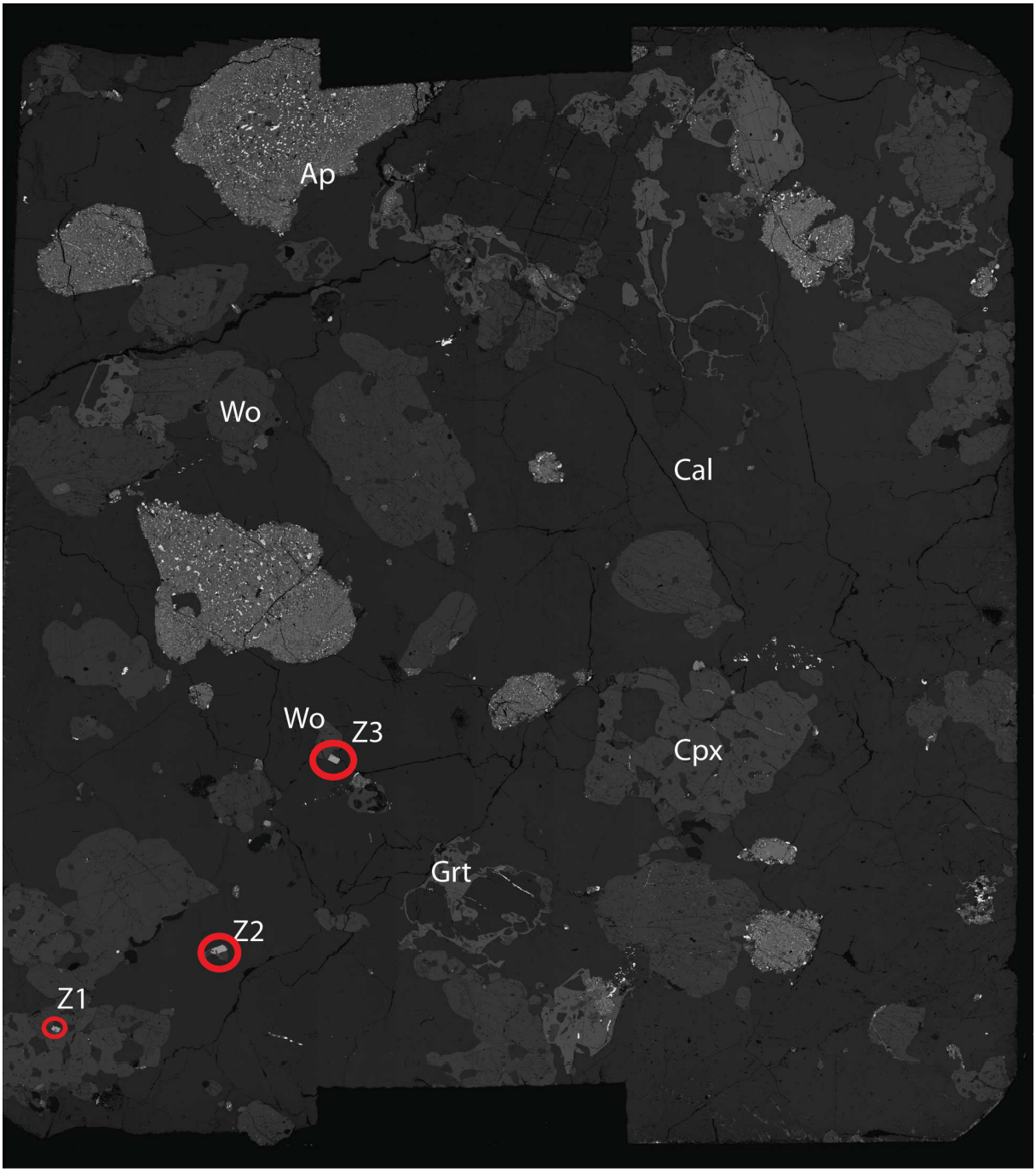

Figure 2 Image MEB-CL de la lame de carbonatite IC2-9Ag et position des zircons analysés

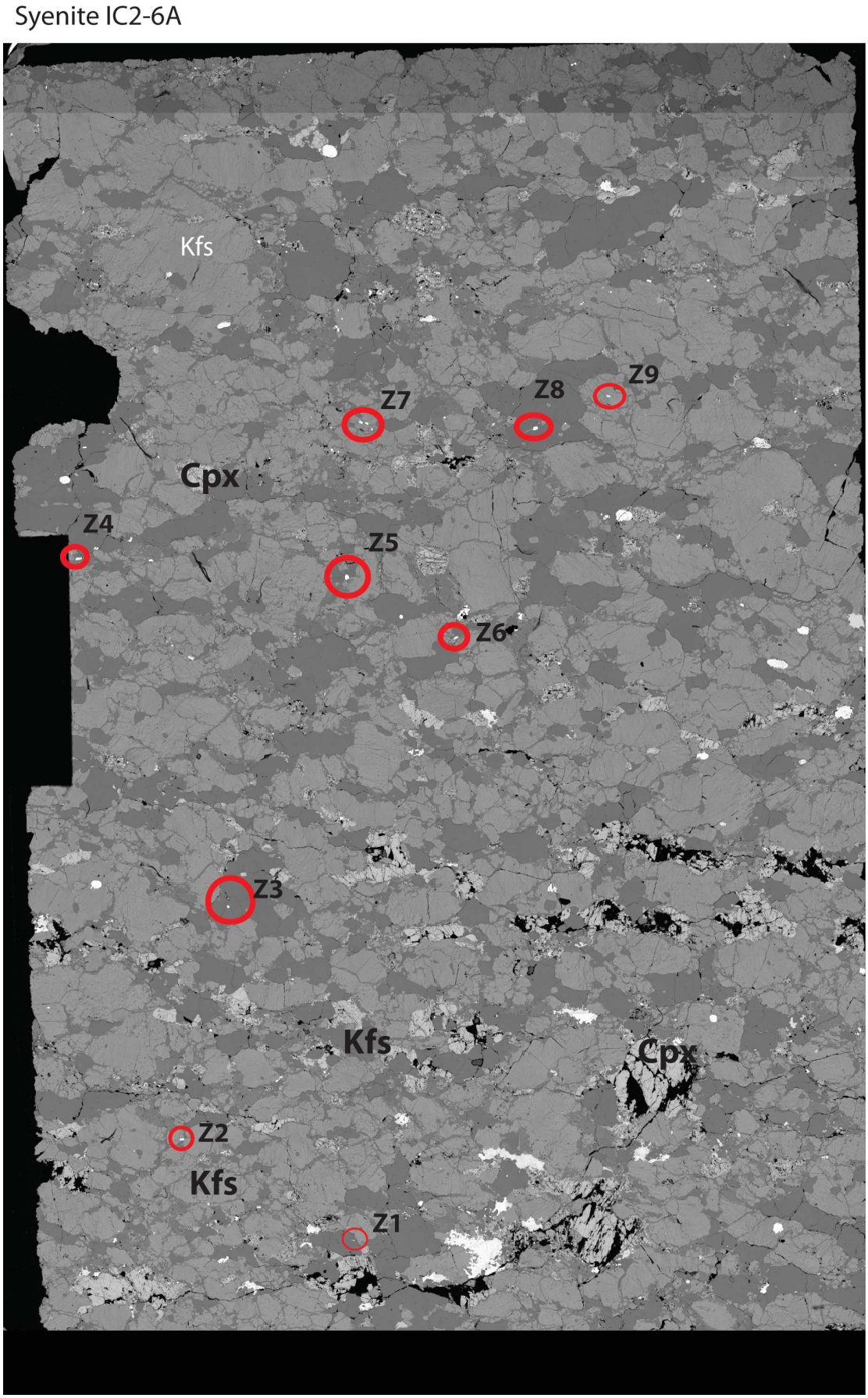

Figure 3 Image MEB-CL de la lame de carbonatite IC2-9Ap et position des zircons analysés

Coordonnées GPS des échantillons étudiés			
Echantillon	**Centre**	**Type pétrographique**	**Point GPS**
IC1-1	Oued Ihouhaouene	pegmatite de syénite	N23° 33' 18,7" E003° 04' 33,7"
IC1-2		carbonatite	N23° 33' 19,8" E003° 04' 35,1"
IC1-3		carbonatite	N23° 33' 21,2" E003° 04' 37,0"
IC1-3D		feldspath pegmatitique	N23° 33' 21,1" E003° 04' 37,5"
IC1-4A		Carbonatite bréchique	N23° 33' 22,1" E003° 04' 39,5"
IC1-5		Carb+Syenite	N23° 33' 20,8" E003° 04' 40,4"
IC1-7A		Dolérite	N23° 33' 23,4" E003° 04' 05,3"
IC1-11		filon de quartz	N23° 33' 29,1" E003° 04' 47,7"
IC1-12A		Syenite rouge	N23° 33' 42,8" E003° 04' 55,0"
IC1-12		Carbonatite bréchique	N23° 33' 42,9" E003° 04' 54,9"
IC1-12E		Carb+Syenite	N23° 33' 41,6" E003° 04' 56,4"
IC1-13		Syénite blanche	N23° 34' 46,62" E003° 5' 1,61"
IC1-13B		pegmatite de syénite	N23° 34' 46,62" E003° 5' 1,61"
IC1-14		quartzite	N23° 34' 46,6" E003° 05' 04,1"
IC1-17A		pegmatite de syénite	N23° 35' 25,8" E003° 00' 39,6"
IC1-24A		Syenite rouge	N23° 34' 44,2" E003° 05' 02,6"
IC2-3A	Wadi Tirahart Sud	Leptynite	N23° 39' 33,7" E003° 17' 54,9"
IC2-5A		cumulats pyroxéniques	N23° 39' 34,4" E003° 17' 58,7"
IC2-7A		pegmatite de syénite	N23° 39' 28,9" E003° 17' 54,8"
IC2-9A		Carb bréchique	N23° 37' 19,7" E003° 16' 08,4"
IC2-10A		Carb + Syenite	N23° 37' 14,0" E003° 16' 06,9"
IC2-11A		carbonatite	N23° 37' 18,1" E003° 16' 18,5"
IC2-15A		Syénite rouge	N23° 36' 41,3" E003° 16' 01,9"
IC2-20A		Carb bréchique	N23° 38' 27,6" E003° 16' 56,3"
IC2-21		carbonatite	N23° 38' 27,6" E003° 16' 56,3"
IC2-27A		Syénite blanche	N23° 38' 27,3" E003° 16' 47,4"
IC3-1A	Wadi Tirahart Nord	Carb bréchique	N23° 40' 22,9" E003° 20' 38,9"
IC3-2A		contact Carb -syenite	N23° 40' 22,3" E003° 20' 38,2"
IC3-4		Syénite rouge	N23° 40' 24,3" E003° 20' 39,8"
IC3-5		Carbonatite	N23° 40' 24,3" E003° 20' 39,8"
IC3-7A		Carbonatite	N23° 40' 24,3" E003° 20' 39,8"
IC3-12		Carb + syénite	N23° 40' 32,6" E003° 20' 59,0"
IC3-15A		Carb bréchique	N23° 40' 46,3" E003° 21' 01,2"
IC3-17		Carb- bréchique	N23° 40' 46,3" E003° 21' 01,2"
IC3-18		Syénite blanche	N23° 40' 05,9" E003° 20' 23,3"
IC3-19A		Carbonatite	N23° 40' 05,9" E003° 20' 23,3"
IC3-20		Carbonatite	N23° 40' 22,4" E003° 20' 49,5"
IC3-21A		Carbonatite	N23° 40' 18,4" E003° 20' 52,3"
IC3-10		Syénite blanche	N23° 40' 22,4" E003° 20' 49,5"
IC3-12B		Syénite blanche	N23° 40' 22,02" E003° 20' 54,9"

Pétrogenèse des carbonatites et magmas alcalins protérozoïques d'Ihouhaouene (terrane de l'In Ouzzal, Hoggar occidental, Algérie)

Asma DJEDDI*

Le craton archéen de l'In Ouzzal représente une succession d'événements intrusifs et métamorphiques depuis l'Eburnéen qui en font un marqueur important des processus géodynamiques à travers les temps géologiques. La région d'Ihouhaouene située au N-W du terrane de l'In Ouzzal en Algérie est unique de par la présence d'intrusions protérozoïques de carbonatites associées à des roches alcalines saturées. Ces carbonatites intracontinentales comptent parmi les plus anciennes et inhabituelles de par leurs diversités et la présence de minéraux à terres rares. Les carbonatites sont pegmatitiques ou bréchiques avec des fragments de syénite. Elles sont des calciocarbonatites composées de calcite (>50 vol.%), apatite, clinopyroxène et wollastonite et sont associées à des syénites rouges ou blanches présentes sous forme massive. Les syénites sont composées d'alternance de niveaux clairs de feldspaths alcalins rouges ou de wollastonites associées aux feldspaths blancs et de niveaux sombres d'apatites et de clinopyroxènes.

Les carbonatites et syénites forment une suite cogénétique caractérisée par une augmentation en SiO_2 et une diminution en CaO et CO_2. Les carbonatites ont des compositions en silice comprises entre 5 et 35 pds.%, 28 et 53 pds.% CaO et 11 à 36 pds.% CO_2. Les syénites montrent une forte teneur en K_2O (12 pds.%) et des teneurs très faibles en Na_2O (1 pds.%). Les carbonatites et syénites sont riches en éléments incompatibles avec des teneurs en REE supérieures à 7000 fois les chondrites et 1000 fois les chondrites dans les syénites, respectivement, et de fortes teneurs en U, Sr et Th. Les éléments en trace dans les minéraux magmatiques (apatite et pyroxène) mettent en évidence des processus complexes à l'origine de ces roches impliquant plusieurs étapes de cristallisation fractionnée et d'immiscibilité à partir d'un magma mélilititique riche en CO_2. Les minéraux des carbonatites riches en silice et des syénites blanches ont des signatures géochimiques similaires et se caractérisent par des rapports élevés en Nb/Ta typiques de magmas riches en carbonate par immiscibilité. Les syénites rouges ont des caractéristiques de liquides silicatés évolués par différentiation. Les minéraux des carbonatites pauvres en silice ont des rapports Nb/Ta très variables, sub-chondritiques (<10), indiquant une cristallisation à partir de liquides très évolués et la présence de magmas carbonatitiques tardifs.

Les apatites, en particuliers, enregistrent divers épisodes magmatiques et également supergènes. Elles présentent dans certaines roches une redistribution et un enrichissement en terres rares variables qui se caractérisent par des exsolutions de britholite dans les carbonatites riches en silice et monazite dans les carbonatites pauvres en silice. Ces exsolutions traduisent des rééquilibrations locales sub-solidus avec des fluides tardi-magmatiques de composition riche en Cl-Th-REE pour l'exsolution de la britholite et S-Ca-P-CO_2 pour les inclusions de monazite.

L'apatite et le zircon présents dans ces roches alcalines et carbonatites, ont permis de déterminer l'âge de mise en place du complexe magmatique de Ihouahouene à 2100 Ma syn-métamorphique et de confirmer l'âge panafricain de son exhumation. L'étude pétrologique, géochimique et géochronologique des carbonatites et syénites d'Ihouhaouene a permis de mettre en évidence l'origine magmatique de ces roches et de définir les interactions fluides-roches supergènes à l'origine des enrichissements en REE. Les carbonatites et syénites d'Ihouahouene proviennent d'un faible taux de fusion partielle d'un manteau Précambrien riche en CO_2. Plusieurs étapes de cristallisation fractionnée et d'immiscibilité ont permis la genèse de ces roches hybrides, piégées le long de grandes zones de cisaillement durant la période de transition Archéen /Eburnéen dans un régime extensif à l'In Ouzzal caractérisé par un environnement granulitique d'ultra-haute-température.

Mots-clés : Carbonatite ; Syénites ; Terres rares ; Immiscibilité ; Hybridation ; Ihouhaouene ; Archéen

* Géosciences Montpellier, Université Montpellier, Place E.

Petrogenesis of Proterozoic carbonatites and alkaline magmas from Ihouhaouene (In Ouzzal terrane, Western Hoggar, Algeria)

Asma DJEDDI *

The In Ouzzal Archaean craton represents a succession of intrusive and metamorphic events since Eburnean, and an important marker of geodynamic processes through geological time. The Ihouhaouene area located in the N-W of In Ouzzal terrane in Algeria is unique by the presence of Proterozoic carbonatite intrusions associated with silica-saturated alkaline rocks. These intracontinental carbonatites are among the oldest and exceptional because of their diversity and the presence of unusual rare earth minerals. Carbonatites are pegmatitic or brecciated with fragments of syenite. They are calciocarbonatites with calcite (> 50 vol.%), apatite, clinopyroxene and wollastonite and are associated with red or white syenites in massive outcrops. Syenites are composed of alternating light levels of red alkaline feldspar or wollastonite associated with white feldspar and dark levels of apatite and clinopyroxene.

Carbonatites and syenites form a cogenetic suite characterized by an increase in silica and decrease in calcium and CO_2 content. The carbonatites have silica content ranging from 5 to 35 wt.%, 28 to 53 wt.% CaO, and 11 to 36 wt.% CO_2. Syenites have high K_2O (12 wt.%) and low Na_2O content (1 wt.%). Carbonatites and syenites have high incompatible element concentrations with high REE content (7000*chondrites and 1000*chondrites, respectively) and high U, Pb, Sr and Th content. Trace elements (eg. Rare Earths, Nb-Ta, Zr-Hf) in magmatic minerals (apatite-pyroxene) of carbonatites and syenites reveal complex magmatic processes at the origin of these rocks involving several stages of fractional crystallization and immiscibility from a CO_2-rich melilititic magma. Silica-rich carbonatites and white syenites are characterized by high Nb/Ta, Y/Zr and Rb/Sr ratios, typical of carbonate-rich magmas by immiscibility. The red syenites have characteristics of immiscible differentiated silicate melt. Silica-poor carbonatite minerals have variable subchondritic Nb/Ta (<10) indicating crystallization from highly evolved liquids and the presence of late carbonatitic magmas.

Apatites, in particular, record various magmatic and supergene processes. They present, in some rocks, redistribution and enrichment in rare earth elements, which are characterized by exsolutions of britholite in silica-rich carbonatites and monazite-quartz-calcite inclusions in silica-poor carbonatites. These minerals reflect local sub-solidus re-equilibration with late-magmatic fluids rich in Cl-Th-REE for the exsolution of britholite and S-Ca-P-CO_2 for monazite inclusions.

The apatite and zircon present in these alkaline and carbonatite rocks, allow determination of the syn-metamorphic crystallization age of the Ihouahouene magmatic complex at 2100 Ma and confirm the pan-African age of its exhumation. The petrological, geochemical and geochronological study of Ihouhaouene carbonatites and syenites highlights the magmatic origin of these rocks and constrains the fluid-rock interactions at sub-solidus conditions leading to REE-enrichment. The carbonatites and syenites result from a low partial melting rate of a CO_2-rich Precambrian mantle. Several fractional crystallization and immiscibility stages allowed the genesis of these hybrid magmas, trapped along large shear-zones during the Archean/Eburnean transition period in the In Ouzzal terrane, characterized by extensive deformation in ultra-high-temperature granulitic environment.

Keywords: Carbonatite; Syenites; Rare earth element; Immiscibility; Hybridization; Ihouhaouene; Archaean

* Géosciences Montpellier, Université Montpellier, Place E. Bataillon, 34095 Montpellier.